

UNCLASSIFIED

AD NUMBER	
AD514827	
CLASSIFICATION CHANGES	
TO:	UNCLASSIFIED
FROM:	CONFIDENTIAL
LIMITATION CHANGES	
TO: Approved for public release; distribution is unlimited. Document partially illegible.	
FROM: Distribution authorized to DoD only; Administrative/Operational Use; 15 APR 1971. Other requests shall be referred to Air Force Cambridge Research Laboratory, Hanscom AFB, MA 01730. Document partially illegible.	
AUTHORITY	
30 Apr 1983, Group 4, DoDD 5200.10; AFGL notice dtd 6 Nov 1980	

THIS PAGE IS UNCLASSIFIED

UNCLASSIFIED

AD NUMBER

AD514827

CLASSIFICATION CHANGES

TO:

CONFIDENTIAL

FROM:

SECRET

AUTHORITY

30 Apr 1974, Group 4, DoDD 5200.10

THIS PAGE IS UNCLASSIFIED

DISCLAIMER NOTICE

THIS DOCUMENT IS THE BEST
QUALITY AVAILABLE.

COPY FURNISHED CONTAINED
A SIGNIFICANT NUMBER OF
PAGES WHICH DO NOT
REPRODUCE LEGIBLY.

MISSING PAGE
NUMBERS ARE BLANK
AND WERE NOT
FILMED

SECURITY

MARKING

The classified or limited status of this report applies to each page, unless otherwise marked.

Separate page printouts MUST be marked accordingly.

THIS DOCUMENT CONTAINS INFORMATION AFFECTING THE NATIONAL DEFENSE OF THE UNITED STATES WITHIN THE MEANING OF THE ESPIONAGE LAWS, TITLE 18, U.S.C., SECTIONS 793 AND 794. THE TRANSMISSION OR THE REVELATION OF ITS CONTENTS IN ANY MANNER TO AN UNAUTHORIZED PERSON IS PROHIBITED BY LAW.

NOTICE: When government or other drawings, specifications or other data are used for any purpose other than in connection with a definitely related government procurement operation, the U.S. Government thereby incurs no responsibility; nor any obligation whatsoever; and the fact that the Government may have formulated, furnished, or in any way supplied the said drawings, specifications, or other data is not to be regarded by implication or otherwise as in any manner licensing the holder or any other person or corporation, or conveying any rights or permission to manufacture, use or sell any patented invention that may in any way be related thereto.

✓
SECRET

AFCRL-70-0496 ✓

SEC No. 5020
Copy No.

**SYSTEM AND INSTRUMENT DESIGN FOR AN EARTH
LIMB MEASUREMENTS PROGRAM (U)**

by

Robert M. Carlson, Joseph S. Titus, Glenn H. Wise

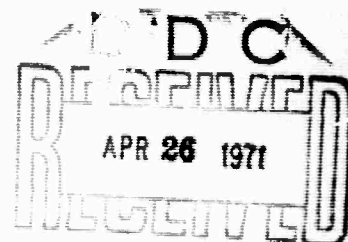
✓ Aerospace Division
Honeywell Incorporated
Minneapolis, Minnesota 55413

Contract No. F19628-69-C-0258 ✓
Project No. 8692

FINAL REPORT

1 April 1969 - 1 January 1970

15 April 1971



The views and conclusions contained in this document are those of the authors and should not be interpreted as necessarily representing the official policies, either expressed or implied, of the Advanced Research Projects Agency or the U. S. Government.

In addition to security requirements which apply to this document and must be met, each transmittal outside the Department of Defense must have prior approval of AFCRL (OPR), L. G. Hanscom Field, Bedford, Massachusetts 01730.

Contract Monitor: Randall E. Murphy
Optical Physical Laboratory

NOTICE

This document contains information affecting the National Defense of the United States within the meaning of the Espionage Laws Title 18, U.S.C. Sections 793-794. Its transmission or the revelation of its contents in any manner to an unauthorized person is prohibited by law.

**GROUP 4
DOWNGRADED AT 3-YEAR INTERVALS,
DECLASSIFIED AFTER 12 YEARS**

Sponsored by
Advanced Research Projects Agency
ARPA Order No. 1366

Monitored by
**AIR FORCE CAMBRIDGE RESEARCH LABORATORIES
UNITED STATES AIR FORCE
BEDFORD, MASSACHUSETTS 01730**

SECRET

DDC CONTROL
NO.
11142

UNCLASSIFIED

Program code	62301D
Effective date of contract	1 April 1969
Contract expiration date	30 January 1970
Principal investigator and phone no	Joseph Titus 617 862-6222 Ext 203
Project scientist or engineer and phone no	Randall E. Murphy 617 861-4903

Qualified requestors may obtain additional copies from the Defense Documentation Center.

CLASSIFICATION

DATE REVIEWED

BY

REASON FOR

DISCONTINUATION

DISTRICT ATTORNEY GENERAL

STATE OF NEW YORK

NO.

FILE NO.

DATE

4

U

UNCLASSIFIED

173
SECRET

18
AFCRL 70-0496

1 SYSTEM AND INSTRUMENT DESIGN FOR AN EARTH
LIMB MEASUREMENTS PROGRAM (U).

by

19 Robert M./Carlson, Joseph S./Titus, Glenn H./Wise

Aerospace Division
Honeywell Incorporated
Minneapolis, Minnesota 55413

15 Contract No. F19628-69-C-0258, ARPA Order - 1366
Project No. 8692

16 AF-3012
17 FINAL REPORT.

18 1 Apr 69 - 1 Jan 70.

19 15 Apr 71

The views and conclusions contained in this document are those of the authors and should not be interpreted as necessarily representing the official policies, either expressed or implied, of the Advanced Research Projects Agency or the U. S. Government.

In addition to security requirements which apply to this document and must be met, each transmittal outside the Department of Defense must have prior approval of AFCRL (OPR), L. G. Hanscom Field, Bedford, Massachusetts 01730.

Contract Monitor: Randall E. Murphy
Optical Physical Laboratory

NOTICE

This document contains information affecting the National Defense of the United States within the meaning of the Espionage Laws Title 18, U.S.C. Sections 793-794. Its transmission or the revelation of its contents in any manner to an unauthorized person is prohibited by law.

GROUP 4
DOWNGRADED AT 3-YEAR INTERVALS
DECLASSIFIED AFTER 12 YEARS

Sponsored by
Advanced Research Projects Agency
ARPA Order No. 1366
Monitored by
AIR FORCE CAMBRIDGE RESEARCH LABORATORIES
UNITED STATES AIR FORCE
BEDFORD, MASSACHUSETTS 01730

DDC CONTROL

11142

402551
SECRET

UNCLASSIFIED

UNCLASSIFIED ABSTRACT

Requirements for a spectral radiometer to measure the earth limb in the long-wavelength infrared have been established. Temporal and spatial sampling requirements for an experimental program to define the variation in the limb radiance have been investigated. An experimental program using probes has been designed to meet these requirements. The conceptual design of a long-wavelength infrared spectral radiometer is included in the experiment design.

UNCLASSIFIED

CONTENTS

	Page
SECTION 1	INTRODUCTION AND SUMMARY
1.1	System Requirements
1.2	Instrument Requirements
1.3	Instrument Design
1.4	System Design
1.5	Program Plan and Costing
SECTION 2	INSTRUMENT REQUIREMENTS
2.1	Viewing Geometry
2.2	Sensitivity Requirements
2.3	Stray Light Attenuation Requirements
2.4	Spectral Attenuation Requirements
2.5	Angular Line-of-Sight Accuracy Requirements
2.5.1	System Coverage Studies
2.5.2	Angular/Radiance Error Correspondence
2.6	Dynamic Range and Amplitude Accuracy Requirements
2.7	Results of Atmospheric Model and Summary of Measured Data
SECTION 3	SYSTEM REQUIREMENTS
3.1	Basis for Sampling Requirements
3.1.1	Low-Altitude Atmospheric Model
3.1.2	Temperature
3.1.3	Radiance Variations
3.1.4	Horizontal and Vertical Distributions
3.1.5	Ozone Concentration
3.2	Number of Profiles per Flight
3.3	Scan Pattern
3.4	Number of Flights
3.4.1	Statistical Analysis of Radiance Variations
3.4.2	Solar Radiation
3.4.3	Rocket Probe Launch Sites and Coverage
3.4.4	Flight Plans
SECTION 4	INSTRUMENT DESIGN
4.1	Background
4.2	Off-Axis Radiation Effects on S/N
4.3	Detector Selection
4.3.1	Detector Mechanisms and Comparison of Detector Types
4.3.2	Detector Load Resistor and Noise
4.4	Diffraction Analysis
4.4.1	General Discussion
4.4.2	Determination of Flux Through the Pinhole
4.4.3	Diffraction Calculations

	Page
4. 5 Off-Axis Radiation	121
4. 5. 1 Scattering	126
4. 5. 2 Baffle Interior Irradiance Analysis	134
4. 5. 3 Integral Limit Functions	139
4. 6 Parametric Analysis	148
4. 6. 1 Radiometric Input	148
4. 6. 2 S/N Consideration When Noise in Signal Cannot be Ignored	148
4. 7 Optical Design	160
4. 7. 1 General Design	160
4. 7. 2 Optical Materials	163
4. 8 Spectral Characteristics and Monochromator Definition	164
4. 8. 1 Proposed Monochromator	164
4. 8. 2 Spectral Separation Tradeoffs	169
4. 8. 3 Monochromator Tradeoffs	170
4. 9 Structural Design	172
4. 9. 1 Optical Housing and Mirrors	172
4. 9. 2 Radiation Shield and Outer Skin	172
4. 9. 3 Mechanical. Thermally Isolated, Support System	173
4. 10 Cryogenic System Design	176
4. 11 Calibration	188
4. 11. 1 Description of Honeywell Chamber	191
4. 11. 2 Calibration Tests	192
 SECTION 5	
SYSTEM DESIGN	194
5. 1 Candidate Rocket Vehicles	194
5. 1. 1 Vehicle Comparison	194
5. 1. 2 Summary and Conclusions	199
5. 2 Selected Vehicle Description	200
5. 3 Auxiliary Subsystems	211
5. 3. 1 Attitude Control Subsystem	214
5. 3. 2 Attitude Determination Subsystem	220
5. 3. 3 Telemetry Subsystem	239
5. 3. 4 Tracking Subsystem	243
5. 3. 5 Electrical Power Subsystem	244
5. 3. 6 Structure	245
 SECTION 6	
PROGRAM PLAN AND COSTING	248
6. 1 Ground Rules	248
6. 2 Statement of Work	250
6. 3 Testing	257
6. 3. 1 Development Testing	257
6. 3. 2 Qualification Testing	258
6. 3. 3 Performance Testing	258
6. 3. 4 Long-Wavelength Infrared (LWIR) Test and Calibration Chamber	259

	Page
6.4 Task Plans	260
6.4.1 System Task	264
6.4.2 Design and Definition	264
6.4.3 Manufacturing	264
6.4.4 Testing	265
6.4.5 Flight Program	268
6.5 Operation and Maintenance Procedures	268
6.6 Configuration Control	268
6.7 Cost Estimate	269
6.7.1 Ten-Flight Program	271
6.7.2 Three-Flight Program	272

REFERENCES

273

APPENDIX A	SPECTRAL RADIANCE AND SIGNAL-TO-NOISE RATIO AS A FUNCTION OF TANGENT HEIGHT	275
------------	--------------------------------------------------------------------------------	-----

UNCLASSIFIED

ILLUSTRATIONS

Figure		Page
1	Radiometer Design	5
2	Limb Measurement Program Viewing Geometry	10
3	Limb View Geometry	11
4	Attenuation Required to Reduce Off-Axis Earth Radiation to NEFD Level	17
5	Attenuation Required within First Degree Off-Axis for IFOV on Horizon	18
6	Attenuation Requirements - Earth-Diffracted Energy	20
7	Photon Flux at Detector in Optical Cavity	21
8	Maximum Spectral Attenuation Requirements	23
9	Sensor Scan Geometry	25
10	Over-the-Horizon Coverage (no overlap)	25
11	Attitude Determination and Boresight Accuracy Requirements	26
12	Located Horizon Standard Deviation versus Input Constant for Eight Locators	29
13	Comparison of Measured and Analytical CO ₂ Horizon Profiles - Goose Bay	30
14	Limb Measurement Program Dynamic Range Requirements	31
15	Radiance Measurement Error Requirements	32
16	Atmospheric Radiance Limb View, Night and Noon - Altitude = 115 km	34
17	Atmospheric Radiance Limb View, Noon - Altitude = 75, 100 and 110 km	34
18	Atmospheric Radiance Limb View, Noon - Altitude = 60 and 70 km	35,
19	Atmospheric Radiance Limb View, Night and Noon - Altitude = 100 km	35

UNCLASSIFIED

Figure		Page
20	Atmospheric Radiance Limb View, Night and Noon - Altitude = 60 and 80 km	36
21	Atmospheric Radiance Limb View, Night and Noon - Altitude = 60 and 105 km	36
22	Atmospheric Radiance Limb View, Night and Noon - Altitude = 75 km	37
23	Limb Radiance Profile - Nitric Oxide, 5.3 microns	37
24	LWIR Radiance Profiles, Upper Atmospheric Model - Noon Conditions	38
25	Horizon Radiance Profile, Nitric Acid (HNO ₃ , 10.5 to 11.7 microns)	41
26	USSR Data Converted to Limb View Radiance	44
27	Predicted Emission From Noctilucent Clouds and Inter- planetary Dust	46
28	Atmospheric Temperature Variations with Latitude	52
29	Atmospheric Temperature Variations with Longitude	52
30	Arctic Temperature Gradients - Latitude = 60°N, Altitude = 50 - 55 km	54
31	Autocorrelation Function for 15-micron CO ₂ Radiance, February - 30 - 40 km	55
32	Horizontal Radiance Distribution - Minimum Tangent Height = 60 km	57
33	Vertical Radiance Distribution - Minimum Tangent Height = 60 km	57
34	Annual Variation of Ozone Concentration - Altitude = 45 km	58
35	Variation in Ozone Concentration at Various Locations - Altitude = 45 km	59
36	Longitudinal Correlation in Ozone Concentration	60
37	Autocorrelation of Ozone Concentration at 51°N and 80.5°W	61

x

UNCLASSIFIED

UNCLASSIFIED

Figure		Page
38	Cross correlation of Ozone Concentration Between 41°N, 105°W and 51°N, 80.5W	62
39	Diurnal Variation of Ozone	63
40	Limb Measurement Scan Pattern	65
41	Alternate Scan Pattern	66
42	Radiance Sampling Error, Arctic Winter	71
43	Probability Estimation Errors	72
44	Daily Solar Radiation at Top of Atmosphere	73
45	Sine of Solar Altitude, Equinoctial	75
46	Sine of Solar Altitude, Summer Solstice	76
47	Sine of Solar Altitude, Winter Solstice	77
48	Geographical Coverage of Probe Vehicle	82
49	Probability of Observing High-Altitude Layers on Any One Flight	86
50	Power Falling onto Detector from Signal plus Diffraction and Scattering, 5.0- to 5.7-micron Band	94
51	Power Falling onto Detector from Signal plus Diffraction and Scattering, 10.0- to 10.8-micron Band	95
52	Power Falling onto Detector from Signal plus Diffraction and Scattering, 17.0- to 18.0-micron Band	96
53	Power Falling onto Detector from Signal plus Diffraction and Scattering, 18.0- to 25.0-micron Band	97
54	Calculated Maximum Detectivity for (Hg, Cd)Te as a Function of Detector Temperature and a Varying Cutoff Wavelength	103
55	Fundamental Limit as a Function of Wavelength and Temperature	104
56	Calculated Comparative Detectivities of Extrinsic and Intrinsic Detectors as a Function of Temperature	105

x

UNCLASSIFIED

UNCLASSIFIED

Figure		Page
57	Basic Optical System Layout	111
58	Cross-sectional Cuts of Equivalent Earth Radiators	111
59	Parameters in Nagaoka's Approach	112
60	Large-Radius Earth Source Rationalization	112
61	Similarity of Proposed TOM System to System Analyzed by Nagaoka	113
62	Diffraction of On-Axis Point Source at Infinity Illuminating a Circular Aperture	115
63	On-Axis Lens Analogy to TOM System	115
64	Power Determination Integral	117
65	Power Integrals	117
66	Comparison of Nagaoka Configuration to TOM	118
67	Effective Circular Planar Earth Source	118
68	Pattern of Diffracted Energy of First Relay Mirror	122
69	Cumulative Signal and Diffraction Energy at First Relay Mirror	123
70	Cavity (Blackbody) Upper Forebaffles	125
71	Cavity (Blackbody) Lower Forebaffles	125
72	Earth-Focused Image Attenuated in Blackbody Cone and Hood	125
73	Light-Scattering Measurement Technique	128
74	Scatter Characteristics of Sulfur Slab	129
75	Radiometer Geometry	135
76	Transfer Geometry	136
77	Receiver-Point Coordinate System	136
78	Angular Subtense Considerations	138
79	Coordinate Transformations	140

UNCLASSIFIED

Figure		Page
80	Irradiance Calculation Computer Program	142
81	Irradiance Along Top Edge of Tube as a Function of Tilt Angle - 5.0-inch Aperture, 36-inch Length	143
82	Irradiance Along Top Edge of Tube as a Function of Tilt Angle - 5.5-inch Aperture, 36-inch Length	144
83	Irradiance Along Top Edge of Tube as a Function of Tilt Angle - 10-inch Aperture, 36-inch Length	145
84	Irradiance Along Top Edge of Tube as a Function of Tilt Angle - 6-inch Aperture, 36-inch Length	146
85	Irradiance Along Top Edge of Tube as a Function of Tilt Angle - 30-inch Aperture, 36-inch Length	147
86	Target-Equivalent Spectral Radiance versus Wavelength Band	150
87	Signal-to-Noise Ratio versus Spectral Bands	161
88	Simplified Optical System Schematic	163
89	Energy Distribution of a Littrow-Mounted Plane Grating, 6.6-micron Blaze	166
90	Energy Distribution of a Littrow-Mounted Plane Grating, 12-micron Blaze	166
91	Optimum Vignetting of Monochromator	168
92	Detector Array Configuration	168
93	Radiometer Support Points	173
94	Load versus Deflective Curve for Belleville Spring	175
95	Helium Cryogenic Refrigeration Schematic	177
96	Temperature-Entropy Diagrams	179
97	Time of Useful Refrigeration	131
98	Time of Pressurization	182
99	Time Factor in Reaching Venting Pressure	183

UNCLASSIFIED

Figure		Page
100	Proposed Heat-Exchange Tube Configuration	185
101	Bond Line - Heat-Exchanger Tubing Fin Top to Inner Tube Bend	185
102	Canted Storage Container Orientation	187
103	Baffle Length	189
104	Calibration Test Chamber	190
105	Rocket Vehicle Payload/Weight Comparisons	195
106	Black Brant V Apogee versus Gross Payload Weight	202
107	Black Brant VB Configuration	203
108	Black Brant VB Apogee versus Payload Weight	203
109	Black Brant VB Acceleration versus Time	205
110	Black Brant VB Standard Nose Assembly Gross Payload X_{cg} versus Gross Payload Weight	206
111	Black Brant VB Roll Rate versus Time	207
112	Black Brant VB Three-Sigma Impact Dispersion	208
113	Black Brant VB Impact Range versus Gross Payload	209
114	Apogee versus Gross Payload Weight for Boosted and Unboosted Black Brant VB	212
115	Black Brant Probe Trajectories	213
116	Proposed Payload Configuration	215
117	Cutaway View of Gnat Gyro	221
118	Booster Longitudinal Acceleration Characteristics	222
119	Typical Installation of ESG System	225
120	Data Processor Signal Flow Chart	226
121	Processor Block Diagram	227

UNCLASSIFIED

Figure		Page
122	Information Flow Diagram	237
123	Telemetry Subsystem Block Diagram	240
124	Integrated Instrument System Program Plan	249
125	Activities Flow Diagram	261
126	Radiometer Flow Plan	262
127	ARCS Flow Plan	263
128	Test Schedule	266
129	Master Test Plan	267
130	Engineering Change Flow Diagram	270

UNCLASSIFIED

Table	TABLES	Page
1	Instrument Requirements Summary	8
2	Noise Equivalent Flux Density (NEFD) Requirements	13
3	Noise Equivalent Radiance (NER) and Tangent Height Requirements	15
4	Tangent Height Error Corresponding to 10-percent Radiance Error	27
5	Maximum Diurnal Radiance Variation	39
6	Summary of USSR Measurements of LWIR Upper-Atmospheric Radiance	43
7	USSR Probe Measurements Maximum Radiant Emittance Observed with Vehicle within Layer and with Horizontal Viewing	43
8	Summary Data on High-Altitude Clouds	45
9	Summary Data on Interplanetary Dust	45
10	Experiment Requirements Summary	48
11	Low-Altitude Atmospheric Model - Geographic/Seasonal Data Variations	50
12	Low-Altitude Atmospheric Model - Statistical Radiance Variations	51
13	Solar Flare Frequency and Duration	79
14	Potential Rocket Launch Sites	81
15	Launch Times and Places with Solar Radiation Fraction	84
16	Descriptive Summary of Instrument Characteristics	91
17	Operational Summary of Instrument Characteristics	92
18	Comparison of Candidate Detectors	99
19	Spectral Bands	149
20	System Losses	159
21	Instrument Tradeoff Factors	165
22	Research Rocket Summary	196
23	Research Rocket Power Plants Summary	197
24	Black Brant V Motor Characteristics	201
25	Typical Black Brant V Performance Data (308-lb gross payload)	201

UNCLASSIFIED

Table		Page
26	Cost of Black Brant V Rockets	210
27	Performance Comparison of Black Brant Vehicles	211
28	Rocket Payload Size Allocations	216
29	Attitude Control Total Impulse Requirements	219
30	Word Control Gating	231
31	System Weight Breakdown	247

UNCLASSIFIED

SECTION 1 INTRODUCTION AND SUMMARY

This study describes the design of an experimental program to define the radiance characteristics of the upper atmosphere using probes. An atmospheric model was developed prior to this study to permit structuring of the experiment around the problem areas and limitation of the experimental parameters. Hard data regarding the constituent distribution and photochemistry of the upper atmosphere is limited, and it was recognized initially in the design of this experiment that the actual data-gathering process should be iterative; i.e., data from early flights should be used to restructure the remaining experiment. To obtain a reasonable cost estimate for the program, a complete program has been defined, assuming that no major change occurs.

During the study, two major areas for tradeoff were encountered. First, probes are not well-suited for the definition of large-scale geographical phenomena and events with a time scale of the order of days, which at least a portion of the model indicates as the scale of the radiance map and its changes. A complete experiment would necessarily involve the use of satellites to define the geographical and midterm temporal variations of the radiance. The following program attempts to define, within reasonable limits, a probe program to provide at least the first approximation to the temporal-geographical radiance map.

The second area of tradeoff is in the spectral definition of the instrument. An experiment designed solely to obtain information relative to the photochemical status of the upper atmosphere would be designed around a high-resolution spectrometer with limited amplitude accuracy, since line shape by itself is highly informative, and absolute amplitude is not of fundamental importance. At the sensitivity levels for a meaningful experiment, high spectral resolution can only be obtained by degrading spatial resolution an order of magnitude or more below that of an operational instrument. Conversely, an experiment designed solely to furnish information for an operational system, with a well-understood photochemical model, would be designed around a broadband window filter radiometer, with absolute amplitude in the window being the prime objective. Spatial resolution would be of the order of an operational instrument. The experiment described below is a compromise, weighted toward operational system considerations. High-resolution spectral knowledge of the window-region absolute radiance is considered to be the key information required, particularly in the wings of the windows.

This information will permit identification of minor species within the window region and allow for design of filters to optimize performance while

UNCLASSIFIED

operating near strong emission bands. Broadband measurement of the emission bands is used to provide information to identify broadly the emission phenomena and permit extension of the data through an atmospheric radiance model to times and locations other than those measured. Since the operational system will not operate in the emission bands, this is considered a secondary measurement.

Because of the orientation toward gathering data of direct utility to operational system design, an initial decision was made to reproduce the viewing geometry of an operational satellite system insofar as possible with available probes. This decision is partly based on data reported by the USSR which indicates that there are layered phenomena in the upper atmosphere. The difference in signal between viewing through a layer, as in an upward-directed instrument, and viewing along a layer can be two or more orders of magnitude, dependent on the thickness of the layer. The maximum altitude of the USSR data are 500 km with most of the data in the 200- to 300-km range. The probe altitudes were then required to be in the lower range, with a goal of reaching altitudes on the order of 500 km.

1.1 SYSTEM REQUIREMENTS

Sampling requirements have been derived from lower atmospheric models, in part, because the available upper atmosphere models show no geographical variation due to lack of data and, in part, because the estimated target and background emissions in the window regions show feasible detection altitudes in the lower atmosphere.

Geographical sampling requirements were obtained using the assumption that variations in the atmospheric emission are random phenomena. It was assumed that the purpose of the experiment was to develop the distribution of radiance as a function of tangent height. Using a single tangent height (60 km) for simplicity and obtaining the radiance at this tangent height from an analytical model with limiting condition inputs, a sample of the distribution of radiance was obtained. To obtain an estimate of the required number of samples to fix the distribution, a chi-square distribution was used to define the error and confidence limits for the estimate of the variance, and a Student's t distribution to define the error in estimating the confidence limits of the mean as a function of the number of samples. For the empirical distribution used, it was found that the required number of samples was several hundred to yield estimation errors of the order of 10% of the estimated radiance variance and mean.

Correlation distances were estimated from 15-micron CO_2 data, Arctic temperature data and ozone distribution. Correlation distances in terms of gradient structure of the order of 800 km were obtained.

UNCLASSIFIED

A strong diurnal variation is anticipated for the nitric oxide, ozone and 10.4-micron carbon dioxide emission bands. A requirement was established for measurement under full sunlit conditions. A minimum of two samples and preferably four is required to define the expected diurnal variation. Long-term temporal sampling requirements were obtained from the correlation of ozone distributions. Correlation times are of the order of three months.

Resolution requirements were derived from the operational use of the data. A requirement for 2-km vertical resolution and up to 10-km horizontal resolution was derived.

1.2 INSTRUMENT REQUIREMENTS

Amplitude accuracy requirements were obtained from the sensitivity of detection system false-alarm rate to background amplitude error. Allowable errors are approximately 10%.

Spectral requirements are defined from two considerations. First, since the data set will be limited, it will not be sufficient to define completely the radiance distribution without extrapolation, and some form of model of atmospheric constituents and reactions will be required to perform this extrapolation. A measurement of the amplitude of the anticipated reactions is required. It has been assumed that the available model of the major emission bands is spectrally accurate, but, because of unknown constituent distributions, it may be significantly in error in amplitude. A measurement of the emission band amplitude is then sufficient to establish constituent distribution. The spectral measurement in emission bands are thus specified to cover the calculated bandspread. Second, it is a primary goal of these measurements to define the radiance in the window region. Three broadband window measurements are specified. In addition, it is necessary to know in detail the structure of the window bands, particularly in the wings near the high-amplitude emission bands. A narrowband measurement across the windows is specified.

One of the major outputs of this experiment is the minimum altitude to which a target can be viewed. Preliminary calculations using the earth limb model indicate that nominal targets can be viewed as low as 1 deg from the earth. The earth emits strongly in the regions of interest, and radiation from the earth is a source of interference, first as a direct addition to the d-c background flux, thus causing an error in the absolute amplitude measurement and second as a noise source, photon flux noise causing errors even in gradient measurements. An analysis of the stray light problem yields a requirement for approximately 10^{10} rejection at 1 to 2 deg off-axis. Diffraction effects were analyzed and it was determined that the diffracted image must be reduced three orders of magnitude at 1 deg off axis to obtain a valid measurement of atmospheric radiance.

UNCLASSIFIED

At the sensitivity levels of interest for this experiment, a cooled radiometer is required. An analysis has been made of the cooling requirements, and a worst-case lower limit of approximately 30° K was derived, with allowances for gradients along the telescope barrel.

1.3 INSTRUMENT DESIGN

The instrument derived from the above requirements is shown in Figure 1. This is an all-reflective system, using a Heschelian primary and parabolic relay system to provide two focal surfaces for stray radiation blocking. A conical blackbody image trap is used in the first focal surface to eliminate scattering from the focussed earth image. Low-scattering (less than one part in 10^4 referenced to the input energy) surfaces are specified for the primary to reduce off-axis energy impinging on the primary and scattered through the field stop. The field stop is used as a pinhole lens in a reflective analog of the Lyot lens used in solar coronagraphs. Stops are placed in the relay system to absorb diffracted energy.

Spectral resolution is obtained with a combination of a grating spectrometer and superimposed spectral filters. The detectors are mercury-doped cadmium telluride, operating at 12 to 20° K.

1.4 SYSTEM DESIGN

The Black Brant VB was selected as the launch vehicle. This rocket will reach 200- to 250-km altitudes with the design payload weight and can be tower-launched from essentially any test range. An air-snatch recovery system was selected to reduce loads on the payload. An alternate system to obtain high-altitude data uses a Nike-boosted Black Brant VB which also provides an additional 25 to 30 % increase in total measurement time.

A primary flight program involving ten launches over the range of conditions (arctic winter, arctic summer day, night temperate and tropic) was designed to yield data over the full range of expected data variations. Secondary flight programs were designed using three probes to investigate the arctic data.

To obtain radiance profiles with an altitude accuracy consistent with the amplitude accuracy requirements using an experiment probe which could be launched without regard to the local sun time, an electrostatically suspended gyro system is used as a combination attitude determination-attitude control reference system. A cold-gas helium control system is included for vehicle control purposes. Standard telemetry systems are used to transmit and record data.

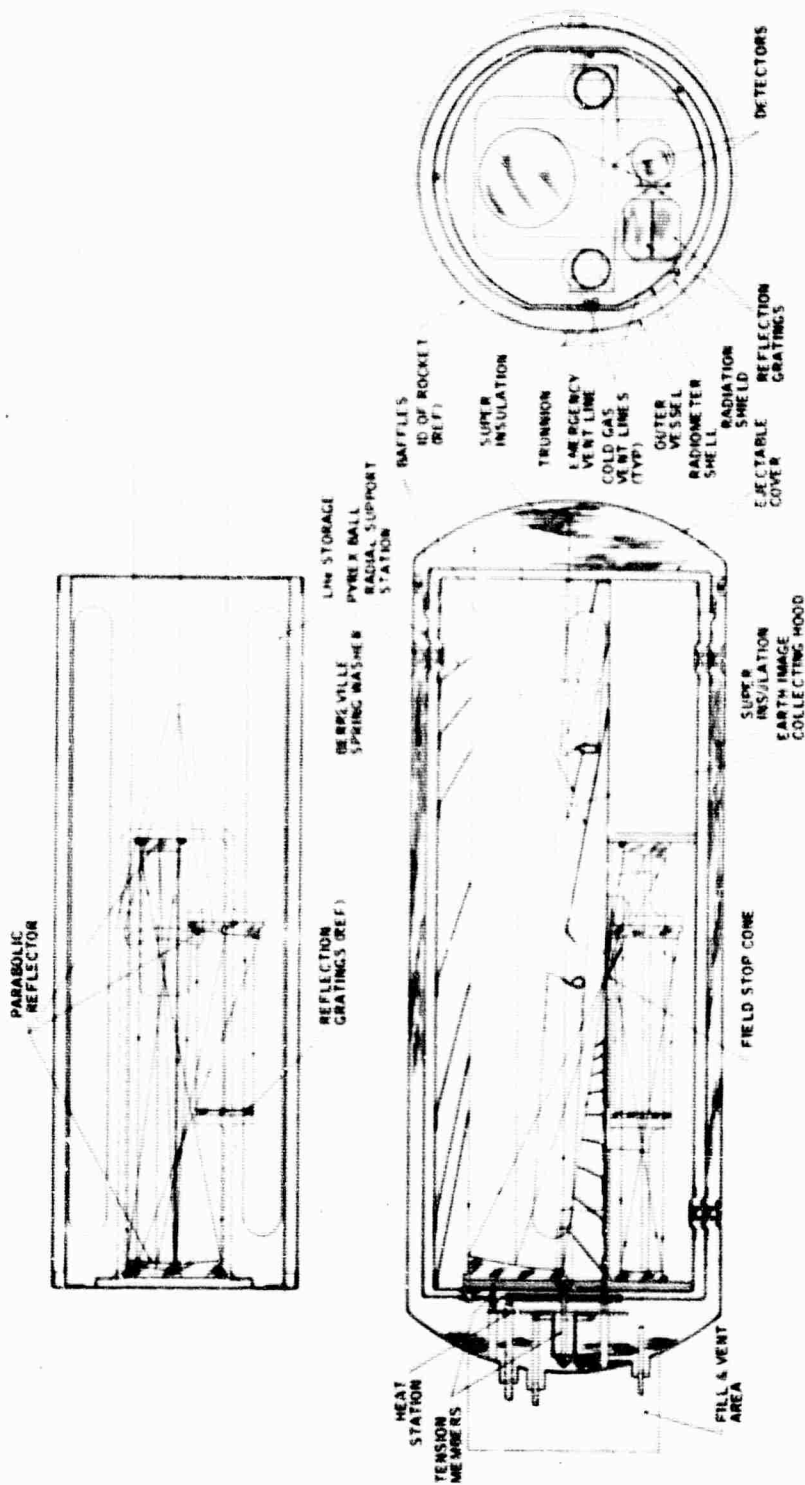


Figure 1. Radiometer Design

UNCLASSIFIED

1.5 PROGRAM PLAN AND COSTING

A minimum-cost program has been defined consisting of three launches. It is highly desirable that the diurnal variation be sampled during these launches, at least to the point of obtaining a near midday sample. As noted earlier, available off-the-shelf attitude determination systems for minute-of-arc-accuracy are generally constrained to night-time or twilight launches. The cost of the ESG system outlined earlier is prohibitive for the minimum-cost program. An alternate procedure, which yields tangent-height errors in the range of 5 to 10 km is the use of the 15-micron CO₂ emission region to define a tangent height and integration of a rate gyro output to obtain the remainder of the curve. Techniques of this nature have been investigated by NASA (LRC) and at Honeywell. A summary error analysis associated with the 15 micron CO₂ profile is given in section 2.5.

UNCLASSIFIED

SECRET

SECTION 2 INSTRUMENT REQUIREMENTS

(S) Instrument requirements have been derived from the overall mission objectives of the Limb Measurement Program which are summarized below:

- Provide Data for Operational Sensor Design -
 - (1) Determine minimum tangent height for successful target detection
 - (2) Identify optimum spectral region/s for maximum signal-to-noise ratio
 - (3) Measure temporal and spatial noise characteristics of background.
- Measure Absolute Radiance of Atmosphere -
 - (1) Under limb viewing conditions with optical field positioned over the earth's horizon
 - (2) For a range of minimum tangent heights from 0 to 500 km
 - (3) In the LWIR spectrum from 4.5 to 25 microns.

(S) The primary objectives of the total data reduction process are: (1) to provide a sample of LWIR limb radiance for early assessment of background interference in terms of the R/V and FCB detection problem and (2) to provide early inputs to other measurement programs so as to aid in establishing instrument requirements.

(S) For purposes of defining instrument requirements herein, a reference target has been assumed with the following characteristics:

- Temperature - 300°K
- Emissivity x area - 1 m^2
- Range - 1000 nm
- Radiant intensity - 120 watts/ster (5 to 25 microns)

(U) Key instrument requirements are briefly summarized in Table 1. A multiple high/low resolution requirement satisfied the dual objective of high spatial resolution for measurement of noise (gradient) characteristics and high spectral resolution for location of band edges.

SECRET

(S) Table 1. Instrument Requirements Summary (U)

Parameter		Requirement
Form of data		Absolute radiance profile versus altitude
Wavelength		4.5 to 25 microns, 10 absorption bands, 3 window regions
Sensitivity	NEFD	3×10^{-18} to 3.5×10^{-17} watt/cm ² *
	NER	3×10^{-12} to 3.5×10^{-11} watt/cm ² -ster*
	Signal-to-noise ratio	10
Resolution	Spatial	$\leq 4 \text{ km}^2$
	Angular	$\leq 10^{-6}$ ster (IFOV)
	Spectral	High - 0.1 micron; low - 0.5 to 7.0 microns
Stray flux level at detector		$\leq 10^7$ to 10^8 photons/sec-cm ² *
Off-axis rejection		$\leq 3 \times 10^{-11}$ between 1 to 2 deg
Spectral rejection		$\leq 10^{-7}$ at 0.5 micron from pass band
Scan rate		0.6 deg/sec (vertical profile)
Dynamic range		5×10^6 (max)*
Calibration Accuracy		
	Angular (attitude and boresight)	1 arc min
	Amplitude (radiance)	10 percent
	Spectral	0.01 to 0.02 micron
Output		PCM, 8-bit log amplitude code
Size		14-in. diameter x 32 in. long
Weight		80 lbs

*Varies with wavelength.

SECRET

(U) Atmospheric background radiance represents the signal to be measured with the instrument described in Section 4; whereas, in terms of the operational detection system, the atmospheric radiance represents a source of noise. Atmospheric background can contribute noise in a detection sensor both in terms of a random arrival of photons and in terms of spatial gradients. A high spatial resolution measurement requirement of 4 km^2 (projected dimensions on horizon) is specified to be consistent with the highest expected resolution in terms of trajectory-prediction accuracy and detectivity requirements imposed on the detection sensor. In this case, the spectral resolution is specified to correspond to the broad spectral features of the atmospheric radiance in the altitude range from 60 km to 115 km (see section 2.4).

(U) A high spectral resolution of 0.1 micron is specified to locate the atmospheric window regions (high transmission) between absorption bands. High spectral resolution is necessary to define the optimum spectral region(s) within which target detection is possible at the lowest tangent height. In this case, the spatial resolution can degrade in the horizontal direction to accommodate the loss of energy due to the narrow spectral bandwidth.

(U) The attenuation of stray radiation on the detector is necessary if the high sensitivity levels are to be achieved. This is a critical instrument requirement, since accurate measurements of atmospheric radiance must be made with the field of view positioned close to the earth's horizon. Stray radiation may illuminate the detector as a result of (1) scattered and diffracted earth radiation and (2) internal cavity emission. In addition, measurements within atmospheric window regions may be corrupted by radiation from adjacent, strong absorption bands. The attenuation requirements are specified in section 2.2 (Table 2).

(S) The attitude determination requirement is specified at 1 km and refers to the accuracy to which the position of the optical axis can be determined with respect to the earth's surface at the local horizon. This requirement corresponds to an angular attitude accuracy at the vehicle of about 1 arc min or greater. Knowledge of the optical line of sight at all times to this accuracy is critical to the data usefulness, since coverage achieved by a given detection sensor will depend to a large extent on the minimum tangent height at which background radiance prevents successful target detection.

(U) Amplitude accuracy in this case refers to the ability to measure absolute radiance and depends on ground (preflight) calibration as well as inflight calibration accuracy. Radiance measurement accuracy is specified at 10 percent of any given level and represents a reasonable goal in terms of the present sensor state of the art. Errors in background-radiance measurements reflect into detection system requirements most critically in terms of the ability to predict false-alarm rates.

SECRET
THIS PAGE IS UNCLASSIFIED

2.1 VIEWING GEOMETRY

Typical sensor viewing geometry along with two key geometrical parameters are given in Figure 2. The sensor is positioned to measure the earth's atmosphere over the horizon within the instantaneous field of view (IFOV). The optical axis is caused to scan by means of vehicle rotation such that data is collected from the earth's surface up to a local horizontal position (90 deg from zenith). Radiation from the earth can be a significant source of interference due to diffraction and internal scattering when the IFOV is positioned in close angular proximity to the horizon. For vehicle altitudes (h) in the range from 100 to 300 km, the angle to the earth's surface (α) from a 50-km tangent height varies from 2.5 deg to about 1.5 deg. This angular separation is used to develop the off-axis rejection requirement imposed on the sensor in section 2.3.

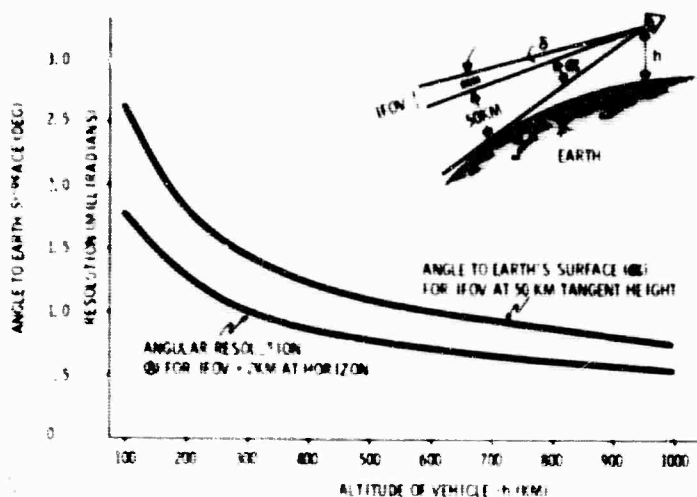


Figure 2. Limb Measurement Program Viewing Geometry

The lower curve in Figure 2 represents the angular tolerance measured at the sensor of a 2-km altitude increment on the horizon. In terms of optical resolution, a 2-km altitude increment corresponds to 1.7 to 1.0 mr in the expected vehicle altitude range. This optical resolution requirement is less than the diffracted point source image of the proposed instrument by a factor between 2 and 5 at 25 microns. Attitude determination requirement of 1 km is equivalent to one-half the IFOV and represents an angular tolerance of the vehicle of 0.5 to 0.4 mr or 1.7 to 1.4 arc min.

Additional geometrical viewing parameters of interest are shown in Figure 3. Throughout the range of vehicle altitudes, it is seen that the slant range to the horizon varies from 1100 to 2000 km, and the total vertical angular coverage is 10 deg at the lower altitudes increasing up to about 17 deg at apogee.

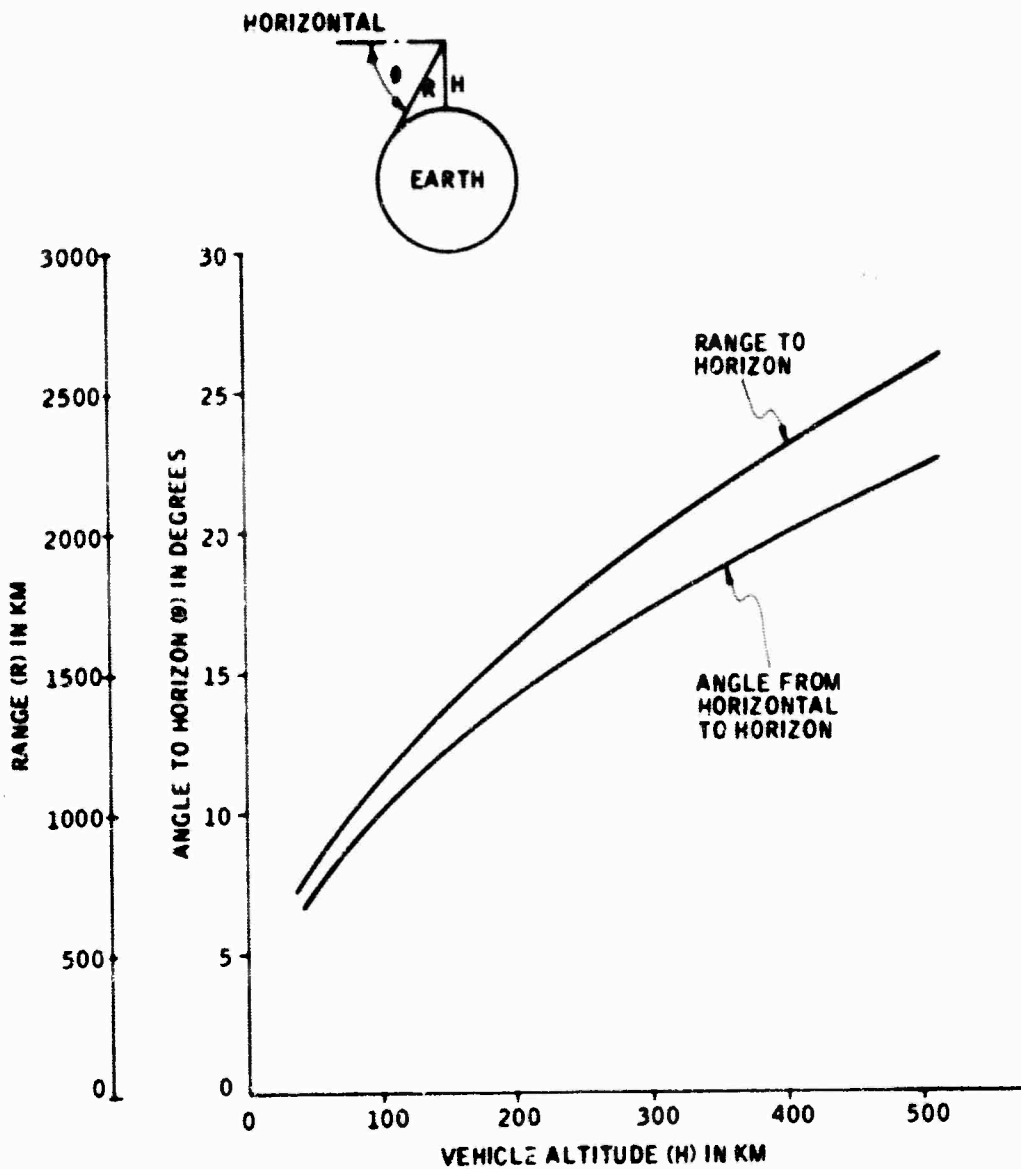


Figure 3. Limb View Geometry

SECRET

2.2 SENSITIVITY REQUIREMENTS

(S) Radiometer sensitivity requirements are developed in this section and are based on the following considerations:

- To provide meaningful information, the noise level of the instrument should be such that the noise equivalent flux density (NEFD) is significantly less than the irradiance from the reference target, permitting the measurement of background flux levels below that of the target.
- The instrument should measure the absolute radiance of the atmosphere under limb viewing conditions.
- High/low spectral resolution should be consistent with spectral radiance from atmospheric model:
 - (1) Low - separation of major atmospheric constituents and window regions
 - (2) High - accurate location of wavelength limits in window regions.
- Nominal signal-to-noise ratio should be 10:1 to maintain amplitude accuracy.
- Spatial resolution should be 4 km^2 .

(U) A summary of results from the atmospheric model which are pertinent to instrument requirements is given in section 2.7. Sensitivity requirements are developed both in terms of NEFD (noise equivalent flux density) and NER (noise equivalent radiance) for 15 spectral regions including 10 absorption bands and 3 atmospheric window regions. The NEFD requirements are listed for each spectral region in Table 2. Each nonwindow region can be identified with a particular radiating species with the exception of the 7.7-micron region. In this case, the CH_4 and N_2O bands overlap to such an extent that they cannot effectively be separated.

(S) The NEFD requirements were determined by the radiation levels of the reference target in each region by the following equation:

$$\text{NEFD} = \frac{\int_{\lambda_1}^{\lambda_2} J(\lambda) d\lambda}{R^2 \times S/N} \quad (\text{watt/cm}^2)$$

SECRET
THIS PAGE IS UNCLASSIFIED

Table 2. Noise Equivalent Flux Density (NEFD) Requirements

Wavelength (microns)	Spectral Resolution			
	Low		High (0.1 micron)	
	Wavelength Limits (μ)	NEFD ₂ (watt/cm ²)	Wavelength Limits (μ)	NEFD ₂ (watt/cm ²)
4.7	4.5-5.0	3×10^{-18}		
5.3	5.0-5.7	3.5×10^{-18}		
6.3	5.7-7.0	2.8×10^{-17}		
7.4	7.0-7.5	1.2×10^{-17}	6.8-7.7	2.4×10^{-18}
7.7	7.5-8.1	1.7×10^{-17}		
8.4	8.1-8.7	1.8×10^{-17}	8.0-9.5	2.9×10^{-18}
	8.1-9.3	3.5×10^{-17}		
9.6	9.3-10.0	2.2×10^{-17}		
10.4	10.0-10.8	2.2×10^{-17}		
11.2	11.0-11.7	2.0×10^{-17}	10.7 x 13.5	2.7×10^{-18}
12.4	11.7-13.0	3.5×10^{-17}		
13.5	13.0-14.0	2.2×10^{-17}		
15	14.0-16.0	3.9×10^{-17}		
17	16.0-18.0	3.1×10^{-17}		
22	18.0-25.0	6.9×10^{-17}		

SECRET

(S) where

$J(\lambda)$ = target spectral radiant intensity

λ_1, λ_2 = wavelength limits of each band

R = range (1000 nm)

S/N = signal-to-noise ratio (10:1)

(U) A measurement is specified in the 4.7-micron band of carbon monoxide (CO) which is beyond the nominal limit of the atmospheric model, since this band may explain the high radiance levels observed during the USSR measurements.

(S) The highest sensitivity levels (lowest NEFDs) are required in the high-spectral-resolution channels necessary to establish the wavelength limits of the three window regions.

(U) The spatial resolution requirements, coupled with the slant range at nominal vehicle altitudes, leads to an instantaneous field-of-view (IFOV) requirement of 10^{-6} steradian. Assuming the background represents an extended source, then the noise equivalent radiance is determined by

$$NER = NEFD/\Omega \text{ (watt/cm}^2\text{-ster)}$$

where Ω = IFOV

(S) Dividing through by the spectral bandwidth leads to the spectral NER requirement for each region; these are given in Table 3. The equivalent radiance level corresponding to the reference target is 10 NER. The values of target equivalent radiance (TER) for each band have been referenced to a tangent height by means of the radiance/altitude profiles generated from the atmospheric model. Tangent height requirements thus developed are also given in Table 3. The tangent heights called out in the table are to be taken as approximate since the upper atmosphere model is expected to be in error due to inaccurate knowledge of constituent distributions, and, in several cases, the tangent-height requirement falls within the transition region between the lower- and upper-atmospheric models. Nevertheless, these tangent heights will be used to specify the altitude below which a signal-to-noise ratio of 10 or better must be achieved.

(U) The tangent height is significant in that it represents the upper bound in terms of angle from the horizon at which valid measurements must be made. The smallest angle off-axis is about 1.8 deg for the 8.4-micron window. The minimum angle off-axis is critical in that earth radiation will be scattered and diffracted into the field of view and reduce detectivity. The requirements to reject earth radiation at small angles off-axis are developed in the next subsection.

SECRET

(S) Table 3. Noise Equivalent Radiance (NER) and Tangent Height Requirements (U)

Atmospheric Constituent	Center Wavelength (microns)	Wavelength Region (microns)	Noise Equivalent Radiance ^a (watt/cm ² -sr-μ)	Tangent Height (km)		
				Day	Night	LTE ^b
CO	4.7	4.5 - 5.0	5.5×10^{-12}	350 - 400	---	---
NO	5.3	5.0 - 5.7	10^{-11}	305	220	>500
H ₂ O	6.3	5.7 - 7.0	2.0×10^{-11}	85	82	80
Window	7.4	7.0 - 7.5	2.5×10^{-11}	74	73	---
CH ₄	7.56	7.5 - 8.1	2.6×10^{-11}	120	119	~160
N ₂ O	7.78	---	---	---	---	---
Window	8.4	8.1 - 8.7	2.85×10^{-11}	62	62	---
		8.1 - 9.3	---	71	71	---
O ₃	9.6	9.3 - 10.0	3.0×10^{-11}	105	105	115 (day) 135 (night)
CO ₂	10.4	10.0 - 10.8	3.5×10^{-11}	108 98	76	78
HNO ₃	11.2	11.0 - 11.7	2.9×10^{-11}	---	---	~90
Window	12.4	11.7 - 13.0	2.5×10^{-11}	66	66	---
CO ₂ (wing)	13.5	13 - 14	2.3×10^{-11}	106	84	---
CO ₂	15	14 - 16	2.0×10^{-11}	115 103	115 102	>115
CO ₂ N ₂ O (wing)	17	16 - 18	1.5×10^{-11}	111	111	135
H ₂ O	Rotation	18 - 25	10^{-11}	---	---	78

^aIFOV = 10^{-6} ster.

^bLocal thermodynamic equilibrium.

SECRET
THIS PAGE IS UNCLASSIFIED

2.3 STRAY LIGHT ATTENUATION REQUIREMENTS

To achieve the measurement goals of this experiment, it is necessary that state-of-the-art sensitivity levels be achieved in the instrument, i.e., signal-noise-limited operation. Since the noise level is then a function of incident stray radiation, it is therefore a requirement that all sources of stray radiation be reduced such that the noise contribution is small in comparison to the signal noise for the worst case. This requirement is particularly critical in this experiment because the optical field of view must be positioned close to the earth.

Three primary sources of stray radiation have been identified:

- Earth radiation scattered by the primary mirror
- Earth radiation diffracted by the limiting aperture
- Thermal emission from optical cavity

Earth radiation will illuminate the primary mirror directly from the edge of the field of view to an angle defined by the length/diameter (L/D) ratio of the forebaffle.

For a baffle with an L/D corresponding to 10 deg, the irradiance at the mirror from the earth near 12 microns is shown in Figure 4. This irradiance level assumes the earth radiates as a blackbody at 270°K and that the atmosphere has unity transmission. An off-axis angle of zero represents the earth's hard horizon. This radiation will illuminate the primary mirror, and a portion will be scattered into the field stop. The off-axis attenuation required to reduce this flux level to the NEFD level at 12 microns is also shown in Figure 4. Thus, within the first degree of the earth, the optics must attenuate by 10^{-10} . For a field of view of 10^{-6} steradian, the required mirror scattering coefficient is $10^{-10}/10^{-6} = 10^{-4}$. Increased attenuation is required for larger angles off-axis since the earth subtends a larger solid angle.

The required off-axis attenuation is a function of wavelength since (1) the NEFD level varies, and (2) the effective earth temperature is less within atmospheric absorption regions. Assuming the earth radiates as a 220°K blackbody in absorption bands, the attenuation required within the first degree off-axis is shown in Figure 5 for the various measurement channels. The 7.4-micron window represents the limiting case with a required attenuation factor of 3×10^{-11} .

It is also required that the optical system have a high rejection factor with respect to earth radiation diffracted at the aperture. In terms of diffracted energy, preliminary calculations were made based on the following approximate equation:

$$I(v) = \frac{\lambda}{-3 r \sigma}$$

UNCLASSIFIED

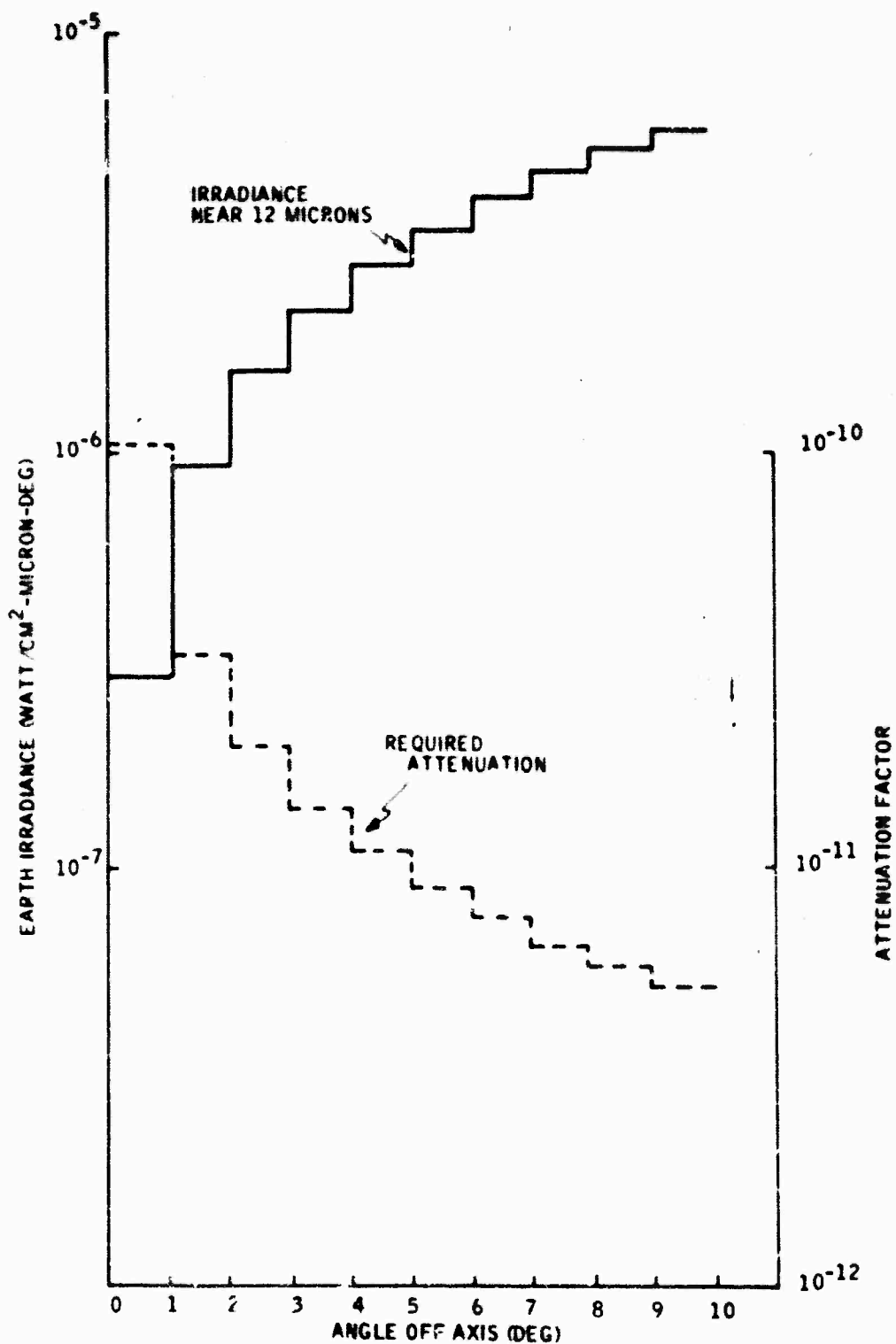


Figure 4. Attenuation Required to Reduce Off-Axis Earth Radiation to NEFD Level

UNCLASSIFIED

UNCLASSIFIED

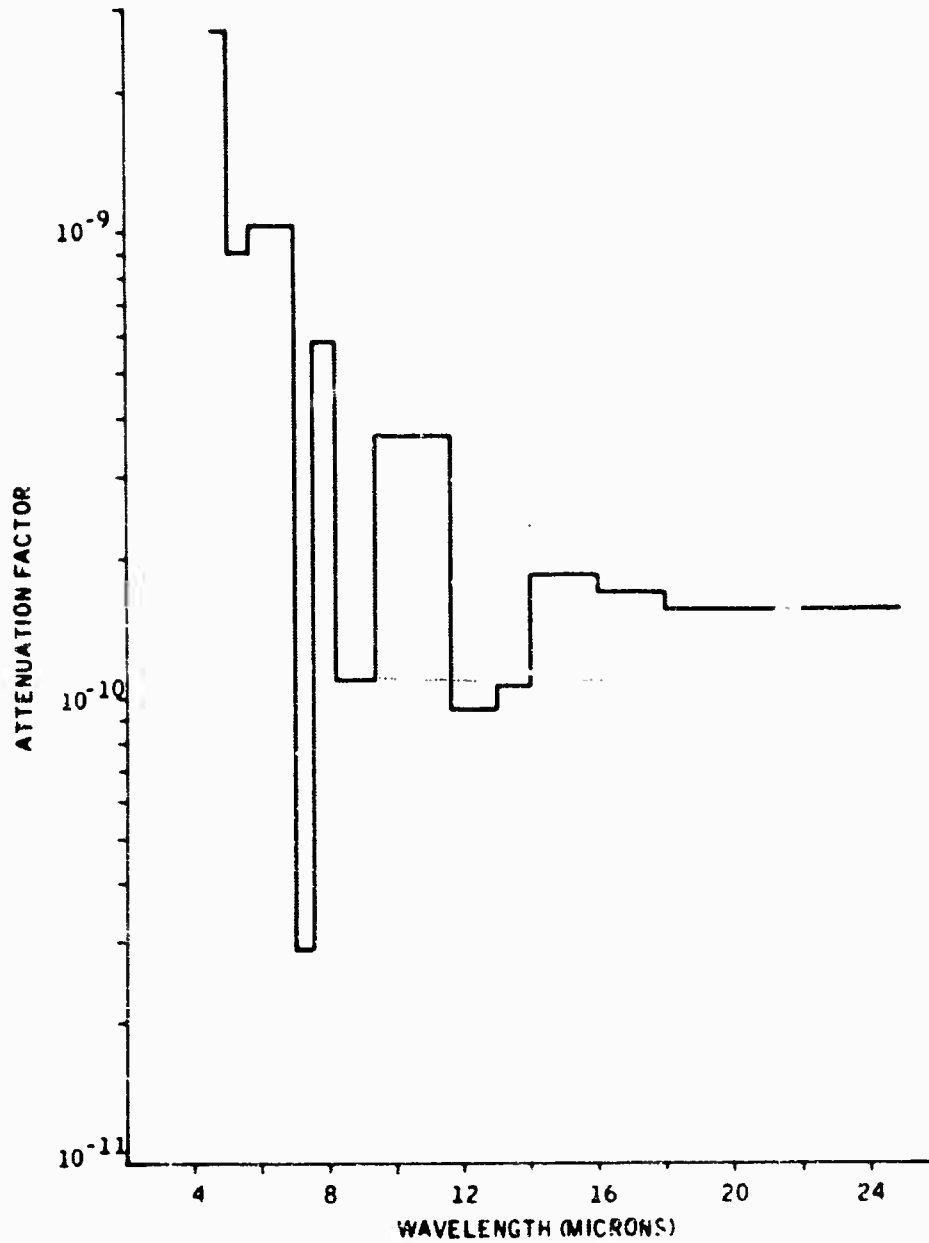


Figure 5. Attenuation Required within First Degree Off-Axis for IFOV on Horizon

UNCLASSIFIED

UNCLASSIFIED

where

$I(v)$ = fraction of radiation within IFOV as compared to nadir view

λ = wavelength

r = aperture radius

α = angle of IFOV from earth's surface

The intensity of diffracted energy is seen to decrease linearly as the angle from the horizon increases. Since the atmospheric radiance decreases exponentially, the effect of diffraction is to limit the altitude at which useful measurements can be made.

Using the tangent heights of interest for each wavelength region and an aperture diameter of 5.0 m., the performance requirements in terms of earth-diffracted energy were computed. The required attenuation is compared to the attenuation achieved by a circular aperture in Figure 6. It is clear that a circular aperture of this size will not meet the measurement requirements of this experiment. The largest discrepancy occurs in the 7.4-micron window and amounts to a factor of about 7.5×10^3 . The improvement factor necessary is 10^3 or larger for all window regions and for wavelengths beyond 13 microns. The use of coronagraph techniques to achieve this improvement factor is discussed in Section 4.

Radiation emitted from the internal housing and other parts of the optical cavity will contribute to the total photon flux on the detector depending on the temperature, emissivity, and view factor. A conservative estimate of the cavity contribution results from assuming the detector view factor to the cavity is 2-steradians, and the emissivity is unity. Under these conditions, the required cavity temperature can be determined from Figure 7. A temperature of 25°K or less ensures that cavity noise will not significantly degrade sensitivity even at longer wavelengths. To the extent that the detector is constrained to view only mirror surfaces, the effective cavity emissivity will be less than unity. The actual emissivity will depend on the f/number cone angle and the mirror diffuse scattering coefficient. In addition, if a cold ($< 10^\circ\text{K}$) stop surrounds the detector, then the solid angle of view will be less than 2-steradians. An improvement factor on the order of 500 to 1000 may be achieved which would allow an external cavity temperature as high as 30°K to 35°K.

The chopper must also be cooled to ensure a zero radiation reference level. The chopper will contribute photon flux to the detector both by reflections of internal cavity radiation and by thermal emission. To reduce reflections, the chopper can be painted black to yield a reflectivity on the order of 2.5×10^{-2} . For a cavity temperature of 25°K, the flux on the detector from reflections off the chopper blade will be about 10^5 photons/sec-cm². Cooling the chopper to 20°K reduces the contribution from thermal emission to about 5×10^4 photons/sec-cm² on the detector. Under these conditions, the total flux from the chopper blade is sufficiently low to guarantee a zero reference level.

UNCLASSIFIED

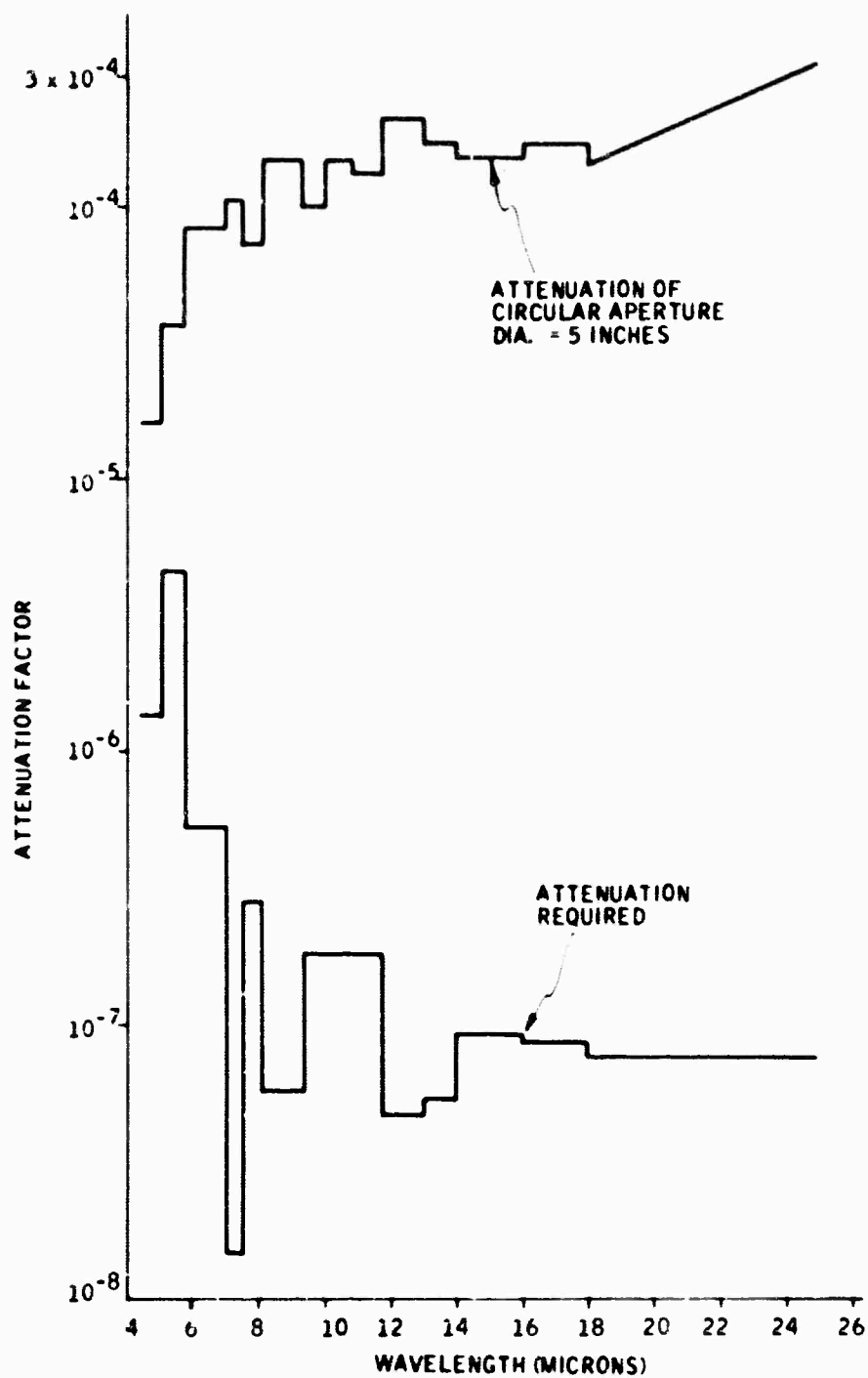


Figure 6. Attenuation Requirements - Earth-Diffracted Energy

UNCLASSIFIED

SECRET
THIS PAGE IS UNCLASSIFIED

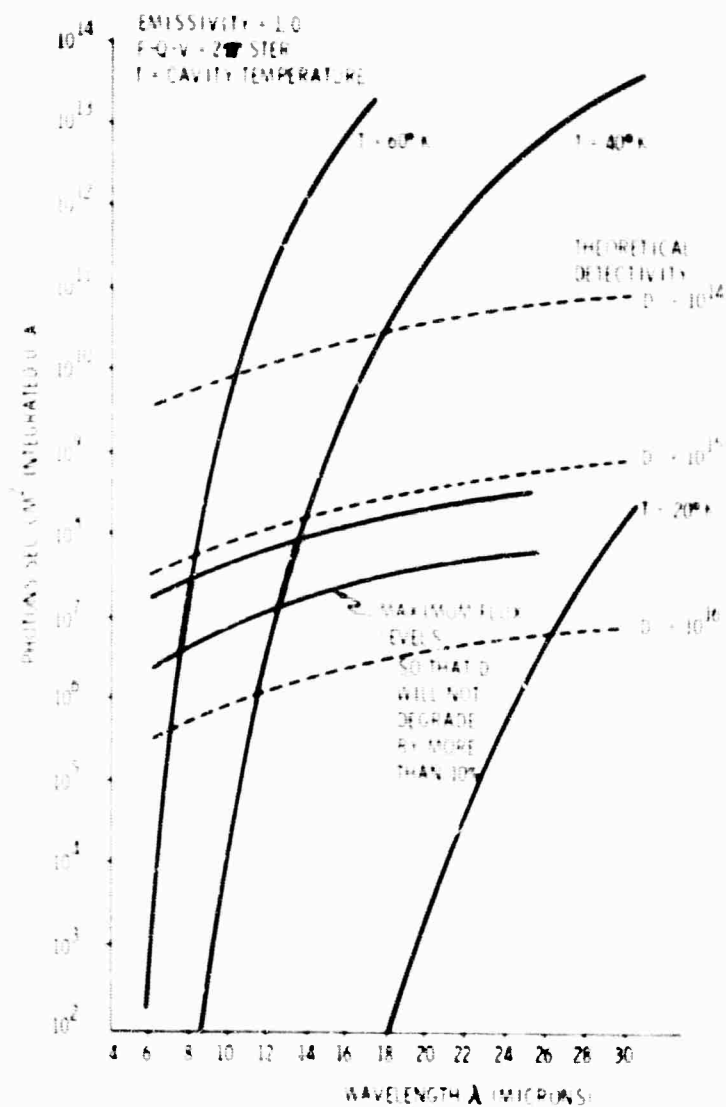


Figure 7. Photon Flux at Detector in Optical Cavity

THIS PAGE IS UNCLASSIFIED
SECRET

SECRET

2.4 SPECTRAL ATTENUATION REQUIREMENTS

(U) This requirement is related to resolution and specifically concerns the rejection of energy outside the nominal spectral bandwidth of a given measurement channel. Sufficient attenuation of this "out-of-band" radiation will ensure measurement accuracy and good resolution and is particularly critical where the radiance spectra is structured as in the case of high-altitude atmospheric radiance in the LWIR.

(U) The atmospheric radiance spectra generated by the GCA model atmosphere was used to derive spectral attenuation requirements. The maximum attenuation requirements as a function of wavelength deviation from nominal cutoff (zero wavelength interval) are shown in Figure 8. These maximum requirements result from the sharp band edges between atmospheric window regions and adjacent strong absorption bands near 7.5, 8.1 and 10.8 microns. The attenuation function shown in Figure 8 is such that absorption-band radiation will contribute less than 10% to the total in-band radiance level in adjacent window regions. For wavelength increments (beyond nominal cutoff) between 0.55 and 1.0 micron, an attenuation factor equal to or less than 10^{-4} is sufficient. In addition, beyond 1.0-micron wavelength separations, an attenuation factor of 10^{-8} is required.

2.5 ANGULAR LINE-OF-SIGHT ACCURACY REQUIREMENTS

(S) Two factors are developed in this subsection to establish angular, line-of-sight accuracy requirements in terms of attitude determination and boresight alignment:

- The impact of line-of-sight position errors on satellite system coverage studies
- The line-of-sight accuracy which corresponds to a 10% amplitude accuracy through the radiance/altitude profile

(U) These two factors lead to divergent angular accuracy requirements; and, for atmospheric measurements near 70 km tangent height, there exists a difference in requirements by about a factor of 10. An rms angular accuracy requirement of 1 arc min is specified for this limb measurement program for the following reasons:

- It is compatible with existing state of art with respect to attitude and boresight measurement systems.
- A potential exists for determining attitude to specified accuracy without the use of inflight celestial sightings.
- It provides about a factor of 4 more accuracy than is required for system coverage studies.

SECRET
THIS PAGE IS UNCLASSIFIED

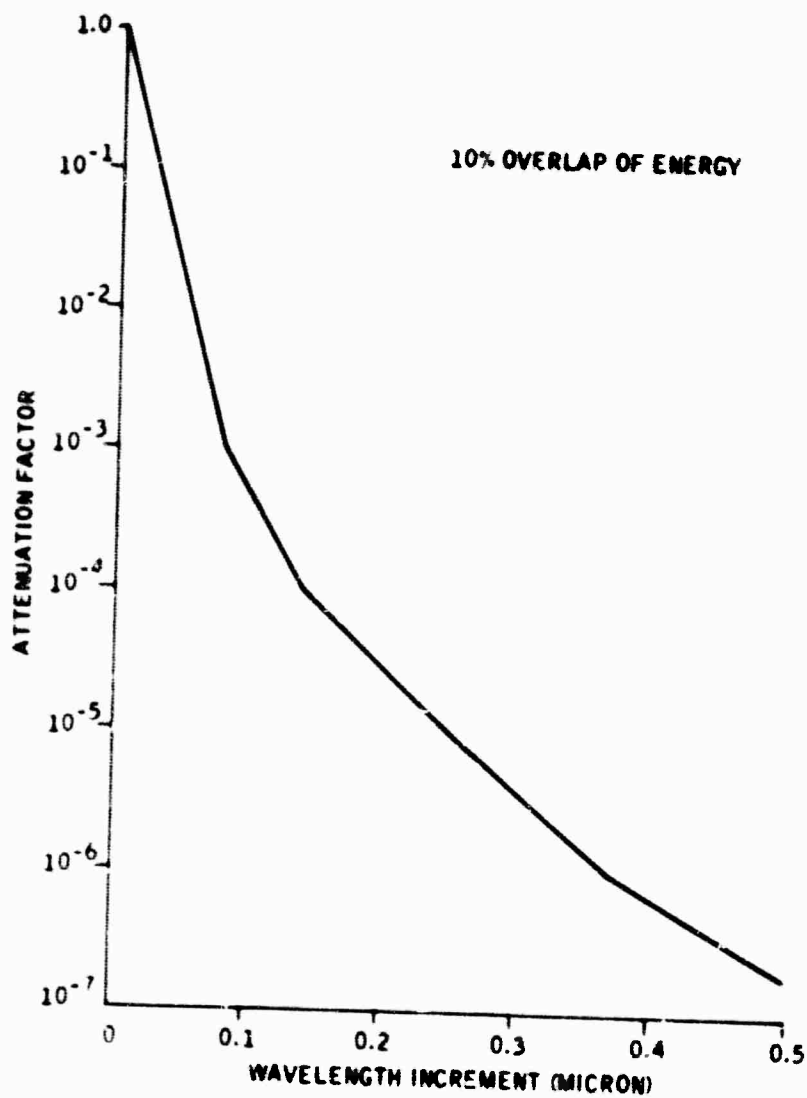


Figure 8. Maximum Spectral Attenuation Requirements

THIS PAGE IS UNCLASSIFIED
SECRET

SECRET

(U) Both factors are developed in terms of rms tangent-height error which is related to angular, line-of-sight accuracy through the viewing geometry. For a probe vehicle at 300 km altitude, the slant range to the horizon is about 2000 km and a 1 arc min angular accuracy corresponds to a tangent-height error equal to 0.58 km.

2.5.1 System Coverage Studies

(S) Tangent-height error is related to satellite system coverage in the following sense: A midcourse target sensor is constrained to view over-the-horizon only, and, as a result, its geographical coverage is limited as shown in Figure 9. For a given minimum view tangent height (h) and for a target altitude (H), the instantaneous coverage angle is θ . As the sensor scans in azimuth, a total solid angle is swept out by the angle θ revolving about the line OS. This solid angle when compared to 4π steradians is the fractional coverage of any sensor. Inverting this fraction gives the minimum number of sensors required for complete coverage, assuming no overlap between individual coverage patterns. The sensitivity of total sensors required to minimum tangent height can be seen in Figure 10. In this case, the target altitude (H) is 100 nm. The number of sensors required is an integer (N), and a variation of h_q is considered significant if it results in a unit change in N . It is clear that, as h_q approaches H , the coverage per sensor decreases, and a small change in h_q will result in a unit change in number of sensors. The rms variation in h_q which causes a unit change in N is shown in Figure 11, where h in this case is 150 km or about 80 nm, and the satellite altitude is 500 nm. Also it has been assumed in Figure 11 that on the average a 50% overlap in coverage exists between individual coverage patterns. For a range of tangent heights from 60 to 70 km, an rms angular line-of-sight accuracy of about 1 arc min or 2.3 km on the horizon is required.

2.5.2 Angular/Radiance Error Correspondence

(S) A secondary consideration which involves the angular accuracy specification is developed from the slope of the altitude radiance profile and the required radiance measurement accuracy. The sensitivity of false-alarm rate predictions to radiance errors had led to an amplitude accuracy requirement of 10%. A given incremental change in radiance will translate into a corresponding incremental change in tangent height via the slope of the radiance profile the results of which depend on the absolute tangent height. For the various atmospheric constituents and wavelengths of interest, the model profiles have been used to generate tangent-height errors for a 10% radiance error. The results are given in Table 4. As before, the absolute tangent heights used for each wavelength region correspond to the point at which the atmospheric radiance is equivalent to the reference target, 1000 nm distant. The tangent-height errors of Table 4 are bounded and generally increase as the absolute tangent height increases.

SECRET

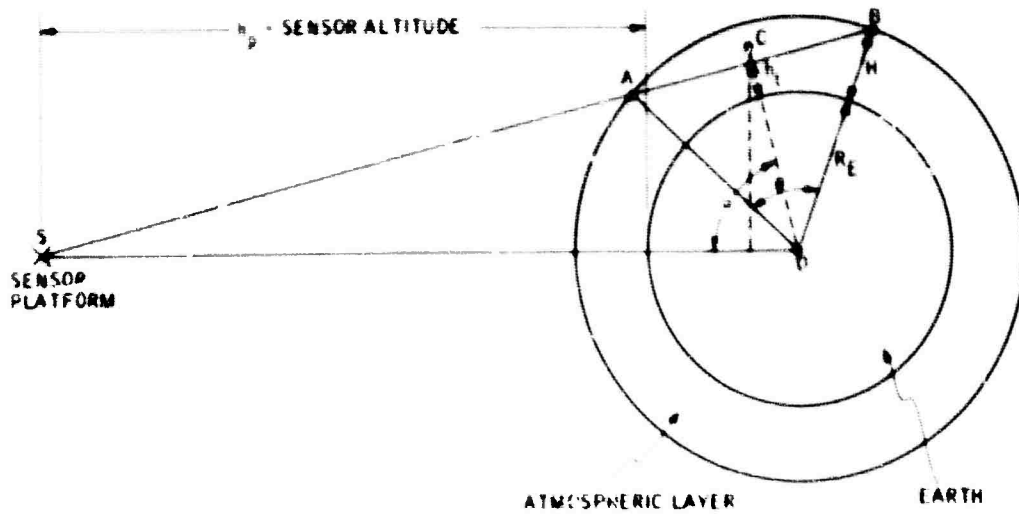


Figure 9. Sensor Scan Geometry

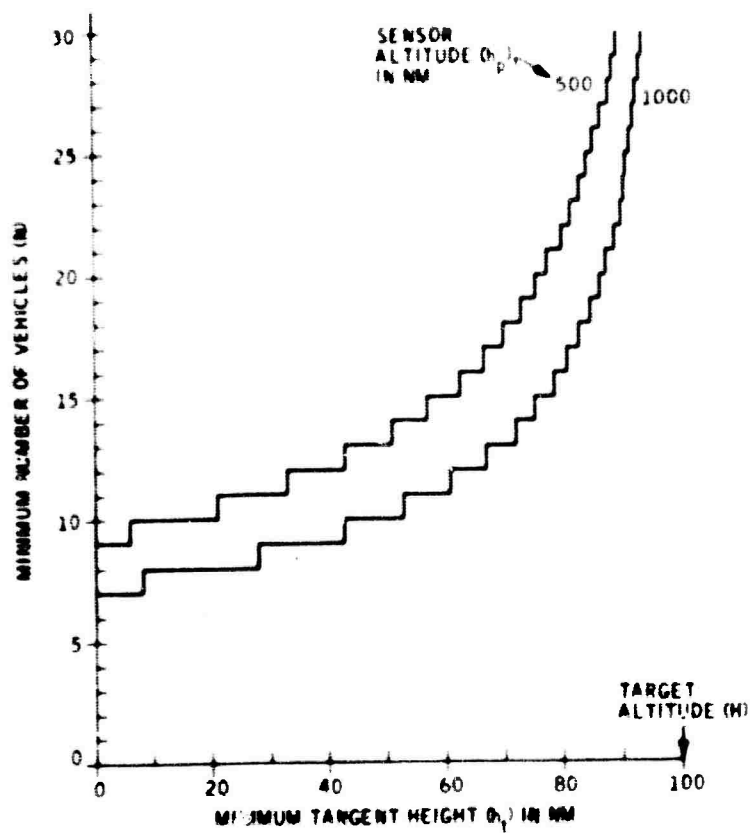


Figure 10. Over-the-Horizon Coverage (no overlap)

SECRET

SECRET

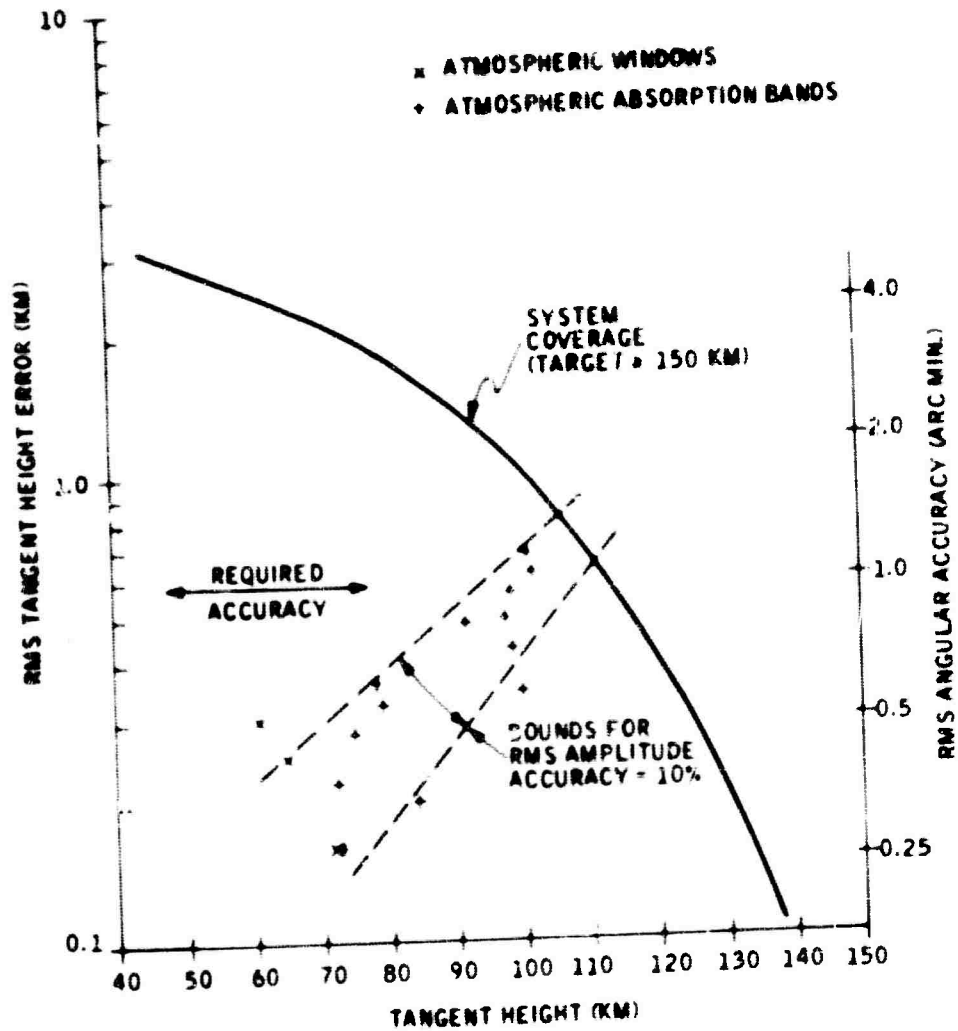


Figure 11. Attitude Determination and Boresight Accuracy Requirements

SECRET

SECRET
THIS PAGE IS UNCLASSIFIED

Table 4. Tangent-Height Error Corresponding to 10-percent Radiance Error

Constituent and Wavelength (microns)	Tangent Height (km)	Radiance Slope (watt/cm ² -ster-km)	Tangent Height Error (km)
NO/5.3 Day	265	1.5×10^{-11}	1.8
Night	150	9×10^{-12}	3.1
H ₂ O/6.3 Day	79.5	3.3×10^{-10}	0.32
Night	78	2.9×10^{-10}	0.36
7.4 (window)	72	3.2×10^{-10}	0.16
N ₂ O/7.7	112	10^{-10}	0.63
8.4 (window)	66	5.6×10^{-10}	0.25
O ₃ /9.6 Day	100	2.5×10^{-10}	0.34
Night	98	1.5×10^{-10}	0.56
CO ₂ /10.4 Day	92 - 101	$1.4 - 2 \times 10^{-10}$	0.48 - 0.68
Night	73	$4.3 - 6 \times 10^{-10}$	0.16 - 0.22
HNO ₃ /11.2	85	4×10^{-10}	0.2
12 (window)	61	4.3×10^{-10}	0.3
CO ₂ /15 Day	98.5 - 113	$3.8 - 7 \times 10^{-10}$	0.23 - 0.42
Night	97 - 112	$3.3 - 4.3 \times 10^{-10}$	0.37 - 0.49
N ₂ O/17	102	2×10^{-10}	0.61
H ₂ O/18 - 25	76	10^{-9}	0.28

SECRET

(S) (See Figure 11). The highest precision is required for measurements within atmospheric window regions (lower left in Figure 11) where the slope of the radiance profiles is relatively steep. The specified angular accuracy of 1 arc min is consistent with a 10% radiance error in some absorption bands. However, in the window regions and in the H_2O bands, it corresponds to radiance errors on the order of 20 to 30%. To produce consistent accuracies in all wavelength regions would require an angular accuracy on the order of 15 arc sec.

(C) This represents a substantial improvement as compared to the specified 1 arc min, and is not instituted for this program due to the increased complexity and cost of the necessary hardware.

(U) In terms of a minimum-cost program, data collected within the 15-micron CO_2 band may be used to position the line of sight at altitudes near 30 to 40 km.

(U) Figure 12 shows the error in determining a location on the 15-micron tangent height curve for various arithmetic operations on the curve as a function of a constant which is inversely related to the signal-to-noise ratio of the instrument. As can be seen, the standard deviation of the error is below 5 km for small values of the constant, which is where this system will operate. The information shown on Figure 12 was derived from an analytical simulation of the CO_2 emission band. Figure 13 shows a comparison of the analytically derived profile and a measurement taken from the NASA Scanner program.

2.6 DYNAMIC RANGE AND AMPLITUDE ACCURACY REQUIREMENTS

(U) Dynamic range requirements for each spectral interval have been derived from the model atmosphere radiance profiles. It is required that sufficient dynamic range exist in the detector, electronics, and telemetry to ensure intensity measurements to an accuracy of 10% throughout an altitude range from 0 to the tangent height where the atmospheric radiance is on the order of the noise level. The required dynamic range is shown in Figure 14. From the model profiles, the maximum dynamic range requirement of 3 to 5×10^6 exists in the 15-micron CO_2 band. Through the use of a log transfer function to achieve a constant error (10%) in terms of input flux, it is seen from the figure that an eight-bit PCM code telemetry system is sufficient in all cases.

(S) The amplitude accuracy requirement in terms of background radiance measurements had been developed from the effects on detection system false-alarm rate predictions. These effects are shown in Figure 15 for a detection process which incorporates thresholding to eliminate low-level noise. In this case, for typical threshold-to-rms-noise ratio's of 5 or greater, there are errors in estimating false-alarm rate that are critically dependent on the accuracy of background-radiance measurements. A requirement of 10% amplitude accuracy is specified to ensure a false-alarm rate prediction error less than a factor of 10.

UNCLASSIFIED

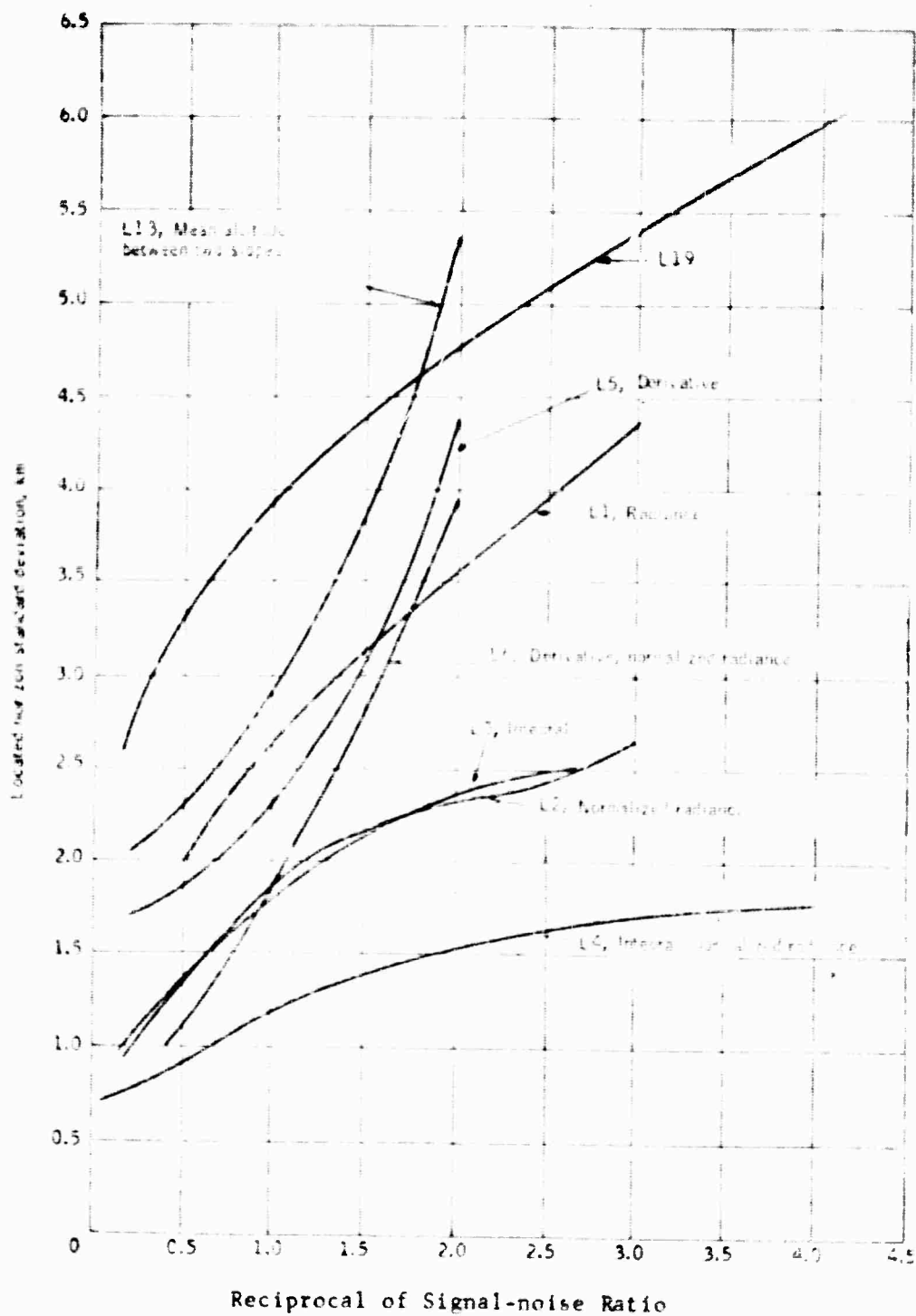


Figure 12. Located Horizon Standard Deviation versus Input Constant for Eight Locators

UNCLASSIFIED

UNCLASSIFIED

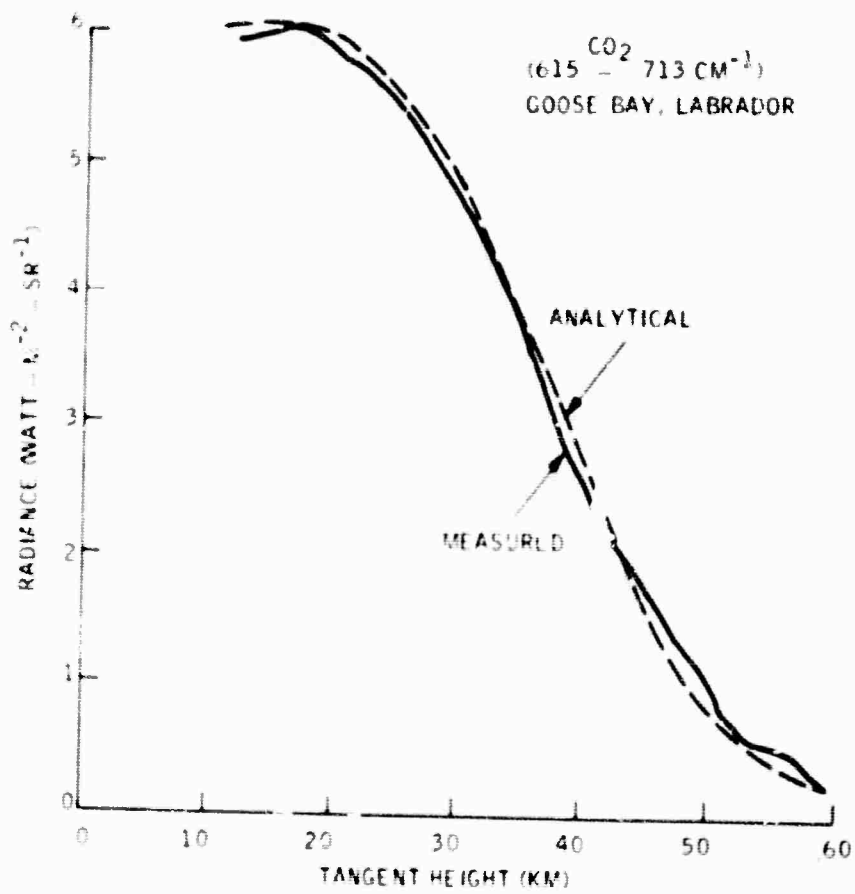


Figure 13. Comparison of Measured and Analytical CO₂ Horizon Profiles - Goose Bay (From Ref.1)²

UNCLASSIFIED

UNCLASSIFIED

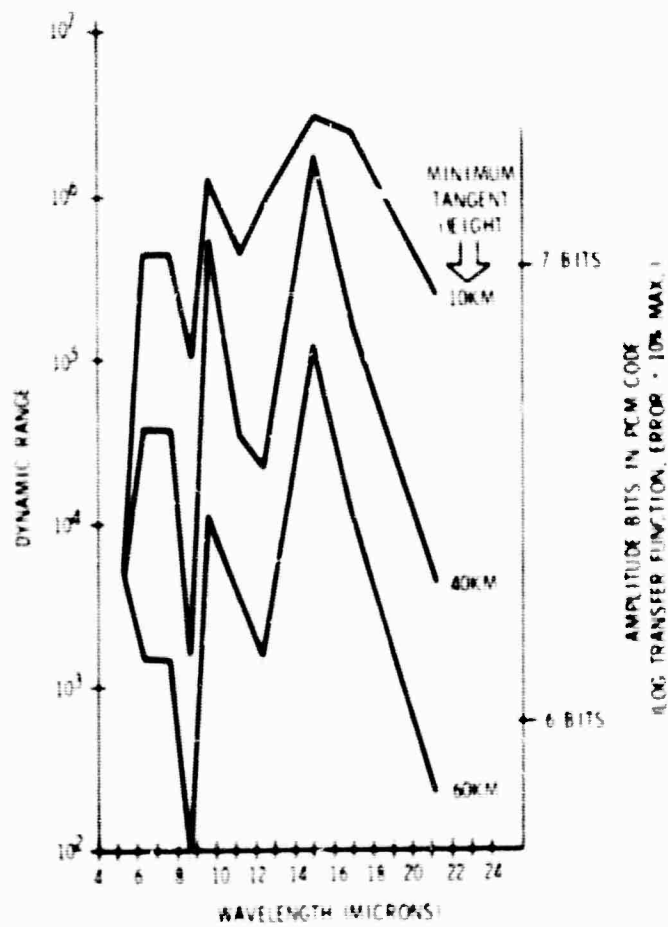


Figure 14. Limb Measurement Program
Dynamic Range Requirements

UNCLASSIFIED

UNCLASSIFIED

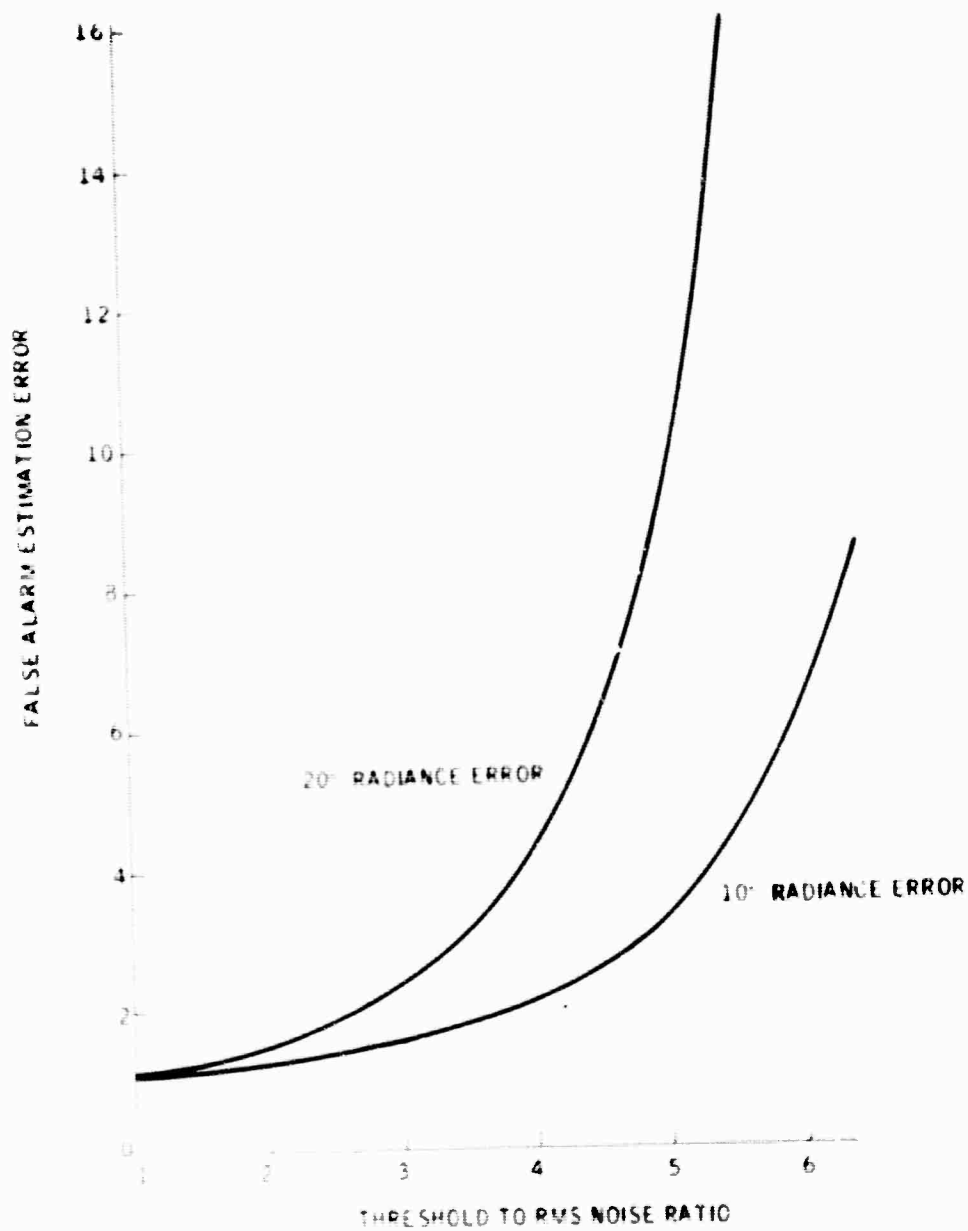


Figure 15. Radiance Measurement Error Requirements

UNCLASSIFIED

UNCLASSIFIED

2.7 RESULTS OF ATMOSPHERIC MODEL AND SUMMARY OF MEASURED DATA

A mathematical model of the radiative mechanisms and estimates of constituent densities has been made for the upper atmosphere (60 to 500 km) and reported in Reference 2.

Spectral radiance and radiance/altitude profiles were generated and results were used as an aid in establishing instrument requirements. This subsection summarizes the pertinent results of the atmospheric modeling studies, as well as the USSR data, as they apply to instrument requirements.

Dominant spectral features of atmospheric radiance are shown in Figures 16 through 22 for tangent heights varying from 60 to 115 km and, in some cases, under both daytime and nighttime illumination. Ten absorption bands and three atmospheric window regions have been identified from these spectra for measurement. These spectral regions and the required sensitivity levels were discussed in section 2.2.

High radiance levels are predicted within the 5.3-micron band of nitric oxide (NO) and are expected to persist up to altitudes of 250 and 300 km, higher than most other bands. The radiance/altitude profiles at 5.3 microns are shown in Figure 23 for both daytime and nighttime conditions. A large diurnal change in radiance level is predicted; however, the spectral character remains almost the same as seen from Figure 16.

High radiance levels are also predicted in the 4.7-micron band of carbon monoxide (CO). This constituent was not modeled during this study, but preliminary calculations show the radiance in this band may be as high as 10^{-5} watt/cm²-ster at a 120-km altitude. This level exceeds the radiance predicted for nitric oxide at 5.3 microns by about a factor of 100. Representative radiance profiles for several absorption bands as derived from the upper-atmosphere model are shown in Figure 24.

Large diurnal radiance variations are expected in some other bands, namely ozone (O₃) at 9.6 microns and carbon dioxide (CO₂) at 10.4 microns. The maximum predicted diurnal variations and the associated altitude regions for these and other bands are given in Table 5. A significant diurnal variation is also predicted for the short-wavelength wing (13 to 14 microns) of the 15-micron CO₂ band as shown in Figure 21. Clearly, both daytime and nighttime measurements are dictated by the extent of diurnal radiance variations.

The large diurnal variation noted for the 10.4-micron CO₂ band also involves a change in spectral character as seen in Figures 19 and 20. The spectral region chosen for measurement at 10.4 microns (10.0 to 10.8 microns) is based on daytime spectra.

UNCLASSIFIED

UNCLASSIFIED

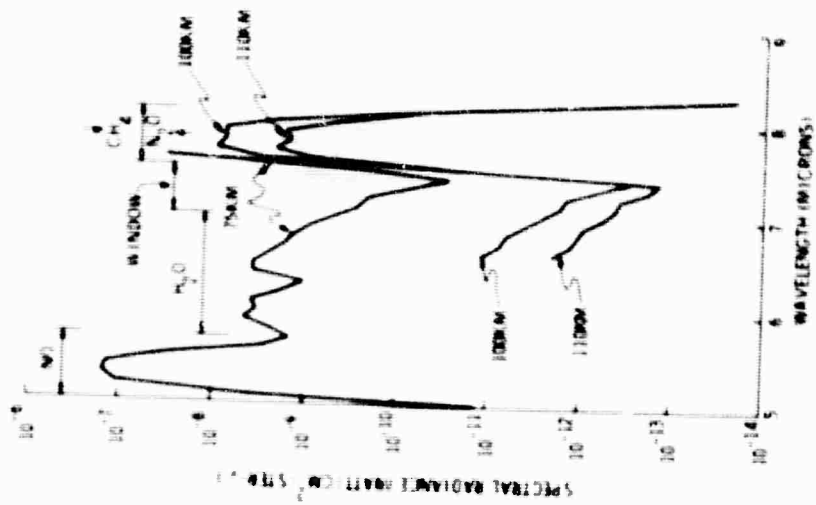


Figure 17. Atmospheric Radiance
Limb View, Noon -
Altitude = 75, 100
and 110 km

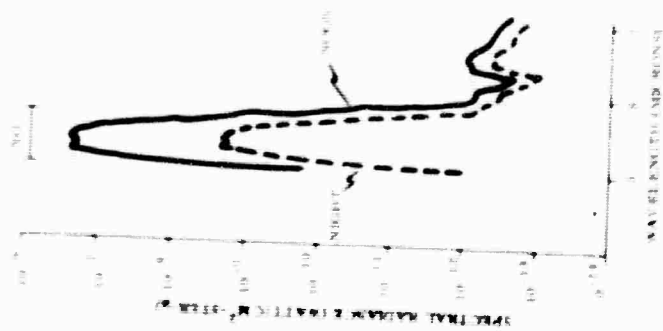


Figure 16. Atmospheric Radiance
Limb View, Night and
Noon - Altitude = 115 km

UNCLASSIFIED

UNCLASSIFIED

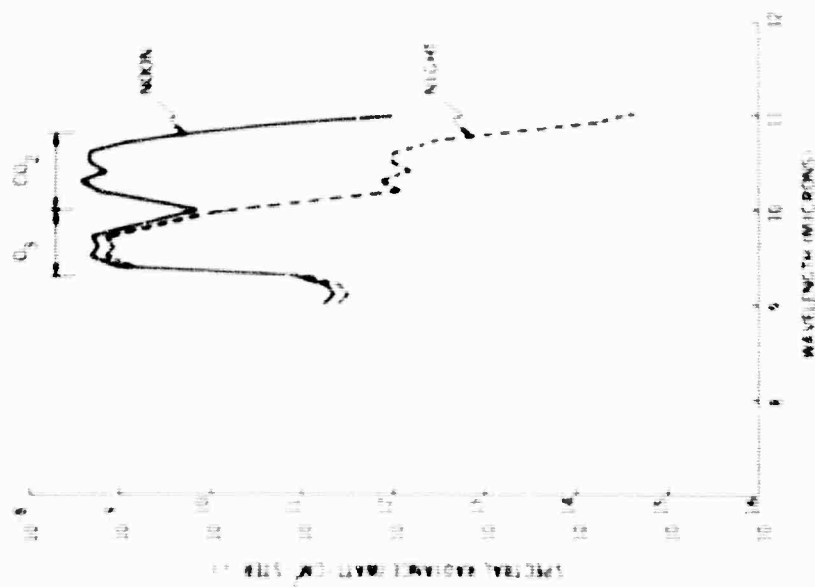


Figure 18. Atmospheric Radiance Limb View, Noon - Altitude = 60 and 70 km

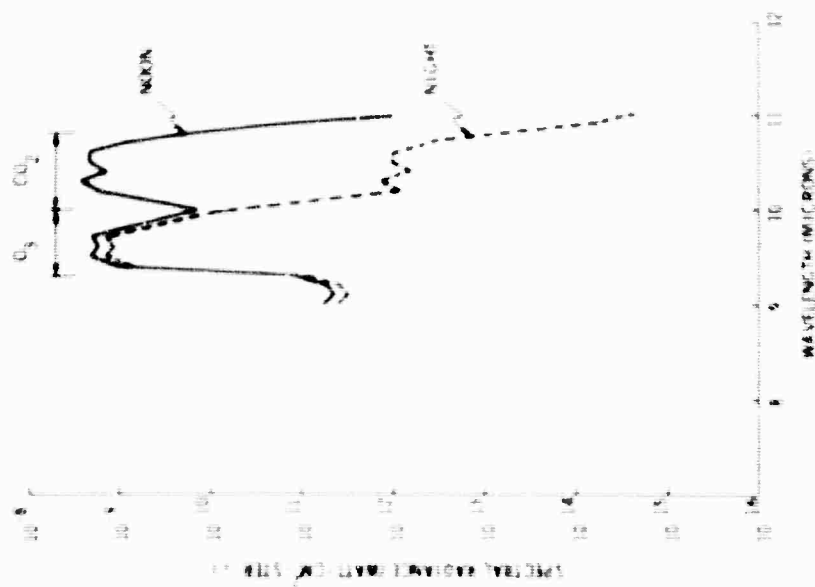


Figure 19. Atmospheric Radiance Limb View, Night and Noon - Altitude = 100 km

UNCLASSIFIED

UNCLASSIFIED

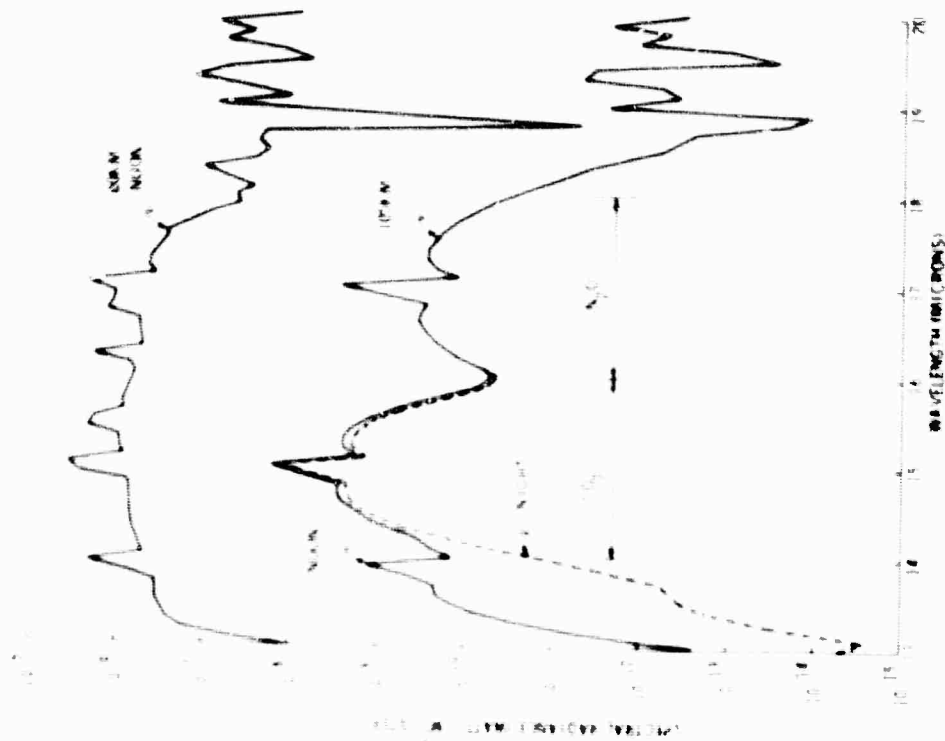


Figure 21. Atmospheric Radiance Limb View, Night and Noon - Altitude = 60 and 105 km

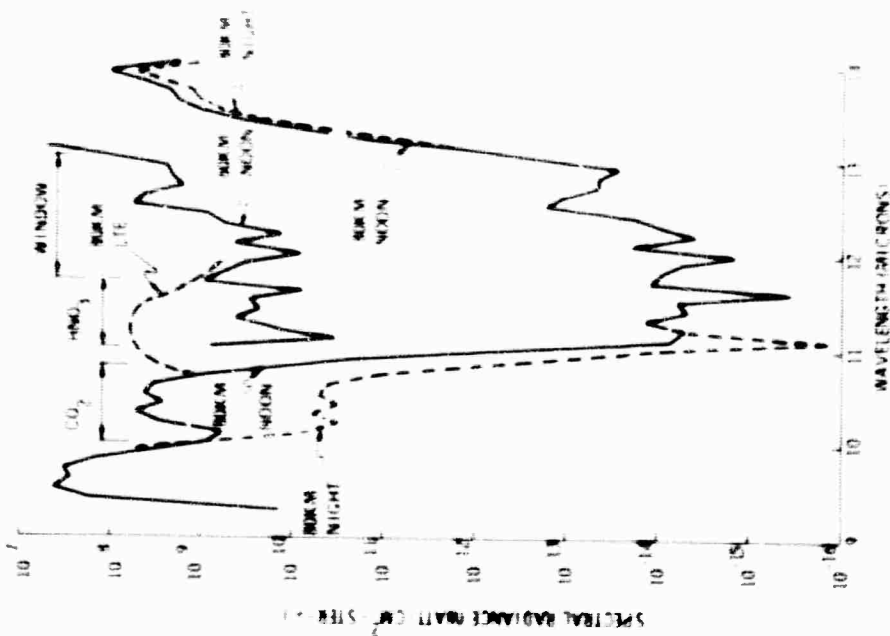


Figure 20. Atmospheric Radiance Limb View, Night and Noon - Altitude = 60 and 80 km

UNCLASSIFIED

UNCLASSIFIED

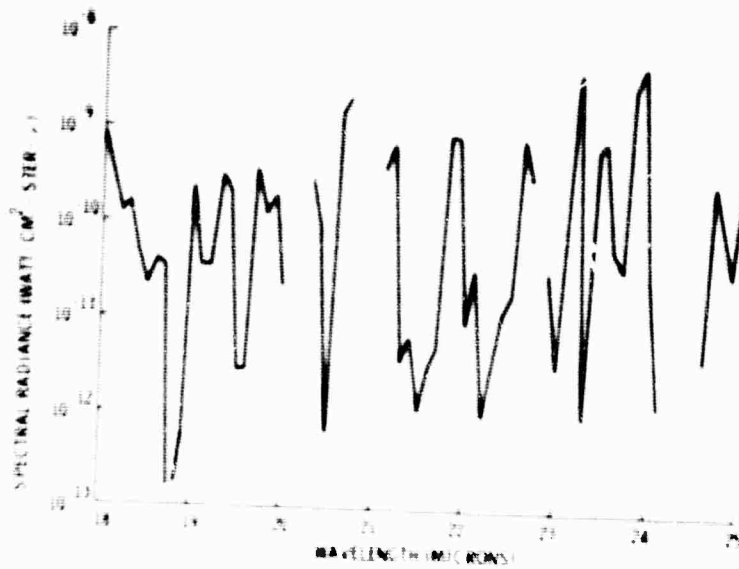


Figure 22. Atmospheric Radiance Limb View, Night and Sunrise - Altitude = 75 km

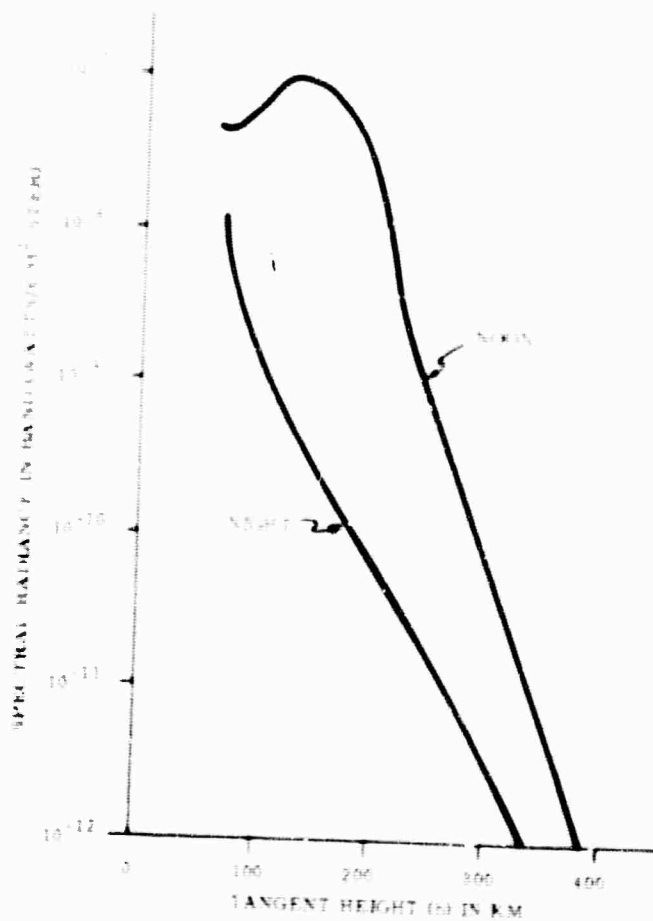


Figure 23. Limb Radiance Profile - Nitric Oxide, 5.3 microns

UNCLASSIFIED

UNCLASSIFIED

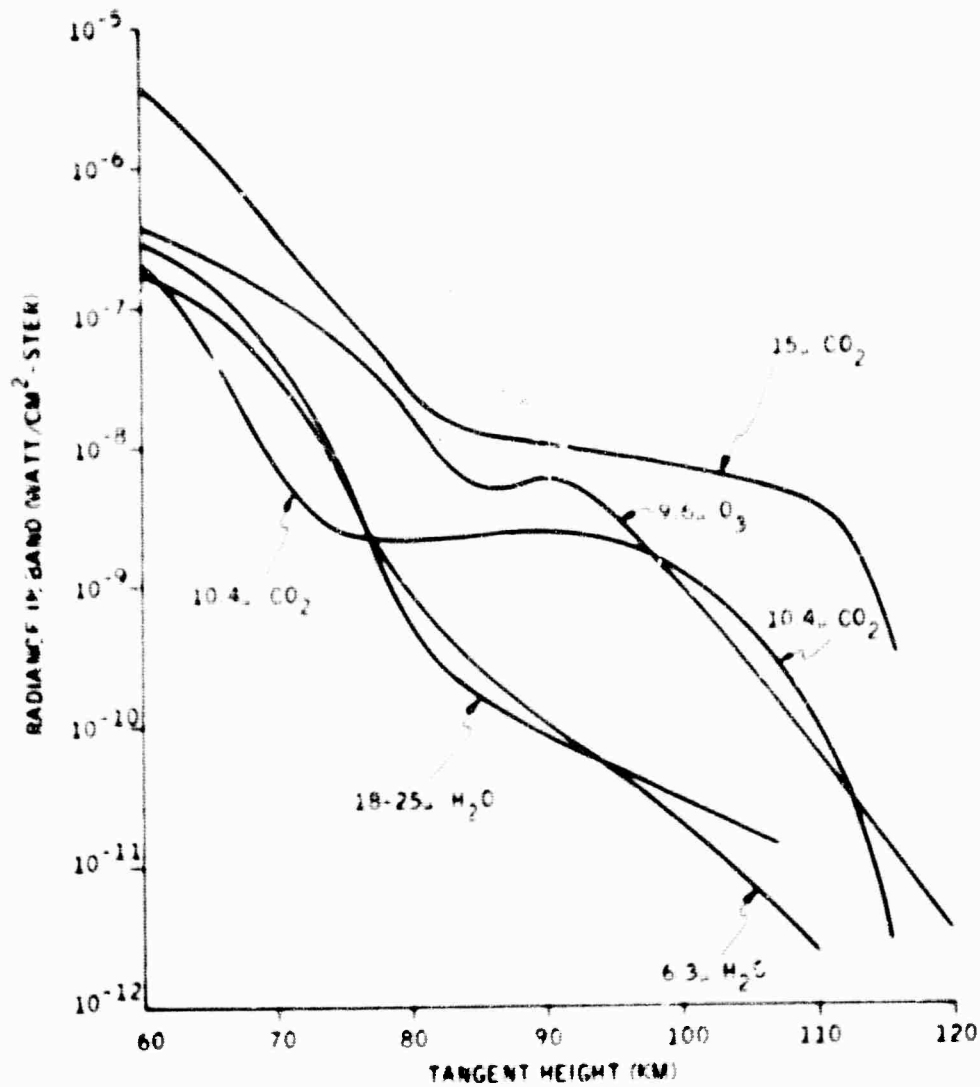


Figure 24. LWIR Radiance Profiles, Upper Atmospheric Model - Noon Conditions

UNCLASSIFIED

UNCLASSIFIED

Table 5 Maximum Diurnal Radiance Variation

Atmospheric Constituent	Wavelength (Microns)	Altitude (km)	Radiance (watt/cm ² ster)		Ratio Night/Day
			Night	Day	
NO	5.3	140	5×10^{-10}	10^{-7}	200
H ₂ O	6.3	85	1.1×10^{-10}	2.2×10^{-10}	2
CH ₄	7.66	105	1.2×10^{-10}	1.5×10^{-10}	1.2
N ₂ O	7.78	100	2.2×10^{-10}	3.2×10^{-10}	1.2
O ₃	9.6	90	1.8×10^{-10}	5.4×10^{-10}	3
		120	3.5×10^{-12}	7×10^{-13}	0.2
CO ₂	10.4	85	10^{-12}	2×10^{-9}	2000
CO ₂	15	85	5×10^{-10}	8.2×10^{-9}	1.6
N ₂ O	17		No diurnal variation expected		1.0

UNCLASSIFIED

UNCLASSIFIED

No change in spectral character is predicted with variations in tangent height with the exception of CO_2 and N_2O radiation in the range from 14 to 18 microns (see Figure 21). At the lower altitudes, near 60 km, radiation from the two bands overlap to the extent that they cannot be separated. At higher altitudes, in excess of about 100 km, a separation of the two bands is noted. The higher-altitude spectra is used to specify wavelength regions for measurements, i.e., 14 to 16 microns for CO_2 , and 16 to 18 microns for N_2O .

From an operational system standpoint, the atmospheric-window regions are of most interest since they allow target detection at lower altitudes. The three window regions which have been identified from the spectra are located at 7.4, 8.4, and 12 microns. The 7.4-micron window is a narrow window, bounded on the short-wavelength side by the 6.3-micron, H_2O band and on the long-wavelength side by the combined $\text{CH}_4/\text{N}_2\text{O}$ bands near 7.7 microns. Diurnal variations within this window are not expected to produce significant changes in spectral character nor are altitude changes as seen from Figure 17.

The window region near 8.4 microns is bounded on the short-wavelength side by the combined $\text{CH}_4/\text{N}_2\text{O}$ band near 7.7 microns and on the long-wavelength side by the O_3 band at 9.6 microns. The spectral distribution in this window is shown in Figure 18. This region has been subdivided for two measurements, (1) the narrow window from 8.1 to 8.7 microns within which very low radiance values are predicted and (2) the wider region from 8.1 to 9.3 microns with correspondingly higher radiance values. Only minor diurnal changes are expected within this window region.

The atmospheric window of most interest exists near 12 microns, the predicted spectra of which is shown in Figure 20. This region is potentially the best region for target detection since it may be the widest window, and it exists near the spectral maximum of the target radiation. The short-wavelength limit of this window region is in question due to the recent discovery of nitric acid (HNO_3) in the lower atmosphere.

Recent balloon measurements in the LWIR by D. G. Murcray at the University of Denver have identified nitric acid (HNO_3) radiating near 11.2 microns in the lower atmosphere. From these data, an HNO_3 concentration distribution was postulated and incorporated into the lower atmospheric model at Honeywell. The resulting radiance profile for HNO_3 is shown in Figure 25, and its spectral definition is given in Figure 20. If nitric acid exists to this extent up to an 80-km altitude, then its radiation could significantly reduce the width for the 12-micron window. On the other hand, if nitric acid does not exist in the proportions expected, then the short-wavelength limit could be closer to 11 microns as determined by CO_2 radiation at 10.4 microns which has a large diurnal effect. The long-wavelength limit is determined by CO_2 radiation at 15 microns which shows some diurnal effect beyond 13 microns even as low as 80 km. The 12-micron window is subdivided into two broad regions for measurement, primarily to isolate the radiation from nitric acid.

UNCLASSIFIED

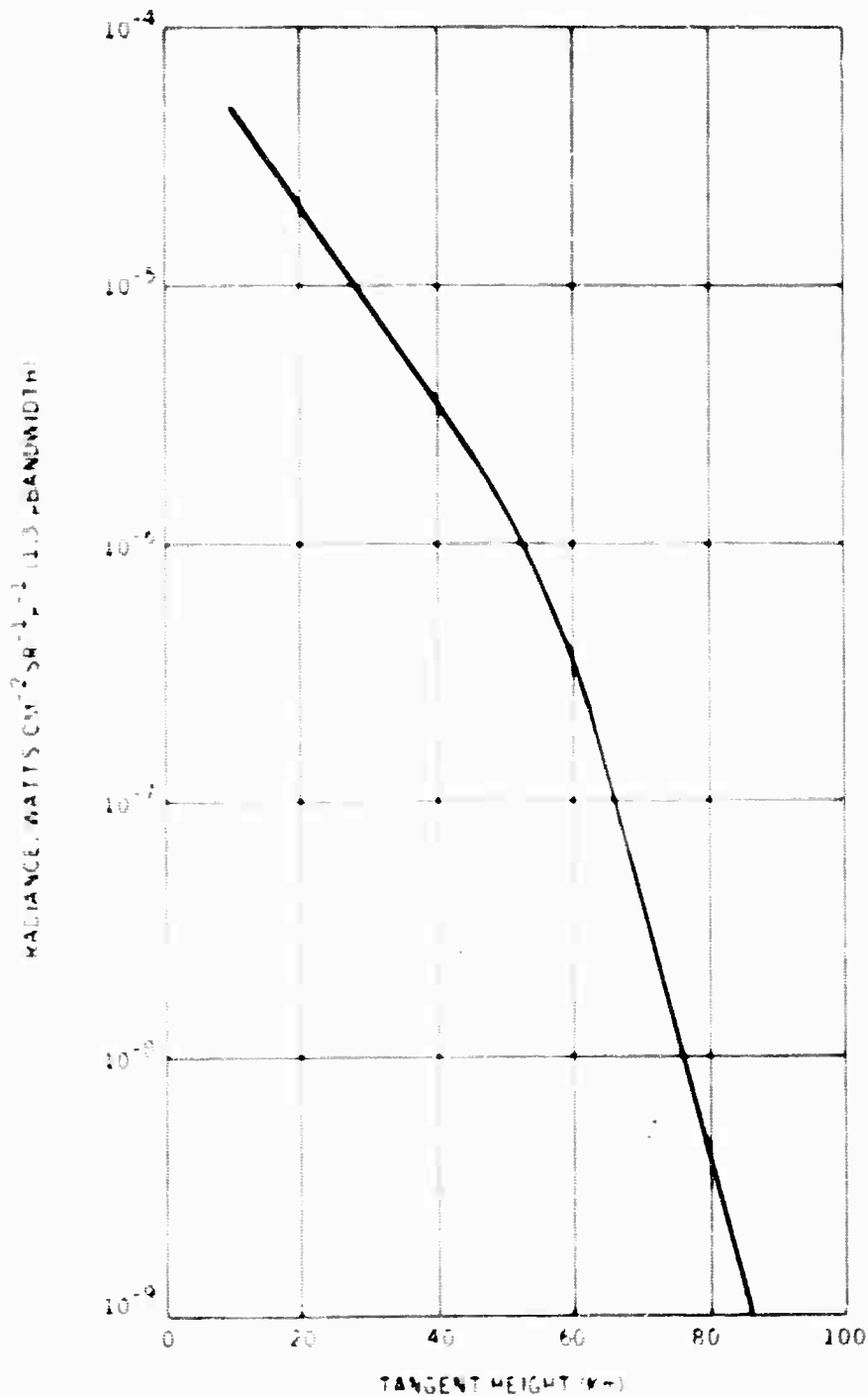


Figure 25. Horizon Radiance Profile, Nitric Acid (HNO₃, 10.5 to 11.7 microns)

UNCLASSIFIED

UNCLASSIFIED

The steep slopes in spectral radiance predicted near all window regions dictate that high spectral resolution (~ 0.1 -micron) measurements be made in order that the wavelength limits can be accurately located. As a result, high-resolution spectra are specified in each of the three window regions.

Additional data which relate to this limb measurement program were collected by Markov (USSR) and are reported in Applied Optics, Vol. 8, No. 5, May 1969, 887. A brief summary of pertinent results is presented in Table 6.

Of significant interest with respect to the USSR data are the high-altitude layers reportedly measured during four out of a total of 30 probe flights. The expected radiance levels of these layers as would be observed by a limb viewing instrument are shown in Figure 26. These radiance levels are seen to be considerably in excess of the highest radiance level predicted from the model. Also of interest is the fact that the radiance level measured within these high altitude layers is directly correlated with the geomagnetic index as seen in Table 7.

Further results of the atmospheric modeling studies which are of some interest include the spectral radiance levels expected from noctilucent clouds and interplanetary dust. Summaries of relevant facts are given in Tables 8 and 9. Regarding noctilucent clouds, it can be concluded that they may represent a considerable source of interference since they exhibit the following:

- Radiance in excess of the nominal target over a broad wavelength region
- Altitudes in the range of interest
- Occurrence over high-priority geography
- Sharp spatial gradients

The actual probability of occurrence however is uncertain. The presence of noctilucent clouds within a given data set may be identified by the radiance peaks near 20 and 25 microns, given a spectral resolution on the order of 1 micron.

Interplanetary dust may also represent a significant source of interference if data is collected within close angular proximity of the sun. Although this source of interference will be difficult to recognize, it may be possible to make identification of the sharp radiance peak in the atmospheric window near 12 microns.

The spectral radiance for noctilucent clouds and interplanetary dust as estimated from the model is compared to the reference target in Figure 27.

UNCLASSIFIED

Table 6. Summary of USSR Measurements of LWIR Upper-Atmospheric Radiance

<u>Flight Conditions:</u>	
Number of Flights:	30 probes - daytime 2 (+) satellites - day and night
Altitude Range:	Probe 100 - 500 km Satellite 200 - 350 km
Dates:	August 1958 to October 1965
Geomagnetic Index:	$K_p = 0$ to $K_p = 5$
<u>Results:</u>	
High-Radiance Layers:	
Occurrence:	4 Probes + satellites
Altitudes:	150 km, 280 km, 430 km and 500 km
Horizontal Emittance:	100 km (high-altitude) to 30 - 40 km
Layer Thickness:	10 km (high altitude) to 30 - 40 km (low altitude)
Ratio Path Length to Thickness:	100:1
Conditions Observed:	Day and night latitude ± 65 degrees
Highest Radiance Observed:	Probe at layer altitude; optical axis horizontal high geomagnetic index
Spectral Distribution:	Maximum in 4.5 - 8.5 μ
	30% (day) and 20% (night) in 0.8 - 4.5 μ
	3% (day) in 8.5 - 40 μ

Table 7. USSR Probe Measurements Maximum Radiant Emittance Observed with Vehicle within Layer and with Horizontal Viewing

Altitude (km)	Geomagnetic Index						
	K _P	0	1	2	3	4	5
	a _P	0	4	7	15	27	48
200						250	
240						150	
250/300		< 10					
290							690
320		20					
400		< 10					
420						220	650
450						180	
500		< 10				160/220	

Note: Units of radiant emittance are watts/m²

Wavelength increments are 0.8 - 40 μ and 2.5 - 40 μ

UNCLASSIFIED

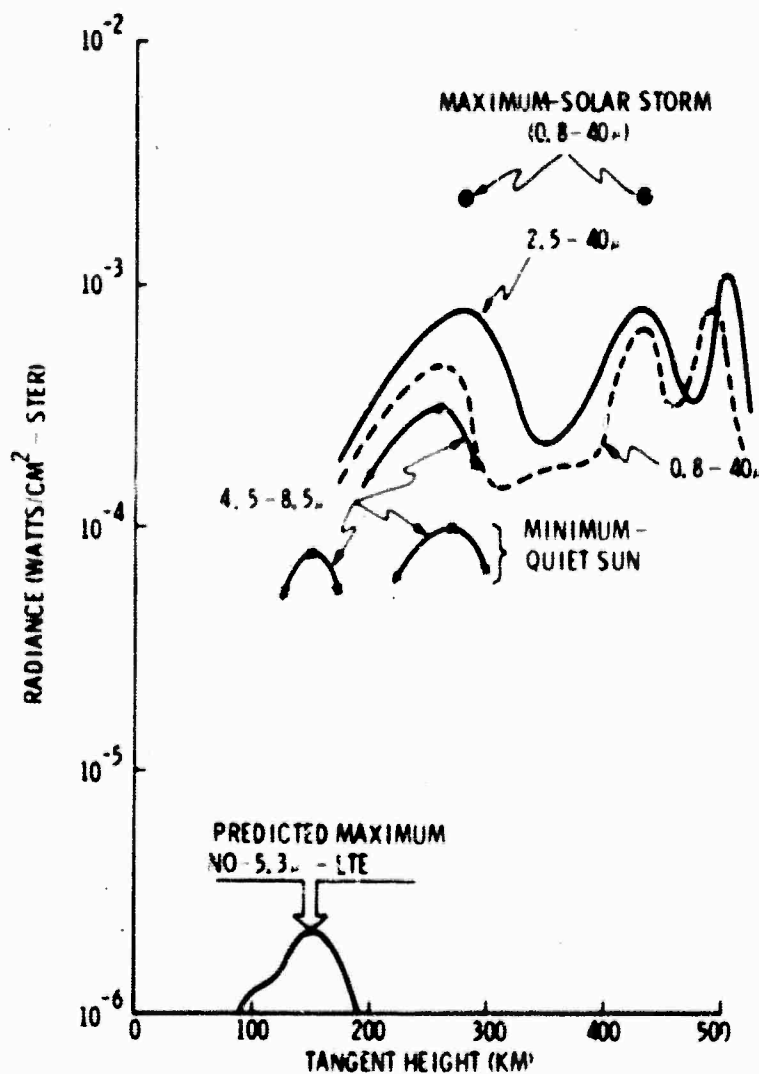


Figure 26. USSR Data Converted to Limb View Radiance

UNCLASSIFIED

UNCLASSIFIED

Table 8. Summary Data on High-Altitude Clouds

<u>Noctilucent (Natural)</u>	
Altitude	- 72 km to 92 km
Thickness	- 2 km average (0.5 to 5 km)
Latitude	- 45 degrees to 60 degrees North and South - 60 degrees most probable
Season	- Sharp summer maximum
Duration	- Several minutes to several hours
Composition	- Small (0.2-0.3 μ)-meteoric - Large (0.3-0.5 μ)-ice
Density	- 200 per cm ³ (size > 0.05 μ)
Temperature	- 135°K to 160°K
Geography	- Scandinavia and Northwest U.S., S. R.
<u>Nacreous</u>	
Altitude typically < 30 km	
Expected radiation levels much less than gaseous emission of CO ₂ , O ₃ and H ₂ O in lower atmosphere.	

Table 9. Summary Data on Interplanetary Dust

<u>Theoretical Model:</u>	
•	Heliocentric zodiacal dust cloud lenticularly shaped around plane of ecliptic which may extend as far as Jupiter
•	Composition: "Dirty" quartz
•	Number density: 10 ⁻⁹ to 10 ⁻⁸ per cm ³ at 1 au
•	Radiance measured only for: Wavelength near 2.2 μ and within 2-3 degrees of Sun
•	Extrapolated radiance (emission) using model:
	$N \sim 10^{-9} - 10^{-10}$ watt/cm ² -ster- μ at 50 degrees from Sun
	$N \sim 10^{-10} - 10^{-11}$ watt/cm ² -ster- μ at 90 degrees from Sun
•	Scattering small compared to emission beyond 5 μ

UNCLASSIFIED

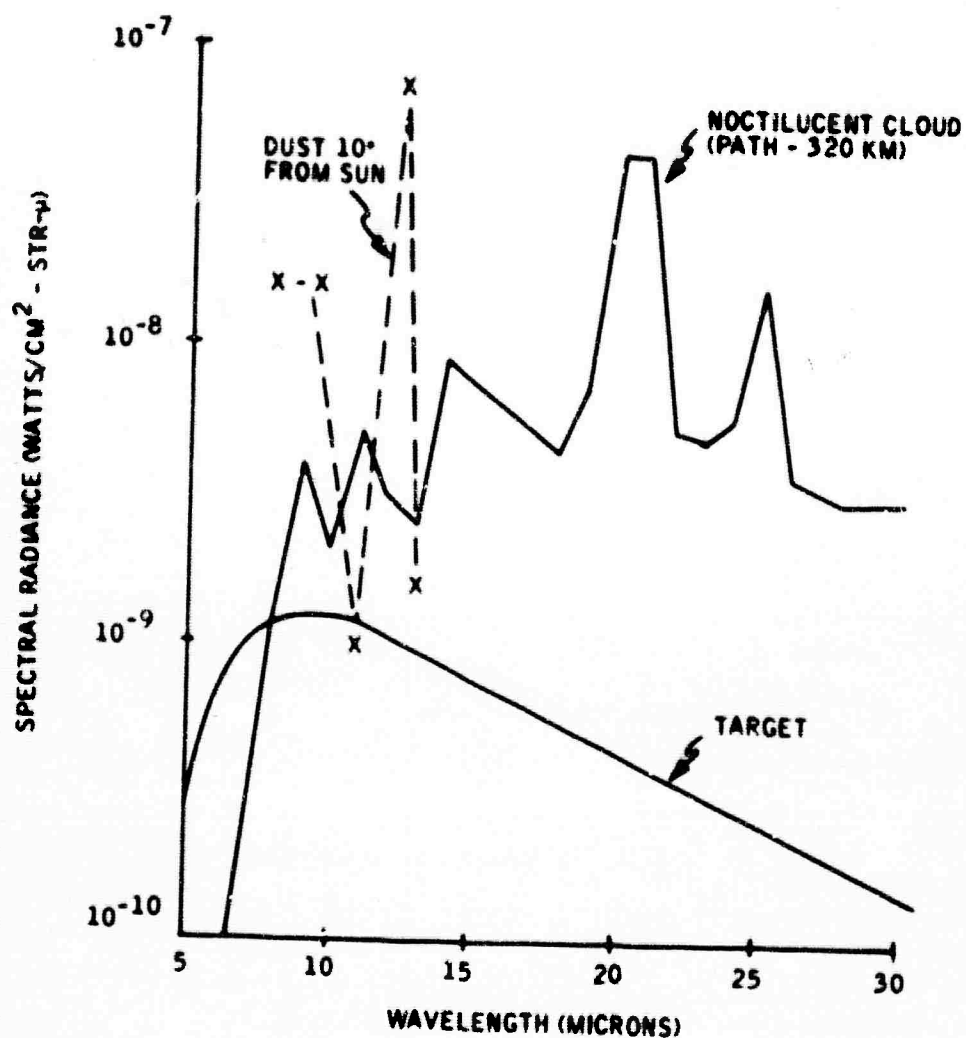


Figure 27. Predicted Emission From Noctilucent Clouds and Interplanetary Dust

UNCLASSIFIED

SECRET

SECTION 3 SYSTEM REQUIREMENTS

(S) The ultimate goal of a background measurement is estimation of the radiance distribution for amplitudes exceeding a level of interest defined by a model target. In the following, the problem of estimating the distribution from a limited number of samples is addressed, and error estimates are derived for the sample mean and variance as a function of the number of independent samples using information derived from a model atmosphere. The sampling defined above is obtained from the physics of the problem, deliberately weighted for measurements of extreme conditions which should sample the infrequent cases. An assumption of uniform sampling can then be used to obtain the upper bound of the error in estimation of the distribution.

(U) In the process of this examination, an estimate of the correlation lengths and times of the LWIR atmospheric radiance map was obtained. This information is of value in fixing the sample spacing for a scan and for a probe sequence in that the periodicity of the data is defined by these lengths and times.

(U) A summary of experiment requirements is given in Table 10.

3.1 BASIS FOR SAMPLING REQUIREMENTS

(U) Atmospheric characteristics used to obtain sampling requirements are taken from a low-altitude atmospheric model at 70 km, ozone concentration in North America at 45 km, 15-micron CO₂ radiance data from 30 to 40 km and arctic temperature gradient data near 50 km. A preliminary estimate of the number of samples required was made by computing the variance (annual) of the radiance, derived from the low-altitude model for all conditions modeled. A sample size was derived, in terms of estimating the mean (annual) radiance of all geographical regions, based on radiance profiles from the low-altitude atmospheric model, assuming all data were independent. This did not provide a means of establishing the number of probes and profiles per flight.

(U) To arrive at more definition of the sampling requirement, the spatial and temporal variations of available data were examined. For the most part, data were available only at altitudes less than those of interest for this measurement program. These data were used as a conservative (over) estimate of the actual number of samples required to define variations in the upper atmosphere.

SECRET
THIS PAGE IS UNCLASSIFIED

Table 10. Experiment Requirements Summary

Item	Requirement
Source of radiance	Earth's atmosphere
Altitude range	0 - 500 km
Background	Space
Viewing geometry	Limb view from earth's horizon to horizontal
Measurement platform	Probe vehicle altitude range 100 to 300 km
Vertical angular coverage	20 deg
Azimuthal angular coverage	360 deg
Horizontal profile spacing	1000 km
Number of profiles per flight	8 to 10
Geography	(1) Arctic and (2) temperate and (3) tropical
Season	(1) Winter and (2) summer
Time of day	(1) Noon, (2) midnight, and (3) sunrise, sunset
Number of flights	10 (optimum program) 6 (minimum program) 3 (limited objectives)

UNCLASSIFIED

3.1.1 Low-Altitude Atmospheric Model

Spectral radiance and radiance/altitude profiles were generated using the low-altitude atmospheric model. Within this model, there exists a variety of geographical and seasonal data variations. The model includes Arctic, temperate and tropical data during winter and summer, and involves variations in temperature, water vapor and ozone concentrations. The carbon dioxide mixing ratio is assumed constant at 320 ppm. Some examples of data variations used in the low-altitude model are given in Table 11. Radiance profiles within the 5- to 25-micron region were generated for ten different sets of conditions within the Arctic (winter), and five sets of conditions in the other region/seasons. The largest radiance variations at the higher altitudes were observed in the 6.3-micron H_2O absorption band. The mean radiance and standard deviation for this band at 70 km are given in Table 12. The large variability can be observed from the high percent standard deviation as compared to the mean, particularly in the Arctic region. The radiance variations in the 6.3-micron H_2O band will be used later to derive sample statistics. However, they are not sufficient since there is no information regarding how far apart, in either space or time, the different sets of conditions should be placed. Correlation studies will be presented in the next three subsections which relate to this question.

3.1.2 Temperature

Temperature is related directly to radiance in the low-altitude model since local thermodynamic equilibrium is assumed. Spatial and temporal variations in CO_2 radiance, for example, will largely be determined by temperature variations since the concentration is assumed constant. Within the altitude range of interest, the maximum temperature occurs near the 50-km altitude. An example of temperature variations with latitude in January is shown in Figure 28. The mean temperature increases as the tropical region is approached, with maximum variations about the mean on the order of $\pm 2.5^\circ K$. Since spatial gradients are of interest to the operational system in terms of background noise characteristics, the variations about the mean value will be emphasized in this and the following subsections.

To determine the significance of a $\pm 2.5^\circ K$ temperature differential, radiance variations were correlated with temperature at 12 microns by using the low-altitude model. It was found that, for absolute temperatures near $260^\circ K$, a $1^\circ K$ temperature differential resulted in a radiance variation of about 10% of the mean value. Thus a $\pm 2.5^\circ K$ temperature increment would be expected to cause a $\pm 25\%$ radiance variation at 12 microns, which is significant in terms of the goals of this measurement program.

Table 11. Low-Altitude Atmospheric Model -- Geographical/
Seasonal Data Variations

Geography and Season	Temperature (°K) (Altitude = 50 km)			Water Vapor Con- centration (ppm) (Altitude = 10 km)			Ozone Concen- centration (ppm) (Altitude = 35 km)		
	Cold	Mean	Warm	Low	Mean	High	Low	Mean	High
Arctic Winter	243	253	263	3.5	6.1	24	5.3	7.3	9.3
Arctic Summer	--	270	--	17	30	190	5.2	8.0	10.6
Temperate Winter	--	266	--	11	20	105	8.84	11.5	14.2
Temperate Summer	--	276	--	54	110	560	9.7	11.0	12.3
Tropical (Annual)	--	270	--	35	87	520	13.1	14.5	15.9
Extremes			Altitude = 80 km						
220			--	320	0.10	0.633	5.0		

UNCLASSIFIED

Table 12. Low-Altitude Atmospheric Model -
Statistical Radiance Variations

Geography and Season	Spectral Radiance (watt/cm ² -ster-micron)		Standard Deviation as a Percent of the Mean
	Mean	Standard Deviation	
Arctic Winter	14.6×10^{-9}	13.8×10^{-9}	95
Arctic Summer	8.9×10^{-9}	7.35×10^{-9}	83
Temperate Winter	11.2×10^{-9}	4.2×10^{-9}	38
Temperate Summer	9.4×10^{-9}	6.1×10^{-9}	65
Tropical (annual)	8.9×10^{-9}	5.5×10^{-9}	62

Note: Wavelength Region - 6.3 micron, H₂O Band
Altitude - 70 km

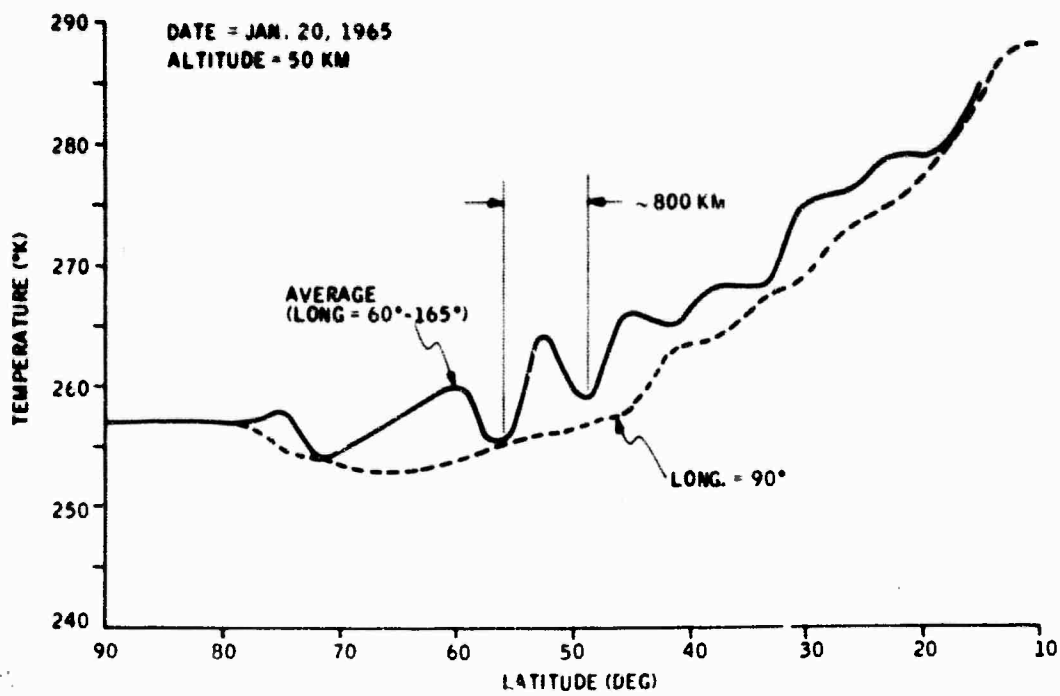


Figure 28. Atmospheric Temperature Variations with Latitude

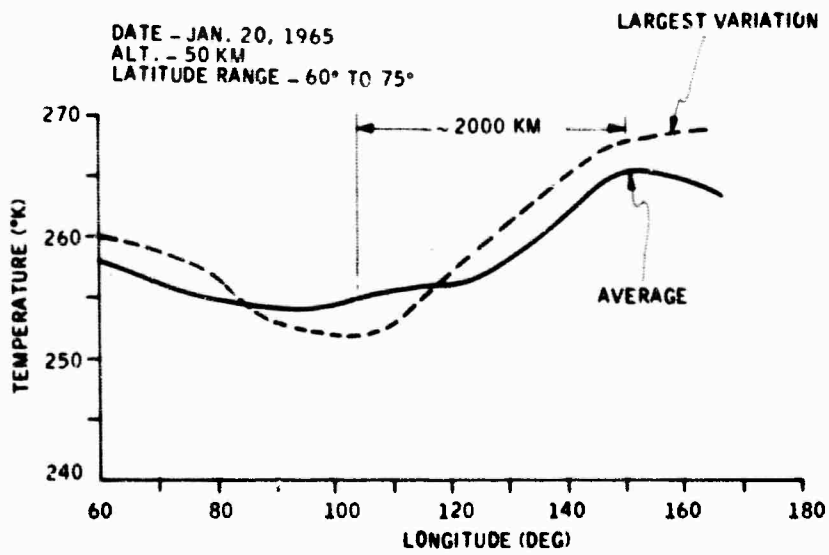


Figure 29. Atmospheric Temperature Variations with Longitude

UNCLASSIFIED

It can also be seen from Figure 28 that a temperature differential of $\pm 2.5^\circ$ K can occur over spatial increments as small as 7 deg (latitude) or about 800 km.

Longitude variations in temperature about the mean in polar latitudes are about the same magnitude as latitude variations, however, they occur at distances on the order of 2000 km as seen in Figure 29.

Seasonal variation of temperature gradients in the Arctic region have been computed from analyses published by A. J. Kentor (Ref. 3). These temperature gradients are computed over a 15-deg latitude increment and are shown in Figure 30. A semiannual variation is clearly evident with the largest gradients, greater than 0.5° K per degree latitude, occurring in the winter (January, February) as well as the summer (May-July).

3.1.3 Radiance Variations

Limb radiance variations in the 14- to 16-micron CO_2 band have been studied extensively for horizon sensor applications. In terms of this program, however, previous analyses have been concerned with variations at higher flux levels and lower tangent heights. Two such studies which included correlation distances and times were performed by Honeywell (Ref. 4) and Sperry Gyroscope (Ref. 5). Both studies were concerned with radiance at the 10 millibar level or generally from a 30- to 40-km altitude.

During the Horizon Definition Studies at Honeywell, correlation coefficients were computed in the residue variations in absolute radiance after removing systematic variations through a curve-fitting process.

Correlation analysis was performed on more than 1000 synthesized radiance profiles on a global basis. Significant results in terms of absolute radiance are:

- Temperature is highly correlated with absolute radiance at 10 mb.
- Correlation distances were on the order of 800 to 900 km (see Figure 31).
- Correlation times were on the order of 15 days.
- A strong frequency component was observed for periods of from 50 to 75 days.
- Diurnal variation was insignificant.

UNCLASSIFIED

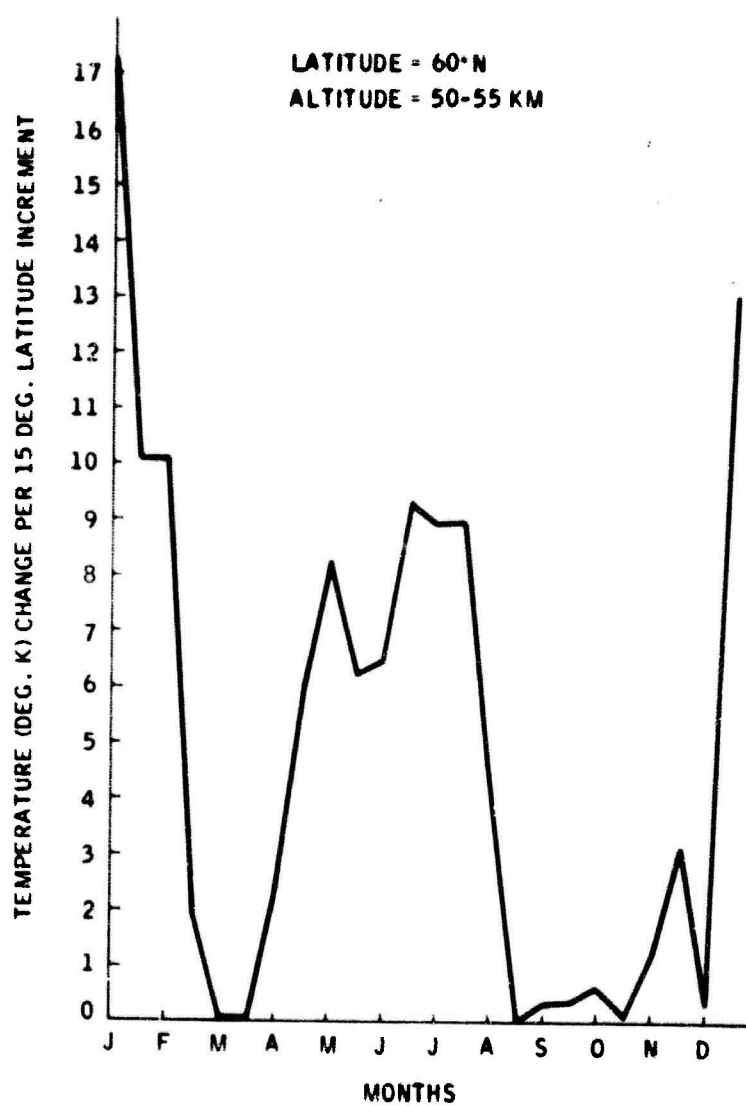


Figure 30. Arctic Temperature Gradients -
Latitude = 60°N, Altitude = 50 -
55 km

UNCLASSIFIED

UNCLASSIFIED

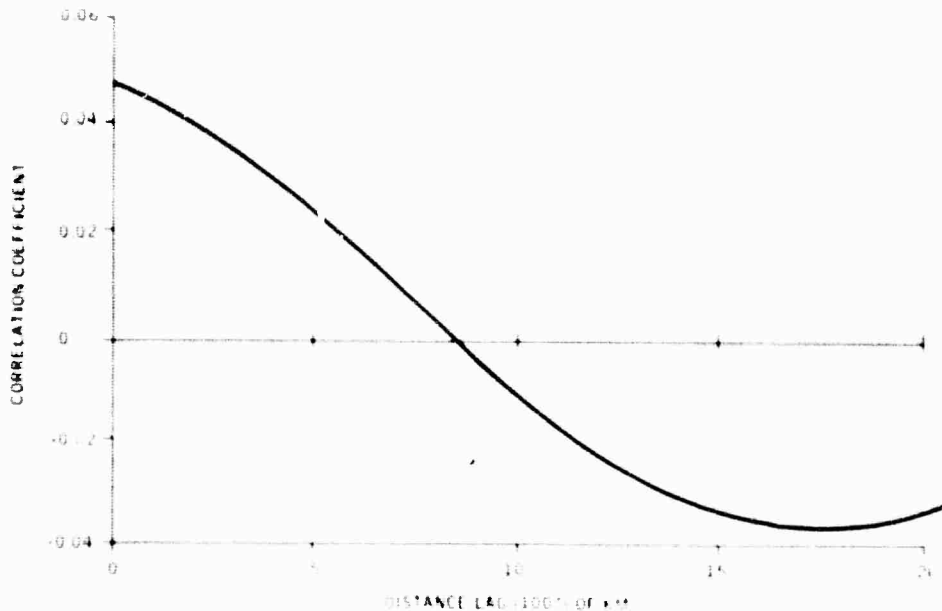


Figure 31. Autocorrelation Function for 15-micron CO₂ Radiance, February - 30 - 40 km

Other studies (Ref. 5) were performed on the absolute variations of 15-micron, CO₂ radiance. These studies indicate representative correlation lengths on the order of 2500 nm (approximately 40 deg on the earth) and correlation times ranging from 7 to 15 days.

Two conclusions drawn from the results of these two correlation studies are:

- Regional grouping of arctic, temperate, and tropical, provides high assurance of data independence even in terms of absolute radiance variations.
- Data collected within a period of less than one week is expected to be highly correlated.
- Data taken closer together than approximately 800 km are highly correlated and cannot be treated as independent samples.

UNCLASSIFIED

UNCLASSIFIED

3.1.4 Horizontal and Vertical Distributions

Using the low-altitude atmospheric model, horizontal and vertical radiance distributions were computed for limb viewing conditions. Horizontal radiance distribution, in this case, shows how energy accumulates along the line of sight in a horizontal direction. The data shown in Figure 32 is a typical distribution for radiance in the 15-micron CO_2 absorption band. The largest fraction of the total radiance observed by an exatmospheric sensor is contributed by atmosphere near the minimum tangent height. As the horizontal dimension (D) expands about the minimum tangent height, the contribution to the total radiance decreases. A shift to the left in the horizontal distribution is caused by the large absorption for a longer slant path. It can be seen that a total horizontal dimension of 1000 km is sufficient to account for the total radiance when the limb is viewed at a minimum tangent height of 60 km.

Therefore, if measurements are made at the same azimuthal position, a separation of 1000 km on the surface will be sufficient to ensure that redundant measurements are not made on the same set of atmospheric constituents. It is expected that this distance would be somewhat larger in atmospheric window regions and at higher altitudes.

The corresponding radiance distribution with altitude is given in Figure 33. Since the minimum tangent height is 60 km, there will be no contribution to the total radiance at lower altitudes. The distribution is sharply peaked near the minimum tangent height, with 90% of the total radiance accumulated between the altitude limits of 60 to 67 km.

3.1.5 Ozone Concentration

Variations in ozone concentration will cause variations in limb radiance in the 9.6-micron absorption band. Spatial and temporal variations in ozone concentration have been studied (Ref. 6), by means of Umkehr data on altitudes up to 45 km. Eleven stations throughout the world reported data on a yearly basis; a sample of results for the three North American stations is given in Figure 34. The ozone concentration latitude gradient between the various stations was computed on a monthly basis and is shown in Figure 35. The North American stations had the largest gradients, up to 1.5×10^{10} molecules per cm^3 per degree, and showed a semiannual cycle. In this case, the spring and fall seasons produced the largest gradients. To determine the influence of ozone concentration gradient on 9.6-micron radiance, a number of atmospheric conditions were compared using the low-altitude model.

It was found that a 10% change in concentration results in a 5% change in radiance. Thus, during the spring and fall, a 25% change in 9.6-micron radiance may be expected over a 3- to 5-deg latitude increment with respect to the North American stations.

UNCLASSIFIED

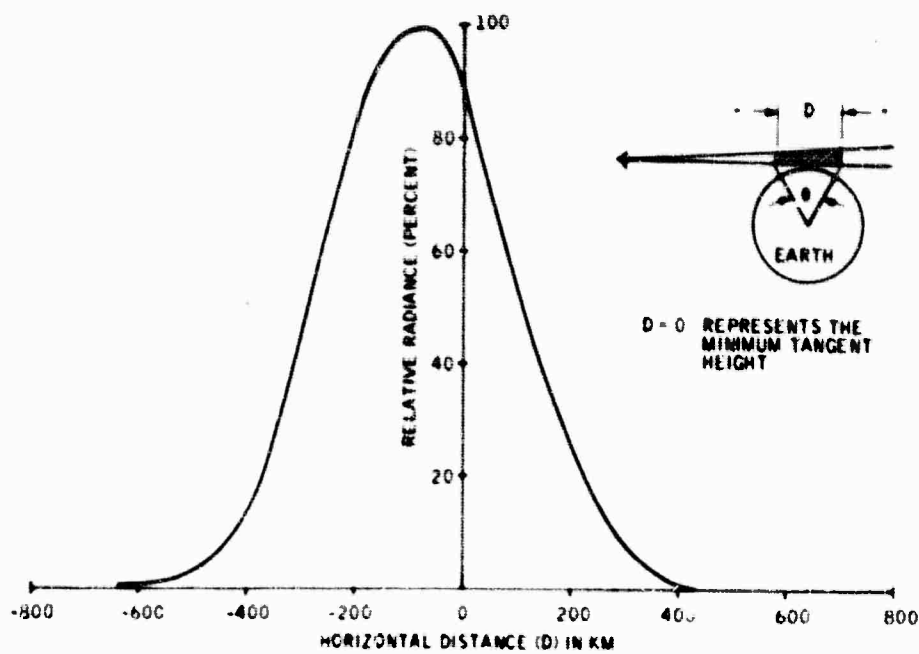


Figure 32. Horizontal Radiance Distribution - Minimum Tangent Height = 60 km

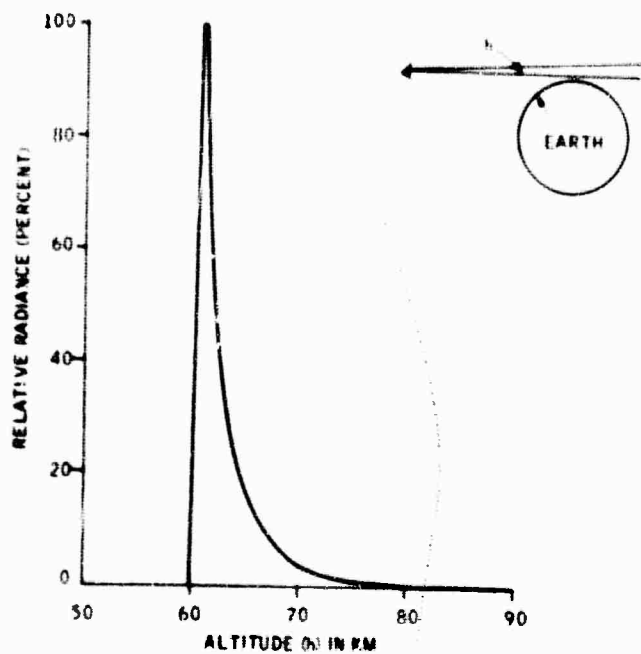


Figure 33. Vertical Radiance Distribution - Minimum Tangent Height = 60 km

UNCLASSIFIED

UNCLASSIFIED

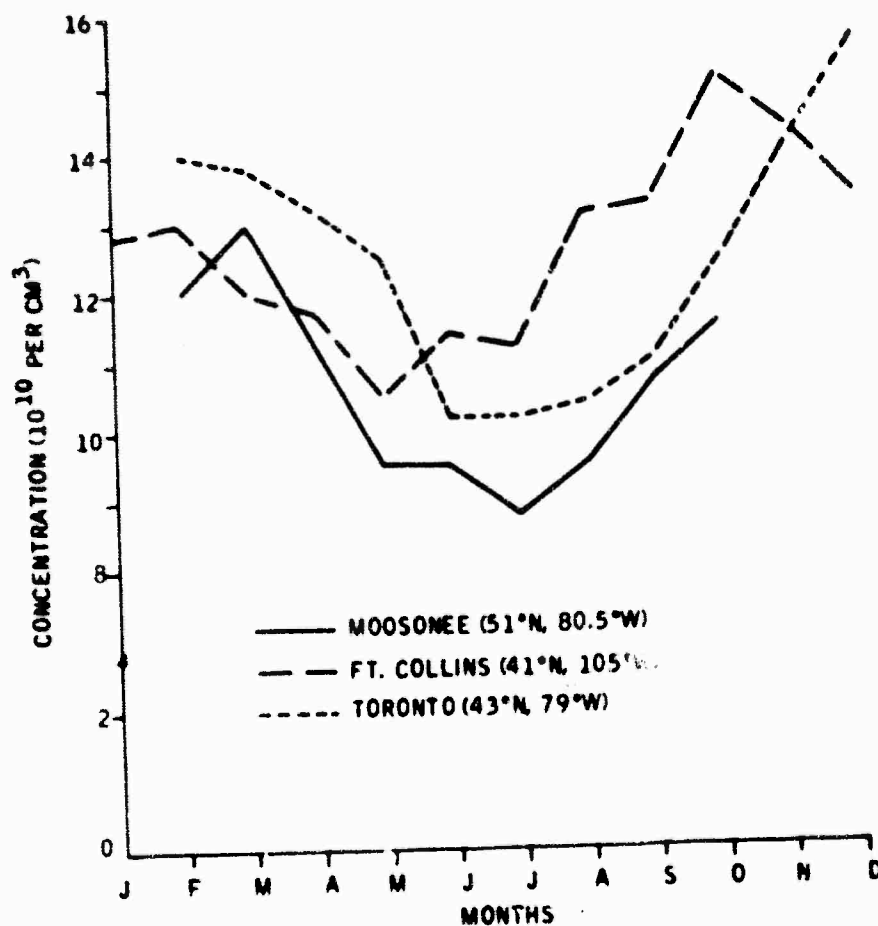


Figure 34. Annual Variation of Ozone Concentration -
Altitude = 45 km

UNCLASSIFIED

UNCLASSIFIED

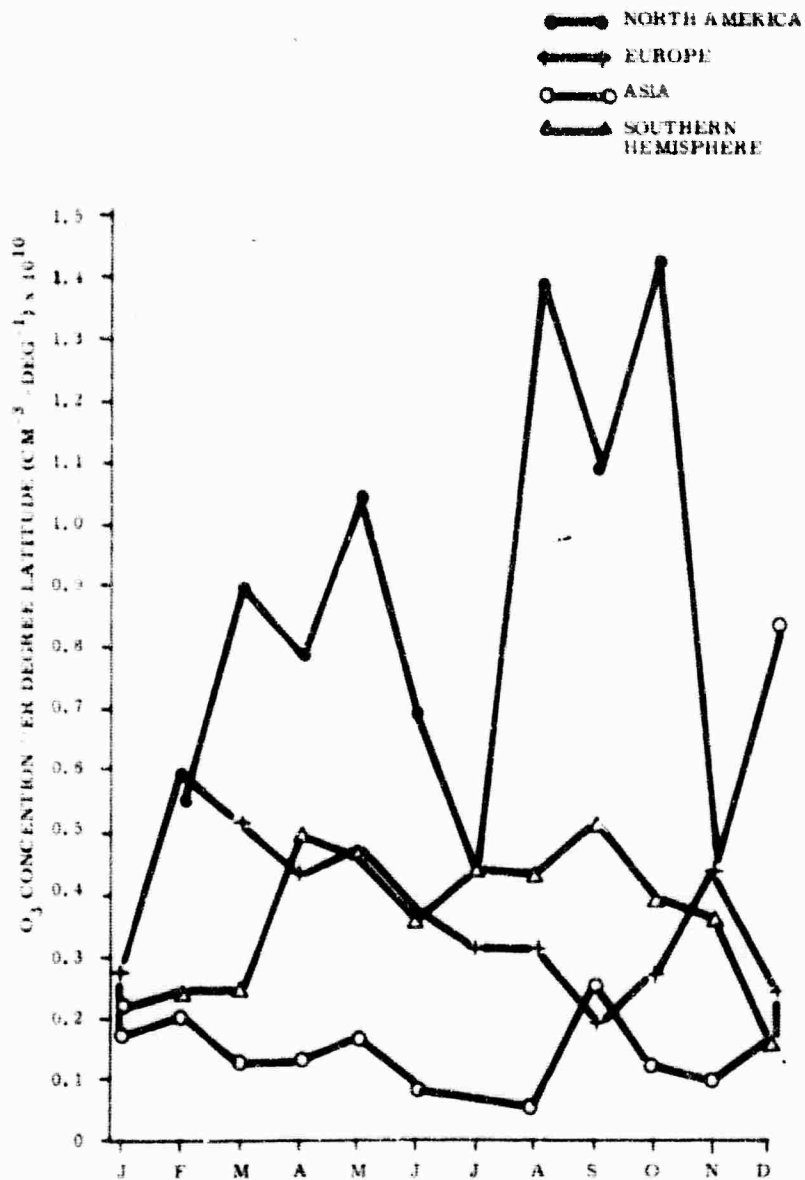


Figure 35. Variation in Ozone Concentration at Various Locations - Altitude = 45 km

UNCLASSIFIED

UNCLASSIFIED

Data from the eleven stations were used to derive the spatial correlation coefficient of ozone concentration gradients. The results are shown in Figure 36. This curve represents the best fit through a relatively small number of data points within a longitude spread of 2000 km. In this case, a correlation distance for ozone of about 600 km is indicated.

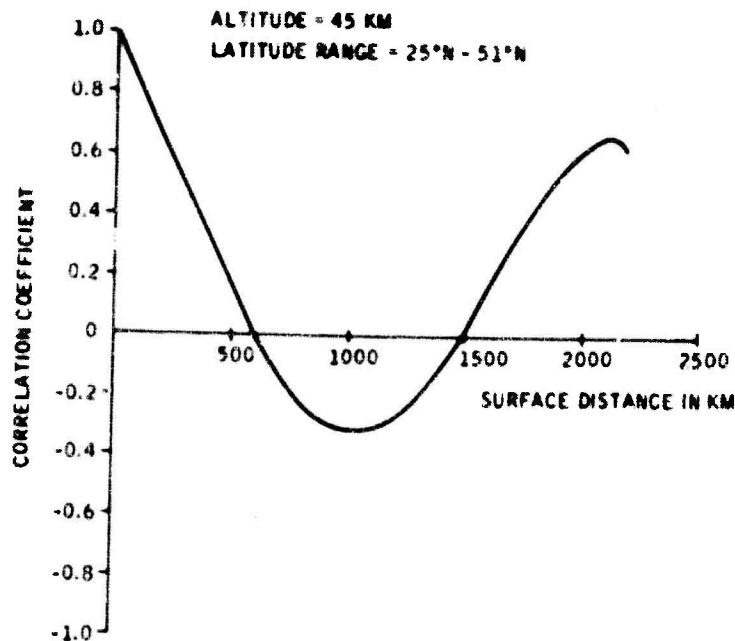


Figure 36. Longitudinal Correlation in Ozone Concentration

Autocorrelation and crosscorrelation functions were derived using data from the various stations to determine the seasonal correlation time. Two such correlation functions involving two North American stations are shown in Figures 37 and 38. These two functions show the shortest and longest correlations times found, namely from two to four months.

The diurnal variation in ozone concentration has been estimated by B. G. Hunt (Ref. 7). According to these estimates, the largest diurnal variation in concentration occurs at an altitude of 76 km and involves rapid changes near sunset and sunrise (see Figure 39). The atmospheric radiance model does not predict large diurnal changes in 9.6-micron radiance at this altitude; however, large change in radiance (nearly a factor of 3) is predicted for tangent heights near 90 km.

UNCLASSIFIED

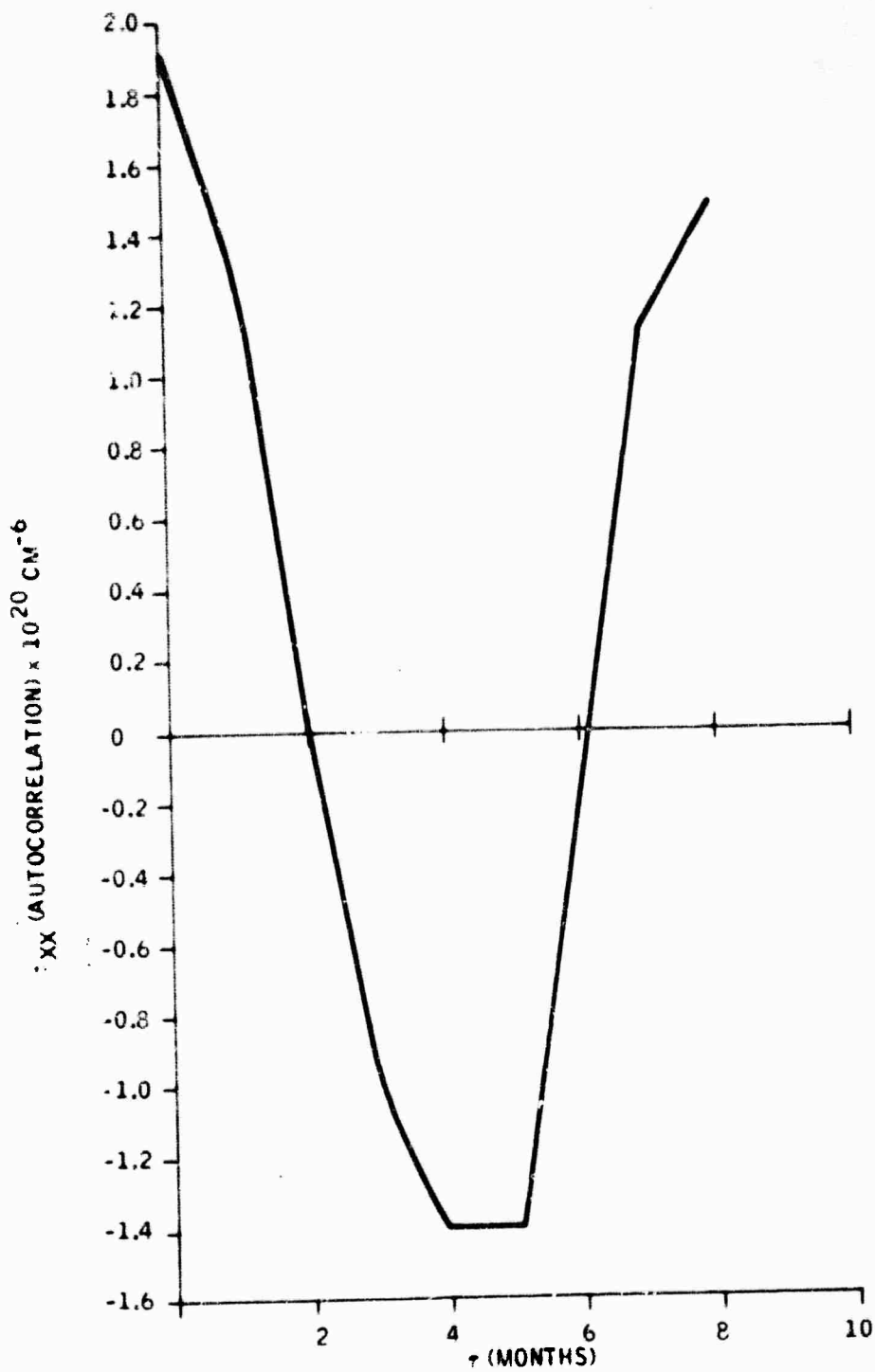


Figure 37. Autocorrelation of Ozone Concentration at 51°N and 80.5°W (Moosonee)

UNCLASSIFIED

UNCLASSIFIED

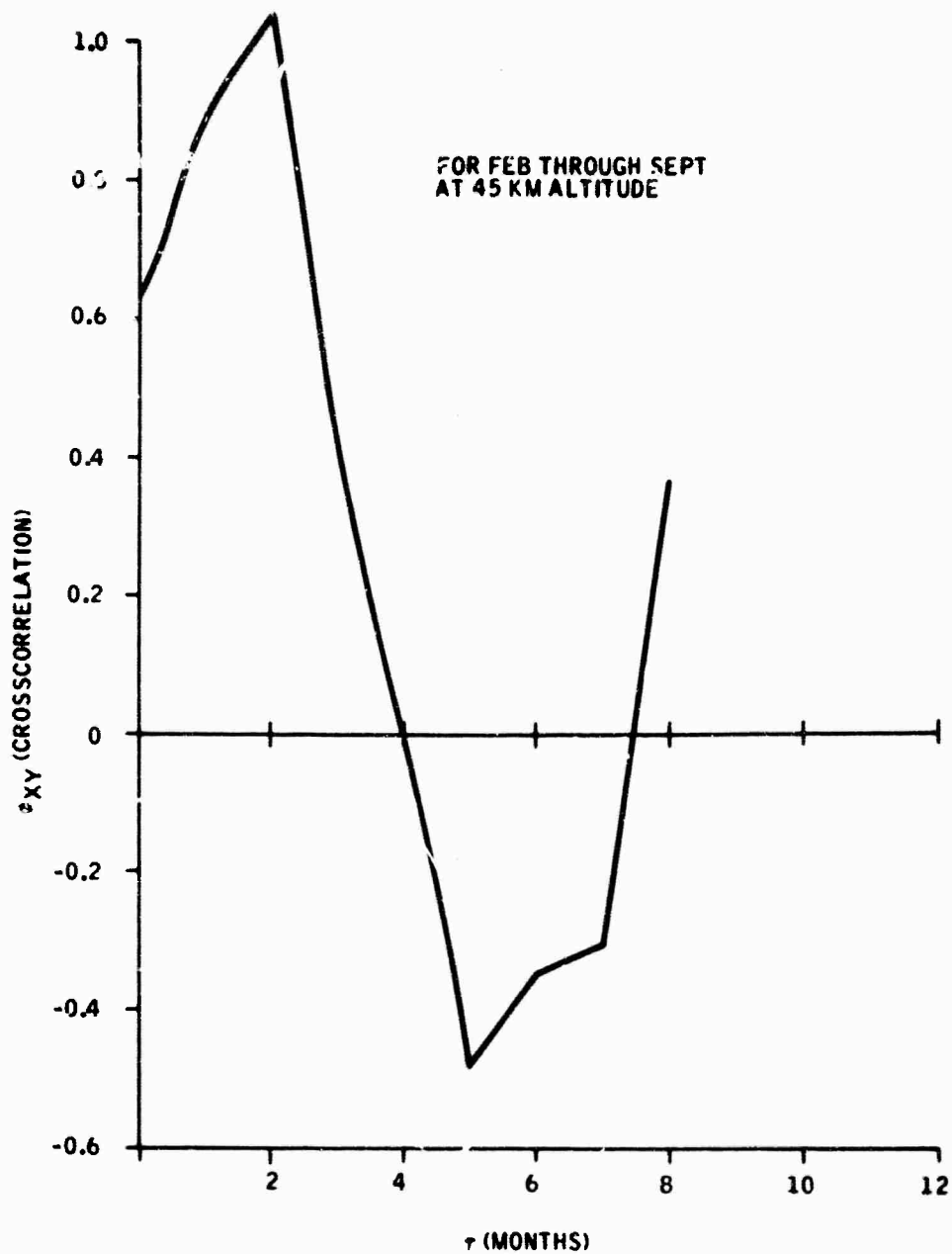


Figure 38. Crosscorrelation of Ozone Concentration Between 41°N, 105°W and 51°N, 80.5°W (Fort Collins and Moosonee)

UNCLASSIFIED

UNCLASSIFIED

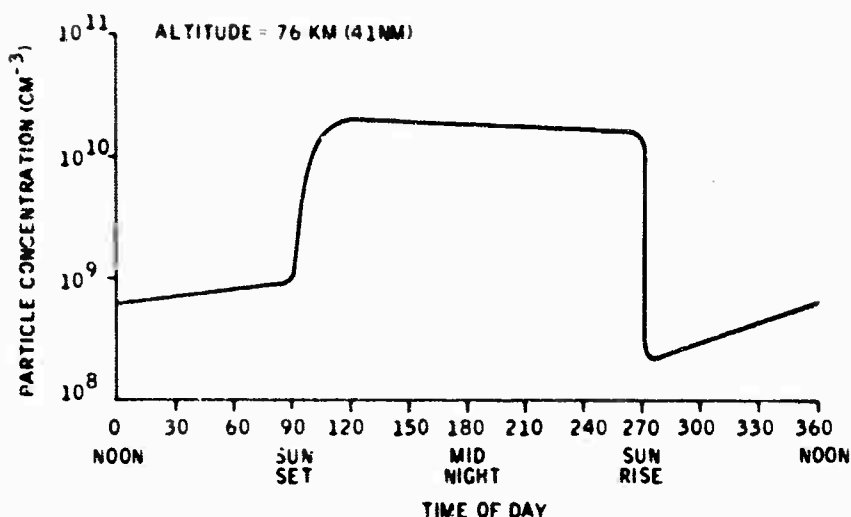


Figure 39. Diurnal Variation of Ozone (from Ref. 7)

3.2 NUMBER OF PROFILES PER FLIGHT

A number of considerations are involved with the specification of how many profiles are to be collected on each flight. They are:

- Spacing between profiles
- Vertical extent of profiles
- Maximum scan rate
- Total time of flight

The approach used here to specify the spacing between profiles is designed to ensure a spacing sufficiently wide that each profile can be considered an independent piece of information. To do this, it is necessary to ensure that each profile is separated by at least one correlation distance. The correlation distance in terms of gradient structure in the lower atmosphere has been estimated in the previous subsection to be in the range of 600 to 900 km depending on constituent per wavelength.

During a given probe flight, it is expected that measurements will be taken throughout a vehicle altitude range from 100 to 300 km. In this altitude range, the circumference on the horizon changes from 7000 to 11,000 km.

Based on the assumptions that:

UNCLASSIFIED

UNCLASSIFIED

- (1) most profiles are collected at the higher altitudes (horizon circumference $\sim 10,000$ km, and
- (2) correlation distances of gradient structure in the upper atmosphere will be larger (~ 1000 km) than in the lower atmosphere

the number of profiles, spaced evenly throughout one complete azimuthal revolution is $10,000/1000 = 10$. In terms of azimuth angle, the profiles are 36 deg apart.

In this way, uniform sampling is provided in all directions from the vehicle position with reasonable assurance that each profile will represent an independent sample. This specification is not necessarily a fixed requirement for all flights. For example, if after the first one or two flights, the estimates are found to be inaccurate it is not difficult to reprogram the vehicle control system to provide a different azimuthal spacing. Nevertheless, it will be assumed for purposes of this study that 10 profiles per flight represents a reasonable goal, and this number will be used during further analyses.

3.3 SCAN PATTERN

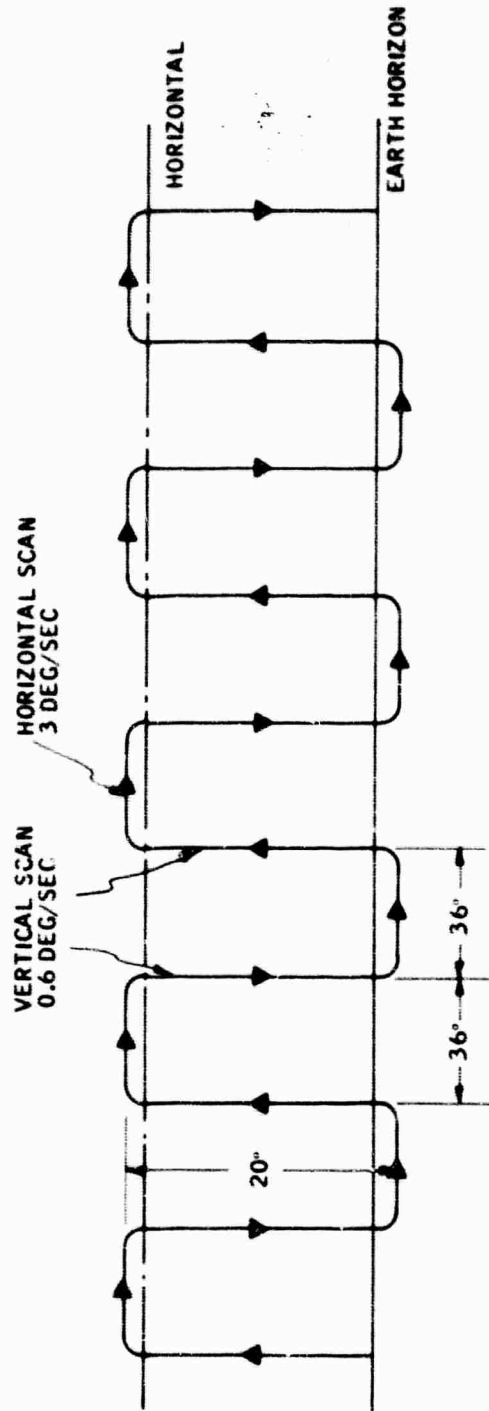
Since the scan motion must be provided by some means external to the radiometer itself (internal scanning mirrors are not recommended), it is desirable that the pattern be as simple as possible. In this way, unnecessary mechanical constraints are minimized as is the impact on vehicle dynamics.

The objective of each flight is to collect 10, evenly spaced, vertical profiles. A vertical profile involves scanning the field of view from the horizon to a horizontal direction. For a vehicle at a 300-km altitude, the vertical-angle requirement is somewhat more than 17 deg and, to allow for a ± 1.5 -deg attitude control tolerance, a 20-deg vertical scan is specified.

Scan rate limitations which result from vehicle and sensor studies are:

- Maximum scan rate to maintain radiometer sensitivity
= 0.6 deg/sec.
- Maximum rate of vehicle rotation between profiles = 3.0 deg/sec.

A simple scan pattern which collects the required data with high efficiency is shown in Figure 40. In this case, each vertical scan consumes about 33 sec, and 12 sec are consumed between profiles. For one complete revolution collecting 10 vertical profiles, the total required time is $330 + 108 = 438$ sec. This total time is compatible with the time available above 100 km using a



NOTE: ANGLES MEASURED AT SENSOR

Figure 40. Limb Measurement Scan Pattern

UNCLASSIFIED

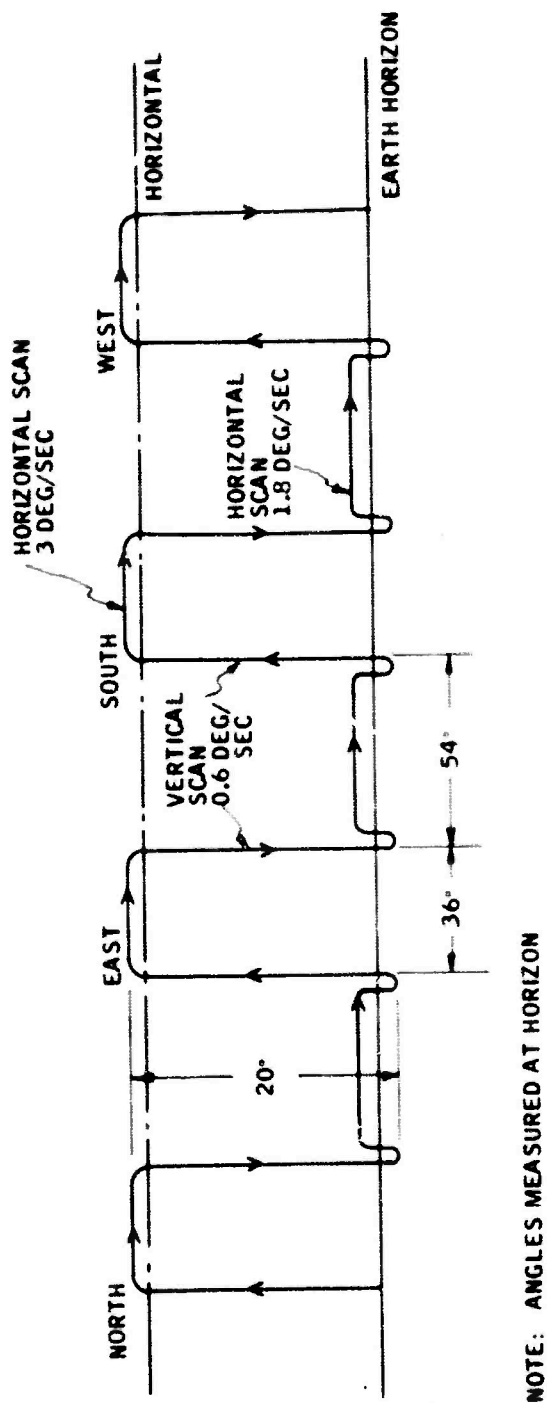


Figure 41. Alternate Scan Pattern

UNCLASSIFIED

SECRET

(U) Nike-boosted Black Brant VC probe vehicle. This vehicle provides about 480 sec of measurement time; thus a 10% time margin is available which should be sufficient for turn-around maneuvers.

(U) With the same scan pattern, a total of eight vertical profiles could be collected using the Black Brant VB vehicle. An alternate scan pattern which provides for data collection both in a vertical and a horizontal direction, is shown in Figure 41. Data collected while scanning in a horizontal direction would be a useful addition to the total set, since an operational detection sensor would scan in this mode. The line-of-sight would be positioned from 1 deg to 2 deg above the earth's horizon during horizontal data collection to provide data on horizontal gradient structure near the tangent heights of interest to this program. Since the sensor instantaneous field of view is larger in a horizontal direction, the horizontal scan rate can be increased by a factor of 3 to maintain the minimum dwell time.

(U) At the top of the scan pattern, horizontal separation of 36 deg will ensure independence of the vertical profiles. A total, of eight vertical profiles and about 160 deg (4500 km) of horizontal data could be collected in 405 sec. With a Nike-boosted Black Brant VC vehicle, a nearly 20% margin exists for turn-around maneuvers.

3.4 NUMBER OF FLIGHTS

(U) The approach used to arrive at the total number of samples, and therefore total number of flights, is based on applicability of the resulting data to operational system design.

(S) The detection system design problems of interest herein can be stated generally as follows:

- What is the probability that a target detection sensor will encounter a level of background radiation sufficiently high so as to prevent detection?
- Under what conditions of geography and time (diurnal and season) is target detection impossible due to the high level background radiation?
- What is the minimum tangent height at which successful target detection can be accomplished on a global basis with high probability?

(U) These three questions are interrelated and form the basis for the sampling analysis which follows. The sampling analysis in this subsection represents a statistical approach using the variance predicted from the

SECRET
THIS PAGE IS UNCLASSIFIED

low-altitude model to derive probability estimation errors with a given number of samples. In the next subsection, a flight plan is developed based on the influence of solar radiation on radiance variations in the upper atmosphere.

Overall conclusions from these two approaches can be stated as follows:

- A probe vehicle is most suited to the collection of extreme value data. A small number of probe flights could satisfy the following objectives:
 - (1) Verify form of probability distribution at low levels where estimation errors are compounded.
 - (2) Establish bounds on requirements for subsequent satellite flight program.
 - (3) Provide early assessment of sensor performance under flight conditions.
 - (4) Update atmospheric model in terms of high-altitude radiative processes and constituent distributions.
- The atmospheric model can be used to provide approximate launch locations and times for collection of extreme radiance data. Independent temperature, solar flux and geomagnetic index would be valuable.
- A probe is not a suitable vehicle with which to collect the complete global data set necessary for operational system design.

3.4.1 Statistical Analysis of Radiance Variations

A distribution of radiance values was generated for the lower-atmosphere model using the program developed in the first phase of this study and 40 sets of input data, covering climatic and constituent distribution extremes. These data were summarized in Table 12.

For simplicity, the mean and variance over a climatic zone (Arctic, temperate, and tropic) were examined rather than the distribution proper. Using the sample mean as an estimate of the population mean, the functional dependence of accuracy, confidence limits and number of samples was derived. The same approach was used to derive accuracy and confidence limits for the sample variance.

SECRET

(U) The statistical analysis made herein is in terms of the variance expected in the limb radiance of the 6.3-micron H_2O band at an altitude of 70 km. This band produced the largest variance and would lead to a conservative sampling requirement.

The basic approach developed in this subsection can be stated as follows:

- Given a finite sample (N) of radiance profiles, assume the population of all radiation profiles is normally distributed with mean μ and variance σ^2 .
- Fit a normal distribution through the data points and estimate μ and σ^2 .
- Extrapolate using the fitted distribution to probability levels of interest to the operational system, i.e., 1% probability that background exceeds target.
- Determine the errors in estimating probability in terms of the total number of samples (N).

(U) The inputs to this process are the mean and variance of the radiance predicted from the low-altitude model which were given in Table 12. The Arctic and temperate regions are subgrouped into two seasons, winter and summer, which represent the annual extremes in the model. No seasonal variation is programmed for the tropical region.

(U) Data independence is reasonably assured with seasonal grouping since few of the correlation or gradient structure studies of section 3.1 indicated correlation times greater than a period of three months. In addition, using the winter and summer seasons to represent the data extremes is consistent with temperature gradient data and therefore 15-micron CO_2 radiance. In terms of ozone concentration, the maximum gradients were observed in the spring and the fall seasons over North America. However, in all other regions, the gradient structure showed little seasonal dependence.

(S) The numerous atmospheric combinations available within the model were assumed to be independent and were programmed to yield radiance profiles. The mean and the standard deviation of radiance variations at the 70-km altitude was computed. It can be seen from Table 12 that, for all regions/seasons, the mean and standard deviation in radiance represent significant values in terms of the noise equivalent radiance (NER) in this band ($NER = 2 \times 10^{-10}$ watt/cm²-ster-micron). Since the NER is based on the reference target, it is concluded that the five regions/seasons frequently produce radiance variations in the order of 50 to 150 times the target level and therefore must be included in a minimum program to collect a meaningful global sample.

SECRET
THIS PAGE IS UNCLASSIFIED

Standard statistical methods were used to derive estimation errors for a given sample size. The assumption involved with these methods is that the population is normally distributed. The two population parameters estimated from the sample data are the mean (μ) and standard deviation (σ).

The population mean (μ) is estimated to be the sample mean \bar{x} with confidence limits established by the Student's t distribution. If s is the sample standard deviation then the estimation error is determined by the inequality

$$\left| \frac{(\bar{x} - \mu) \sqrt{N-1}}{s} \right| < t_m$$

where

N = sample size

m = 1 - confidence level

The population variance (σ^2) is estimated to be the sample variance (s^2) with confidence limits established by the chi-square distribution with $N-1$ deg of freedom. In this case, the following inequality is used:

$$\frac{N_s^2}{X_2^2} < \sigma^2 < \frac{N_s^2}{X_1^2}$$

where X_2^2 and X_1^2 are set by the confidence level.

Using the mean and standard deviation for the Arctic winter case, the two errors were determined at the 80% confidence level. These errors are shown for sample sizes from 10 to 60 in Figure 42. For purposes of estimating probabilities beyond the one sigma point, the total error will be the sum of the error in the mean and the error in the standard deviation. For a single flight during the arctic winter which collects 10 independent profiles, the total radiance error at the 80% confidence level is nearly 100%.

This error is distinguished from the radiance error on any given profile which is determined by instrument calibration. The radiance sampling error relates to the ability to fit a normal distribution to the sample profiles and its accuracy in terms of the expected population mean and variance. To reduce the total sampling error to the order of the calibration error (10%) would require on the order of 600 to 700 samples. The other regions/seasons are expected to require fewer samples but not significantly in terms of a probe program where only 10 profiles are collected per flight.

SECRET

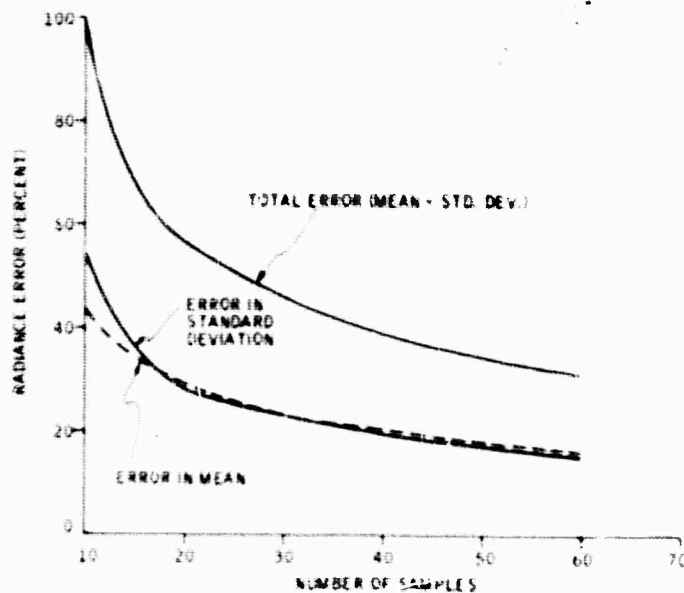


Figure 42. Radiance Sampling Error, Arctic Winter

(S) The radiance sampling error can be related to probability estimation errors through the use of Figure 43. These curves show the error in estimating how often the background exceeds the target level as a function of total radiance error. For example, if it is significant that the background exceeds the target 1% of the time for a given operational system, then data collected from a single flight in the arctic winter (100% radiance error) will lead to errors in estimating that probability level which are considerably in excess of a factor of 10. To reduce this error to less than a factor of 2 would require about a 10% radiance error and 600 to 700 samples.

(U) This situation applies for the most part to the other regions/seasons as well. On this basis, the total number of vehicles required to sample the five regions/seasons would be on the order of 300. The obvious conclusion is that a probe flight program, as structured in this report, is not suitable for the collection of a global sample of data such that the total population can be estimated within tolerable accuracy bounds.

(U) On the other hand, a probe flight program would be useful to sample radiance extremes to the extent that the extreme conditions can be predicted in advance. As such, the form of the population distribution could be verified at the low end of the probability scale where a simple "Gaussian" assumption can be orders of magnitude in error.

An attempt to isolate extreme conditions is made in the next subsection in terms of solar input flux to the upper atmosphere.

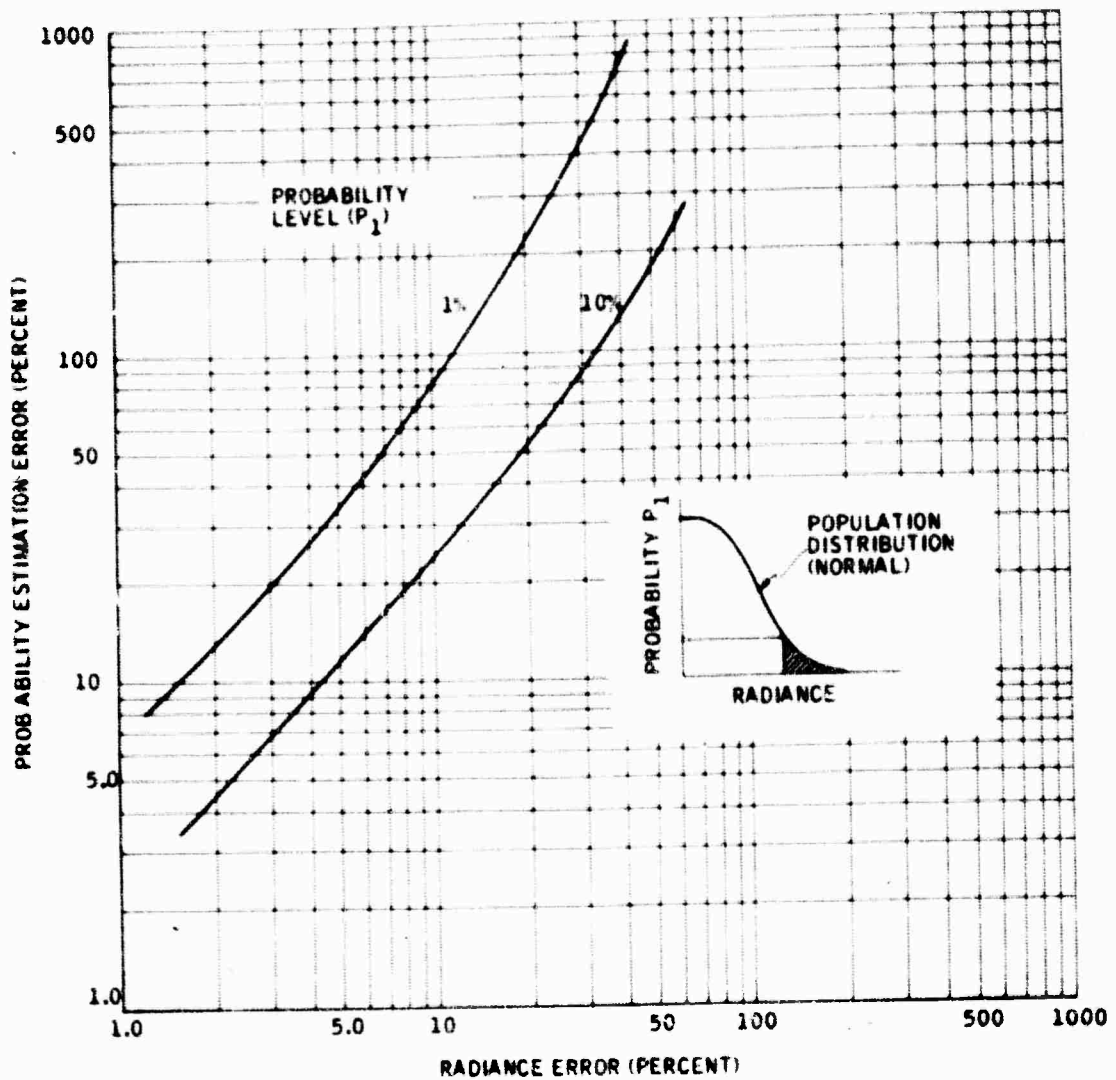


Figure 43. Probability Estimation Errors

SECRET

3.4.2 Solar Radiation

(U) Upper atmospheric radiance levels in some wavelength regions has been clearly related to the level of solar radiation exciting certain molecular species. The large diurnal effect which results has been discussed in section 2.7.

(S) In this subsection, the variations in solar radiation as well as solar disturbances are examined in terms of their influence on a flight measurement program. Very little is known about the effects of solar disturbances on LWIR radiance with the exception of the correlation of the USSR data with geomagnetic index. As a result, solar disturbances are considered to be of secondary importance in establishing a flight program based on probe vehicles.

Temporal and Geometric Characteristics of Solar Radiation -- (U) Because solar radiation has a dominant influence on the excitation state of the earth's atmosphere, attention has been given to defining solar illuminance with respect to the location, timing, and altitude of sounding rockets for limb radiance measurement.

(U) Figure 44 shows the daily integrated solar radiation reaching a unit horizontal area at the top of the atmosphere for different latitudes and months of the year.

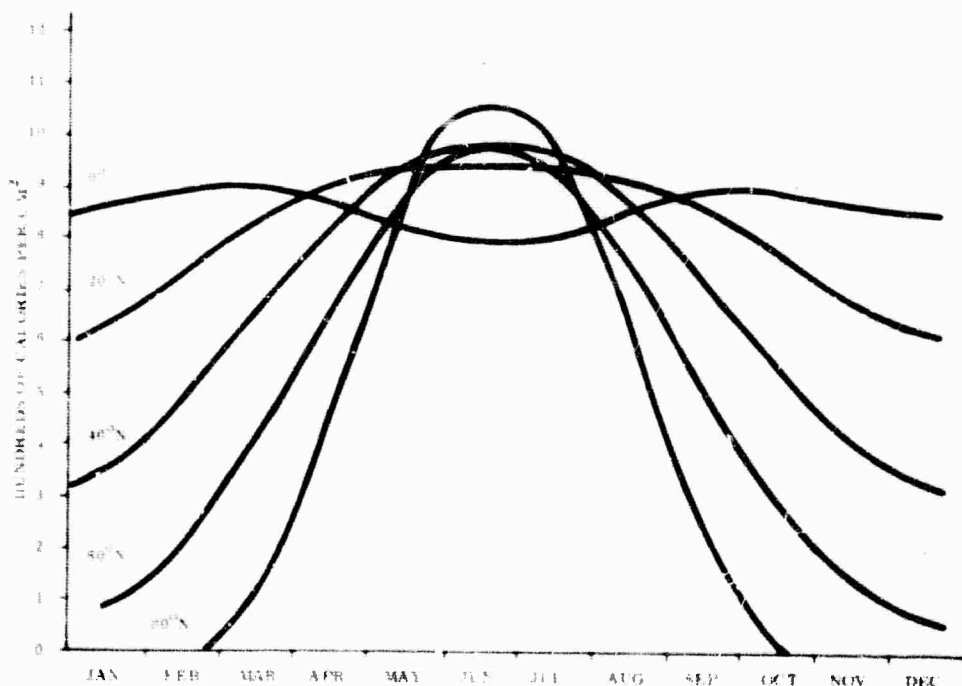


Figure 44. Daily Solar Radiation at Top of Atmosphere (U)

SECRET
THIS PAGE IS UNCLASSIFIED

Section of Figure 44 shows the constancy of equatorial irradiance, the great range of radiation levels occurring at winter solstice, and the effect continuous radiation at Arctic latitudes in summer.

The intensity of solar radiation at the earth is proportional to the sine of the solar altitude angle and is plotted for the morning hours at different latitudes and times of year in Figures 45, 46 and 47. These plots show the interval and magnitude of solar radiation onset from sunrise to noon. The approximate symmetry of the solar ascent and descent about noon permit these plots to be used to describe the solar radiation decline toward sunset as well. The rates of radiation onset after sunrise are seen to be faster at low latitudes, and equinoctial rates are faster than solstitial. Particularly long onset periods occur in northern latitudes at summer solstice. The noon maxima vary from 1 to 2% of that occurring with sun zenith at latitudes just below the Arctic Circle at winter solstice to the 80 to 100% range at temperate and tropic latitudes at summer solstice.

It is seen that solar radiation rate at the polar region at summer solstice is less than that for lower latitudes. However, this region is of interest for limb radiance measurement because of its continuous light and dark periods. In addition, the so-called auroral zone, a ring of substantial width centered about the geomagnetic pole (75°N, 101°S), is of observational interest. In the northern hemisphere this zone lies roughly between geomagnetic latitudes 60°N to 70°N with most of the land area underneath lying in northern Canada. The potential occurrence of noctilucent clouds in this region further emphasizes the interest in arctic measurements.

In summary, lacking specific information as to the rate of atmospheric reactions to incident sunlight, it seems reasonable to prescribe measurement intervals which sample the atmosphere periodically according to the amount of radiation prevailing. Conditions of interest would be as follows:

- Newly irradiated atmosphere
- Peak irradiance
- Newly darkened atmosphere
- Nocturnal atmosphere

Solar Disturbances -- Solar disturbances give rise to transients in the energy distribution of the atmosphere. The increase in high-energy photon flux from disturbances can result in immediate changes in the ionosphere throughout the sunlit hemisphere. Increased corpuscular radiation flux produces changes in a period of days after the disturbance which are evident equally in the sunlit and dark hemispheres.

In addition to sudden ionospheric disturbances caused by rectilinear radiation emitted during flares, there are subsequent ionospheric and magnetic

UNCLASSIFIED

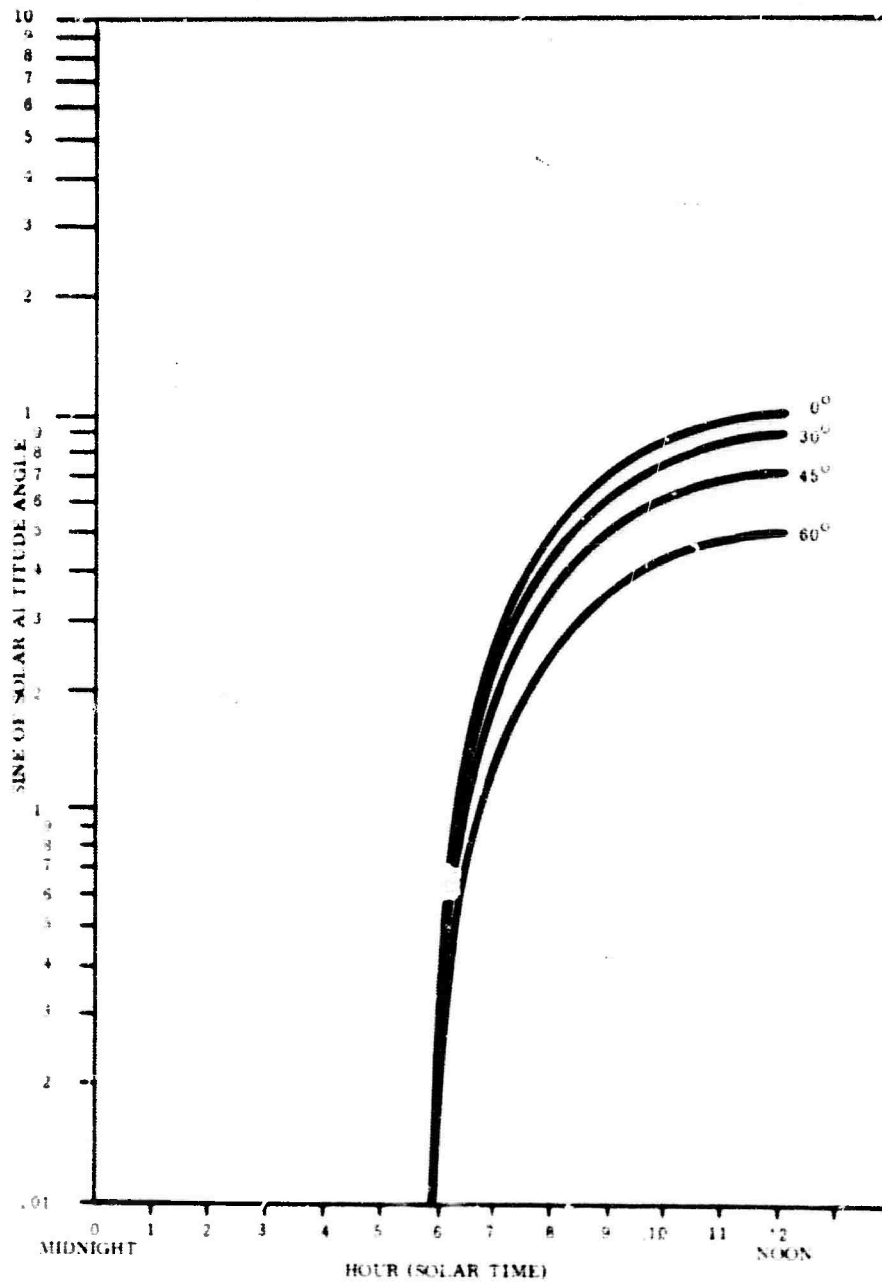


Figure 45. Sine of Solar Altitude, Equinoctial

UNCLASSIFIED

UNCLASSIFIED

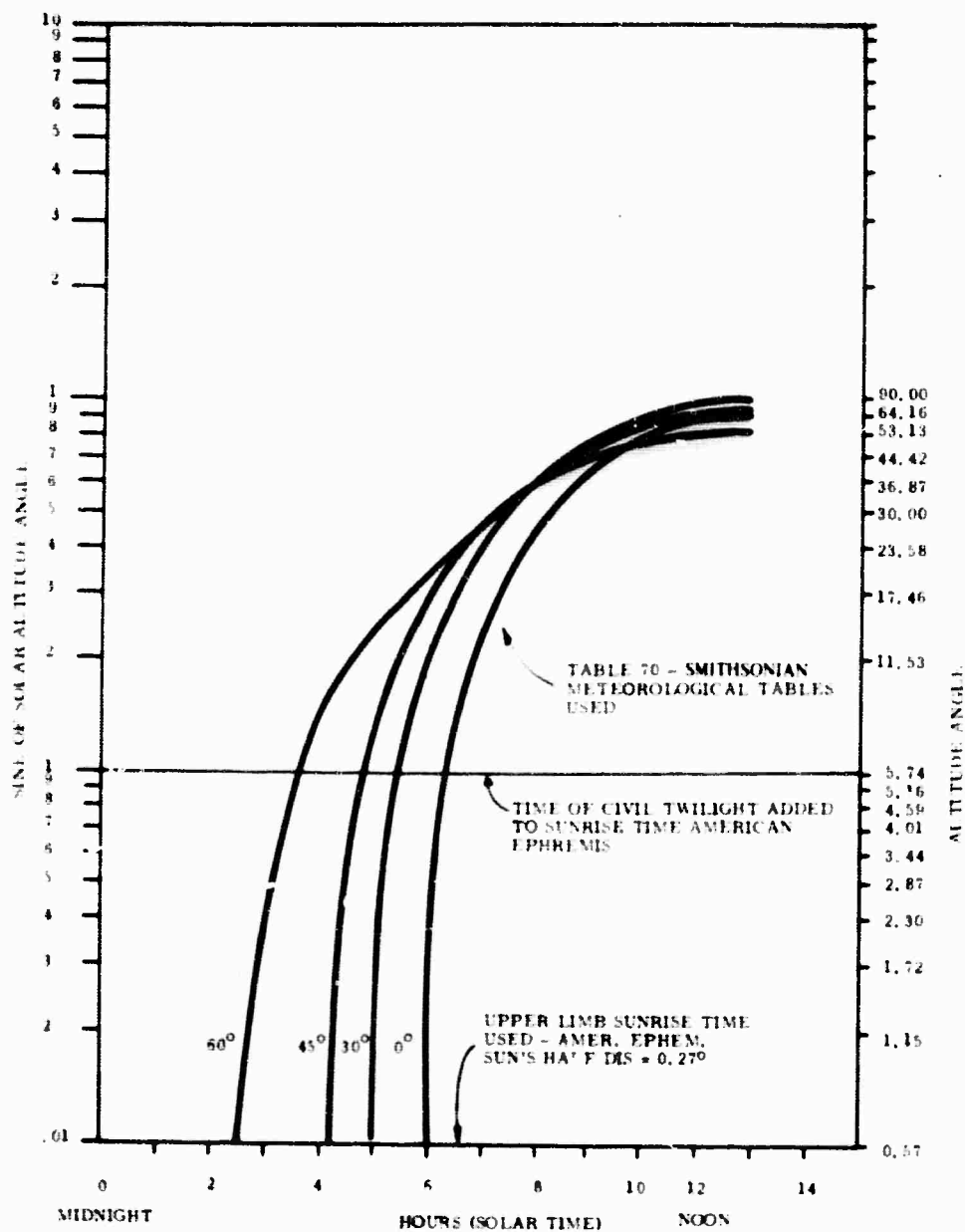


Figure 46. Sine of Solar Altitude, Summer Solstice

UNCLASSIFIED

UNCLASSIFIED

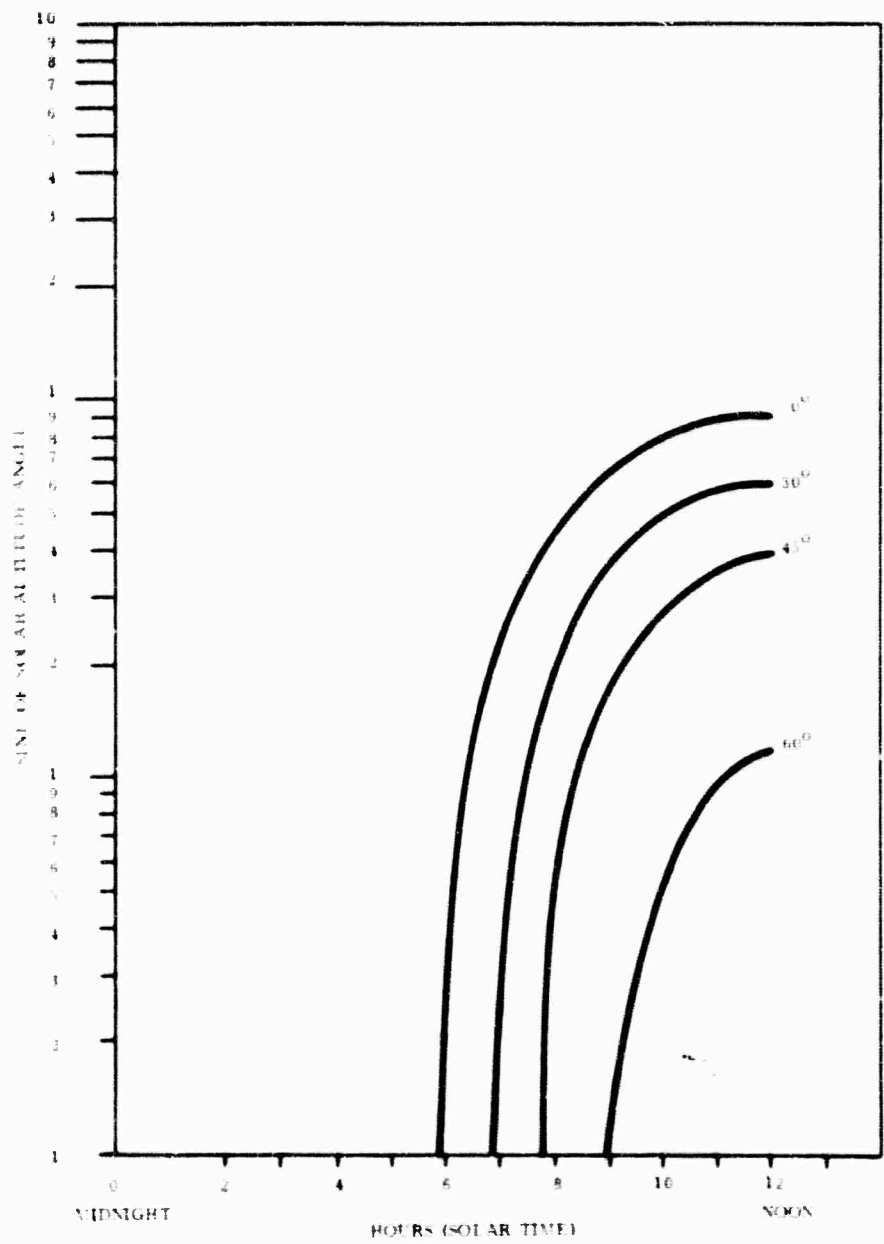


Figure 47. Sine of Solar Altitude, Winter Solstice

UNCLASSIFIED

UNCLASSIFIED

disturbances produced by corpuscular radiation. This form of radiation can have sporadic or recurrent terrestrial effects depending on whether the emission is short-lived or long-lived with respect to the sun rotation period. The evidence connecting solar events with storms is statistical and circumstantial; apparently though nearly all major (2+ or greater) flares occur near sizable sunspots, and about half of the major flares are followed within three days by a magnetic storm. (Storms are denoted by a high daily magnetic index - a parameter founded on field variations over three-hour intervals throughout the day). Solar sources of recurrent storms have not been fully identified and there are indications that weaker magnetic fields, not associated with sunspots, may be the cause.

Thus, during quiet sun years, storm activity is appreciable; the maximum storm activity appears to occur two years after the year of maximum sunspot number (about the end of 1970 in the present cycle).

Ionospheric storms are nearly always associated with magnetic storms, the disturbance can last several hours or even days, and the effects are observable on the light and dark sides of the earth equally. All regions of the ionosphere are involved, with changes occurring in temperature, atmospheric, ion, and electron densities, ionospheric currents, etc. In general, the storm phenomena are dependent on the earth's magnetic field, and at high latitudes aurora may occur along with alterations of electron number densities in the ionosphere and the derivation of "bays" on standard magnetogram records. At the geomagnetic equator a decrease occurs in the horizontal magnetic field component with relatively little ionospheric disturbance either at the equator or polar regions.

It is known that atmospheric disturbances resulting from solar activity may occur virtually simultaneously on the occurrence of an optically observable event, or may occur with a time lag of days after such an event. Despite the years of study about the effects of solar activity on high-frequency radio communications, there is at present no way to predict the day-to-day variations of the atmosphere. Such predictions are only for average conditions expected within a given month.

The random nature of flare occurrence, the relative infrequency, of larger flares capable of disturbing the atmosphere, and the fact that they can be predicted only on a statistical basis makes correlation with a probe measurement difficult. Predictions of atmospheric disturbances thought to be attributed to the so-called "M" regions, weak magnetic field locations not linked to the high-field regions adjacent to the sunspots, would be of tenuous nature as well although there may be 27-day periodicity associated with sun rotation. Routine observations and reporting of solar-associated events include: daily sun mapping, ionosonde and magnetogram monitoring WWV broadcasts of radio propagation conditions and geolerts, daily forecasts by the World Warning Agency, and ESSA's monthly Ionospheric Predictions.

UNCLASSIFIED

Collecting data coincidentally with solar disturbances has precedent* but is difficult because of the random nature of the disturbances and short flight time of a rocket. It does not appear desirable to assign a rocket specifically for limb measurement during sudden disturbances, and probably not for gradual solar events. Generally, day and night measurements will encompass a range of atmospheric excitation states, as indicated by ionospheric ion/electron concentrations, comparable to those accompanying auroras and magnetic variations resulting from solar disturbances. The limb measurement program should include means for measuring ionization levels over the region of observations. This can be done by onboard electron counters and remote ground ionosonde measurements. In this way, LWIR measurements can be correlated with electron densities and atmospheric ionization levels at various locations and altitudes.

Solar flares are sudden, short-lived brightenings of the sun surfaces in the region of a sunspot producing increased ultraviolet and x-radiations and resulting in simultaneous ionization enhancement in the sunlit hemisphere of the earth's atmosphere. This enhancement, or sudden ionospheric disturbance (SID), produces radio transmission effects and augmentation of the earth's magnetic field. Most SID phenomena lag 5 or 10 minutes behind the flare maximum, although magnetic effects are seen more quickly and are usually of shorter duration than either the SID or flare. Return to normal may take from 15 minutes to 2 hours.

Sun maps are published daily, and about 90% of the solar flares are being observed. Flares are classified as to size and only those of large size have accompanying SID's. Frequency and duration of flares are shown in Table 13.

Table 13. Solar Flare Frequency and Duration

Class	Duration (minutes)		Frequency of Occurrence	Possible Electron Enhancement at 60-km Height
	Average	Range		
1	20	4-43	0.044 R	2.5
2	30	10-90	0.015 R	4.5
3	60	20-155	0.002 R	7.0
3+	180	50-430		9.4
			R = sunspot number	

The 1970-71 time period is just past the time of maximum sunspot number. The current Ionospheric Predictions of ESSA predict an R of 99 at the beginning of 1970 and an R of 50 at the end of 1971. Thus, Class 2 flares may occur at a rate of 0.75 to 1.5 a day in this biennium; Class 3 at a rate of 0.1 to 0.2 a

NRL used Nike-Deacon and Nike-Asp rockets to measure x-ray flux produced by solar flares prior to their solar radiation monitoring satellite program.

UNCLASSIFIED

day. Since SID's occur most frequently with Class 3 and 3+ flares, it might be necessary to hold a rocket at launch readiness for several days for its flight to coincide with such a flare. Launching would need to be accomplished within minutes after observing the flare optically and with the benefit only of a statistical predictive technique.

3.4.3 Rocket Probe Launch Sites and Coverage

It would be desirable to make use of existing launch sites and prior launch experience as much as possible in the earth limb radiance measurement. In this connection, Table 14 lists potential launch sites and locations of the U.S. and foreign countries. Sites in the U.S. which are national or service ranges, or which have considerable rocket launching experience, are designated in the table as "established." Such sites would be most likely to have existing support services necessary for the radiance measurement program. Of the foreign sites, Fort Churchill would be a desirable site because of its considerable rocket launch history and its northerly location.

Since solar radiation is a dominant factor in establishing atmospheric states, earth surface temperatures, and surface cover types, it would be expected that a rationale for determining the time and place of limb radiance measurements would be considerably dependent on solar radiation characteristics. Thus, the north-south viewing extent from one, or more, launch latitudes should be able to encompass the range of solar radiation levels occurring throughout the hemisphere. The onset and decline of solar radiation can be observed by one, or several temporally-spaced, probes viewing sufficient longitude to cover the entire sunrise-noon and noon-sunset intervals. Moreover, the launch sites can be selected to give viewing coverage of a range of surface types whose temperatures and reflectance dictate the amount of earth emission.

The latitude coverages of the five U.S. sites, all of which are within 10 degrees of latitude of one another, are not greatly different. Of the five, Wallops is the most northerly and affords the best opportunity for Arctic viewing. Cape Kennedy, followed by Eglin, affords the best opportunity for tropic viewing; although at altitudes above 300 km, all five view into the region where zenith solar radiation occurs at some time during the year.

If only U.S. sites are to be considered, the small difference in latitude coverage among them suggests that only one site need be used to cover the solar radiation field. If Fort Churchill is to be considered as a launch site as well, a southerly site, such as Cape Kennedy or Eglin, can be used in conjunction to provide full hemisphere coverage. For example, the geographical coverage overlap of the Eglin site with Fort Churchill is shown in Figure 48.

UNCLASSIFIED

Table 14. Potential Rocket Launch Sites

United States Sites		Foreign Sites	
<u>Established</u>		Algeria: Colomb Bechar	31°N 2°W
Wallops Island	38°N 75°W	Argentina: Chamical	30°S 66°W
Vandenberg/Pt. Mugu	34°N 120°W	Mar Del Plata	38°S 58°W
White Sands	32°N 106°W	Ascension Island	8°S 14°W
Eglin	30°N 86°W	Australia: Woomera	31°S 137°E
Cape Kennedy	28°N 80°W	Brazil: Cassino	32°S 52°W
Kauai	22°N 159°W	Natal	6°S 35°W
Johnston Island	17°N 170°W	Canada: Ft. Churchill	59°N 94°W
Kwajalein	9°N 167°E	Resolute Bay	75°N 95°W
<u>Not Established</u>		Greece: Koroni	37°N 22°E
<u>Alaska</u>		Greenland: Thule	76°N 69°W
Pt. Barrow	71°N 156°W	India: Thumba	
Ft. Wainwright	71°N 160°W	Japan: Akita	40°N 140°E
Ft. Greely	64°N 145°W	New Zealand:	
<u>Puerto Rico</u>		Cape Karikari	35°S 173°E
Arecibo	18°N 67°W	Norway, Andog Island	69°N 16°E
		Pakistan, Sonmiana	25°N 67°E
		Surinam	~6°N 55°W
		Sweden: Kiruna	68°N 20°E

UNCLASSIFIED

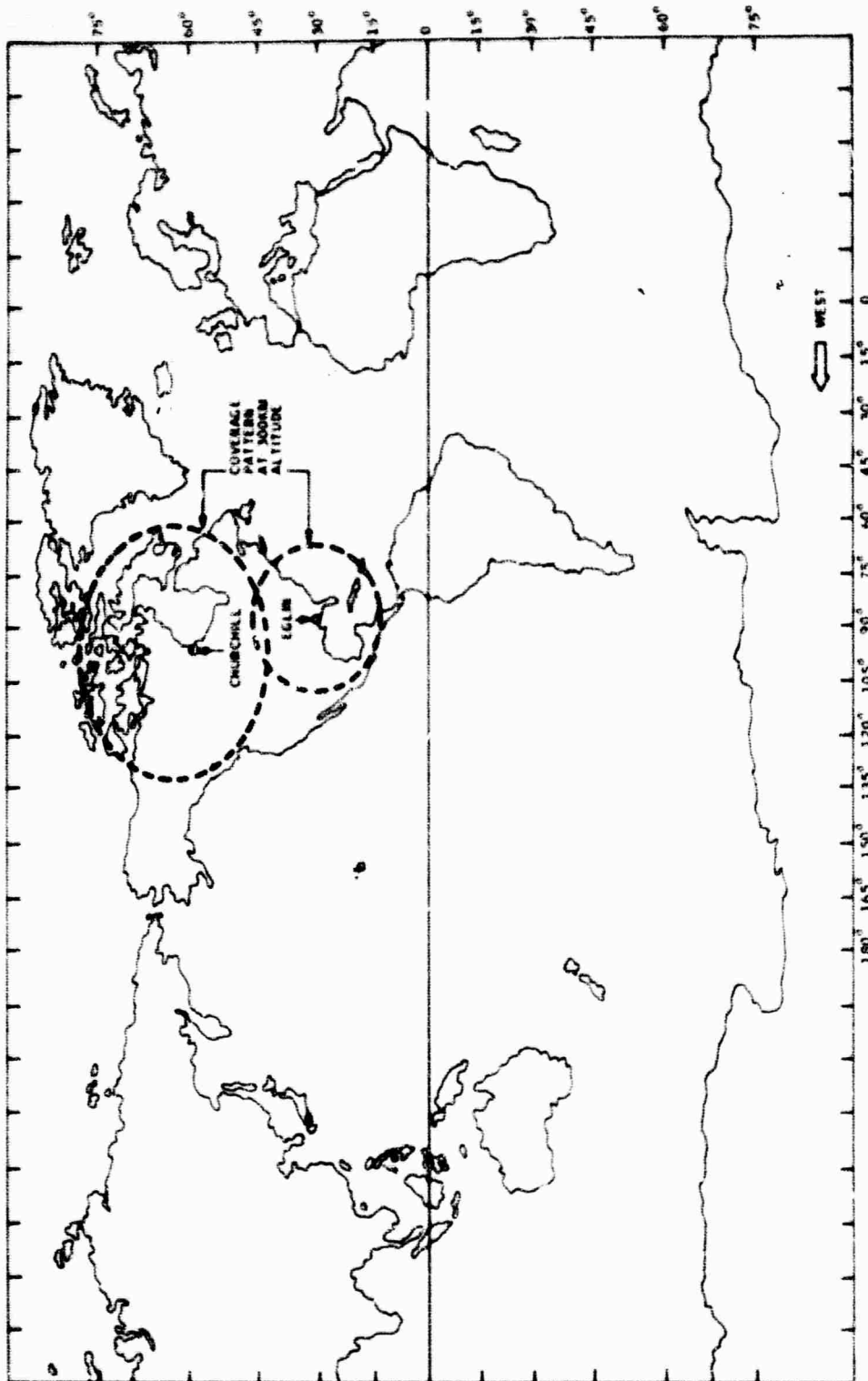


Figure 48. Geographical Coverage of Probe Vehicle

UNCLASSIFIED

UNCLASSIFIED

3.4.4 Flight Plans

In this subsection, a flight scheme is suggested which includes a range of solar radiation conditions occurring throughout the northern hemisphere at various seasons of the year, a mix of earth-surface cover types, and the use of existing launch sites.

The flight plan involves a series of launches at times of winter and summer solstice. At winter solstice there is a wide range of solar radiation intensities throughout the hemisphere from which to sample atmospheric radiance. In order to sample solar zenith radiance and the effects of earth reflectance emission during the extremes of hemispheric solar irradiation, launches at summer solstice are suggested as well. This is of particular importance from a systems standpoint where extremes are desired to obtain data bounds. The apogee altitudes suggested are commensurate with the performance of existing rocket vehicles with payloads of 500-pound class.

A tentative flight schedule is given below:

Launch sites: Churchill (or alternate Arctic site) and Eglin

Apogee altitude: 350 kilometers

Flights: Winter solstice:

Churchill 3

Eglin 3

Summer solstice:

Churchill 4

Total 10

As noted previously, the observational conditions of interest in the diurnal solar passage are: dynamic response of atmosphere to solar radiation onset and decline; peak level of atmospheric radiance; levels of radiance in newly darkened and nocturnal atmospheres. Table 15 gives the times and places of launches for the suggested flight scheme together with the solar radiation fraction prevailing at the view perimeter. Each flight series for a given place and date begins with a flight in which the westerly view is darkened below 150-km tangent height and ends with a flight in which this condition exists in the east. (An exception is made for the Fort Churchill summer solstice series since the sun does not fall this far below the horizon in this case; here a tangent height of 35 km has been used in calculating solar altitudes and radiation fractions.) Thus, the westerly view of the initial flight of the day is of an atmosphere which has been darkened all night, and the last flight of the day has an easterly view of newly-darkened atmosphere. Intervening flights in the series

UNCLASSIFIED

Table 13. Launch Times and Places with Solar Radiation Fraction

Launch Site	Launch Date	Priority	Flight Apogee Solar Time	Radiation Fraction			
				East	South	West	North
Churchill	12/22	1	8:52	0.104	0.156	0 ^a	0 ^c
		5	12:00	0.070	0.375	0.070	0 ^c
		3	15:04	0 ^b	0.174	0.087	0 ^c
	6/22	2	3:25	0.309	0 ^a	0 ^a	0.242 ^d
		5	9:09	0.089	0.077	0.454	0.559
		3	12:00	0.731	0.951	0.743	0.602
		3	20:33	0 ^b	0 ^b	0.292	0.242 ^d
Eglin	12/22	4	7:01	0.242	0.139	0 ^a	0.242
		3	12:00	0.559	0.766	0.574	0.391
		4	16:54	0 ^b	0.139	0.225	0 ^b

^aNocturnal atmosphere

^bNewly darkened atmosphere

^cContinuous night

^dContinuous day

UNCLASSIFIED

are made throughout the day with higher solar altitudes up to the maximum which can occur within the view.

The radiation fraction cited in Table 15 is the sine of the solar altitude, or solar radiation intensity, at the appropriate latitude and longitude, and would, of course, have the value of one for the zenith sun position. The northerly views from Fort Churchill are within the Arctic Circle where continuous solar radiation, or lack thereof, exists.

The more northerly site of Fort Churchill has appreciably longer twilight duration than the Eglin site with twilight all night near the summer solstice. The maximum coverage provided by vehicles launched from these sites can be seen in Figure 48. Launches from Fort Churchill will sample the Arctic and North Temperate regions whereas launches from Eglin will overlap somewhat the North Temperate region and also provide tropical coverage.

The flight program described in Table 15 is sufficient to meet the following objectives:

- (1) Sample up to 85% to 95% of the maximum possible solar illumination level for all five regions and seasons.
- (2) Provide a reasonable probability of encountering high-altitude layer structure as observed during USSR measurements.
- (3) Sample all diurnal conditions including nocturnal, sunset, continuous day and night, and high noon in the Arctic region.
- (4) Sample nocturnal, sunset, and high noon in temperate and tropical regions.

Some redundant coverage of intermediate solar intensities exists within the temperate region between the winter Churchill flights when viewing south, and the winter Eglin flights when viewing north.

In terms of objective (2), a statistical estimate can be made of the probability of observing high radiance layers based on the USSR measurement experience. It is reported that on four out of a total of 30 probe flights, equivalent (limb view) radiance levels in excess of 3×10^{-5} watt/cm²-ster were observed in the altitude range from 100 to 300 km while viewing horizontally.

The probability of observing high-altitude layers on any one future flight may be estimated by using the binomial distribution, given as follows:

$$P_s = \sum_{x=0}^n \frac{n!}{x!(n-x)!} p^x q^{n-x}$$

UNCLASSIFIED

where

P_s = probability of success

n = total number of flights

x = 1.0

p = $4/30 = 0.133$

2 = $1 - p = 0.867$

On this basis, the probability of success increases with number of flights as shown in Figure 49. With a total of 10 flights, the probability of success is about 0.75.

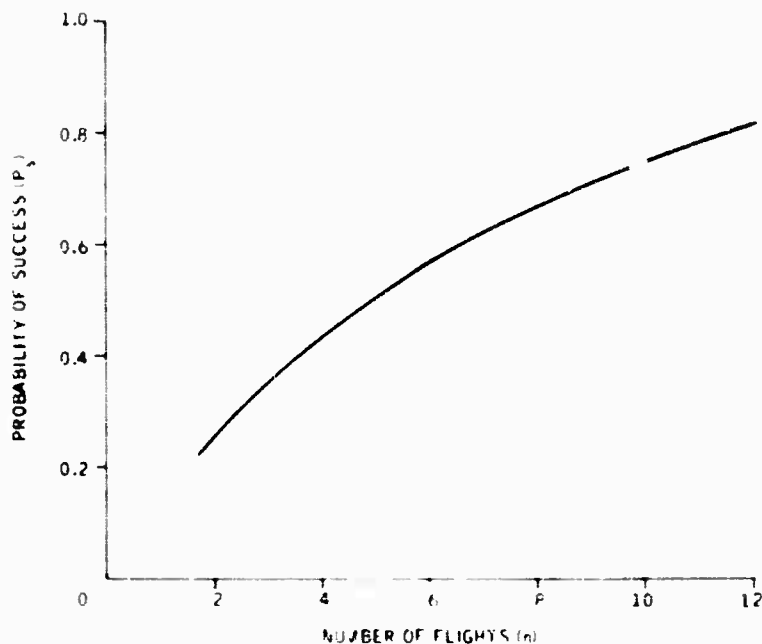


Figure 49. Probability of Observing High-Altitude Layers on Any One Flight'

The priority assigned to each flight (Table 15) is based on the number of objectives or different conditions encountered on that flight and can be used to scale down the flight program. Two flights [priority (5)] launched from Churchill may be eliminated without loss of generality but with about a 10% loss in objective (2), i. e., probability of observing high-altitude layered structure. In addition, two flights from Eglin [priority (4)] could be eliminated with the loss of the minimum solar illumination conditions in the tropical region only, i. e., nocturnal, sunset, and up to relative illumination levels of about 0.25. Without these Eglin flights, some intermediate illumination levels in the temperate winter are also lost, as well as an additional 15% loss in objective (2).

UNCLASSIFIED

The remaining six flights [priorities (1), (3)] are considered to represent the minimum flight program necessary to sample the wide range of atmospheric and solar illumination conditions expected to influence LWIR limb radiance. For purposes of reducing overall cost, further reductions in the number of flights could be made based on a limited set of objectives.

Two alternative three-flight programs are proposed. One samples the diurnal cycle with three flights closely spaced in time. The other does not cover the diurnal cycle but gives wider coverage of solar altitudes and radiation intensities, including continuously lighted and darkened atmosphere in the Arctic, and requires fewer payloads.

The first program, designed to sample the diurnal cycle, would not include seasonal or wide geographical coverage and would have a reduced opportunity to measure during magnetic storms. To sample the diurnal cycle, the three flights would be timed at sunrise, noon, and sunset. The sunrise flight would be timed to view the nocturnal atmosphere in a direction opposite the solar azimuth. In this direction the atmosphere will have been quiescent throughout the night. In the direction of the solar azimuth, the sensor will view newly irradiated atmosphere. The noon flight would sample during the maximum solar intensity. The sunset flight will sample newly darkened atmosphere (opposite solar azimuth) and atmosphere irradiated throughout the day (direction of solar azimuth). Conducting these three flights within a time period of less than one week ensures high data correlation but also prevents the reuse of a given payload.

The second alternative program provides time to refurbish the payload after recovery and therefore involves a smaller cost. This program would sample virtually the entire range of solar intensities throughout the seasonal cycle from a given Arctic station, Fort Churchill, for example. The flights would be launched near local noon on or about the winter and summer solstices, and at an equinox. As such, the range of relative solar intensity varies from a low of 0.07 to a high of 0.92 and includes a sample of continuous sunlit and darkened atmospheres north of the Arctic Circle. The latter flight would be launched near the autumnal equinox during which there exists the maximum monthly frequency of aurora.

UNCLASSIFIED

UNCLASSIFIED

SECTION 4 INSTRUMENT DESIGN

4.1 BACKGROUND

The design of an infrared spectroradiometer for a measurement of the earth limb requires the solution of several difficult problems not usually encountered in more conventional infrared radiometers. The spectral radiances to be measured are extremely low, spatial resolution is to be high, and the wavelength bands of interest extend over a broad range. This means that a cooled optics instrument of very high sensitivity is mandatory. The spectral energy measurements must be made in spatial locations of the atmosphere which are very close to the earth. The earth radiates very strongly in the spectral bands of interest, since it is roughly a 300°K blackbody and therefore a strongly interfering source of unwanted stray radiation. Stray radiation can reach the infrared detector by diffraction and by diffuse scattering. The problem of performing a successful IR earth limb measurement is somewhat similar to the problem of measuring or observing the corona of the sun without an eclipse. Therefore, the technique and theory of coronagraph design is utilized in the proposed limb measurement spectroradiometer.

Attenuation of stray radiation is achieved by use of low-scattering optical components and by application of the boundary wave diffraction theory for a series of baffles and apodized stops to attenuate diffraction noise. Internal thermal radiation is suppressed by cooling all parts of the instrument, including the optics, to a temperature of 20°K or less. The great majority of existing high-sensitivity cryogenic infrared radiometers use a folded reflecting telescope design which may be roughly categorized as Cassegrain-style systems. For limb measurement applications the diffraction from the secondary mirror support struts becomes a serious problem. If the use of struts is avoided by supporting the secondary mirror on a refracting window or corrector as is done in certain catadioptric designs (such as the Questar telescope) then one is faced with the problem of providing a large-diameter refracting element which transmits over a wide spectral band. In addition, it is necessary to suppress unwanted internal reflections within the refractive element through the use of antireflection coatings. Unfortunately, these coatings must operate over the same wide spectral band of 4.5 to 25 microns. Such problems were avoided entirely by choosing a telescope design based on the use of off-axis sections of parabolic mirrors. It was decided to use multiple focal planes since at a focal plane the desired signal power is concentrated, and therefore any baffle or stop will more efficiently separate the unwanted stray radiation from the desired signal radiation. Since previous Honeywell studies established that conical blackbody cavities were more efficient optical baffles than any other type, the optical design includes such baffles as light traps. In essence, the principle is to form an image of the interfering astronomical source of

SECRET
THIS PAGE IS UNCLASSIFIED

unwanted radiation (in this case, the earth) and then to cause the image power to fall within a cryogenically cooled blackbody-type light trap where the power is pumped away. The stray radiation attenuation will therefore be achieved in the most efficient manner. If diffraction and scattering did not exist, the total entering earth radiation would be removed by this process. Diffraction acts to cause a small portion of the image to "spill over" the trap and proceed through the optical system to the detector. By proper placement of internal stops and by the use of apodization techniques this diffraction power may be attenuated to acceptable levels, consistent with the instrument requirements.

Boundary-wave diffraction theory, a powerful and useful tool for coronagraph design is utilized to describe the interplay between incident radiation, apertures, and resulting diffraction.

The essence of the boundary-wave diffraction theory is that diffraction at an aperture may be completely described by splitting the wave at the aperture into an undiffracted geometric optics component and a boundary-wave component. The geometric-optic-wave component proceeds through the aperture by simple ray-trace optics while the boundary wave originates at the boundary or rim, of the aperture. The great utility of the method or theory is that the boundary-wave component also may be treated using only geometric optics concepts until the next diffracting aperture or edge is encountered, after which the process repeats. Each of the two original wave components can be re-divided at the new boundary into two new components. Using this extremely powerful visualization and computational tool, it is possible to trace the course of diffracted radiation through the optical system of an instrument.

As diffraction radiation becomes attenuated to manageable levels the diffusely and specularly scattered earth radiation could become the dominate optical noise in the system. (For convenience, in this document diffusely and specularly scattered earth radiation will be called "scattering". To distinguish it from the stray radiation scattered from diffraction, we will refer to the latter as "diffraction".) Scattering occurs whenever the relatively intense earth irradiates any surface of the instrument in such a manner that unwanted radiation enters the optical system. The most obvious and conventional solution to the problem of minimizing scattering is to shield the objective aperture of the telescope using an optical baffle assembly. It is possible to minimize the scattering from direct irradiance of the primary objective mirror by demanding an exceptionally high polish on the mirror to reduce the scattered component of the transmitted wave and by hiding the remainder of the optical system behind a small aperture (pinhole) in the first focal plane. By far the most effective means of minimizing scattering is to use a forebaffle which shields the objective aperture as completely as possible. In the design of the forebaffle, an attempt was made to make all light traps in the baffle as close to a conical blackbody cavity as practical in the allowed baffle volume.

SECRET

(S) The spectral separation means proposed is an out-of-plane dual-grating Littrow monochromator whose entrance aperture (slit) is placed at the second focal plane of the optical system. The Littrow system meets the design goals while preserving the high off-axis attenuation ratio of the telescope. No moving parts are required other than a radiation chopper. Spectral separation of the bands is achieved by the use of an array of 29 individual detectors. The height of each detector (corresponding to the vertical dimension in the earth's atmosphere) is a constant 0.5 m, while the width of each cell is a function of the width of each spectral band. Either doped germanium photoconductive detectors or photoconductive mercury cadmium telluride may be used in the instrument providing either choice leads to an array where each detector is in the 10^{14} or better D^* range. Recent measurements at Lockheed Missiles and Space Co. with a Honeywell mercury cadmium telluride photoconductive detector has indicated that a value $D^* = 5 \times 10^{14} \text{ cm}^2 \text{ sec}^{-1/2} \text{ watt}^{-1}$ was achieved with a standard (Hg,Cd)Te cell optimized for reconnaissance work at a 10-micron wavelength at 12 K.

(U) There is a novel treatment of the long-wave IR channel from 17 to 25 microns. Because of the wide bandwidth and long wavelength of this channel it is not practical to achieve its spectral separation in the grating monochromator. The grating monochromator therefore operates from 4.6 to 18 microns, and the long-wave channel is split out of the optical beam by reflection off an angled flat folding mirror mounted on the back of the blade of the radiation chopper. The radiation is thereby folded to the side every time the chopper closes off the main beam. A simple blocked multilayer interference filter is used to isolate the 17- to 25-micron band. There happens to be adequate signal power in this channel, so it is not even necessary that the following mirror intercept the entire converging beam. It is therefore possible to mount a mirror on one blade of a two-blade "scissors" type chopper to minimize the amplitude required for chopper motion. Tables 16 and 17 summarize the proposed instrument characteristics.

4.2 OFF-AXIS RADIATION EFFECTS ON S/N

(U) Using the methodology derived in sections 4.1 and 4.4, values for the power falling on the detector as a function of tangent height were calculated for four representative spectral regions (5.0 to 5.7 microns, 10.0 to 10.8 microns, 17.0 to 18 microns, and 18 to 25 microns). The radiation levels obtained were for the worst conditions in all cases; in fact, such items as the filtering effects (transmission losses) of the atmosphere as well as losses incurred in the instrument (optical transmission etc.) were not considered. Therefore, as a first approximation to account for these effects, the calculated values of diffraction were reduced by a factor of 10. Next, the effects on the diffraction level caused by adding apodization were investigated. The results showed a reduction factor of 100 may be achieved with proper design. Thus, the calculation of diffraction radiation falling on the detector was reduced by an additional factor of 100.

SECRET

(S) Table 17. Operational Summary of Instrument Characteristics (U)

Item	Characteristic
Instrument	Size: 17-in. diameter x 48-in. length Field of view: 0.5 mr (azimuth) x 1.5 mr (altitude) System f/no.: 1.3
Attenuation	Baffle: 10^{-11} (to 1 degree off-axis) Apodization: 10^{-3} (due to Lyot stop, apodized apertures)
Operating Temperature	Optical cavity: 20 K to 25 K
Detectors	Size: 0.6 x 3.2 mils Arrays: two sections, 0.168 m. long and 0.200 m. long D value: 6×10^{14} $\text{cm}^{-1/2} \text{ watt}^{-1}$
Cryogenic Schedules	Cool Down: 3 hrs Hold: 2 hrs Operate: 20 min
Calibration	Inflight LED

UNCLASSIFIED

The calculation approximating diffraction plus scattering radiation falling on the detector as a function of tangent height is shown in Figures 50 through 53. Also plotted on each curve is the limb radiation falling on the detector. Notice in Figure 50 that the diffraction plus scattering radiation is negligible compared to the signal. Figure 50, however, shows the unwanted radiation is equal to the signal at about 100 km. Fortunately, the S/N varies as the square root of the sum of the two curves. A more thorough analysis is required to this band to evaluate the actual effects of diffraction and scattering about 100 km. Figure 52 shows that the diffraction and scattering do not affect this band. Figure 53 shows the 16- to 25-micron band in which the effects of diffraction and scattering are the most serious and equals the signal radiation at 85 km. Several factors, however, may help this band. The atmosphere, for example, has a large attenuation in this interval which may help reduce the unwanted radiation when a more precise calculation is performed. Also, the band is split off by itself and does not go through the monochromator; thus, masking optimization can be performed, i. e., an evaluation to find if the signal level drops faster or slower than the diffraction and scattering levels as the field of view is varied.

In conclusion, a preliminary calculation of the effects of diffraction and scattering show that, in most cases, they are negligible, and, in the remaining cases, there is hope that a more thorough analysis and design can eliminate or minimize the effects.

4.3 DETECTOR SELECTION

The choice of detectors for this application involves several tradeoff factors (see Table 10). The primary consideration is the detectivity, which ultimately determines the instrument sensitivity. Other factors relating to the choice of detector are operating temperature, limiting optics f/number, spectral and frequency response, size limits, array technology, and state of development. The detectors considered for this application were Ge:Hg, Ge:Cl, Ge:Cu, and HgCdTe. Because all detectors in the spectral regions of interest are to operate within the same optical system and, therefore, at the same focal surface, it is desirable that they all achieve their best performance at or near the same temperature, to minimize thermal gradients in the focal plane. For this reason, and to reduce manufacturing cost and schedule, it is desirable that all detectors be of the same type, if possible.

A first-order tradeoff study was conducted to determine the most satisfactory detector for this application and the results are discussed in the following paragraphs.

The Ge:Hg detector was not suitable for this application because of its lack of response in the 3- to 25-micron region and was subsequently eliminated from further consideration.

UNCLASSIFIED

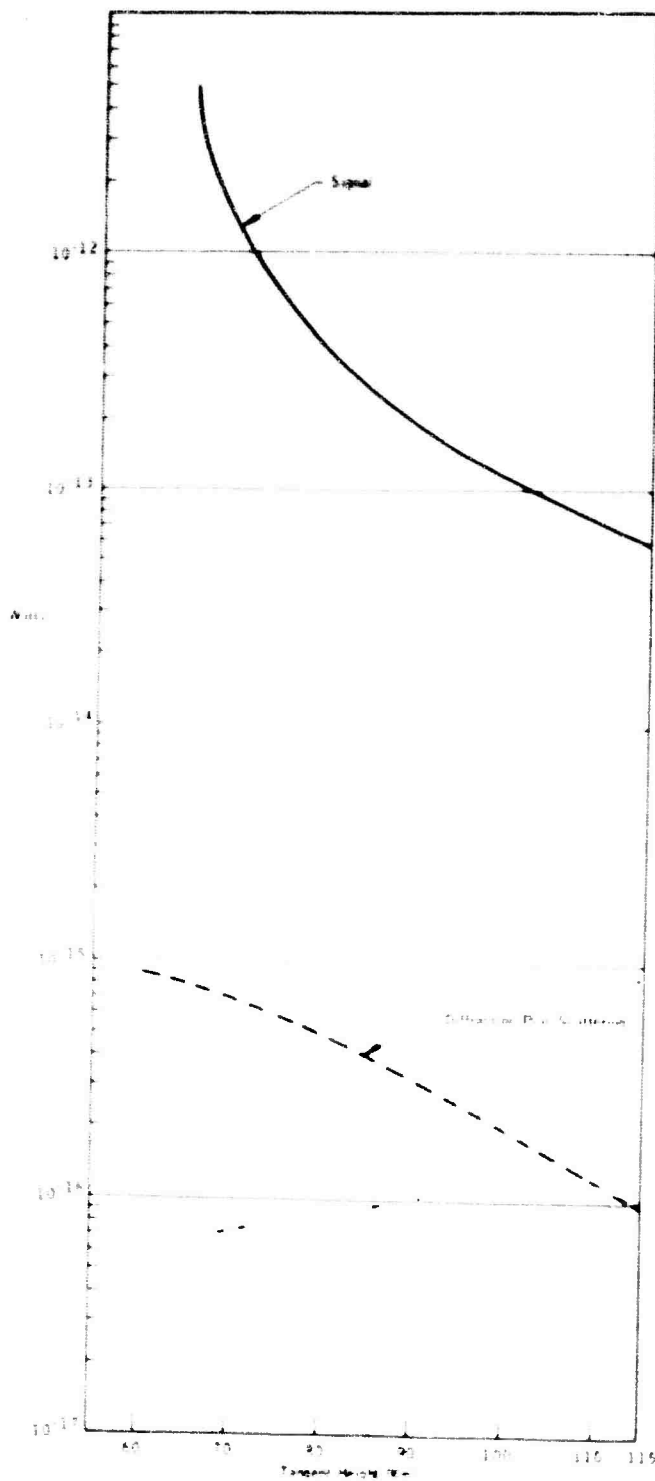


Figure 50. Power Falling onto Detector from Signal plus Diffraction and Scattering, 5.0- to 5.7-micron Band

UNCLASSIFIED

UNCLASSIFIED

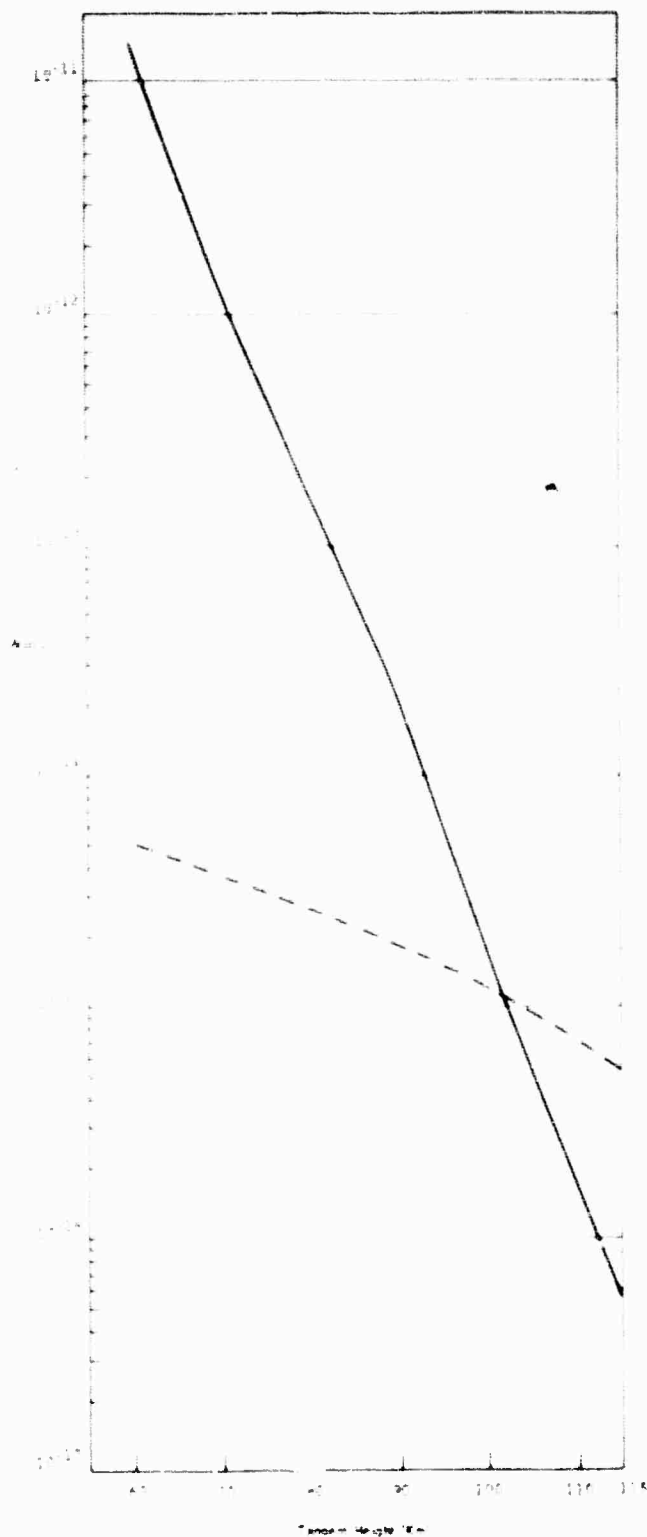


Figure 51. Power Falling onto Detector from Signal plus Diffraction and Scattering, 10.9- to 10.8-micron Band

UNCLASSIFIED

UNCLASSIFIED

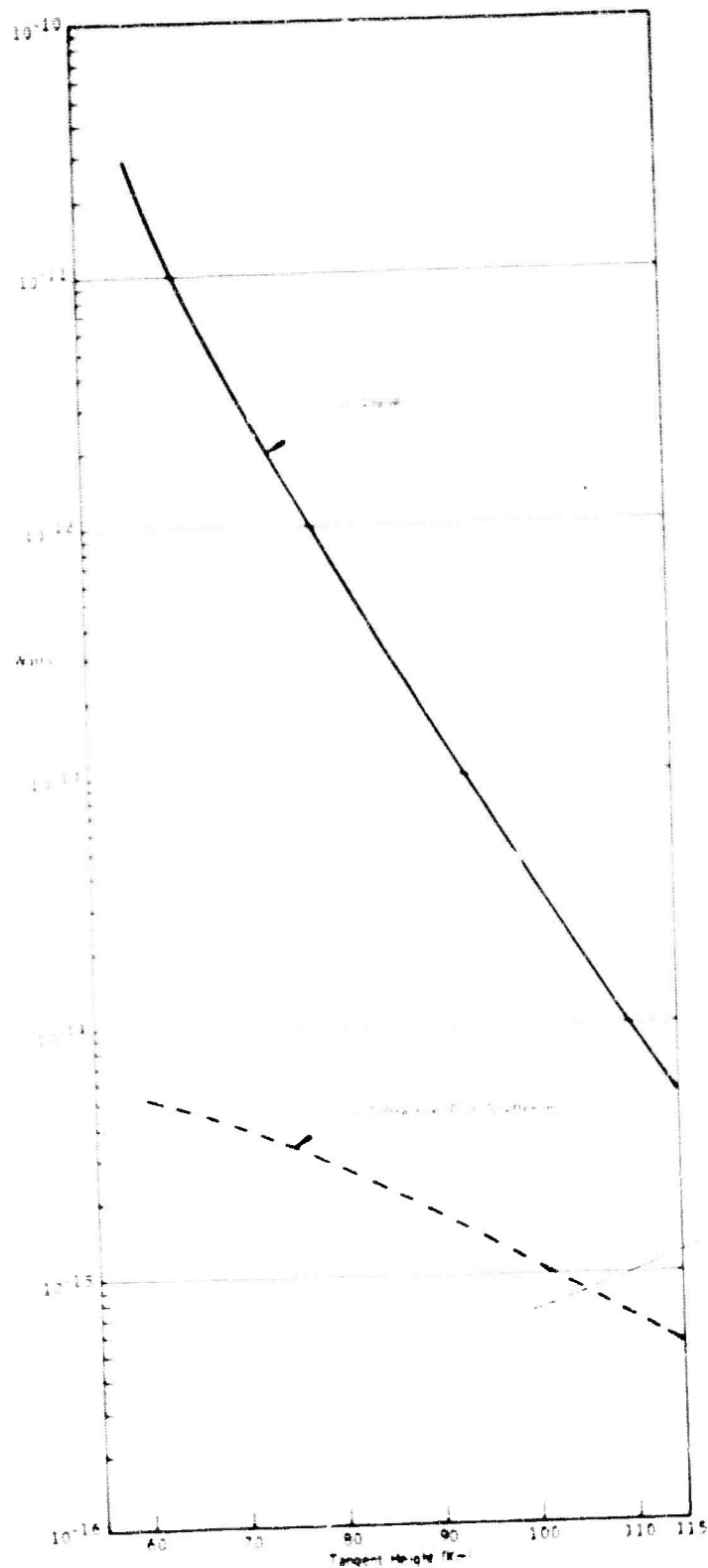


Figure 52. Power Falling onto Detector from Signal plus Diffraction and Scattering, 17.0- to 18.0-micron Band

UNCLASSIFIED

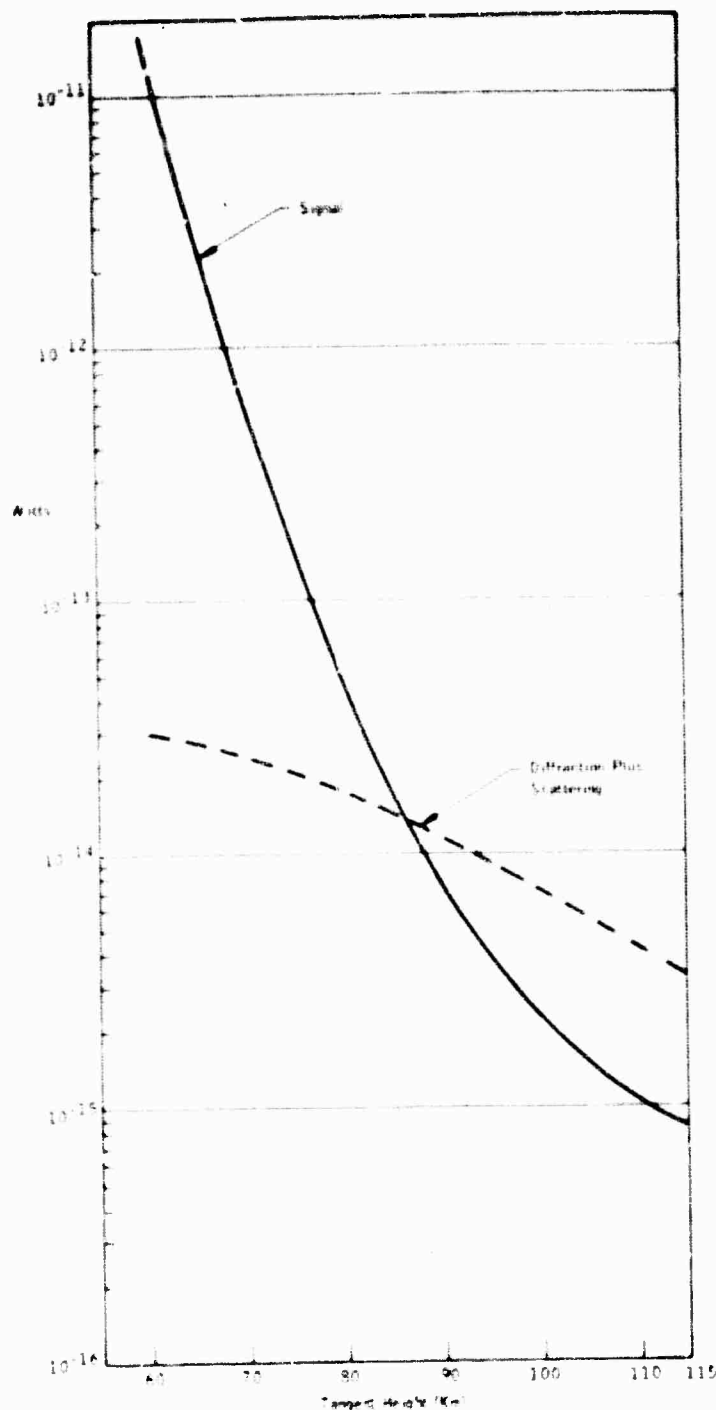


Figure 53. Power Falling onto Detector from Signal plus Diffraction and Scattering, 18.0- to 25.0-micron Band

SECRET

(S) The Ge:Cu was eliminated, even though it had demonstrated a D^* of greater than $5 \times 10^{14} \text{ cm sec}^{-1/2} \text{ watt}^{-1}$, because of more severe operating temperature requirements.

(S) The two remaining candidate detectors, Ge:Cu and (HgCd)Te, both have exhibited capabilities of D^* values of $5 \times 10^{14} \text{ cm sec}^{-1/2} \text{ watt}^{-1}$; however, high electronic crosstalk during operating and the necessity for cryogenic preamplifiers make the Ge:Cu detectors much less attractive than the HgCdTe detectors. The (HgCd)Te detectors exhibit low crosstalk (due to the inherently low impedance) and operate from standard uncooled pre-amplifiers.

(U) Therefore, a first-order tradeoff study dictates the use of (HgCd)Te detectors. The parameters entering into the tradeoff study are summarized and compared in Table 18.

4.3.1 Detector Mechanisms and Comparison of Detector Types

(U) An ideal quantum detector may be defined as a detector which has a quantum efficiency (η) of unity up to a certain cutoff wavelength (λ_c) and η equal to zero beyond λ_c . Such a device can detect all quanta incident on the active area and contains no internal noise. The detectivity of such detector is limited by the unavoidable fluctuations in the background radiation due to its quantized nature. These fluctuations set an upper limit to the detectivity, or D_{λ_c} , of a detector which depends on the background temperature. Photons obey Bose-Einstein statistics which determine their distribution with wavelength as well as their variance in a particular energy interval. For background temperatures less than 290°K and wavelengths less than 50 microns, Boltzmann statistics give a good approximation to the Bose-Einstein statistics, and the variance, $(\Delta J_B)^2$, is equal to the total number of quanta J_B detected by the detector with an area of 1 cm^2 . The root mean fluctuations per second are given by

$$\sqrt{(\Delta J_B)^2} = \sqrt{J_B}$$

The value of J_B is determined by the cutoff wavelength (λ_c) and background temperature.

$$J_B = \int_0^{\lambda_c} N_\lambda(T, \lambda) d\lambda$$

where N_λ is the Planck photon spectral density. The best detectivity of an ideal detector is achieved at the spectral responsivity peak λ_c . We assume a signal-to-noise ratio of unity for the minimum detectable signal.

SECRET

(S) Table 18. Comparison of Candidate Detectors (U)

Parameter	Ge:Hg	Ge:Cu	Ge:Cd	Hg Cd Te
4- to 25-micrometer response	No	Yes	Yes	Yes
Element size (typical)	---	1 mm	---	0.1 mm
Time constant (nsec)	--	10 to 100	---	10 to 100
D^* ($\text{cm Hz}^{1/2} \text{W}^{-1}$)	---	5 to 10×10^{14}	---	7×10^{13}
NEP (watts)	---	$1 \text{ to } 2 \times 10^{-16}$	---	1.4×10^{-16}
Impedance (ohms)	---	10^{13}	---	300 to 500
Responsivity (v/w)	---	10^8	---	10^8
Operating temperature (°K)	14	10	14	15
Type of preamp	---	Cryogenic MOSFET	---	Uncooled standard
Array technology	---	Thick crystals (0.3 cm) can be arrayed	---	Extremely thin crystal 0.5 mu standard photo-etch techniques can be used, arrays 0.001 in. between elements
Radiation susceptibility	---	Susceptible due to thick crystal atomic weight MOSFET preamp	---	Should be less susceptible due to thin crystal, atomic weight, standard preamps
Reason for rejection	Spectral response	Operating temperature	High crosstalk, cryogenic preamp	Should be considered for application

SECRET

SECRET
THIS PAGE IS UNCLASSIFIED

Then $hc/\lambda_c \sqrt{J_B t A} =$ monochromatic signal power (P_s) where t is the counting interval in seconds, A the detector area. In terms of electrical bandwidth,

$$P_s = \frac{hc}{\lambda_c} \sqrt{J_B 2\Delta f A}$$

Thus the background-limited infrared performance (BLIP) spectral detectivity is defined as

$$D_{BLIP} \frac{\sqrt{A} \sqrt{\Delta f}}{P_s} = \frac{\lambda_c}{\sqrt{2hc} \sqrt{J_B}} \text{ (cm Hz}^{1/2}/\text{watt)}$$

For photoconductors, internal noise (generation-recombination noise) is double the background noise, and the quantum efficiency is less than unity. Thus

$$D_{\lambda} (PC-BLIP) = \frac{\lambda_c (-1)^{1/2}}{2hc \sqrt{J_B}}$$

Any detector can approach BLIP D_{λ} if its dominant noise is due to the background and its quantum efficiency is close to unity. As the background temperature is reduced, noise due to the background is reduced, and this noise mechanism loses its dominance.

The background-induced noise voltage across the detector can be defined as

$$\sqrt{v_B^2} = q(-1)^{1/2} \sqrt{J_B / w \Delta f} \left[\frac{-\mu E_x}{I} \right] \approx \frac{J}{wt}$$

If the detector has unlimited photoconductive gain, G_{PC} , where

$$G_{PC} = \frac{-\mu E_x}{I}$$

then v_B is always dominant, the detector is close to BLIP. Saturation of the gain, due for example to "sweep-out" usually limits the cold background performance of non-ideal detectors.

The ultimate limit of detectivity is the thermal equilibrium detectivity, D_{λ}^* (pronounced D-dagger or lambda). This value of detectivity is based on a state of thermal equilibrium existing between the detector and its environment,

UNCLASSIFIED

i. e., the detector temperature is equal to the temperature of the spherical background. The signal is a small perturbation on the lattice temperature. We write D_{λ} as follows:

$$\lim_{\theta \rightarrow 0} D_{\lambda_p}(\lambda_p, f, 1, \text{FOV}) = D_{\lambda_p}^*(\lambda_p, f, 1, 180^\circ)$$

$$\theta = 0 \text{ RAD}$$

$$v_{g-r} \gg v_j$$

$$v_{g-r} \approx v_{1/2}$$

$$= \frac{\tau_{\lambda_p}}{2ne (dG_1)^{1/2}}$$

$$T_{\text{DET}} = T_{\text{BKG}}$$

This condition follows from the near intrinsic noise behavior to be expected in n-type intrinsic photoconductors. However, because we have neglected the effects of sweep-out, the equation also assumes the existence of an unlimited photoconductive gain. Furthermore, the equation also assumes that the dominant mechanism for free-carrier recombination is radiative. When this is true, the photoconductive lifetime may be written

$$\tau_{\text{PC}} = \frac{n_i^2}{G_r (n_0 + p_0 + \Delta n)}$$

where G_r , the rate of spontaneous recombination radiation at thermal equilibrium, is given by

$$G_r = \frac{8\pi}{h^3} \left(\frac{r_i}{C} \right)^2 \int_0^\infty \frac{\epsilon(\epsilon) (h\epsilon)^2 d(h\epsilon)}{(\exp(h\epsilon/kT) - 1)}$$

$$\approx 2.52 \times 10^{11} r_i^2 T_{\text{DET}}^3 \int_{\epsilon_0}^\infty \epsilon^2 n(\epsilon) \exp(-\epsilon) d\epsilon$$

$$\approx 2.52 \times 10^{11} r_i^2 T_{\text{DET}}^3 \left[\frac{1}{2} (\epsilon_0^2 + 2(\epsilon_0 + 1)) \exp(-\epsilon_0) \right]$$

if $\epsilon_0 \gg 1$

where $\epsilon_0 = E_{\text{gap}}/kT_{\text{DET}}$

UNCLASSIFIED

The value of G_r depends explicitly on the material parameters, i. e., the average absorption coefficient α , the index of refraction n , and the bandgap E_{gap} . Therefore, D_λ which has already been normalized by definition to a 1-cm² detector and a noise bandwidth of 1 Hz truly represents the ability of a given material to detect far infraed radiation.

Finally, the optimum value of thickness, d , must be determined experimentally. The chosen value will represent a trade-off between maximizing the responsivity, spectral peak, and quantum efficiency, and by minimizing the effects of surface recombination velocity. Figure 54 is a plot of D_λ for (Hg, Cd)Te.

Figure 55 expands Figure 54 to show the behavior of D_λ in the 8- to 14-micron region. Detectivities in the range of 10^{13} - 10^{14} cm² Hz^{1/2}/watt require operating temperatures below approximately 50°K at 10 microns. At 15 microns, the cooling requirement is more severe and the temperature must be decreased to the 40°K range.

The D_{BJIP} line has been evaluated for a background temperature of 295°K and a 180-deg field of view. Note that the D_{BJIP} line establishes the detector temperature and wavelength at which aperturing becomes ineffective. For example, the detectivity of an 11-micron detector will be invariant with field of view for all temperatures greater than 120°K.

The upper limits for 14-micron (HgCd)Te are compared with extrinsic doped Ge in Figure 56. The conditions for the calculation were:

- Background temperature, $T_b = 77$ K
- Background emissivity, $\epsilon = 0.02$
- Field of view, $\Omega = 15$ deg
- $\Delta\lambda = 8$ -14 microns, unless otherwise noted.
- Length = 0.01 cm
- Width = 0.01 cm
- Thickness, (HgCd)Te = 15 microns, thickness, (Ge) = 0.2 cm
- Quantum efficiency = 0.5
- Lifetime: $\tau = 1.0$ microsecond and varied as a function of temperature.

Note the inherent theoretical advantage of (HgCd)Te with respect to higher operating temperatures when compared with the doped germanium detectors.

4.3.2 Detector Load Resistor and Noise

Doped germanium detectors have been studied at low background temperatures by D. E. Bode of Santa Barbara Research Center (Ref. 8). With a background irradiation of 10^6 photon cm⁻² sec⁻¹ detectivities of $D_\lambda \geq 1 \times 10^{14}$ cm² Hz^{1/2} watt⁻¹ have been observed in 0.5 mm x 1.5 mm (3 mm²)

UNCLASSIFIED

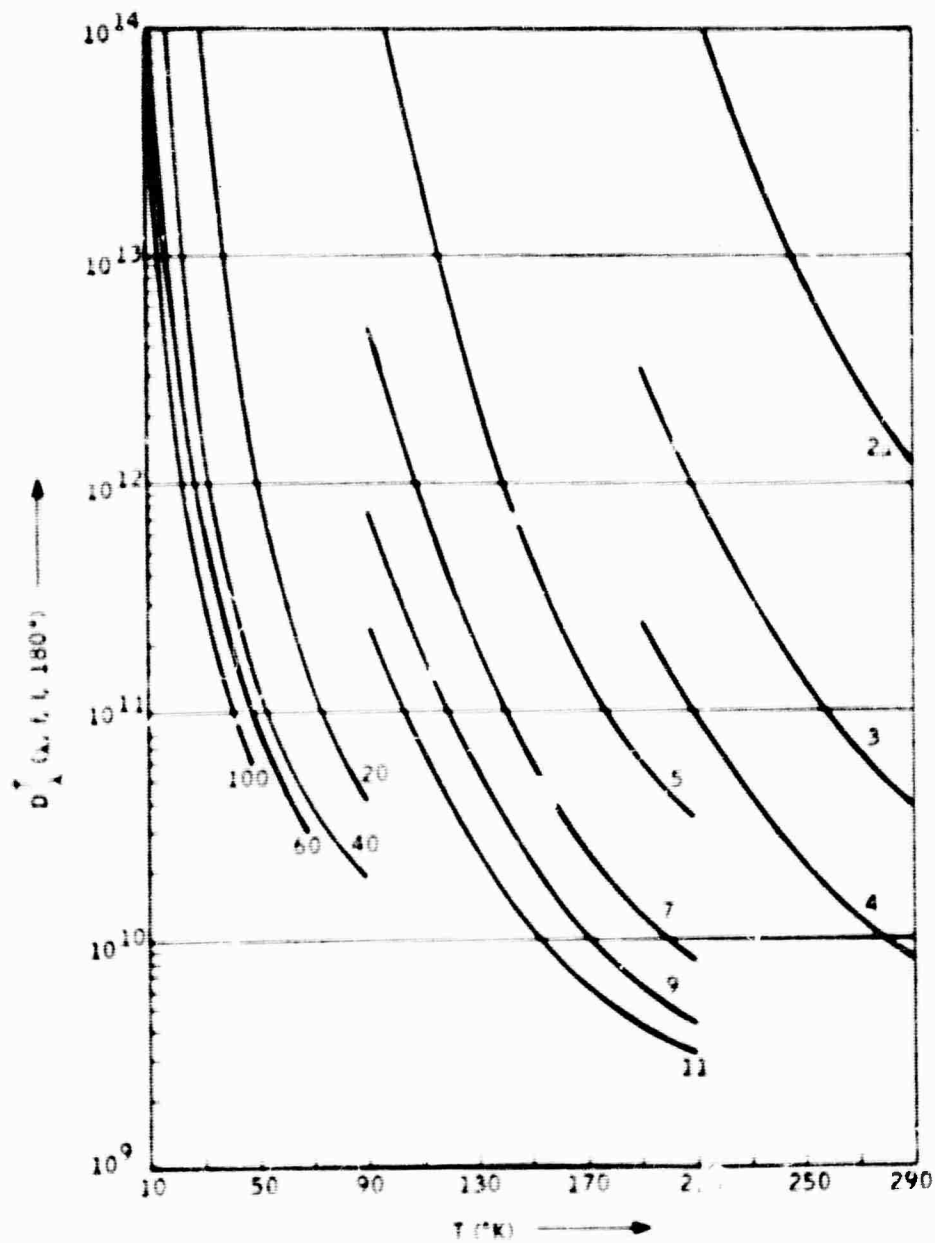


Figure 54. Calculated Maximum Detectivity for (Hg,Cd)Te as a Function of Detector Temperature and a Varying Cutoff Wavelength

UNCLASSIFIED

UNCLASSIFIED

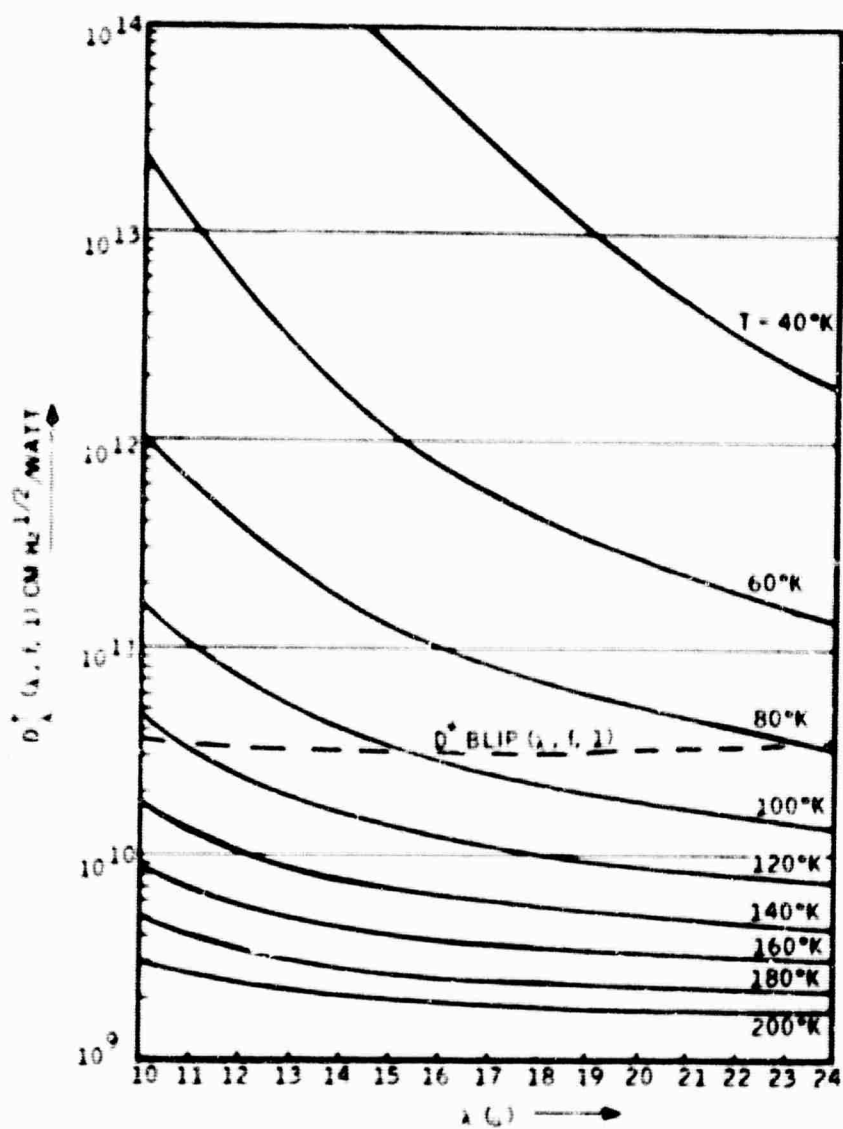


Figure 55. Fundamental Limit as a Function of Wavelength and Temperature

UNCLASSIFIED

UNCLASSIFIED

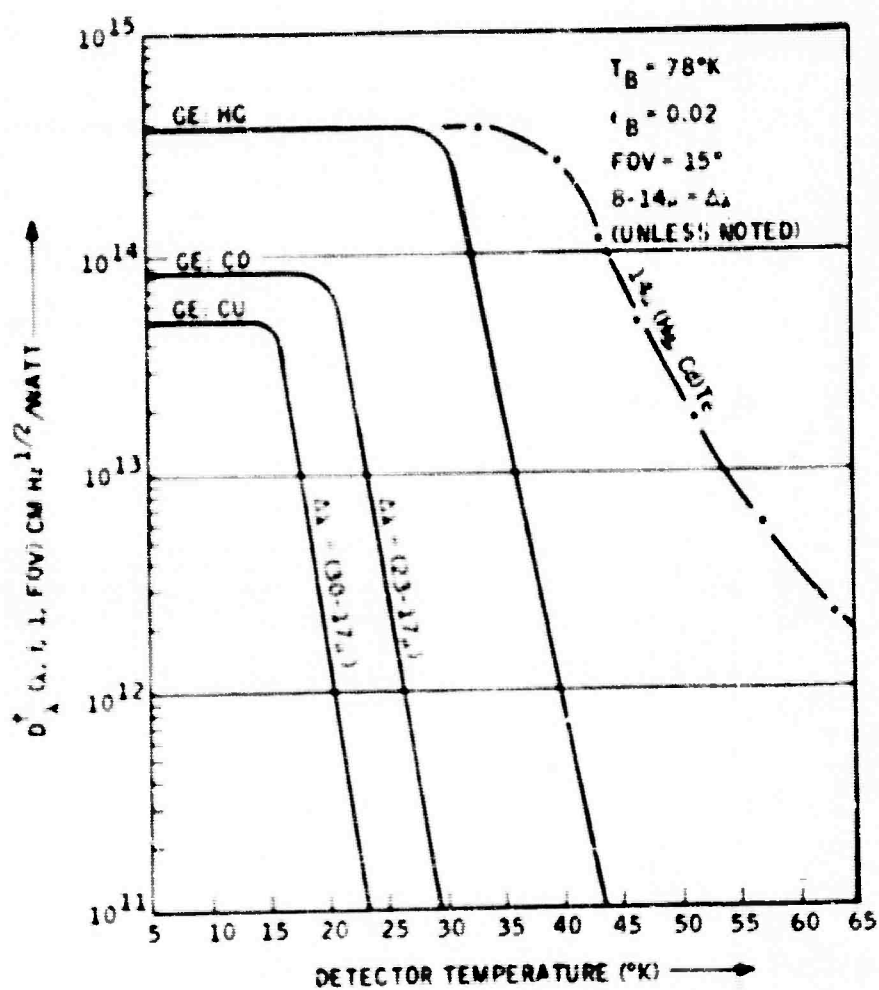


Figure 56. Calculated Comparative Detectivities of Extrinsic and Intrinsic Detectors as a Function of Temperature

UNCLASSIFIED

UNCLASSIFIED

detectors. In smaller devices (0.1 mm x 0.1 mm) with 3×10^{10} photon $\text{cm}^{-2} \text{sec}^{-1}$ D's on the order of 1.4×10^{13} have been observed. Similar performance is expected in mercury cadmium telluride (HgCdTe) detectors of the same active area or smaller.

One of the operating difficulties with doped germanium is its very high resistance. Under very low background conditions, its resistance will be between 10^{12} and 10^{14} ohms. In order to couple the signal into an amplifier it is necessary to use a load resistor which must be kept to a reasonable value such as 10^6 to 10^8 ohms. Such a value of load resistor thus appears as a short circuit to the detector. The preamplifier sees the load resistor, and both load resistor and preamplifier must be cooled to detector temperature in order to minimize their Johnson noise. The signal noise should limit the system in the ideal case. The signal voltage provided to the preamplifier is given by

$$V_s = i_s R_L$$

where V_s = signal voltage

i_s = short-circuit current

R_L = load resistor

The photosignal is

$$i_s = (\eta Q_s A) e \mu \epsilon / L$$

where η = quantum efficiency

Q_s = signal photon irradiance in photon $\text{cm}^{-2} \text{sec}^{-1}$

A = detector area

τ = carrier lifetime

e = electron charge

μ = mobility

ϵ = electric field

L = separation between field contacts

The photoconductive gain (G_{pc}) is defined by

$$G_{pc} = \frac{\tau \mu \epsilon}{L}$$

UNCLASSIFIED

Hence

$$I_s = (-Q_s A) e G_{pc}$$

and $V_s = (-Q_s A) e G_{pc} R_L$

The noise per unit bandwidth is made up of two components, namely G-R noise and Johnson noise. The $1/f$ noise will not be considered in this argument. The rms G-R noise per unit bandwidth is given by

$$V_{n,G-R} = 2 (-Q_s A)^{1/2} e G_{pc} R_L$$

and the rms Johnson noise per unit bandwidth is given by

$$V_{n,J} = (4k T_L R_L)^{1/2}$$

where k = Boltzmann's constant

T_L = temperature of load resistor R_L

The signal-to-noise ratio is obtained by combining all these terms

$$\frac{S}{N} = \frac{V_s}{V_n} = \frac{V_s}{\sqrt{V_{n,G-R}^2 + V_{n,J}^2}} = \frac{(-Q_s A) e G_{pc} R_L}{\left[4(-Q_B A) (e G_{pc} R_L)^2 + 4k T_L R_L \right]^{1/2}}$$

where Q_B represents background photons.

In order to maintain BLIP performance the G-R noise term must be the largest contributor in the total noise expression. In a photoconductor, the G-R noise is twice the background photon noise. Hence, to keep BLIP performance the ratio of G-R noise to Johnson noise must be as large as possible:

$$\frac{V_{n,G-R}}{V_{n,J}} \geq \left(\frac{-Q_B A}{k T_L} \right)^{1/2} e G_{pc} R_L^{1/2}$$

This equation shows that the load resistor must be cooled for the doped germanium detectors and the value of the load resistor must be as high as possible. The quantum efficiency and photoconductive gain are fixed for a given device but both should be as high as possible. As the background radiance is reduced, the load resistor, R_L , or the detector active area must increase in order to keep the same G-R noise to Johnson noise ratio so that BLIP performance is maintained. For mercury cadmium telluride detectors this ratio becomes

UNCLASSIFIED

$$\frac{V_{n, G-R}}{V_{n, J}} = \left(\frac{-Q_B A}{k T_D} \right)^{1/2} e^{-G_{pc} R_D^{1/2}}$$

where R_D = (HgCd)Te detector resistance

T_D = detector temperature

because the (HgCd)Te detector can act as its own load resistor. For cells operating near $T_D = 4.2K$, the value of R_D is about 50 ohms. In comparison to the use of germanium $R_D \ll R_L$ which means that the preamplifier now responds to the detector output open circuit voltage. The bias supply load resistor R_L is not seen by the preamplifier, and hence it need not be at the cryogenic detector temperature. Because the (HgCd)Te detector has such a low impedance the connecting cables may be quite long thus allowing the use of a conventional room-temperature preamp outside of the cryogenic environment. The quantum efficiency of (HgCd)Te is 0.5 because of its high absorption and this value can be increased to 0.9 by the use of antireflection coatings.

In (HgCd)Te the lifetime depends inversely on the square root of background radiance so that as the background is reduced, the lifetime increases, and, more importantly, the photoconductive gain increases:

$$G_{pc} = \frac{e \mu \tau}{L} \\ \tau = \frac{K}{Q_B^{1/2}} \text{ where } K = \text{normalizing constant}$$

Therefore

$$G_{pc} = \frac{K \mu \tau}{Q_B^{1/2} L}$$

Placing this into the ratio expression for the two noise components

$$\begin{aligned} \frac{V_{n, G-R}}{V_{n, J}} &= \left(\frac{-Q_B A}{k T_D} \right)^{1/2} \frac{e K \mu \tau}{Q_B^{1/2} L} R_D^{1/2} \\ &= \left(\frac{-A}{k T_D} \right)^{1/2} \frac{K \mu \tau}{L} R_D^{1/2} \end{aligned}$$

This last equation shows that (HgCd)Te has an automatic gain feature that maintains the same ratio of G-R noise to Johnson noise no matter how the background is reduced. Once a detector of this type is BLIP at 10^{13} photon $\text{cm}^{-2}\text{sec}^{-1}$ it will remain fully BLIP to the lowest of background radiances

SECRET

(U) with only a loss of electrical bandwidth. This means that the detector can operate over a very wide dynamic range of background irradiance with little degradation in performance. The doped germanium detectors, on the other hand, with their cooled load resistors of very high value, must only be used at low background levels if BLIP performance is to be preserved. At $T_L = 5k$ the ratio of G-R noise to Johnson noise is given by

$$\frac{V_{n, G-R}}{V_{n, J}} = 1.09 \times 10^{-9} (R_L Q_B)^{1/2}$$

(U) For example, in order for this ratio to have a value of 2 with a background of $Q_B = 10^9$ photon $\text{cm}^{-2}\text{sec}^{-1}$ a load resistor of 4×10^6 ohms would be required. With amplifier input resistances of such a high value it is possible to get coupled EMI problems. In addition the germanium quantum efficiencies are about 0.15 such that when the two types of detector are compared, the mercury cadmium telluride will show up quite well.

4.4 DIFFRACTION ANALYSIS

4.4.1 General Discussion

(U) The problem of interference from diffracted light is a major one, in a limb measurement instrument. The main light source which contributes to diffracted light, interfering with the limb spectroradiometer system, is the earth, represented as a blackbody ranging in temperature from 220 to 300°K.

(S) When off-axis radiation from the earth is received by the instrument, the primary optics form a diffracted earth image at the primary focal plane. Some of the diffracted energy appears on-axis at this point and may be of sufficient level to obscure the target unless it is properly attenuated.

(U) The application of coronagraph principles to the design of this instrument are best explained by examining in detail an analysis of the "boundary-wave diffraction theory." This theory, presented by Thomas Young in 1802 and mathematically substantiated by Rubinowicz, proposes that diffraction occurring within the geometrical image of the object is due to superposition of the direct illumination from the source and cylindrical wavefronts originating at the boundary or rim of the aperture, while diffraction occurring within the geometrical shadow of the aperture arises from only the cylindrical wavefronts originating from the aperture boundary. Using this theory, the evolved technique allows calculation of diffraction effects as simply as establishing the geometrical shadow boundaries.

SECRET
THIS PAGE IS UNCLASSIFIED

Diffraction effects in the system may be examined beginning with the optical system layout, illustrated in Figure 57. This system will image a source such that irradiance at the center of the image is found by

$$H_i = \frac{\pi N}{4 (f/\text{no.})^2} \quad (1)$$

where

H_i = image irradiance

N = peak Lambertian radiance level

$f/\text{no.}$ = f /number of the system

provided the source is Lambertian on-axis, at infinity, and the exit pupil half-angle allows $\sin \theta' \approx \tan \theta' \approx \theta'$. These conditions are all met (within a minimal error) in the spectroradiometer system.

The earth being considered a Lambertian source, possesses an infinite number of effective source radiators as shown in Figure 58. Choosing the most convenient equivalent radiating surface, namely the plane located at AA' (refer to Figure 58) we have an off-axis plane source imaged by a circular mirror onto the back focal plane of that mirror. The aperture stop of the system is the combination of the baffle enclosure and the primary mirror, subtending at the exit pupil a half-angle satisfying the conditions for equation (1). In addition, the earth source is less than $\tan^{-1} (2R/L)$ degrees off-axis for all inclination angles of interest so the irradiance of the image will not change appreciably with inclination because of the functional dependence of the source radiance being that of a cosine. Therefore, the irradiance as calculated by equation (1) is valid for the undiffracted image. However, diffraction does occur and spreads the image at the edges. The amount of this diffracted energy within the geometrical shadow of the source is needed since, in the spectroradiometer system, this is the stray diffracted energy which appears on-axis to interfere with the target.

A technique for extrapolation of the diffraction pattern was given in a paper by H. Nagoaka (Ref. 9). The paper describes an on-axis circular source, illuminating a circular aperture. The image "skirt" shape is shown to become nearly invariant with source radius for source radii $> r = 100$ where $r = KR \sin \theta$ (see Figure 59 for parameter definition). This may permit treatment of the aperture-limited image as a circular one, provided the above mentioned limit has been surpassed by the source subtense. The geometrical edge of this effective source must be colinear with that of the true source in the vicinity of the optical axis (see Figure 60) and as shown in 4.4.2, this is the case. Therefore, the "skirt" of the true earth image (which is not circular) may be considered to be caused by an effective circular source of very large

UNCLASSIFIED

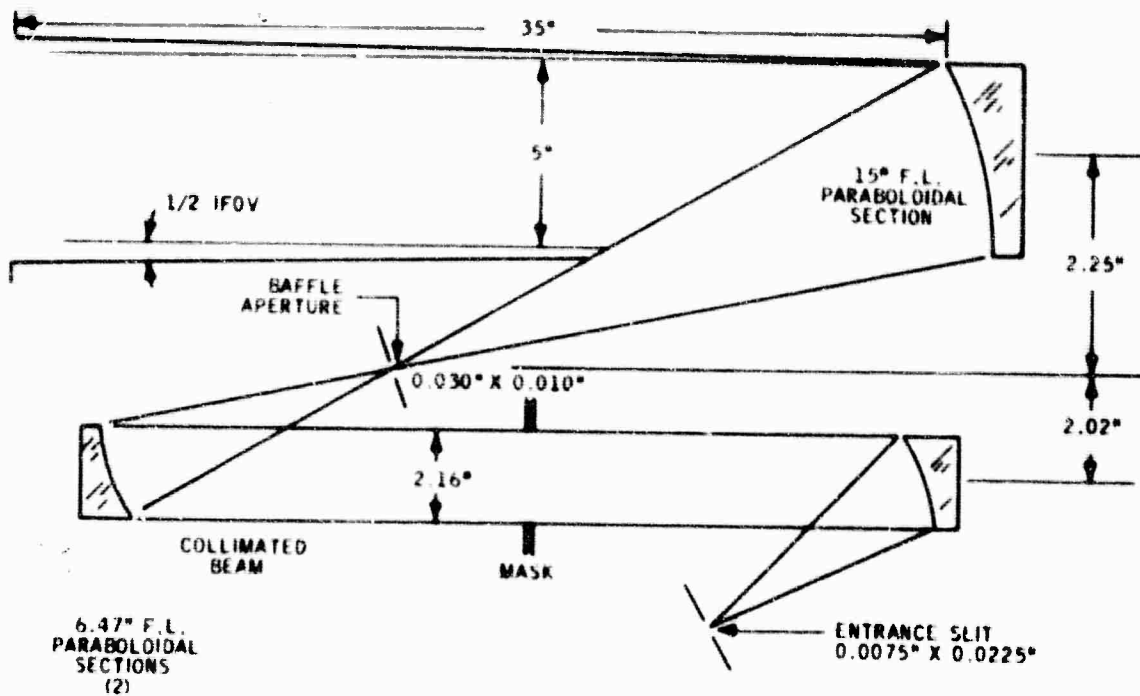


Figure 57. Basic Optical System Layout

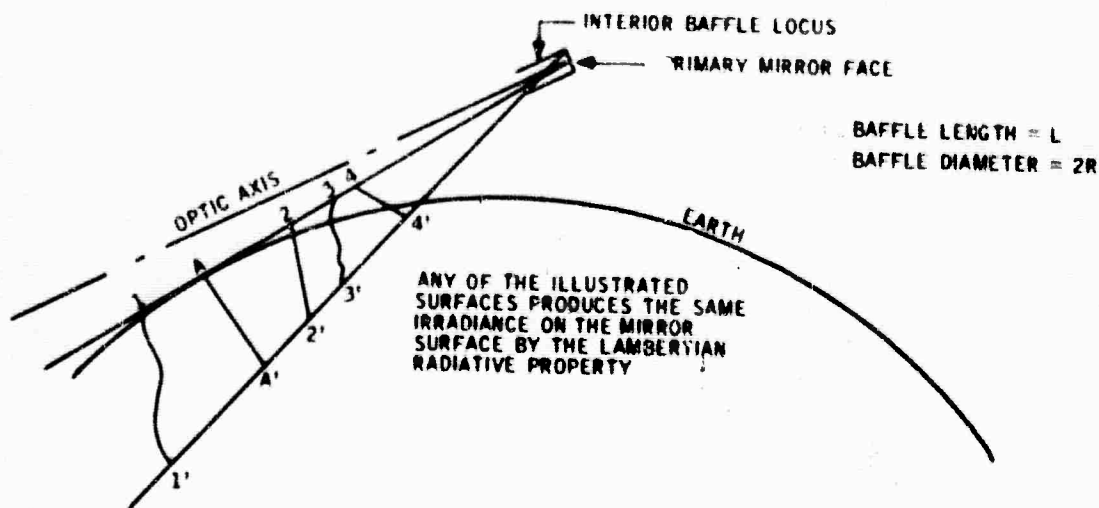


Figure 58. Cross-sectional Cuts of Equivalent Earth Radiators

UNCLASSIFIED

radius. Off-axis position will be considered to have a negligible effect on skewing the diffraction pattern. Therefore, the technique of Nagaoka may be utilized wherein the irradiance of a point off-axis (on the "skirt") is calculated. The geometry of the spectroradiometer system relative to the Nagaoka treatment is shown in Figure 61, where it can be seen the baffle aperture or pinhole lies at the image plane on-axis. Using the described approach, the pinhole irradiance may be easily calculated. Assuming the energy distribution to be uniform over the pinhole, the power transferred is simply the product of the irradiance calculated and the pinhole area.

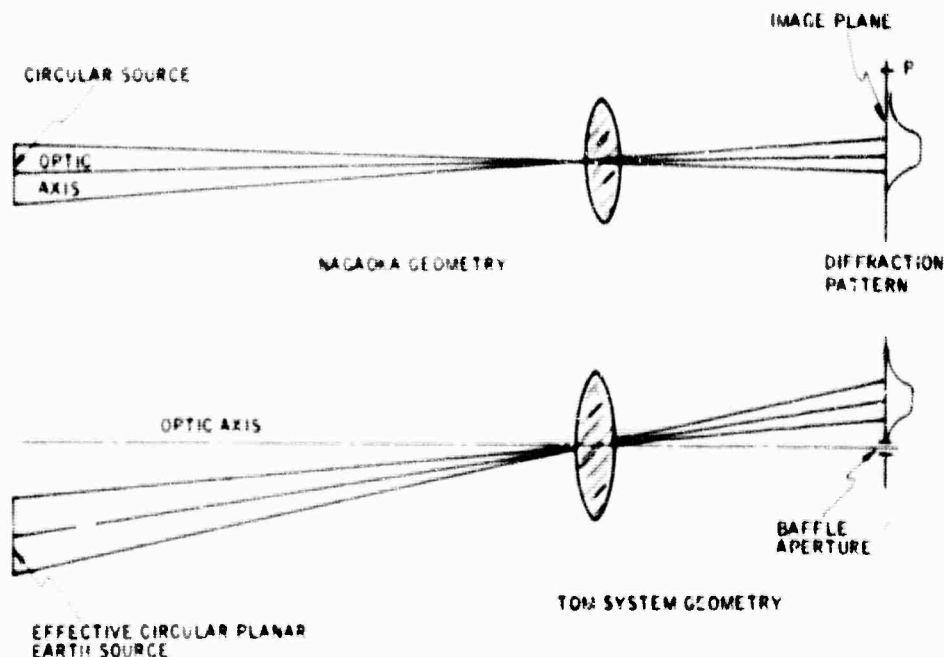


Figure 61. Similarity of Proposed TOM System to System Analyzed by Nagaoka

The boundary wave theory of Thomas Young allows the calculated energy present at the pinhole to be traced throughout the remainder of the spectroradiometer system. Referring to Figure 61, it may be seen that the pinhole lies within the geometrical shadow of the circular earth source, and, therefore, wavefronts causing its diffraction irradiance are due only to the ring or aperture rim component source. Therefore, diffraction effects after the mirror may be considered by treating this ring source as that source causing all ensuing diffraction.

Calculating the diffraction pattern on the second mirror becomes the problem of calculating the intensity distribution of a locus of point sources radiating through the pinhole, the locus being the true aperture (not all the

primary mirror is illuminated with earth light, and the true locus is the periphery of this illuminated region). However, the assumption of a circular locus (the complete mirror periphery) is made to simplify the mathematics. Stretching this point, the assumption of all images on-axis or equivalently, an on-axis optical system, will be taken for the remainder of the report. Consideration of the angle involved in the physical system layout justifies this first-order approximation.

Returning to the character of the true point source locus, two rim components are evident: (1) the aperture rim and (2) the mirror rim -- each contributing four distinct regions of elemental earth radiation. The assumption is that this locus contains only one of these components, namely, the mirror rim. Proceeding from this point, now, the intensity distribution on the second mirror can be found by the line integral of the locus of point sources around the mirror rim. However, an easier method is offered by the principle of superposition by making the assumption of a circular pinhole instead of rectangular. The mechanics of integrating the irradiance over the pinhole are considerably reduced by the fact that the resulting diffraction pattern from a point source on the primary mirror rim is axially symmetric. Therefore the total pattern from all points on the rim will likewise be axially symmetric. The power on the secondary mirror (the integral of the diffraction pattern over the mirror area) for each component point source on the rim is the same due to their axially symmetric property, and the total power from the rim is simply the sum of all component powers. Diffraction from each source can easily be found, neglecting the off-axis skewness, by considering the classic condition of a point source on-axis illuminating a circular aperture at a distance such that Fraunhofer diffraction dominates. The far-field intensity distribution is well known and is shown in Figure 62. Integration over the mirror yields total power passing through the mirror. The mechanics of this integral are reviewed in section 4.4.2. This approximation -- replacing the rectangular aperture by a circular one having a diameter of the shortest rectangular dimension -- is valid for order-of-magnitude power levels; however, whether the result is worst-case can only be derived from further analysis.

A mask is applied to the collimated beam as shown in Figure 57 such that applying the boundary wave theory, the energy passing through the mirror is caused only by the rim source of the pinhole, the mirror now being the geometrical shadow of the original point source (as shown by the effective mask in Figure 63). The pinhole rim source, now is the sole source of diffracted light for the remainder of the system. Imaging it onto the detector through the collimating system produces a $(\sin x/x)^2 (\sin y/y)^2$ type of pattern for one point on the pinhole (rectangular rim) rim source. The total pattern is a rectangular locus of centers, each pattern having the $(\sin x/x)^2 (\sin y/y)^2$ form. Mirror power integration is simplified by assuming (again) a circular baffle aperture and using the aforementioned integral technique. This method is elaborated in 4.4.2, for the approximation case, namely, a circular pinhole.

UNCLASSIFIED

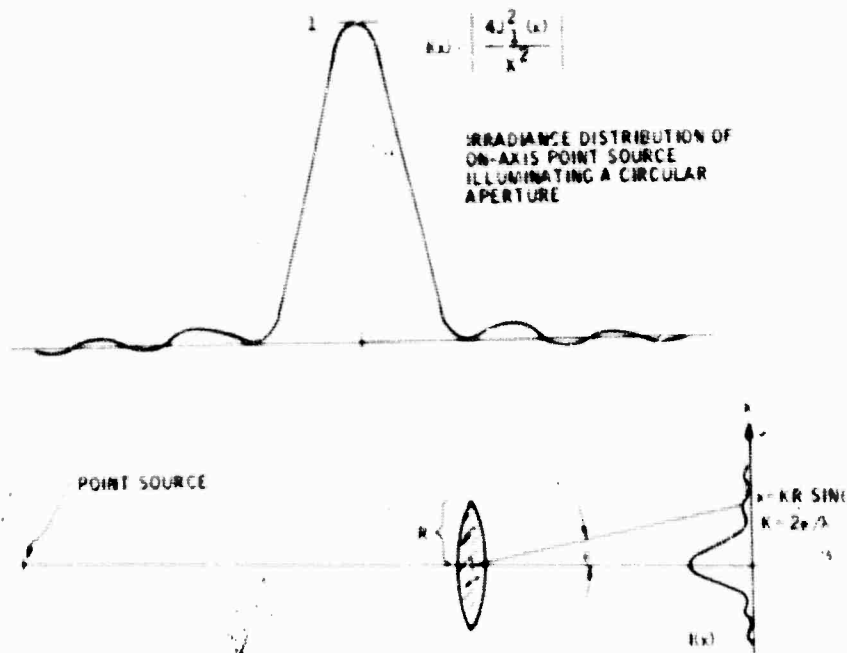


Figure 62. Diffraction of On-Axis Point Source at Infinity Illuminating a Circular Aperture

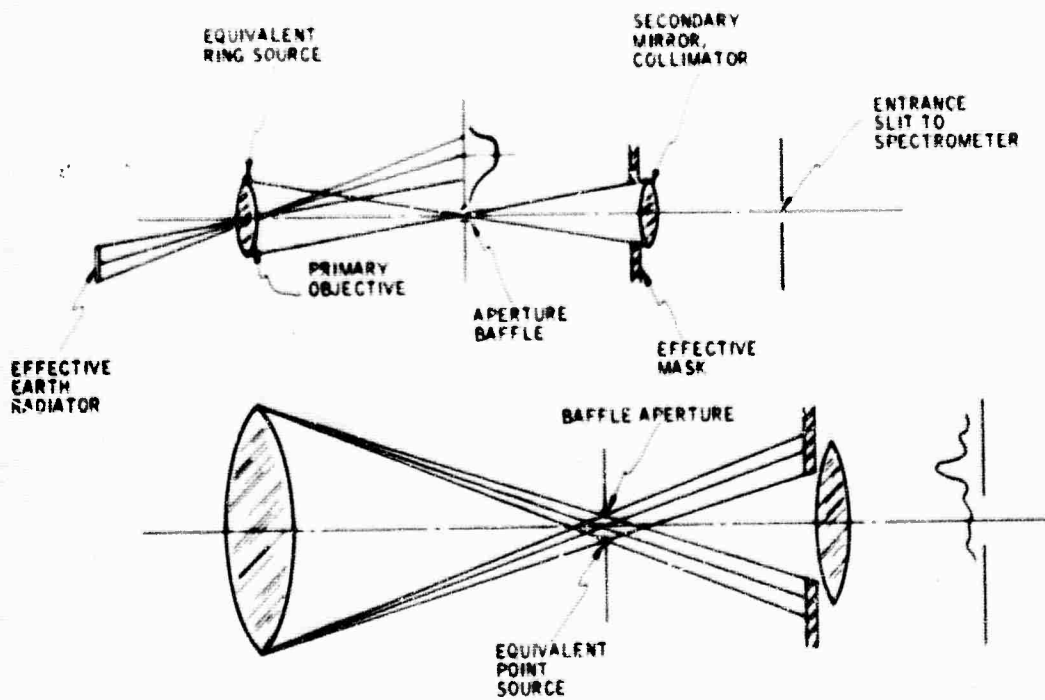


Figure 63. On-Axis Lens Analogy to TOM System

UNCLASSIFIED

4.4.2 Determination of Flux Through the Pinhole

Determination of flux through the pinhole (baffle aperture) will now be examined. Referring to the treatment of Nagaoka, the power at an off-axis point for a circular source illuminating a circular aperture is

$$P_T = \frac{1}{\pi} \int_{\text{Source Image}} \left[\frac{2J_1(u)}{u} \right]^2 dA$$

where the origin is at the point of interest. (Refer to Figure 64 and Figure 65 for the geometry of the situation.) The constant normalizes to unity the total incident power passing through the aperture. This integral, in the language of modern optics, can be transformed into a two-dimensional convolution. Proceeding to the determination of a and b to be:

$$a \approx KR \left[\frac{\beta - \alpha}{2} \right]$$

$$b \approx KR \alpha$$

where α and β are defined in Figure 66. What is being done here is to inscribe within the true earth plane radiator a circle, and then determine whether its image radius justifies the large-radius circular-source approximation. If such is the case, the inscribed circular planar earth source can then be used in calculating the skirt of the diffraction pattern. The resulting integration is much easier than had the true earth source (a noncircular source) been used. This is illustrated in Figure 67. Applying Nagaoka's procedure to a computer (for the case of points outside the source image), the irradiance level is easily found. Multiplication by the hole area yields total power, as the intensity is nearly constant over the pinhole. This is the amount of diffracted light passing through the pinhole produced by the primary mirror.

Stationing the mask in the collimated beam effectively places the secondary mirror in the geometrical shadow of the primary mirror rim source, and we can easily calculate the diffraction produced by the baffle aperture, utilizing the circular aperture approximation. Lumping the rim source of the primary mirror into its power-equivalent point source, the resulting distribution is a Bessel-type intensity over the secondary mirror (neglecting skewing of the image). Integration over the mirror yields power through the mirror (Figure 65).

Now treating the diffraction produced by the final mirror, the source of diffracted light is the pinhole power-equivalent point source, again treating the rectangular aperture as circular. Diffraction over the detector is found by simply imaging this point source onto the back focal plane of the mirror. The resulting intensity distribution is similar to the far-field pattern produced by the pinhole, namely a Bessel of revolution. Detector power is simply its integral over the detector.

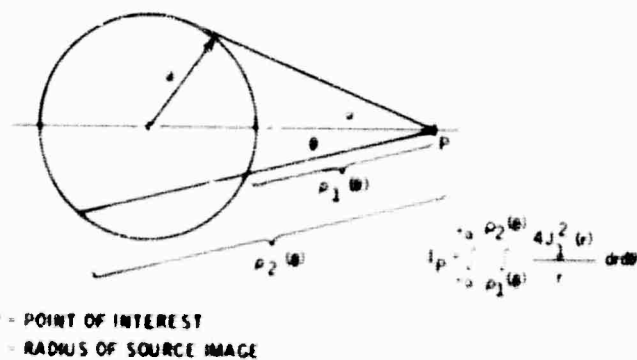
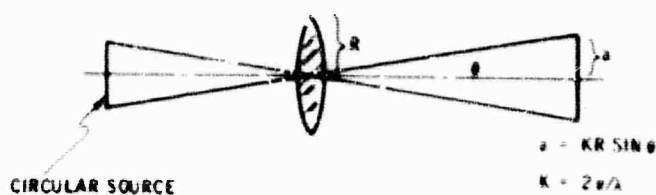
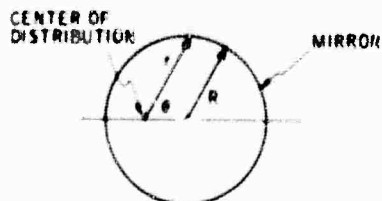


Figure 64. Power Determination Integral

SECONDARY MIRROR POWER

$$P = \frac{1}{2} r(\theta) \left[\frac{2J_1 \left(\frac{KR}{r} \right)}{\frac{KR}{r}} \right]^2$$



λ = WAVE NUMBER
 R_0 = APERTURE RADIUS
 f = FOCAL LENGTH

DETECTOR POWER

$$r(\theta) = R \cos \theta + \sqrt{R^2 - a^2 \sin^2 \theta}$$

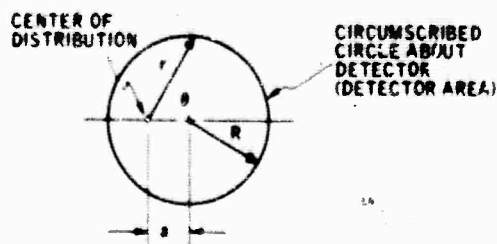


Figure 65. Power Integrals

UNCLASSIFIED

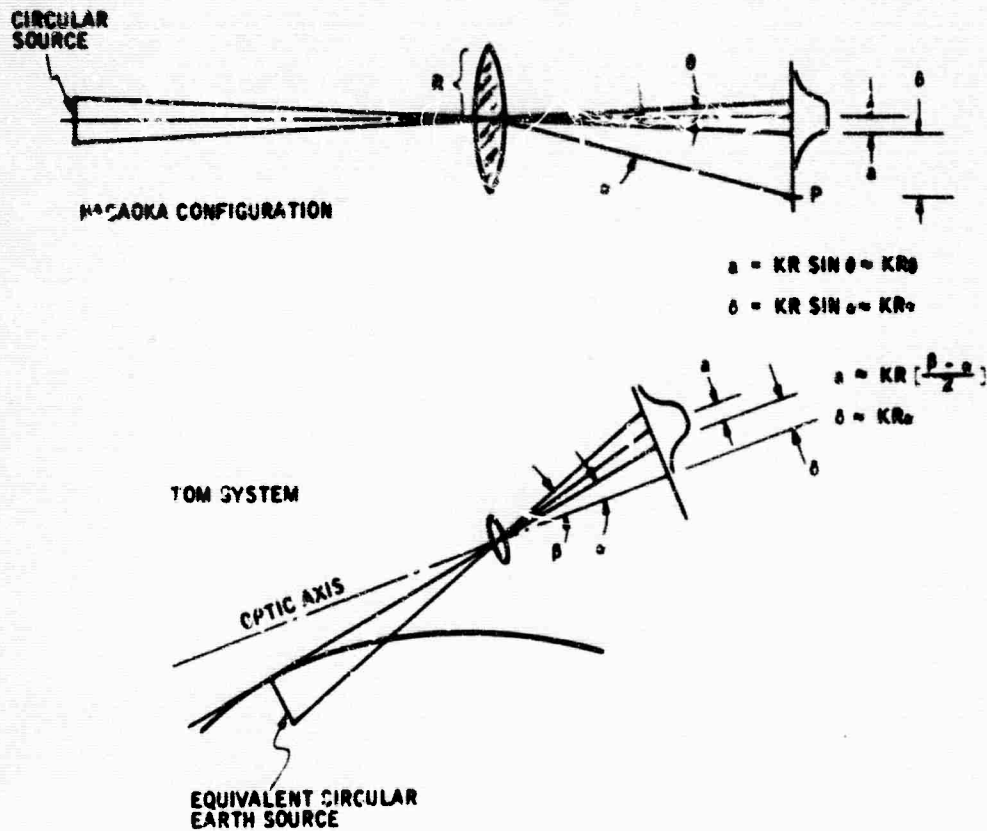


Figure 66. Comparison of Nagaoka Configuration to TOM

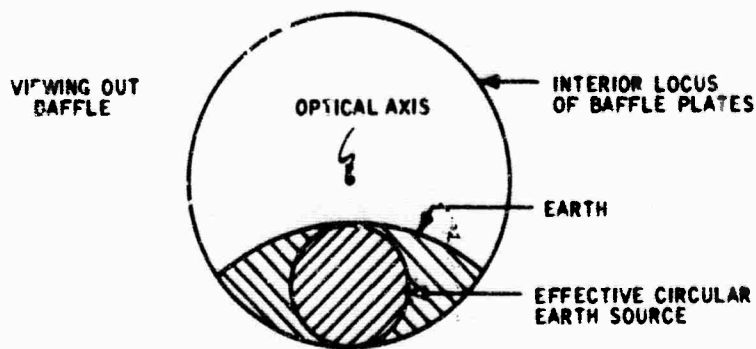


Figure 67. Effective Circular Planar Earth Source

UNCLASSIFIED

UNCLASSIFIED

The integration used in power determination with the circular aperture approximation in effect, given an off-axis point source at infinity illuminating a circular aperture, will now be examined.

Receiver power for $a = R$ (see Figure 65) is

$$P_R = H_0 \int_{-\pi/2}^{+\pi/2} \int_0^{r(\theta)} \left[\frac{2J_1\left(\frac{KR_0 r}{f}\right)}{\left|\frac{KR_0 r}{f}\right|} \right] r dr d\theta$$

where H_0 is peak irradiance at the center of the distribution. Integration over all image space yields

$$H_0 = \frac{\pi R_0^2 P_t}{(\lambda f)^2}$$

In these expressions

$$K = 2\pi/\lambda$$

$$R_0 = \text{aperture radius}$$

$$P_t = \text{total power through aperture}$$

$$f = \text{focal length}$$

Simplifying

$$P_R = 8H_0 \int_0^{\pi/2} \int_0^{2R \cos \theta} \left[\frac{J_1(u)}{u} \right]^2 r dr d\theta$$

where

$$u = \frac{KR_0 r}{f}$$

Transforming variables

$$P_R = 8H_0 \int_0^{\pi/2} \int_0^{\frac{2KR_0 R \cos \theta}{f}} \frac{J_1(u)}{u} \left| \frac{f}{KR_0} \right|^2 du d\theta$$

Realizing the identity

$$\frac{J_1^2(u)}{u} = -\frac{1}{2} \frac{u}{du} \left\{ J_0^2(u) + J_1^2(u) \right\}$$

the above reduces to

$$\begin{aligned} P_R &= \frac{2P_T}{\pi} \int_0^{\pi/2} \int_0^{u(\theta)} \frac{J_1^2(u)}{u} du d\theta \\ &= \frac{2P_T}{\pi} \left(-\frac{1}{2} \right) \int_0^{\pi/2} \left\{ J_0^2(u) + J_1^2(u) \right\} \bigg|_0^{u(\theta)} d\theta \\ &= \frac{P_T}{\pi} \int_0^{\pi/2} \left\{ J_0^2(u) + J_1^2(u) \right\} \bigg|_0^{u(\theta)} d\theta \\ &= \frac{P_T}{\pi} \int_0^{\pi/2} \{ y[u(\theta)] \} d\theta \end{aligned}$$

where

$$u(\theta) = \frac{2KR_0 R \cos \theta}{f}$$

$$y[u(\theta)] = 1 - J_0^2[u(\theta)] - J_1^2[u(\theta)]$$

4.4.3 Diffraction Calculations

The previous discussion, using Nagaoka's procedure, related the diffraction resulting from the illumination of a circular aperture by a large circular source. These principles have been applied to a computer program written to evaluate the level of diffracted energy and to trace it through the optical system. The resulting values are derived from diffraction occurring at the

UNCLASSIFIED

front baffle of the system and entering the tube. Some of the diffracted energy reaches the primary mirror while the remainder is absorbed and attenuated by the forebaffle system.

In the one-dimensional approximation computer program, a line source was assumed, infinite in azimuth and displaced from the instrument optical reference along the elevation. The following parameters also apply:

Primary mirror diameter = 4 in.

Primary mirror focal length = 12 in.

Pinhole diameter = 0.01 in.

Collimating mirror focal length = 7.5 in.

Blackbody earth source temperature = 300°K

Figure 68 is a characteristic plot of the diffracted energy at the first relay or collimation mirror for a tilt angle of 1 deg and a wavelength of 10 microns. Since the pattern is symmetric, only half has been plotted. Figure 69 shows the result of integration of the diffracted energy in comparison with the signal energy and indicates the effectiveness of placing a Lyot stop (mask) in the system between the collimating mirrors in order to reduce the relative effect of diffraction.

In the same manner, a two-dimensional case computer program was utilized to calculate the diffracted energy through the pinhole. The results were as follows:

<u>Primary Mirror</u>	<u>λ (μ)</u>	<u>λ Spread (μ)</u>	<u>Pinhole Energy (watts)</u>
4-in. dia.	5.35	5-5.7	4.4×10^{-15}
4-in. dia.	10.4	10-10.8	2×10^{-13}
4-in. dia.	12.95	12.8-13.1	5.7×10^{-14}
6-in. dia.	21.5	18-25	2.2×10^{-12}

4.5 OFF-AXIS RADIATION

Attenuation of off-axis earth radiation by factors of 10^{-8} to 10^{-11} , depending on the wavelength, is required of this instrument to prevent masking of limb radiation by a 1-deg off-axis earth. This earth radiation may be coupled into the limb sensor field of view by diffraction at various apertures, scattering from optical surfaces and edges, and by internal reflections. The required attenuation is achieved by a combination of cooled blackbody cavity baffles, a low-scattering primary mirror, and a series of apodized stops.

UNCLASSIFIED

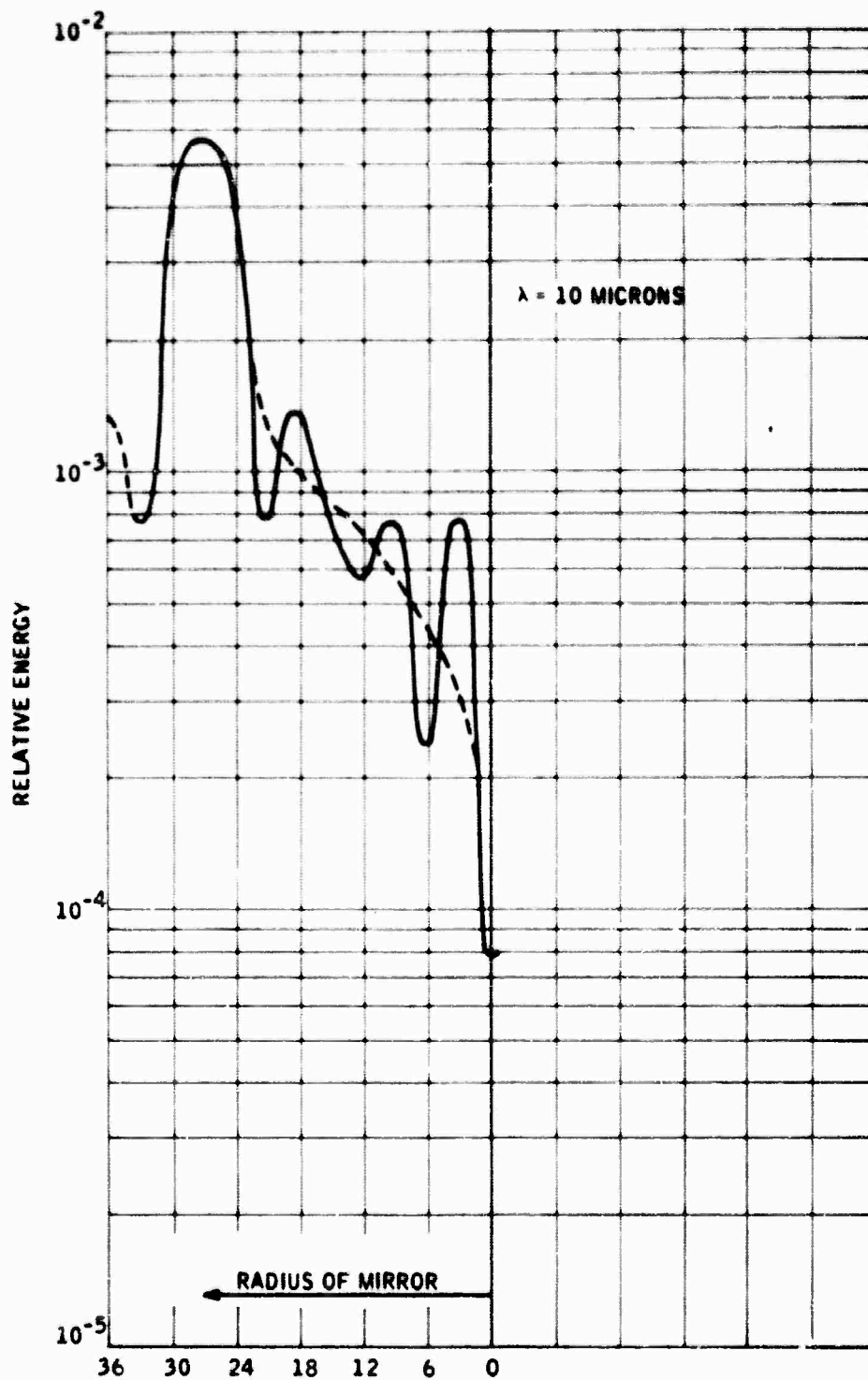


Figure 68. Pattern of Diffracted Energy of First Relay Mirror .

UNCLASSIFIED

UNCLASSIFIED

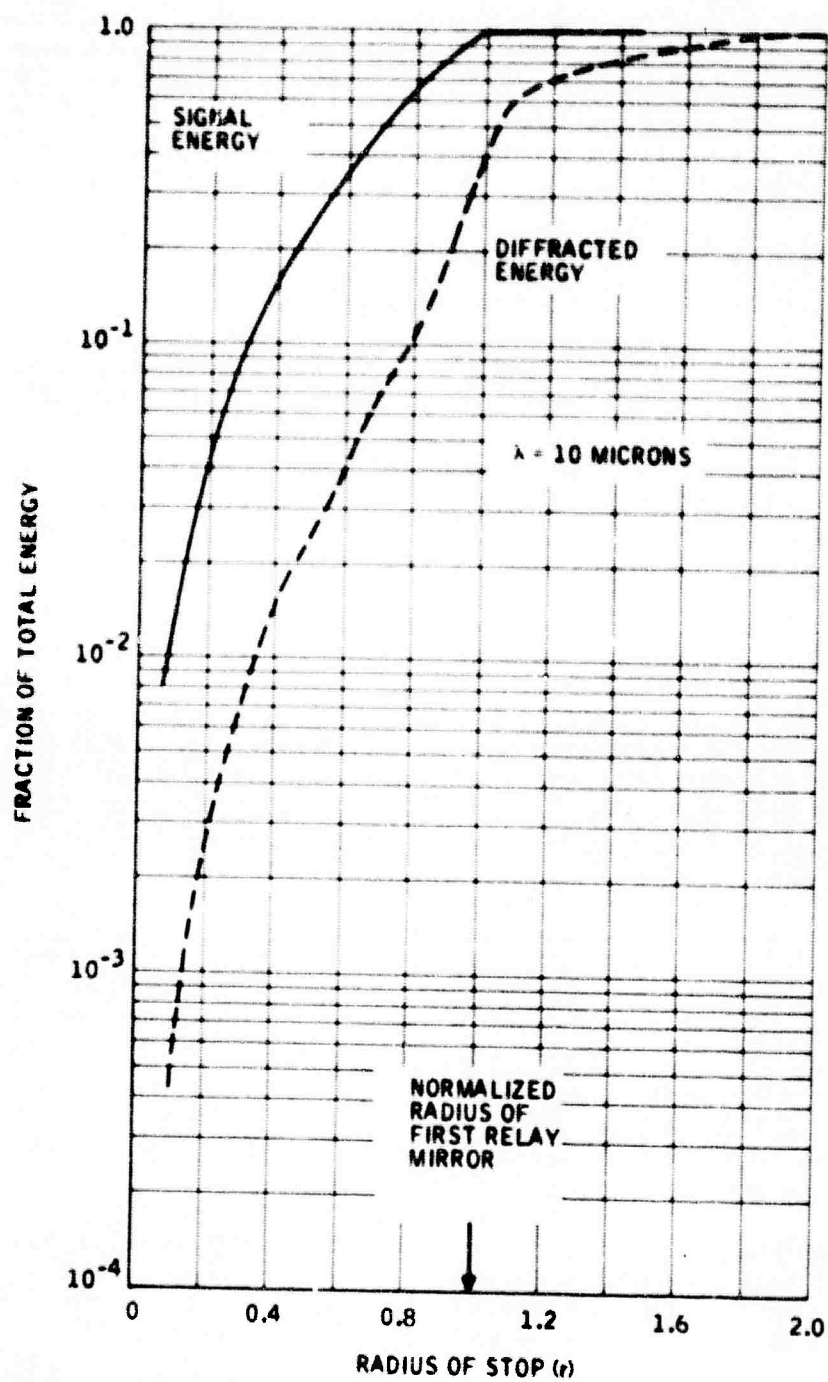


Figure 69. Cumulative Signal and Diffraction Energy at First Relay Mirror

UNCLASSIFIED

UNCLASSIFIED

As was stated earlier, diffracted earth energy is reduced by an optical design similar in concept to that employed in the Lyot solar coronagraph. Most of the energy diffracted at the front baffle is absorbed by a blackbody cavity hood and cone at the primary focus. A major portion of the remainder passing through the focal plane pinhole is blocked by a Lyot aperture located between the collimating mirrors. (For its effectiveness, see Figure 68.)

A Fourier transform computer program has been compiled to calculate the diffracted field strength throughout the system. A preliminary analysis has shown that 10^{-12} watts of diffracted earth energy in the 18- to 25-micron band-pass through the focal plane aperture when the earth is $1/2$ deg off-axis. This increases to 2×10^{-12} watts in the 10- to 10.9-micron band. The first baffle was confirmed to be the primary contributor of diffracted energy.

Further diffraction reduction necessary for adequate system performance will be accomplished by the Lyot stop. Its effectiveness is increased by apodization with a serrated edge. This directs energy diffracted by the stop away from the optical axis toward radiation traps.

Stray earth infrared radiation also reaches the detectors by reflections at surfaces within the sensor. This reflected radiation is reduced by a series of forebaffles and a post baffle (Figures 70, 71, and 72) using the blackbody cavity as the basic design element. The forebaffles consist of a series of cone traps intercepting off-axis energy included within an 82-deg cone, as radiated from the earth into the entrance aperture. The post baffle is a blackbody hood with an inner cone that accepts and attenuates the off-axis earth image as focussed by the primary at the first focal plane. This energy is that within a 7.5-deg cone for this preliminary design.

Figure 72 shows the 8-deg baffle acceptance angle and illustrates the image of the earth at the first focal plane from the earth radiation directly impinging on the primary. The small cone provides the first aperture stop. The hood (semi-cone) provides a blackbody cavity for the earth image. Honeywell tests on blackbody cavities have resulted in attainment of greater than 10^{-5} rejection with an L/D ratio of approximately 4.5 to 1. The L/D ratio, as proposed, is approximately 7.5 to 1 for the post baffle. Cascading of the two baffles should provide a rejection capability of greater than 10^{-10} , and further testing is expected to verify this.

The basic purpose of the upper forebaffle design is to provide conical or blackbody baffles such that earth energy as it impinges on the upper portion of the radiometer barrel cannot be seen by the primary on the first bounce (specular) or the first source of reflected radiation (diffuse).

Even though no direct earth radiation impinges on the bottom side of the instrument, the upper baffle edges are diffusing and scattering. The most critical edge in radiation effect is the last baffle edge. The lower forebaffles are positioned to block scattered radiation from this edge, such that no surface reflects or diffuses in a third-order effect.

UNCLASSIFIED

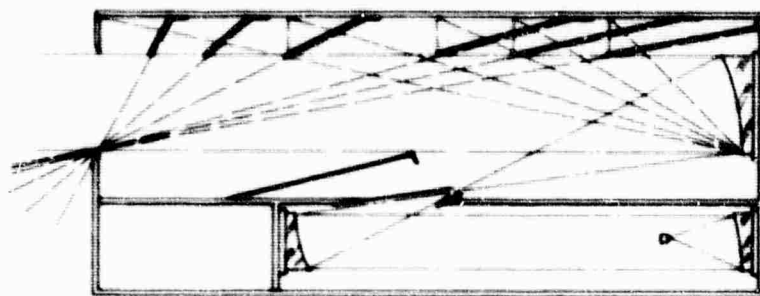


Figure 70. Cavity (Blackbody) Upper Forebaffles

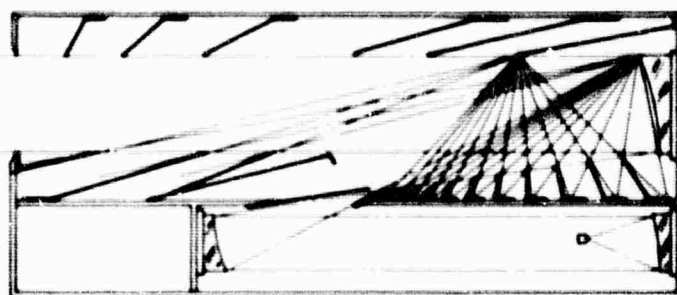


Figure 71. Cavity (Blackbody) Lower Forebaffles
(total developed design)

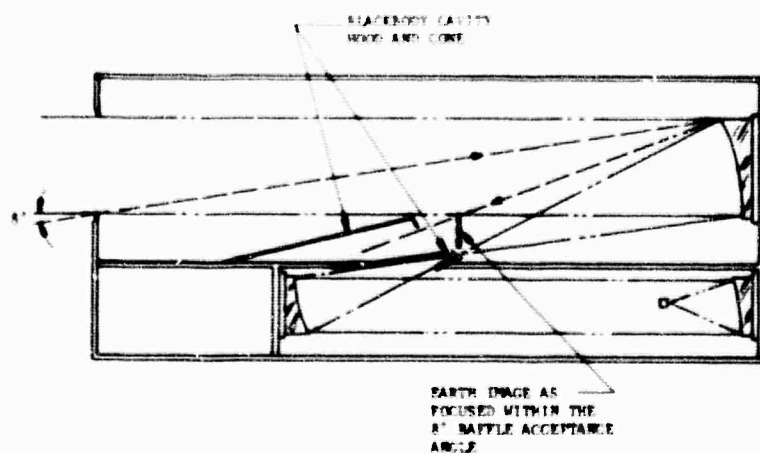


Figure 72. Earth-Focused Image Attenuated in Black-
body Cone and Hood

UNCLASSIFIED

UNCLASSIFIED

This design provides an attenuation of off-axis, stray-light earth energy in a manner such that direct energy is attenuated in a cavity. No surface is exposed to the primary that radiates second-order reflected (specular or diffuse) energy. Each baffle edge is slightly off (0.010 to 0.020 in.) the field of view. It follows, therefore, that off-axis, stray-light effects are predictably attenuated except for edge effects. Specular reflections at the edges of stops and baffles can only be prevented by having sharp edges. The Honeywell Radiation Center has fabricated for the Canopus Tracker (Mariner '69) a baffle edge with a radius equal to or less than 30×10^{-6} in. The same technique can be used in this proposed application.

Some direct earth irradiance impinges on the primary directly. It is not practical to completely shield the primary behind the forebaffle because it is desired to measure the earth atmosphere to within 1 deg of the hard horizon. The forebaffle length for a 5-in. diameter primary would have to be $L = 5 \text{ in.} / \tan 1.0 \text{ deg} = 286 \text{ in.} = 24 \text{ ft}$ long to completely shade the primary. Efforts to increase the L/D ratio by the use of a honeycomb (soda straw) forebaffle fail because the forebaffle tubes, themselves, greatly increase diffraction, and stray reflections occur within the tubes to produce unacceptable noise levels.

The direct-earth irradiance on the primary mirror is directly focussed into the blackbody trap in the first focal plane. A small component of this radiation is diffusely scattered into 2π steradians, and the slit aperture in the blackbody focal plane baffle intercepts a portion of the scattered component. Once the scattered radiation enters the first baffle slit, it is within the optical path and cannot be attenuated further. It is, therefore, mandatory that the scattering coefficient of the primary objective mirror be low. Subsequent optical surfaces do not need this quality of finish.

4.5.1 Scattering

General -- Earth radiation scattered from the primary optics and passing through the instrument field stop must be controlled and minimized because, unless the scattered radiation is of a sufficiently low amplitude, it may obscure the target energy being received by the detector.

The primary mirror in the instrument is illuminated with direct earth radiation H_{id} and with indirect earth radiation H_{ii} coming from the instrument internal baffle surfaces. The amount of radiant power intercepted by the mirror, then, is given by

$$P_m = (H_{ii} + H_{id}) A_m$$

where

$$A_m = \text{mirror area}$$

UNCLASSIFIED

The radiation incident on the mirror at an angle α scatters according to a scattering coefficient $\delta(\alpha)$, which defines the amplitude and direction of the scattered component. The pinhole receives the scattered energy directed into its field of view as given by

$$P_h = P_m \delta(\alpha) \Omega_h$$

where Ω_h = the solid angle subtended by the pinhole at the primary mirror. Examination of the final equation for the power received at the pinhole

$$P_h = (H_{id} + H_{ii}) A_m \delta(\alpha) \Omega_h$$

shows that the scattered radiation can be minimized by minimizing a number of variables. However, because of the instrument requirements on aperture size, illumination, and field of view, the only variables which can be controlled are H_{ii} and $\delta(\alpha)$. The indirect earth radiation has already been discussed.

The scattering coefficient $\delta(\alpha)$ is the function of wavelength, angle of incidence, and mirror characteristics such as substrate, overcoating, polish, etc. Recent tests with 14 sample flat mirrors provided by the Speedring Corporation of Warren, Michigan, provided the following data:

<u>Material</u>	<u>Percent of Scattering</u>
304 stainless (no coating)	0.14 - 0.53
440 stainless (no coating)	0.4 - 2.0
Beryllium (no coating)	1.35 - 3.2
6061 aluminum (electroless nickel)	0.14 - 0.46
Brass (no coating)	5.7 - 6.4
Brass (electroless nickel)	0.96 - 0.42
Loc-Alloy (electroless nickel)	0.22 - 0.375
Quartz substrate (dielectric mirror)	0.0005

The testing was performed using a helium-neon laser at 6328Å in order to evaluate quantitatively the characteristics of the different materials. The test specimens were polished using the same technique for essentially the same time. The data do not reflect the best polishing effort but do present a basis for relative comparison. In addition, each of the coated samples (electroless nickel) have been representatively submerged into LN₂ for a shock thermal test of coating adhesion with no trace of crazing.

The resulting data were included in the tradeoff to determine the most suitable material for the system reflective optics. (Further discussion of the

UNCLASSIFIED

choice of material for the optics is presented in 4.6.2. It will suffice at this time to state that mirrors made of aluminum substrate with an electroless nickel overcoating have been chosen.)

Scattering Calculations -- The level of earth radiation scattered from the primary mirror and passing through the field stop can be computed on the basis of mirror scattering measurements recently made at Honeywell. Measurements have been made on three full-scale mirrors made of aluminum with an electroless nickel overcoat and polished to a high degree. Both visible (6328Å) and infrared (10.6-micron) measurements were made using HeNe and CO₂ laser sources incident normally on the mirror surface. A (HgCd)Te (IR) detector + photometer (visible) is used to detect radiation scattered in particular directions, and a chopper modulates the laser beam to distinguish signal energy from the ambient background. Figure 73 shows the typical test setup for the measurement. The detector is first calibrated by measuring the energy scattered by a diffuser plate. A barium sulfate diffuser plate is used in the visible, whereas, in the infrared, a sulfur slab was constructed and exhibited excellent diffuser characteristics. Figure 74 illustrates the Lambertian characteristics of the sulfur slab.

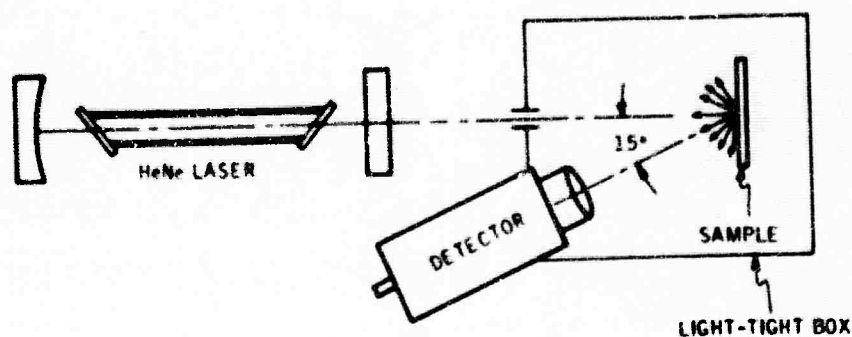


Figure 73.. Light-Scattering Measurement Technique

The illuminated spot is smaller than the detector field of view, and, therefore, with the diffuser in place, the irradiance on the detector is given by

$$H_d = \frac{P_i \rho_d}{\pi r^2} \cos \alpha \text{ (watt/cm}^2\text{)} \quad (2)$$

where

P_i = incident power (watts)

ρ_d = diffuser reflectivity

UNCLASSIFIED

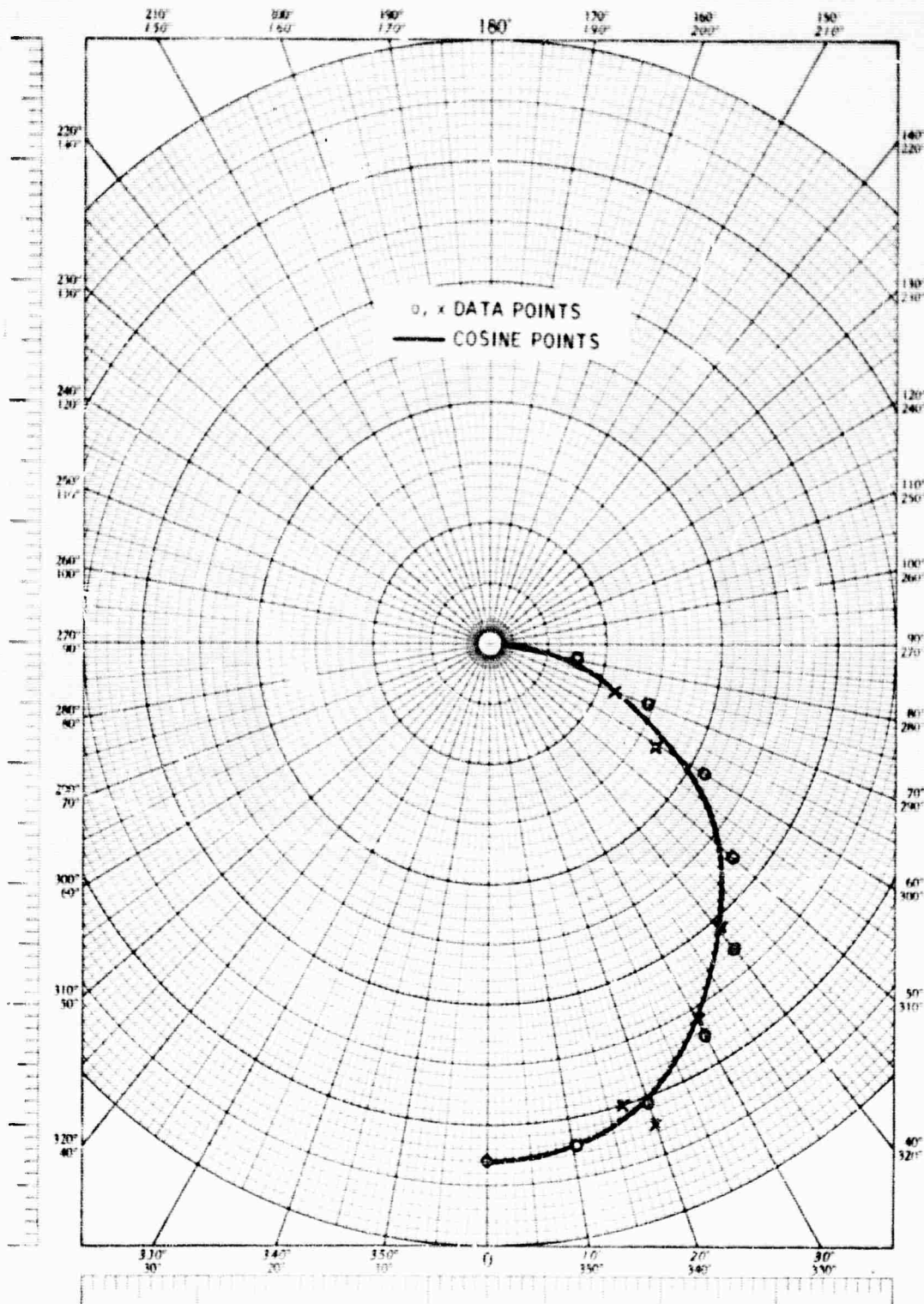


Figure 74. Scatter Characteristics of Sulfur Slab

UNCLASSIFIED

UNCLASSIFIED

α = angle from normal incidence

r = distance from sample to detector

The mirror is a specular reflector and the laser beam is highly collimated. For example, the secondary maxima of the CO₂ laser beam is 10^{-5} of the main beam peak. Therefore, to a first approximation, the intensity at the detector scattered from the mirror sample will be independent of r . The irradiance therefore is given by

$$H_m(\alpha) = \frac{P_i}{A_b} \delta(\alpha) \text{ (watt/cm}^2\text{)} \quad (3)$$

where

A_b = area of illuminated spot

$\delta(\alpha)$ = angular scattering coefficient

Measurements of the primary mirror show that for $\alpha = 15$ deg, the ratio of mirror-scattered intensity to diffuser intensity at 10.6 microns is 10^{-5} . Therefore

$$\frac{H_m(\alpha)}{H_d} = \frac{\pi r^2 \delta(\alpha)}{A_b \rho_d \cos \alpha} = 10^{-5} \quad (4)$$

To apply these measurements to the limb measurement sensor, it is necessary to relate the scattered component to the input flux. The desired quantity is [from equation (3)]

$$\frac{H_m(\alpha)}{H_i} = \delta(\alpha) \quad (5)$$

where

$$H_i = P_i/A_b$$

However, using equation (4)

$$\frac{H_m(\alpha)}{H_i} = \frac{A_b \rho_d \cos \alpha}{\pi r^2} \times 10^{-5} \quad (6)$$

Since $A_b = 7.5 \times 10^{-2} \text{ in.}^2$

$$\rho_d = 0.85$$

UNCLASSIFIED

$$\cos \alpha = 0.966$$

$$r = 4 \text{ in.}$$

Then

$$\frac{H_m(\alpha)}{H_i} = 1.2 \times 10^{-8}$$

In the intended application, earth radiation will directly illuminate the mirror from about 1 deg off-axis to the angle defined by the cotangent of the forebaffle length to diameter ratio. At larger angles off-axis, earth radiation will be absorbed by the interior of the forebaffle before illuminating the primary mirror.

The total irradiance on the mirror is the sum of these two components and, for the 12-micron window region, is estimated under the following conditions:

Temperature of earth = 270°K

Emissivity of earth = 1.0

Minimum baffle angle = 10 deg

Absorptivity of baffle = 0.98 (diffuse)

Spectral bandwidth = 1 micron

Diameter of mirror = 5 in.

Direct illumination within the minimum baffle angle and averaged over the mirror surface can be determined by the sum

$$H_i = \frac{1}{A_t} \sum_{\alpha_1}^{\alpha_2} N \Omega(\alpha) A_m(\alpha)$$

where

N = earth radiance = 6.4×10^{-4} watt/cm²-ster-micron

Ω = incremental solid angle subtended by earth (measured at aperture)

A_m = incremental mirror area

A_t = total mirror area

UNCLASSIFIED

Summing throughout off-axis angles from 0 to 10 deg. yields

$$H_i = 3 \times 10^{-6} \text{ watt/cm}^2$$

Using mirror scattering measurements for $\alpha = 15$ deg, the irradiance at the field stop for direct illumination on the total mirror surface area is

$$H_s = 3 \times 10^{-6} \times 1.2 \times 10^{-8} \times 127 = 4.6 \times 10^{-12} \text{ watts/cm}^2$$

This corresponds to a photon flux of

$$Q_s = 2.8 \times 10^8 \text{ photons/sec-cm}^2$$

This number may be small since the scattering measurements used were for off-axis angles of 15 deg. In the intended application, off-axis angles in the range from 5 to 10 deg contribute the largest fraction of the total direct-scattered component. Measurements yet to be made may show a larger scattering coefficient 5 to 10 deg from the incident beam.

A conservative estimate of the indirect earth radiation reflected from the baffle interior can be made by assuming the baffle is a cylindrical cavity with an effective temperature equal to that of the earth (270°K), and with an emissivity equal to the reflectance of the interior surface. Black paint (such as 3M Black Velvet) will achieve an emissivity on the order of 0.98 with good diffuse reflectance properties.

The radiance of the baffle interior surface is then

$$N_b = 2 \times 10^{-3} \times \frac{1}{\pi} \times 2 \times 10^{-2} = 1.27 \times 10^{-5} \text{ watt/cm}^2\text{-ster}$$

Assuming the entire interior surface of the baffle is illuminated, then the view factor from the mirror is nearly 2π steradians and the irradiance on the mirror will be

$$H_i = 1.27 \times 10^{-5} \times 2\pi = 8 \times 10^{-5} \text{ watt/cm}^2$$

This radiation is incident on the mirror from nearly a full hemisphere and, for the most part, will be reflected off the mirror, outside the detector field of view, to be absorbed by internal baffle surfaces. A small portion, however, will be scattered into the field of view and to compute this quantity, the hemispherical scattering coefficient must be used. For the mirror tested, the hemispherical scattering coefficient is estimated to be 4×10^{-6} .

The scattered component will be distributed throughout a full hemisphere and as a result the radiant intensity for the entire mirror as viewed by the detector will be

UNCLASSIFIED

$$J_m = 8 \times 10^{-5} \times \frac{1}{2\pi} \times 127 \times 4 \times 10^{-6}$$

$$J_m = 6.5 \times 10^{-9} \text{ watt/ster}$$

The focal length of the primary is 31 cm so the irradiance at the field stop is

$$H_s = \frac{6.5 \times 10^{-9}}{(31)^2} = 6.9 \times 10^{-12} \text{ watt/cm}^2$$

This value of flux density at the field stop corresponds to a photon rate of

$$Q_s = 4.1 \times 10^8 \text{ photons/sec-cm}^2$$

The actual photon rate from this source is expected to be somewhat smaller for two reasons, namely:

- The earth does not illuminate the entire interior surface of the baffle.
- The effective emissivity of the baffle interior will be larger than 0.98, due to the presence of numerous knife-edge cavity traps.

Summing the flux from direct-earth illumination with reflected radiation from the baffle interior yields a total photon rate at the field stop of

$$Q_s(\text{total}) = 6.9 \times 10^8 \text{ photons/sec-cm}^2$$

The NEFD requirement translated to flux density at the field stop yields $3.4 \times 10^{-12} \text{ watt/cm}^2$ for a mirror reflectivity of 0.95.

The equivalent noise photon rate is therefore

$$Q_s(\text{NEFD}) = 2 \times 10^8 \text{ photons/sec-cm}^2$$

Based on these calculations, earth radiation scattered from the primary mirror degrades the required signal to noise ratio by a factor of nearly 3.5. In terms of the model radiance/altitude profiles, the scattered component reduces the upper-limit tangent height by about 10% to maintain a signal-to-noise ratio of 10.

UNCLASSIFIED

4.5.2 Baffle Interior Irradiance Analysis

A useful quantity in baffle design is the irradiance from the earth along the top edge of the locus of the interior edges of the baffle plates. From this plot (irradiance on a 1-cm² square versus distance into the baffle tube) the baffle designer can determine an optimal separation and/or arrangement of the plates.

In the analysis of this irradiance function, what is desired is the integrated radiance of the earth source on a square area, the integration being over the solid angle subtended by the source (at a given receiver-square position). In the following analysis, the locus of the interior baffle edges is referred to as a "tube", and the problem is simply that of performing integration on a point receiver with given receiver-source geometry (at each receiver-square position). Tube geometry relative to the earth is shown in Figure 75, the earth-tube system being symmetric about a plane containing the axis of the tube and the center of the earth.

Interior tube irradiance is

$$H_T = \int_{\text{Receiver}} \int_{\text{Source}} \frac{N(\eta_s) \cos \eta_r dA_s}{\rho^2}$$

where

$N(\eta_s)$ = source radiation law

dA_s = elemental source area

dA_r = elemental receiver area

η_s = angle from source normal

η_r = angle from receiver normal

ρ = distance between source and receiver elemental areas

The geometry of this integral is illustrated in Figure 76. The integration is performed within a spherical system centered at the point at which the irradiance is to be determined as shown in Figure 77. Integration over theta (the azimuthal angle) is performed first. Two limit functions $\phi(\theta)$ are necessary, as θ is first determined by the source ($\alpha \leq \theta \leq \phi_1$) and then by the aperture ($\phi_1 \leq \theta \leq \beta$), where $\alpha = 0.5 \text{ deg}$, $\beta = \tan^{-1} (r/l-d)$. These limit functions are shown in 4.5.3 to be

UNCLASSIFIED

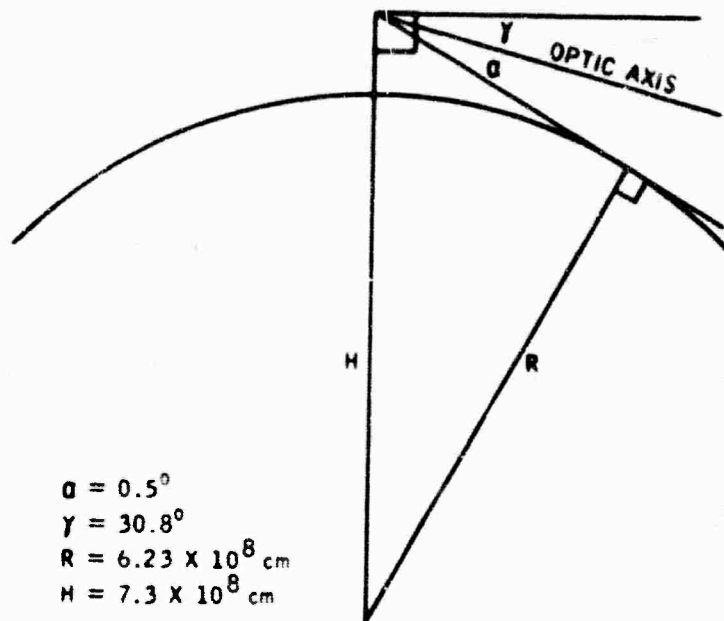


Figure 75. Radiometer Geometry

UNCLASSIFIED

UNCLASSIFIED

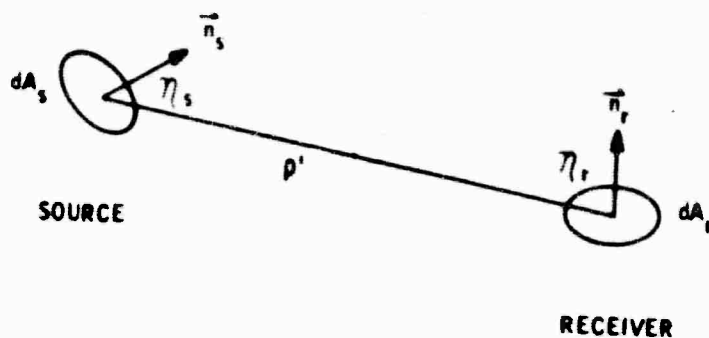


Figure 76. Transfer Geometry

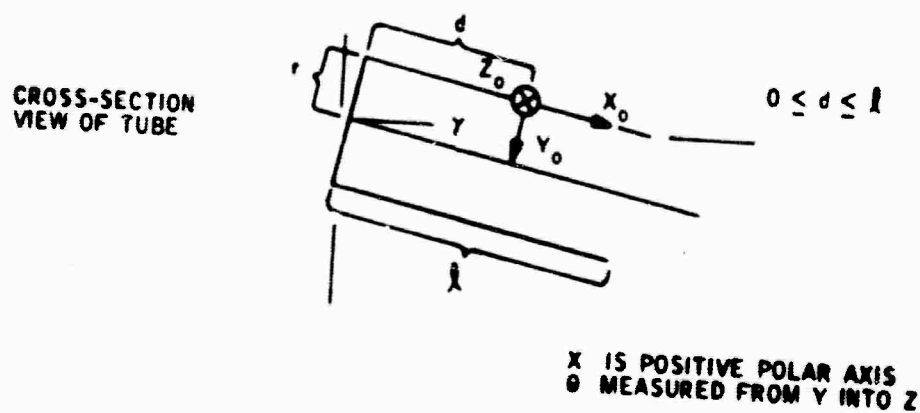


Figure 77. Receiver-Point Coordinate System

UNCLASSIFIED

UNCLASSIFIED

$$\theta_s(\phi, d) = \cos^{-1} \left[\frac{\sin(\gamma + \alpha) - \sin \gamma \cos \phi}{\cos \gamma \sin \phi} \right]$$

$$\theta_A(\phi, d) = \cos^{-1} \left[\frac{(L-d) \tan \phi}{2r} \right],$$

where $\theta_s(\phi, d)$ and $\theta_A(\phi, d)$ are the sphere and aperture limit functions, respectively. Irradiance is therefore

$$H_T(d) = \int_{\alpha}^{\phi_i} \int_{-\theta_s(\phi, d)}^{+\theta_s(\phi, d)} \frac{N(\eta_s) \cos \eta_r dA_s}{\rho^2} + \int_{\phi_i}^{\beta} \int_{-\theta_A(\phi, d)}^{+\theta_A(\phi, d)} \frac{N(\eta_s) \cos \eta_r dA_s}{\rho^2},$$

where ϕ_i is that polar angle determined by the intersection of the limit functions; ϕ_i is shown in 4.5.3 to be

$$\phi_i = \cos^{-1} \left[\frac{r \sin(\gamma + \alpha) - [r^2 \sin^2(\gamma + \alpha) - [2r \sin \gamma - (L-d) \cos \gamma] (L-d) \cos \gamma]^{1/2}}{2r \sin \gamma - (L-d) \cos \gamma} \right]$$

By symmetry and source projection considerations shown in Figure 78, we have (assuming Lambertian radiation)

$$H_T = 2N_s \int_{\alpha}^{\phi_i} \int_0^{\theta_s(\phi, d)} \frac{\rho^2 \sin \phi d\phi d\theta}{\cos \eta_s} \cos \eta_r \cos \eta_s + 2N_s \int_{\phi_i}^{\beta} \int_0^{\theta_A(\phi, d)} \frac{\rho^2 \sin \phi d\phi d\theta}{\cos \eta_s} \cos \eta_r \cos \eta_s$$

UNCLASSIFIED

dA_s = ELEMENTAL SOURCE AREA

dA_c = ELEMENTAL COORDINATE SYSTEM AREA

η_s = PROJECTION ANGLE

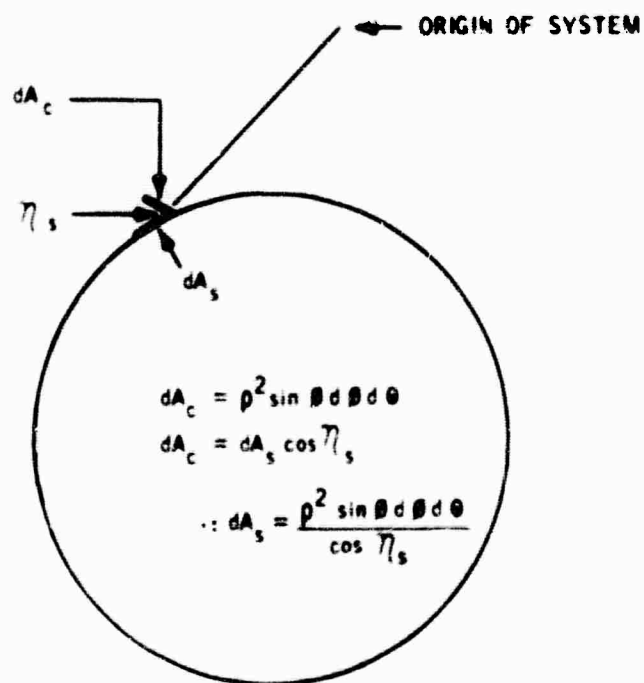


Figure 78. Angular Dense Considerations

UNCLASSIFIED

UNCLASSIFIED

where $N(\varphi_s) = N_s \cos \varphi_s$. Realizing $\cos \varphi_r = \sin \varphi \cos \theta$

$$H_T = 2N_s \left\{ \int_{\alpha}^{\beta} \int_0^{\theta_s(\varphi, d)} \sin^2 \varphi \cos \theta \, d\theta \, d\varphi + \int_{\varphi_i}^{\beta} \int_0^{\theta_A(\varphi, d)} \sin^2 \varphi \cos \theta \, d\theta \, d\varphi \right\}$$

Integrating first over theta

$$H_T = 2N_s \left\{ \int_{\alpha}^{\beta} \sin^2 \varphi \sin [\theta_s(\varphi, d)] \, d\varphi + \int_{\varphi_i}^{\beta} \sin^2 \varphi \sin [\theta_A(\varphi, d)] \, d\varphi \right\}$$

This transcendental integration was done by computer with inputs being earth-tube geometry and radiance level of the source (300°K blackbody).

4.5.3 Integral Limit Functions

The integral limit functions are found by expressing the source (a sphere) and the receiver (a cylinder) in terms of the system shown in Figure 77. Coordinate transformations involved are shown in Figure 79 and are

$$x' = x_0 + d$$

$$y' = y_0 - r$$

$$z' = z_0$$

$$x = x' \cos \gamma - y' \sin \gamma$$

$$y = x' \sin \gamma + y' \cos \gamma$$

$$z = z'$$

UNCLASSIFIED

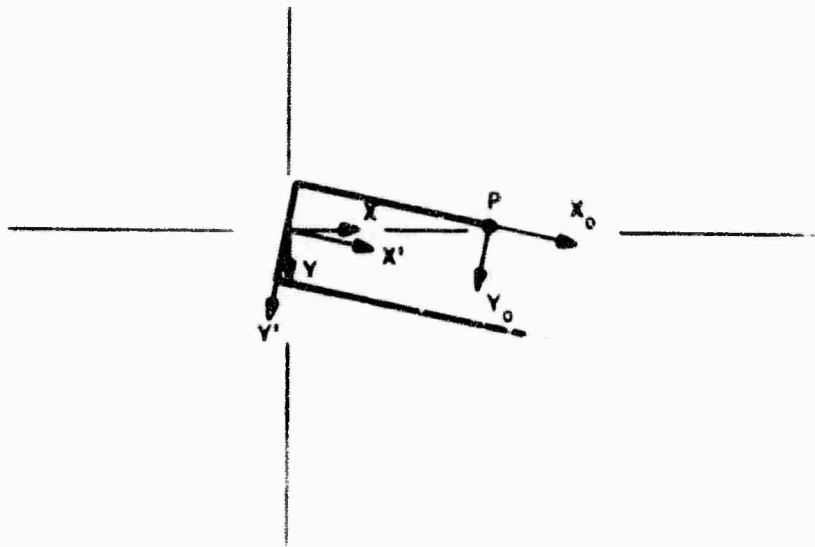


Figure 79. Coordinate Transformations

The aperture expression is

$$y'^2 + z'^2 = r^2$$

$$x' = l$$

while the sphere may be expressed as

$$x^2 + (y - H)^2 + z^2 = R^2$$

In terms of the spherical system,

$$y_0 = \rho \sin \phi \cos \theta$$

$$z_0 = \rho \sin \phi \sin \theta$$

$$x_0 = \rho \cos \phi$$

they are, respectively

$$(\rho \sin \phi \cos \theta - r)^2 + (\rho \sin \phi \sin \theta)^2 = r^2$$

$$\rho \cos \phi + d = l$$

UNCLASSIFIED

UNCLASSIFIED

$$\begin{aligned}
 &[(\rho \cos \phi + d) \cos \gamma - (\rho \sin \phi \cos \theta - r) \sin \gamma]^2 \\
 &+ \\
 &[(\rho \cos \phi + d) \sin \gamma + (\rho \sin \phi \cos \theta - r) \cos \gamma - H]^2 \\
 &+ \\
 &(\rho \sin \phi \sin \theta)^2 = R^2
 \end{aligned}$$

Eliminating ρ from the aperture function yields

$$\cos \theta = \frac{(l-d) \tan \phi}{2r}$$

while recognizing that $\rho = \sqrt{H^2 - R^2}$ is true for all points on the sphere locus, its limit function becomes

$$\begin{aligned}
 &\rho_i^2 + 2\rho_i d \cos \phi + d^2 - 2\rho_i r \cos \theta \sin \phi + r^2 + H^2 \\
 &- 2H [(\rho_i \cos \phi + d) \sin \gamma + (\rho_i \sin \phi \cos \theta - r) \cos \gamma] = R^2
 \end{aligned}$$

where

$$\rho_i = \sqrt{H^2 - R^2}$$

Solving for $\cos \theta$, and recognizing

$$\frac{\sqrt{H^2 - R^2}}{H} = \sin(\gamma + \alpha)$$

the above expression becomes

$$\cos \theta = \frac{\sin(\gamma + \alpha) - \sin \gamma \cos \phi}{\cos \gamma \sin \phi}$$

Equating the $\cos \theta$ expressions produces the ϕ of intersection of the limit functions, ϕ_i . A quadratic results, which is solved for $\cos \phi_i$, namely

$$\begin{aligned}
 &[2r \sin \gamma - (l-d) \cos \gamma] \cos^2 \phi_i - 2r \sin(\gamma + \alpha) \cos \phi_i \\
 &+ (l-d) \cos \gamma = 0
 \end{aligned}$$

This yields the aforementioned expression for ϕ_i . The computer program used for irradiance calculation is shown in Figure 80 and the plots themselves are shown in Figures 81 through 85.

UNCLASSIFIED

UNCLASSIFIED

```

5 PRINT "I", "IRRADI"
10 F1=40/12(1)
20 C1=30.14/180(1)
30 A1=.5/180(1)
40 J=5.0E
50 B1=50.5
60 K=2.4E-3
61 T=A1
62 DEF F1(C1)=C1*(C1+A1)-SIN(C1)*COS(C1)/(COS(C1)*SIN(C1))
64 DEF F2(C1)=A1*(COS(C1)-F1(C1))/2/F1(C1)
66 DEF F3(C1)=(C1-B1)*TAN(C1)/(2*B1)
68 DEF F4(C1)=A1*(SIN(C1)-F3(C1)*F1(C1))/F1(C1)
70 FOR B1=10 TO 11-.0001 STEP .5
80 B1=A1*(2+17(C1-B1))
90 F=F1(SIN(C1+A1))
100 G=50*(C1+2+SIN(C1+A1))-2*(2+B1*SIN(C1))-(C1-B1)*COS(C1):
110 H=(C1-B1)*COS(C1)
110 F=2*B1*SIN(C1)-(C1-B1)*COS(C1)
120 I=(F-G)/H
130 J=A1*(SIN(C1)-I)/I
200 DEF F5(C1)=F1(C1)+F2(C1)+F3(C1)
210 S1=C
220 I2=(J-A1)/F1
230 S1=F1(A1)+I2
240 FOR T=A1+10 TO J STEP 2*F2
250 S1=S1+4*F5(C1)+2*F5(C1+D2)/INT(C1+(1+3+.2/2)/J)
260 NEXT T
300 DEF F6(C1)=F1(C1)*SIN(F6(C1))
310 I2=A1
320 F3=C1-J/I
330 F3=F3+I2
340 FOR T=J+10 TO B1 STEP 2*F2
350 I2=F3+4*F5(C1)+2*F5(C1+D3)/INT(C1+(1+3+.2/2)/J)
360 NEXT T
375 PRINT
380 NEXT D
390 END

```

Figure 80. Irradiance Calculation Computer Program

UNCLASSIFIED

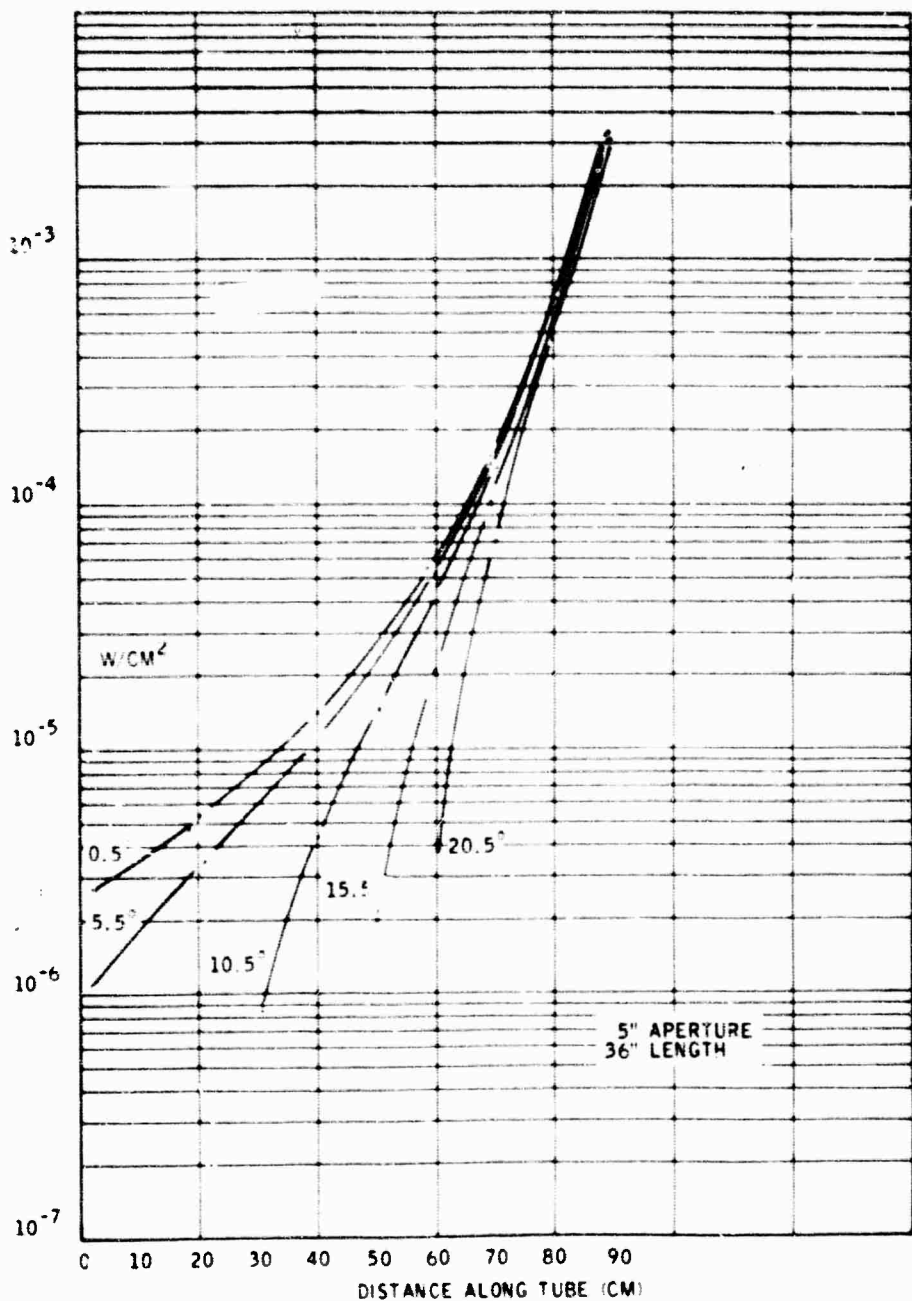


Figure 81. Irradiance Along Top Edge of Tube as a Function of Tilt Angle - 5.0-inch Aperture, 36-inch Length

UNCLASSIFIED

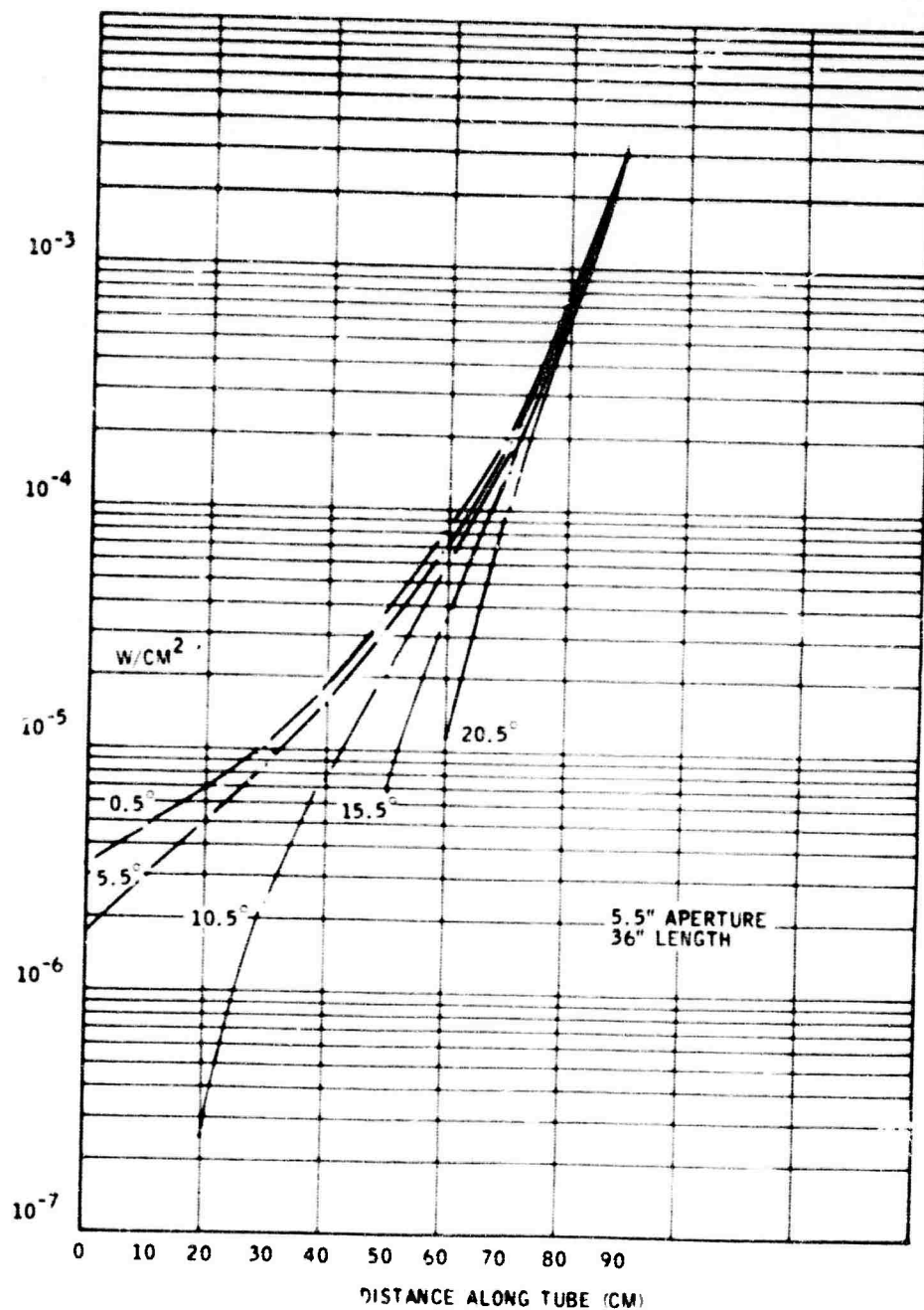


Figure 82. Irradiance Along Top Edge of Tube as a Function of Tilt Angle - 5.5-inch Aperture, 36-inch Length

UNCLASSIFIED

UNCLASSIFIED

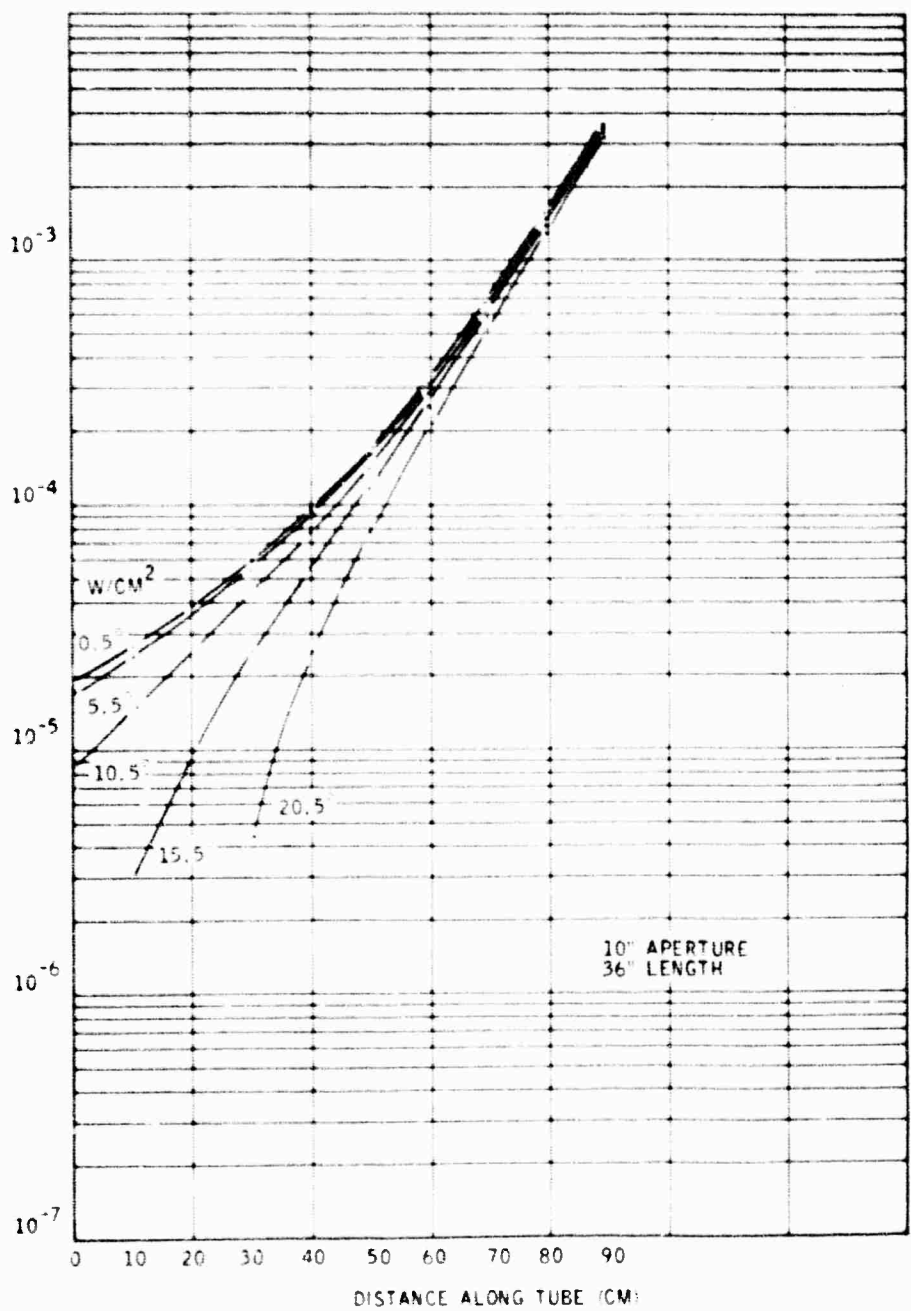


Figure 83. Irradiance Along Top Edge of Tube as a Function of Tilt Angle - 10-inch Aperture, 36-inch Length

UNCLASSIFIED

UNCLASSIFIED

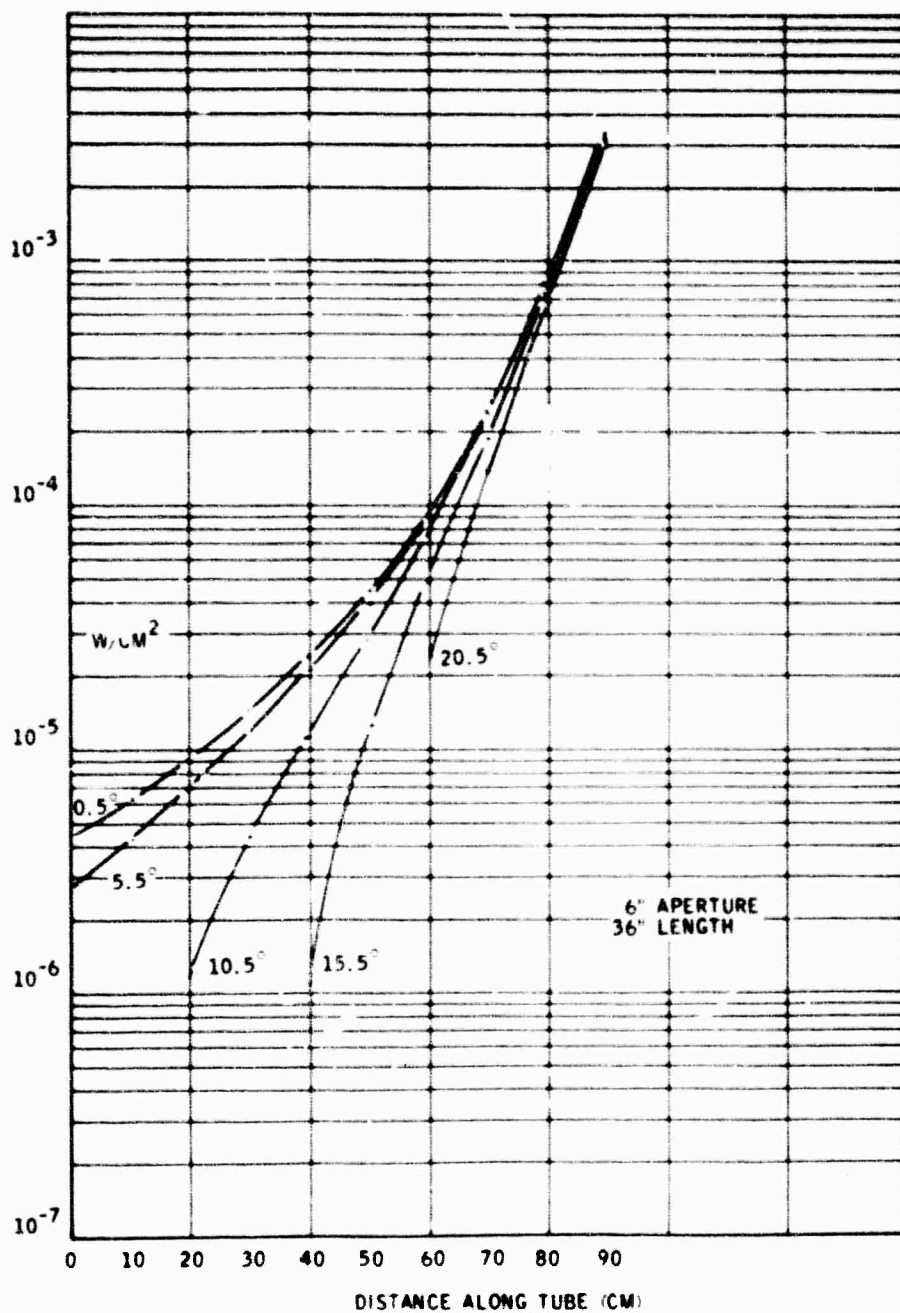


Figure 84. Irradiance Along Top Edge of Tube as a Function of Tilt Angle - 6-inch Aperture, 36-inch Length

UNCLASSIFIED

UNCLASSIFIED

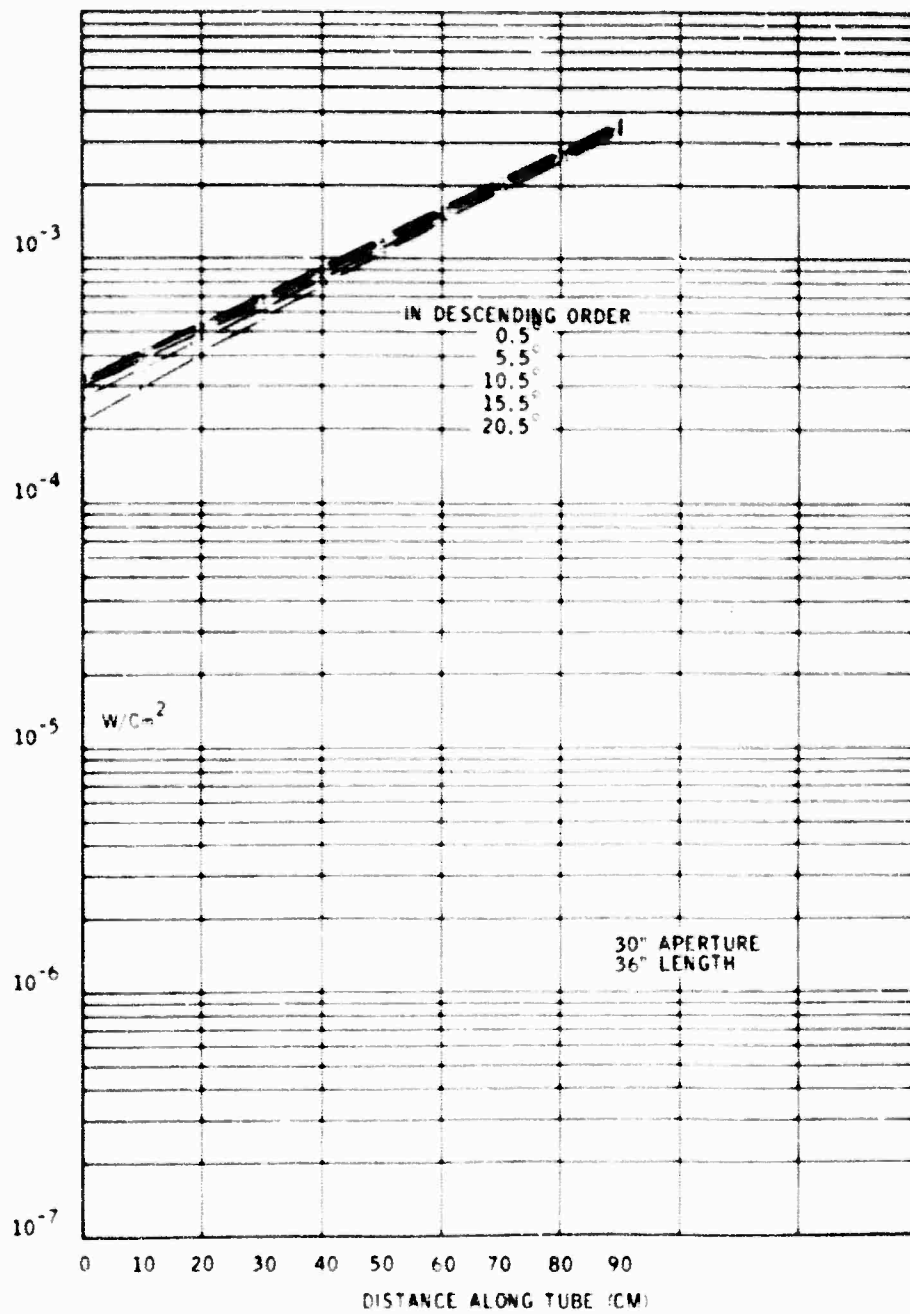


Figure 85. Irradiance Along Top Edge of Tube as a Function of Tilt Angle - 30-inch Aperture, 36-inch Length

UNCLASSIFIED

UNCLASSIFIED

4.6 PARAMETRIC ANALYSIS

The parameters of the proposed spectral radiometer have been generated by analyzing the radiometric inputs and deriving a noise-in-signal-limited signal-to-noise ratio and calculating this S/N for various tangent heights in the selected spectral regions.

4.6.1 Radiometric Input

The radiance levels from the background are derived from the choice of spectral bands, the selected target radiance, and the effects of tangent heights on the radiance level from the background.

Spectral Bands -- Starting with the atmospheric constituents the spectral bands listed in Table 19 were suggested. These bands were then re-evaluated in terms of S/N of the system and detector size using diffraction gratings to spectrally split the radiance. The spectral regions selected as a result of the re-evaluation are listed in Table 19 under proposed wavelength regions. These spectral bands require two diffraction gratings and one beam splitter or, alternatively, one flat mirror. The first grating goes from 4.5 microns to 9.3 microns with a resolution range of 0.2 micron to 0.7 micron which gives a detector aspect ratio change of 3-1/2. The second grating goes from 9.3 to 18 microns with a resolution of 0.3 micron to 1.0 micron which gives a detector aspect ratio change of 3-1/3. Finally the 15- to 25-micron region is achieved using a beamsplitter or a single mirror, and a filter on the detector. Present plans include an optimization of the spectral bands to maximize the energy in each band yet preserve spectral information.

Radiance Levels -- The radiance levels which must be detected with a S/N equal to 10/1 minimum in each spectral region are shown in Figure 86. The radiance values shown for each spectral band correspond to different tangent heights.

Tangent-Height-Effects -- The radiance variation as a function of tangent height for a night limb profile is shown in Figures A1 through A18 of Appendix A. These curves were generated from data produced by GCA under a study entitled "Infrared Radiant Background Studies in the 5 to 25 Micrometer Region." Notice on the curves the variations in tangent heights for the radiance levels contained in Figure 86.

4.6.2 S/N Consideration When Noise in Signal Cannot be Ignored

Figures of merit such as D^* , NEP, NER, NEFD, NET, etc., are useful quantities for the great majority of infrared applications. However, they all ignore noise in signal which predominates in cold-body problems. Therefore, the above figures of merit are of limited usefulness, and care must also be taken with the use of the concept of S/N as will now be shown.

UNCLASSIFIED

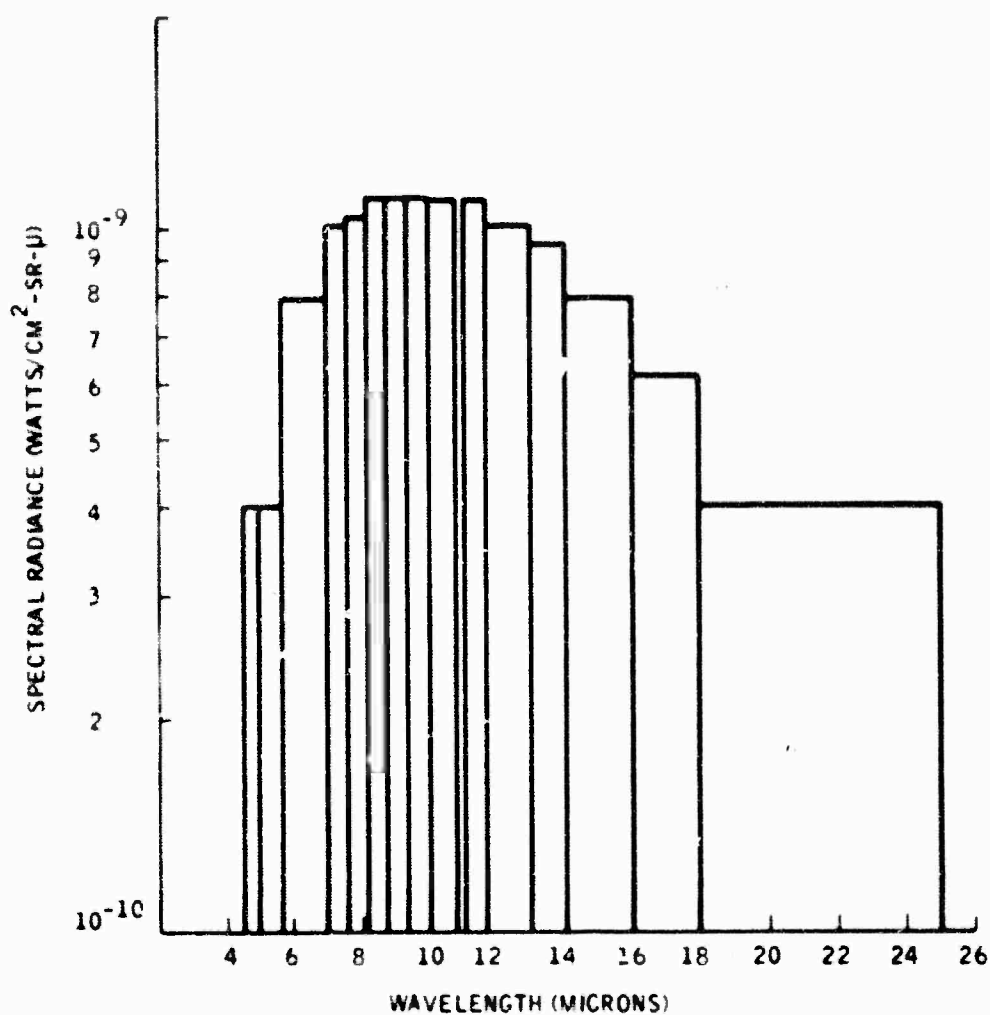


Figure 86. Target-Equivalent Spectral Radiance versus Wavelength Band

UNCLASSIFIED

UNCLASSIFIED

The effective signal is defined by

$$S = \eta_g P_s \tau_o \quad (7)$$

where η_g is quantum efficiency, P_s is peak signal power, and τ_o is optical efficiency.

Photon-Noise-Limited Case -- The mean number of photons in one dwell time \bar{n}_p is

$$\bar{n}_p = \frac{\eta_g (\tau_o P_s + P_B) t_D}{h \nu} \quad (8)$$

where P_B is the background power incident upon detector and t_D is the system dwell time. For noncarrier systems

$$t_D = \frac{1}{2\Delta f} \quad (9)$$

where Δf is the 3-db baseband bandwidth (not the noise equivalent bandwidth).

Therefore

$$\bar{n}_p = \frac{\eta_g (\tau_o P_s + P_B)}{2h\nu\Delta f} \quad (10)$$

and the rms variation in \bar{n}_p is

$$\sigma = \sqrt{\frac{(\tau_o P_s + P_B) \eta_g}{2h\nu\Delta f}} \quad (11)$$

which yields a S/N (for probability of detection) of

$$S/N = \frac{\bar{n}_{ps}}{\sqrt{\bar{n}_p}} = \frac{P_s \tau_o}{\sqrt{2h\nu\Delta f (\tau_o P_s + P_B) \eta_g^{-1}}} \quad (12)$$

incident on detector. For photoconductive detectors the output noise power is double the generation noise due to recombination. Therefore, the output peak signal to rms noise voltage ratio referred to input power is given by

$$S/N = \frac{P_s \tau_o}{\sqrt{4h\nu\Delta f (\tau_o P_s + P_B) \eta_g^{-1}}} \quad (13)$$

ignoring internal detector noise.

UNCLASSIFIED

Internal Detector Noise Contribution -- The rms internal detector noise voltage per root cycle at the output, v_d , can be referred to the input power by responsivity as

$$P_d = \frac{v_d \sqrt{\Delta f_n}}{R} \quad (14)$$

where R is the detector responsivity, and v_d is the spectral voltage density. It is readily apparent from equation (13) that the photon rms noise voltage at the output of detector, v_g is given

$$v_g = R \sqrt{4h\nu \Delta f (\tau_o P_s + P_B) \tau_g} \quad (15)$$

and the total noise is given by

$$v_T = \sqrt{v_g^2 + v_d^2} = R \left[4h\nu (\tau_o P_s + P_B) \tau_g + \frac{\pi v_d^2}{2R^2} \right]^{\frac{1}{2}} \sqrt{\Delta f} \quad (16)$$

where use was made of

$$\Delta f_n = \frac{\pi}{2} \Delta f$$

for 6-dB/octave rolloff. Referring v_T to input power by dividing by R and substituting in equation (13) in place of the photon noise yields

$$S/N = \frac{P_s \tau_g \tau_o}{\sqrt{\left[4h\nu (\tau_o P_s + P_B) \tau_g + \frac{\pi v_d^2}{2R^2} \right] \Delta f}} \quad (17)$$

However, the responsivity can be written

$$R = r (P_s + P_B)^{-1}$$

UNCLASSIFIED

for BLIP detectors yielding

$$S/N = \frac{P_s \tau_g \tau_o}{\sqrt{\left[4h\nu (\tau_o P_s + P_B)^2 \tau_g + \frac{\tau_d^2}{2 r^2} (\tau_o P_s + P_B)^2 \right] \Delta f}} \quad (18)$$

If ν_d is thermal noise it will also be proportional to $(P_s + P_B)^{-1/2}$. However, the limiting noise may be preamplifier noise which will be a complicated function of $(P_s + P_B)$ since the detector resistance changes inversely with $(P_s + P_B)$ in BLIP detectors. The relative contribution of $1/f$ noise may vary with $(P_s + P_B)$ since the crossover frequency will vary. Therefore, for a first approximation the detector noise voltage ν_d will be assumed to vary as $(P_s + P_B)^{-1/2}$ (thermal noise limited) or

$$\nu_d = u_d (P_s + P_B)^{-1/2} \tau_g^{-1/2}$$

and

$$S/N = \frac{P_s \tau_s}{\sqrt{(4h\nu + k_d) (\tau_o P_s + P_B) \Delta f \tau_g^{-1}}} \quad (19)$$

where

$$k_d = \frac{\tau_d^2}{2 r^2} \text{ (watts/Hz) and } \tau_s = \tau_o \tau_e$$

with τ_e the electronic efficiency and τ_s the system efficiency.

These are two possible definitions for the noise equivalent power (NEP) of a system which are: (a) that power incident upon a detector which gives rise to a peak-signal-voltage-to-rms-noise-voltage ratio at the output of unity, and (b) the NEP is the incident power divided by the measured peak-signal-voltage-to-rms-voltage ratio due to the incident power. Both definitions yield the same result as long as the noise is independent of incident signal power, i.e., $P_B \gg P_s$.

From equation (19) the NEP as defined in (b) yields

UNCLASSIFIED

$$NEP = \sqrt{(4h\nu + k_d) (\tau_o P_s + P_B) \Delta f \tau_g^{-1} (\tau_s)^{-1}} \quad (20)$$

whereas the NEP defined in(a) is given by

$$NEP = \frac{(4h\nu + k_d) \Delta f}{\tau_e^2 \tau_g \tau_o} \left\{ \frac{1}{2} \left[1 + \sqrt{1 + \frac{4 P_B \tau_g \tau_e^2}{(4h\nu + k_d) \Delta f}} \right] \right\} \quad (21)$$

and it can be seen that in the limiting cases of

$$h\nu \gg k_d \text{ and } h\nu \gg P_B$$

$$NEP \gg \frac{4h\nu \Delta f}{\tau_e^2 \tau_g \tau_o} \quad (22)$$

$$P_B \gg k_d \Delta f \text{ and } P_B \gg h\nu \Delta f$$

$$NEP \gg \sqrt{\frac{4h\nu P_B \Delta f \tau_g^{-1} \tau_o^{-1}}{\tau_e}} \quad (23)$$

and

$$k_d \gg h\nu \text{ and } k_d \Delta f \gg P_B$$

$$NEP \gg \frac{k_d \Delta f}{\tau_g} \quad (24)$$

which are the appropriate limits.

Whereas equation (20) yields the limits

$$h\nu \gg k_d \text{ and } h\nu \Delta f \gg P_B$$

$$NEP \gg \sqrt{\frac{4h\nu \tau_o P_s \Delta f \tau_g^{-1}}{\tau_s}}$$

which in the limit $P_s \rightarrow 0$ becomes $NEP \rightarrow 0$

UNCLASSIFIED

$$P_B \gg k_d \Delta f \text{ and } P_B \gg h\nu \Delta f$$

$$NEP \gg \frac{\sqrt{4h\nu P_B \Delta f \tau_g^{-1}}}{\tau_s}$$

There is no limiting condition for

$$k_d \Delta f \gg P_s \text{ and } k_d \Delta f \gg P_B$$

which is independent of P_B and P_s .

Therefore, the correct definition for NEP is (a) above as expressed in equation (20) and yields an NEP independent of signal level. With this definition of NEP the peak-signal-voltage-to-rms-noise-voltage ratio is given by

$$S/N = \sqrt{\frac{P_s}{NEP}} \left[\frac{1 + \sqrt{1 + \frac{P_B}{(4h\nu + k_d) \Delta f}}}{1 + \sqrt{1 + \frac{\tau_e^2 P_B}{(S/N)^2 (4h\nu + k_d) \Delta f}}} \right]^{1/2} \quad (25)$$

which represents a quartic equation for S/N . Equation (19) is the proper equation to compute S/N with ease. Equation (25) illustrates the fact that the concept of NEP is not very useful except under the limiting conditions

$$P_B \gg (4h\nu + k_d) \Delta f$$

which yields

$$S/N = \frac{\tau_s P_s}{NEP}$$

UNCLASSIFIED

UNCLASSIFIED

and

$$P_B \ll (4h\nu + k_d) \Delta f$$

which yields

$$S/N = \tau_e \sqrt{\frac{\tau_o P_s}{NEP}}$$

All the other noise equivalent system parameters such as NER, NEFD, NET, etc., are directly related to NEP by system parameters. Therefore, the above comments concerning NEP apply to them equally well.

Probability of Detection and False-Alarm Rate -- In the above derivation for S/N, the noise was computed with signal present and is directly applicable to probability of detection of the signal. However, the S/N to be used for determination of false-alarm rate requires the calculation of the noise in the absence of signal. Hence, the two S/N

$$(S/N)_{pd} = \frac{\tau_e P_s}{\sqrt{(4h\nu + k_d) (P_s + P_B) \Delta f \tau_g^{-1}}}$$

and

$$(S/N)_{fa} = \frac{\tau_e P_s}{\sqrt{(4h\nu + k_d) P_B \Delta f \tau_g^{-1}}}$$

are equal only in the limit $P_s/P_B \gg 0$.

Detection mechanisms and a detailed comparison between germanium and HgCd, Te detectors are found in section 4.3.

UNCLASSIFIED

4.6.3 System Tradeoff

Starting with equation (19) in section 4.6.2

$$S/N = \frac{P_s \tau_s}{\sqrt{(4h\nu + K_d) (\tau_o P_s + P_B) \Delta f \tau_g^{-1}}} \quad (19)$$

and using the assumption that the internal detector noise is negligible ($4h\nu \gg K_d$) and the expression for D^*_λ of a photoconductive detector is

$$D^*_\lambda = \frac{1}{2h\nu} \sqrt{\frac{q}{\tau_o J_s + J_B}} \quad (26)$$

where J_s is the signal photon flux and J_B is the background photon flux. An expression for S/N in terms of D^*_λ can be determined, viz

$$S/N = \frac{\tau_s P_s D^*_\lambda}{\sqrt{(\Delta f) A_d}} \quad (27)$$

where A_d is the detector area.

While equation (27) is correct for the noise-in-the-signal-limited case it cannot be scaled directly since the D^*_λ is also a function of P_s . Therefore, this expression was used to determine the S/N for a particular P_s and scaling is performed by the expression

$$S/N = \sqrt{P_s} \quad (28)$$

To analyze the system, equation (27) must be evaluated.

The system efficiency τ_s is composed of the chopping efficiency preamplifier noise and other system τ_s losses not including optics.

The power from the instantaneous field of view falling on the detector P_s is equal to

$$P_s = N_\lambda \Delta\lambda \tau_o A_o \quad (29)$$

UNCLASSIFIED

where

N_λ = radiance from target (watt/cm²-ster-micron)

Ω = solid instantaneous field of view (ster)

$\Delta\lambda$ = spectral bandwidth (microns)

τ_o = optical transmission (percent)

A_o = area of entrance pupil (cm²)

The D^* term is defined by equation (26). Thus substituting equations (28) and (26) into equation (27) gives

$$S/N = \frac{\eta_s (N_\lambda \Omega \Delta\lambda \tau_o A_o) \eta_g^{1/2}}{2h\nu \left[\Delta f A_d (\tau_o J_s + J_B) \right]^{1/2}} \quad (30)$$

Equation (30) can now be evaluated using the following system parameters:

η_s = η/τ_o = 0.1/ τ_o (see Table 20)

N_λ = See Appendix A

Ω = 1.5 mr (horizontal) by 0.5 mr (vert)

$\Delta\lambda$ = See Table 20

τ_o = See Table 20

A_o = 5 in. diameter, f/3

η_g = 50% for (Hg,Cd)Te = 15% for doped germanium

V = C/λ

C = 2.998×10^{14} micron/sec

λ = 4.5 to 25 microns

Δf = 6.77 Hz

A_d = 22.5 by 7.5 mils

J_s = $P_s/h\nu$ (see Appendix A)

J_B = Negligible $J_s \gg J_B$

Table 20. System Losses

Signal Band (msec)	Primary Mirror		Mirror No. 2		Mirror No. 3		Mirror No. 4		Total Optical Transmission	Signal Losses (msec)
	0.0%	0.9%	0.0%	0.1%	0.0%	0.1%	0.0%	0.1%		
1.5-3.0	0.00	0.00	0.00	0.00	0.00	0.00	0.00	0.00	0.00	0.00
3.0-5.7	0.00	0.00	0.00	0.00	0.00	0.00	0.00	0.00	0.00	0.00
5.7-9.4	0.00	0.00	0.00	0.00	0.00	0.00	0.00	0.00	0.00	0.00
9.4-12.0	0.00	0.00	0.00	0.00	0.00	0.00	0.00	0.00	0.00	0.00
12.0-14.6	0.00	0.00	0.00	0.00	0.00	0.00	0.00	0.00	0.00	0.00
14.6-17.2	0.00	0.00	0.00	0.00	0.00	0.00	0.00	0.00	0.00	0.00
17.2-19.8	0.00	0.00	0.00	0.00	0.00	0.00	0.00	0.00	0.00	0.00
19.8-22.4	0.00	0.00	0.00	0.00	0.00	0.00	0.00	0.00	0.00	0.00
22.4-25.0	0.00	0.00	0.00	0.00	0.00	0.00	0.00	0.00	0.00	0.00
25.0-27.6	0.00	0.00	0.00	0.00	0.00	0.00	0.00	0.00	0.00	0.00
27.6-30.2	0.00	0.00	0.00	0.00	0.00	0.00	0.00	0.00	0.00	0.00
30.2-32.8	0.00	0.00	0.00	0.00	0.00	0.00	0.00	0.00	0.00	0.00
32.8-35.4	0.00	0.00	0.00	0.00	0.00	0.00	0.00	0.00	0.00	0.00
35.4-38.0	0.00	0.00	0.00	0.00	0.00	0.00	0.00	0.00	0.00	0.00
38.0-40.6	0.00	0.00	0.00	0.00	0.00	0.00	0.00	0.00	0.00	0.00
40.6-43.2	0.00	0.00	0.00	0.00	0.00	0.00	0.00	0.00	0.00	0.00
43.2-45.8	0.00	0.00	0.00	0.00	0.00	0.00	0.00	0.00	0.00	0.00
45.8-48.4	0.00	0.00	0.00	0.00	0.00	0.00	0.00	0.00	0.00	0.00
48.4-51.0	0.00	0.00	0.00	0.00	0.00	0.00	0.00	0.00	0.00	0.00
51.0-53.6	0.00	0.00	0.00	0.00	0.00	0.00	0.00	0.00	0.00	0.00
53.6-56.2	0.00	0.00	0.00	0.00	0.00	0.00	0.00	0.00	0.00	0.00
56.2-58.8	0.00	0.00	0.00	0.00	0.00	0.00	0.00	0.00	0.00	0.00
58.8-61.4	0.00	0.00	0.00	0.00	0.00	0.00	0.00	0.00	0.00	0.00
61.4-64.0	0.00	0.00	0.00	0.00	0.00	0.00	0.00	0.00	0.00	0.00
64.0-66.6	0.00	0.00	0.00	0.00	0.00	0.00	0.00	0.00	0.00	0.00
66.6-69.2	0.00	0.00	0.00	0.00	0.00	0.00	0.00	0.00	0.00	0.00
69.2-71.8	0.00	0.00	0.00	0.00	0.00	0.00	0.00	0.00	0.00	0.00
71.8-74.4	0.00	0.00	0.00	0.00	0.00	0.00	0.00	0.00	0.00	0.00
74.4-77.0	0.00	0.00	0.00	0.00	0.00	0.00	0.00	0.00	0.00	0.00
77.0-79.6	0.00	0.00	0.00	0.00	0.00	0.00	0.00	0.00	0.00	0.00
79.6-82.2	0.00	0.00	0.00	0.00	0.00	0.00	0.00	0.00	0.00	0.00
82.2-84.8	0.00	0.00	0.00	0.00	0.00	0.00	0.00	0.00	0.00	0.00
84.8-87.4	0.00	0.00	0.00	0.00	0.00	0.00	0.00	0.00	0.00	0.00
87.4-90.0	0.00	0.00	0.00	0.00	0.00	0.00	0.00	0.00	0.00	0.00
90.0-92.6	0.00	0.00	0.00	0.00	0.00	0.00	0.00	0.00	0.00	0.00
92.6-95.2	0.00	0.00	0.00	0.00	0.00	0.00	0.00	0.00	0.00	0.00
95.2-97.8	0.00	0.00	0.00	0.00	0.00	0.00	0.00	0.00	0.00	0.00
97.8-100.0	0.00	0.00	0.00	0.00	0.00	0.00	0.00	0.00	0.00	0.00

UNCLASSIFIED

Figure 87 shows the solution to equation (30) for the required radiance values. Notice in the figure that only the 4.5- to 5.0 micron band has a S/N=10; the rest of the bands exceed this requirement. Some system tradeoff factors exist with which to optimize sensor design. For example, the aperture diameter is set by the size of the vehicle and the baffling technique. The width of the spectral bands are set by the aspect ratio of the detector and the monochromator design. Thus, the only variables which can be traded are the bandwidth (Δf) and the resolution. Of these two parameters, the more important seems to be the bandwidth. The present design scans at a rate of 13.45 resolution elements per second ($13.45 \times 5 \times 10^{-4} \text{ rad}^2 = 6.725 \text{ milli-radians/sec}$). A faster scan time may be desired, and the scaling of the S/N with bandwidth is as follows:

$$\left(\frac{S}{N}\right)_{\text{new}} = \left(\frac{S}{N}\right)_{\text{orig}} \sqrt{\frac{\Delta f_{\text{orig}}}{\Delta f_{\text{new}}}}$$

Appendix A shows the S/N as a function of tangent height for all spectral bands except the 4.5- to 5.0-micron band. These curves were generated using only the 60-, 90 and 115-km tangent heights and the required radiance level (denoted on the figures by a "d"). The curves show that when measuring the limb of the earth the S/N exceeds a value of 10/1 from tangent heights of from 60 km to an average of about 100 km.

4.7 OPTICAL DESIGN

4.7.1 General Design

The optical design is based primarily on the need for extreme attenuation of unwanted earth radiation when the earth is close to the optical axis. Thus there is a requirement for baffling specially designed for this particular application. Furthermore, the choice of configuration and material is governed primarily by the requirement for low scattering.

In the case of the optical system, the objective system is of major importance in achieving an acceptable background level. For this reason, a single element which minimizes surface defects is selected as the objective system. The narrow field requirement of 1.5 mr x 0.5 mr is compatible with this approach. The objective element is a parabolic reflector offset from its optical axis to avoid interference of the primary image and the incoming radiation.

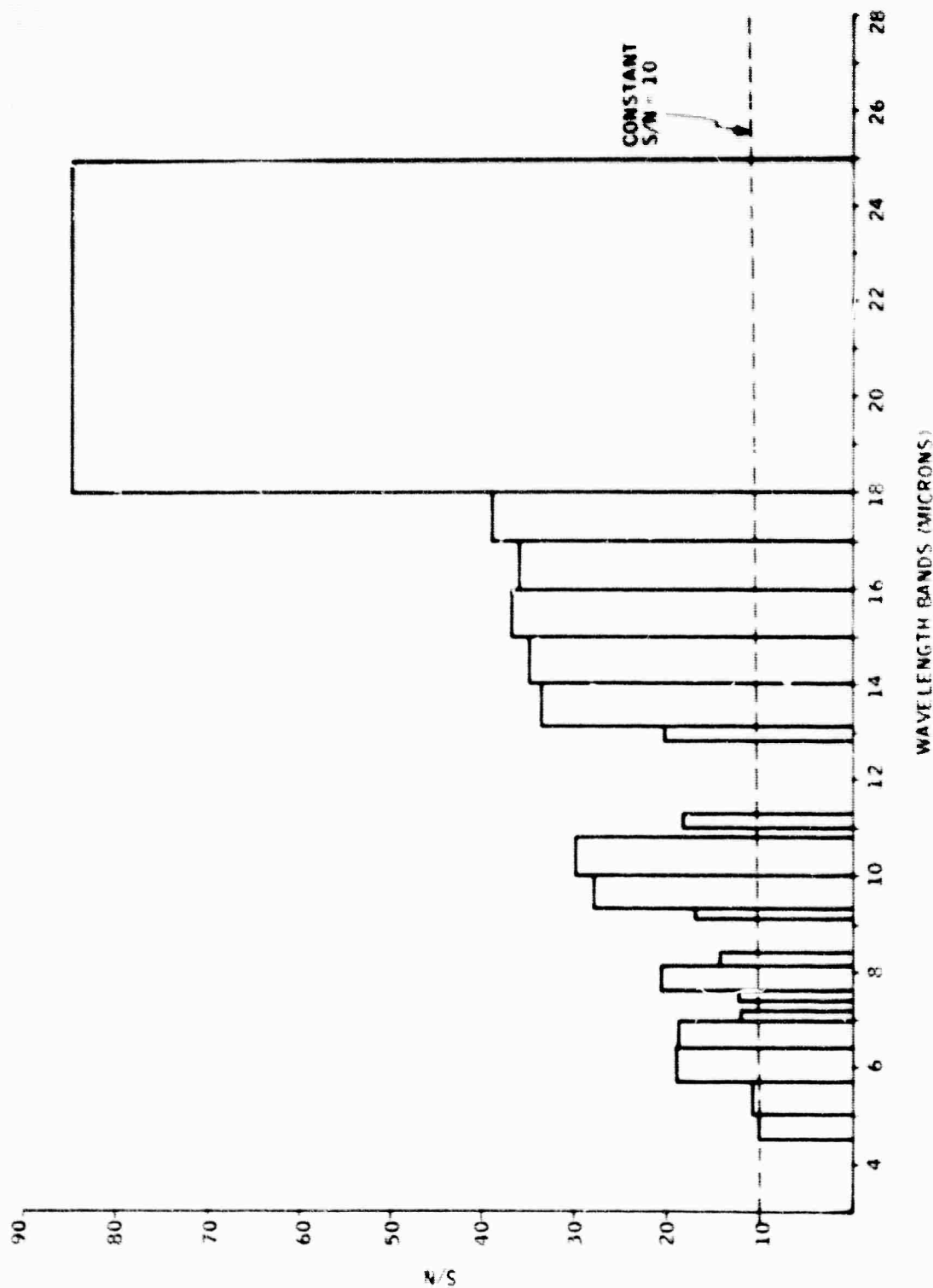


Figure 87. Signal-to-Noise Ratio versus Spectral Bands

UNCLASSIFIED

A field stop covering the 1.5×0.5 mm field is located in the primary image plane. Part of this stop includes a specially designed baffle to trap the earth image radiation. Following the field stop the primary radiation is relayed to the monochromator by two parabolic reflectors, also offset from their optical axes to avoid interference from the primary image of the earth. A Lyot stop is located between the relay reflectors in the plane of the image of the objective element.

The objective element and the first reflector of the relay have a common optical axis, which is parallel to, but displaced from, that of the second relay element.

The optical parameters are summarized as follows:

- | | |
|-------------------------------|--------------------------------------------|
| ● Field of view | 1.5 mr (horizontal) x
0.5 mr (vertical) |
| ● Objective aperture diameter | 5.0 in. |
| ● Focal length objective | 15.0 in. |
| ● Focal length system | 6.4 in. |
| ● f/number | 1.5 |
| ● Primary field stop | 22.5 x 7.5 mils |

While the f /number of the objective is 3, the mirrors are working actually at lower f -values due to the axis offset. The system is working at approximately $f/1$, nevertheless, for the narrow-angle coverage required, the resolution is quite satisfactory.

The image quality of this optical system is limited primarily by coma introduced by the last parabolic reflection, which from an aberration standpoint is working at $f/1$. The point image blurs to approximately 0.0021 in. beyond the horizontal detector edge, due essentially to coma. This corresponds to approximately $1/3$ mr. Blurring at the vertical edge, in the vertical direction, would be approximately $1/12$ mr.

The optical-mechanical design will be specifically configured to be in-figure and in-focus at the cryogenic temperature of the instrument.

Ray tracing and spot diagrams based on the above parameters will be supplied when available as further verification of the proposed design.

A simplified optical layout is illustrated in Figure 88.

UNCLASSIFIED

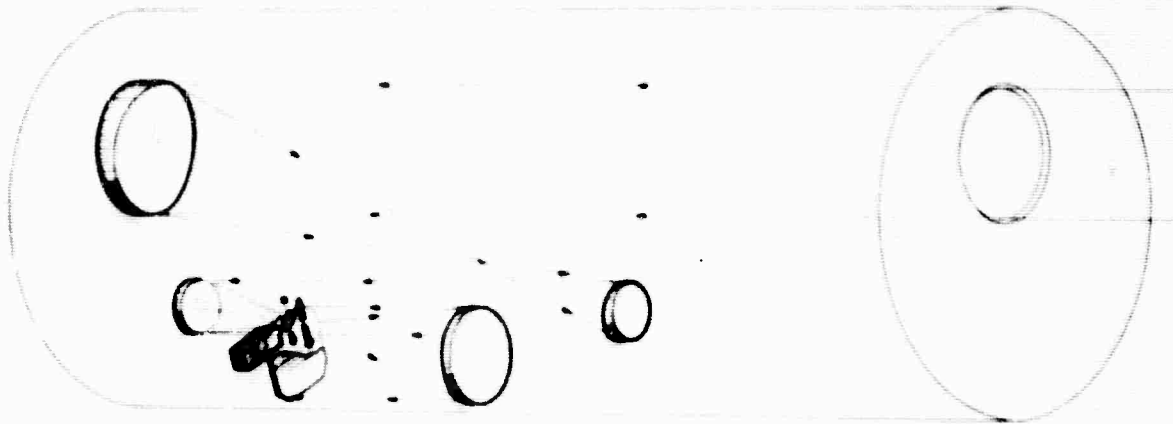


Figure 88. Simplified Optical System Schematic

4.7.2 Optical Materials

The selection of a proper material for the reflective optics was arrived at through tradeoffs among optical, structural, and thermal requirements, all of which were of prime importance.

The subsection on scattering (4.5.1) delineated the need for a low-scattering mirror surface to minimize the off-axis stray radiation. Based on the qualitative testing discussed, quartz substrate provided the possibility for the lowest scattering characteristics with beryllium, aluminum and stainless steel close behind in relative value. However, the thermal requirements for the system dictate the need for optics substrate made from a material with the same thermal characteristics as the basic instrument structure. The only way to achieve this thermal compatibility is through the use of external thermal compensating systems or through the use of materials which are identical. Because of the requirements of the instrument in terms of size, space, weight, and basic optical design (such as the use of off-axis paraboloidal sections, maximum depth of telescope to aperture, etc.), thermal compensation systems would appear to present many difficulties. As a result, it was decided to select a mirror material identical to that of the structure which contains it.

Structural characteristics were examined in detail, and, from testing, aluminum and beryllium by virtue of their densities became the prime mirror and structure candidates.

UNCLASSIFIED

Beryllium is anisotropic in that the z-axis does not thermally behave as the x and y axis. Although Speedring Co. maintains that beryllium, if properly cast using their powdered metallurgy technique, will exhibit anisotropic characteristics sufficiently small that no intolerable misalignment would exist at operating temperatures (10 to 20°K), aluminum does not have this anisotropic characteristic, and sheet, rod, and castings are readily obtainable. As a consequence, aluminum is recommended throughout. The cold-body radiometer that the Radiation Center is building on a Honeywell-funded development program has a 6061 aluminum primary (WEND) with a corresponding aluminum structure.

4.8 SPECTRAL CHARACTERISTICS AND MONOCHROMATOR DEFINITION

The spectral separation and adjacent band rejection requirements of the instrument dictate the use of a combination of a double-grating monochromator and interference filters on each detector. In this subsection, the arguments supporting this conclusion are given, and a nominal design for the monochromator is described.

A comparison of the different methods for spectral separation is contained in Table 21. Notice on the table that all spectral scanning methods are eliminated because of the high sensitivity required in the limited time available for scanning. Since spectrum scanning methods are difficult, each individual spectral channel must have its own detector. The remaining nonscanning instruments are ruled out essentially because of the crosstalk (rejection ratio) between adjacent channels. The proposed solution is a combination of the grating monochromator and individual interference filters on each channel.

4.8.1 Proposed Monochromator

Of the various grating monochromators, the prime candidate is a double grating monochromator with one grating being used over the 4.5- to 9.3-micron region and the other grating being used over the 9.3- to 18-micron region. The 19- to 25-micron channel is split off by a dichroic reflection. Figures 89 and 90 show the energy efficiency for these two gratings which are blazed at the optimum wavelengths of 5.6 and 12 microns respectively. To achieve dispersion such that the minimum-size detector is used in the narrowest spectral channel, a 6-in. focal length monochromator requires only a fairly coarse grating -- nine and six lines per millimeter respectively. This is advantageous because such coarse gratings are not replicas but are ruled directly on an aluminum or magnesium substrate. This assures cryogenic survivability. The resolving power of these monochromators is only 30, so the theoretical limit of resolution requires gratings of only 30 lines total. A grating 1.5 in. wide surpasses the theoretical limit by 12 times. This resolution capability can be traded off to let the monochromator operate at a low f/number.

Table 21 Instrument Tradeoff Factors

Item	Scanning Instruments			Non-scanning Instruments				
	Rotating Circular Vavable Filter	Scanning Monochromator	Microbeam Interferometer	Scatterometer Retroreflector	Scatterometer 2-Beam	Scatterometer 3-Beam	Scatterometer 4-Beam	Scatterometer 5-Beam
Periodic Resolution (s)	0.2 (1.5-9.1)	0.2 (1.5-9.1)	0.2 (1.5-9.1)	0.2 (1.5-9.1)	0.2 (1.5-9.1)	0.2 (1.5-9.1)	0.2 (1.5-9.1)	0.2 (1.5-9.1)
Effective Number of Spectral Reso- lution Elements	31	31	31	31	31	31	31	31
Bandwidth Factor	31 x increase	31 x increase	31 x increase	31 x increase	31 x increase	31 x increase	31 x increase	31 x increase
Total Number of Photons on Detector	31 x decrease	31 x decrease	31 x decrease	31 x decrease	31 x decrease	31 x decrease	31 x decrease	31 x decrease
Signal-to-Noise Ratio	31 x decrease	31 x decrease	31 x decrease	31 x decrease	31 x decrease	31 x decrease	31 x decrease	31 x decrease
Field of View	1.5 deg 0.5	1.5 x 0.5	1.5 x 0.5	1.5 x 0.5	1.5 x 0.5	1.5 x 0.5	1.5 x 0.5	1.5 x 0.5
Rejection Ratio Adjacent Bands	10 ⁻³	10 ⁻³	10 ⁻³	10 ⁻³	10 ⁻³	10 ⁻³	10 ⁻³	10 ⁻³
Special Comments	Too much loss in S/N	Too much loss in S/N	Combination of aperture size and solid angle (10 ⁻³) will not fill the practical area interferometer Too much loss in S/N	Too much loss in S/N	Too much loss in S/N	Too much loss in S/N	Too much loss in S/N	Too much loss in S/N

UNCLASSIFIED

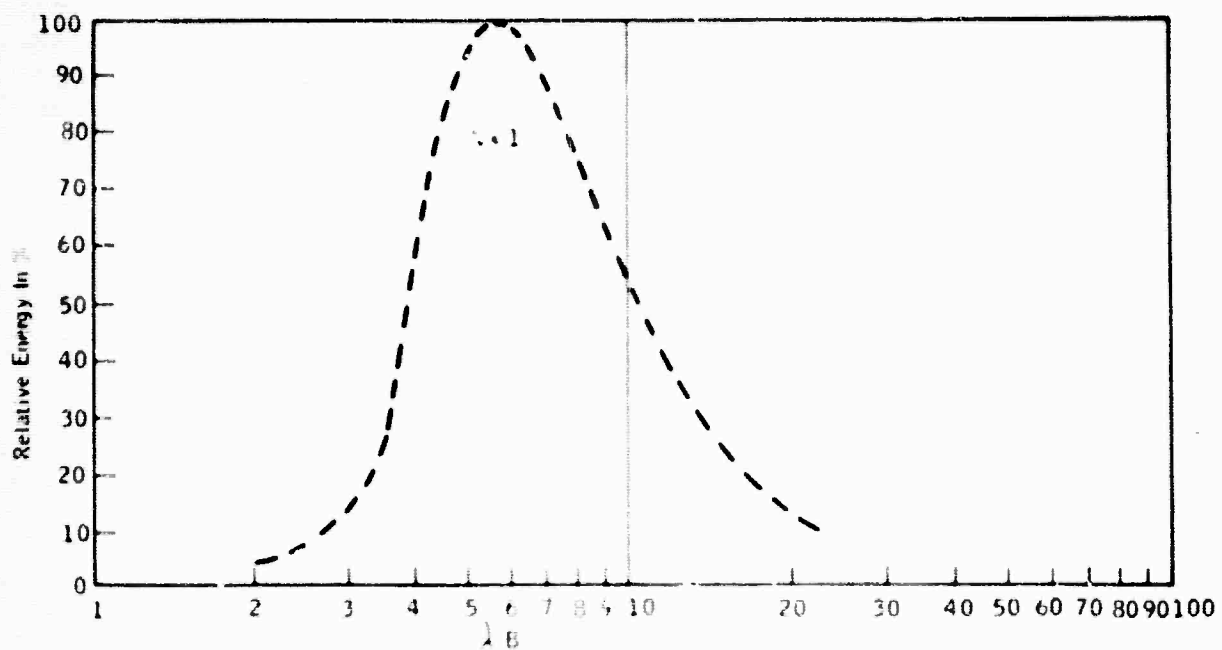


Figure 89. Energy Distribution of a Littrow-Mounted Plane Grating, 5.6-micron Blaze

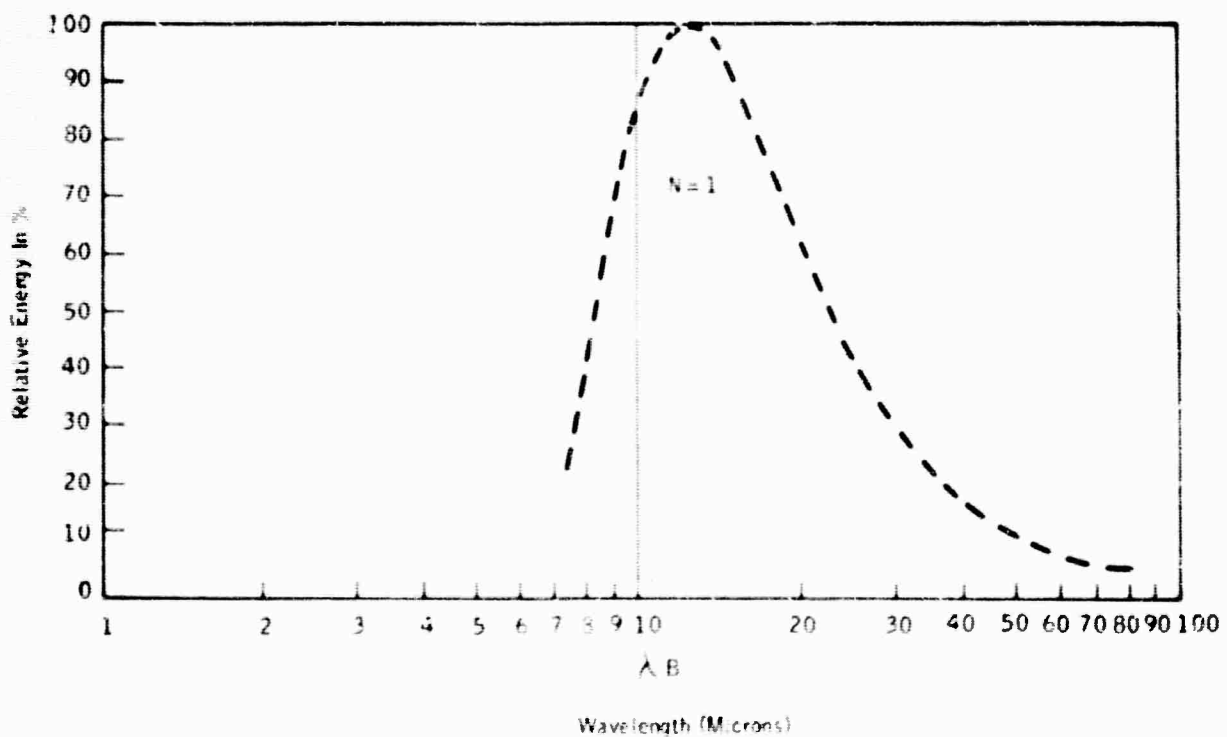


Figure 90. Energy Distribution of a Littrow-Mounted Plane Grating, 12-micron Blaze

UNCLASSIFIED

UNCLASSIFIED

Several monochromator designs are possible within the constraints of a 6-inch focal length and operation at $f/3$. The nominal design of a side-by-side off-plane Littrow is described as follows. A single collimating mirror fills two side-by-side gratings placed at angles such that the focal planes occur on either side of the field stop. The collimating mirror produces a beam dissection resulting in a 50% energy loss. This is overcompensated by making the field stop (and entrance slit) rectangular in the direction parallel to the earth's horizon with an aspect ratio of 3:1. The direction of dispersion is perpendicular to the long axis of the field stop. The focal plane of the 9.3- to 19-micron monochromator subtends an angle of approximately 2 deg to the collimator. As a result of off-axis aberrations, a certain amount of spectral smearing (spectral stray light) occurs. Preliminary calculations indicate that, for a classical Littrow with parabolic collimator, the worst-case spectral stray light (17- to 18-micron channel) will be in the order of 2 to 5%. The spectral stray light is less in the remaining channels since their off-axis angles are smaller. Several variations on this design show promise of reducing the worst-case spectral stray light considerably. However, to ensure reduction of stray-light interference, filters are provided over each channel. The addition of the filter can reduce the stray light by 10³, thus ensuring the integrity of adjacent channels.

An additional requirement of a grating monochromator is that the grating ruled area must be square and must be filled with light from a circular primary. This means that a small amount of vignetting must occur. The optimum compromise results in 15% vignetting loss, as shown in Figure 91. The gratings are not quite filled by the primary, and a small amount of the primary is not seen by the gratings. If the circular area of the primary is circumscribed by the grating area, a loss of spectral resolution occurs, but no loss of energy occurs. If the grating boundary is circumscribed by the primary boundary, there is no loss of resolution but a large loss of energy.

This 15% vignetting loss together with the grating efficiencies are used in the sensitivity analysis which follows. It should be noted that, in spite of these necessary losses, the net signal-to-noise ratios are greater than can be achieved by the other methods of spectral separation; and, in addition, it minimizes the problem of rejecting light scattered by the primary optics.

Figure 92 is a plan of the detector array in the final image plane of the monochromator.

UNCLASSIFIED

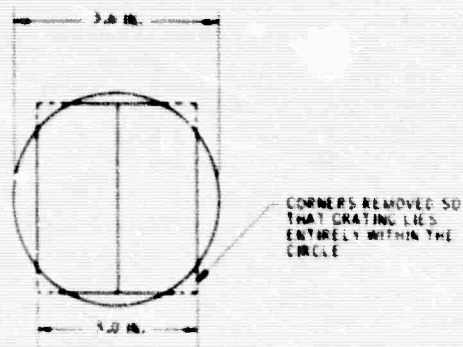


Figure 91. Optimum Vignetting of Monochromator

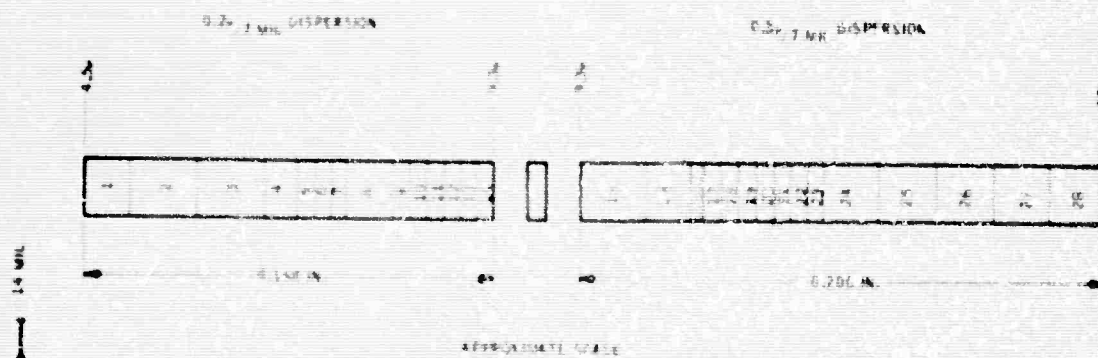


Figure 92. Detector Array Configuration

UNCLASSIFIED

SECRET

4.8.2 Spectral Separation Tradeoffs

(S) The first major decision to be made was whether to use a spectrum-scanning instrument with a single detector or a dispersing instrument with an array of individual detectors, each sensitive to a particular spectral band. Because of the sensitivity required in the time available for scanning, conventional scanning instruments can be ruled out. To achieve a spectral resolution of 0.2 micron from 4.5 to 9.3 microns and a resolution of 0.3 micron from 9.3 to 18 microns, the effective number of spectral resolution elements is 53. In comparison to a non-scanning instrument, a rotating circular variable filter or scanning monochromator would have a 53 times wider bandwidth, 53 times less signal and 53 times more noise. The net result is a loss of a factor of 53 in signal-to-noise ratio. This is a fundamental limitation occurring even if one were able to obtain the higher D^* detectors (approximately 10^{15} $\text{cm}^2 \text{ Hz}^{-1} \text{ watt}^{-1}$) which would be allowed by the lower signal flux. The inability to achieve these D^* values results in a further degradation of signal-to-noise ratio.

(U) Spectrum scanning could also be accomplished with a Michelson-Fourier interferometer which has only the bandwidth limitation. The loss in signal to noise ratio would be only 53. The Fourier interferometer is precluded however by the high angular resolution requirement of the instrument. The combination of aperture size and solid angle (A.7) will not fill the optics of a practical-sized interferometer.

(U) Since spectrum scanning methods are ruled out, each individual spectral channel must have its own detector. There are several ways of accomplishing this, as discussed in the following paragraphs.

Individual Filtered Detectors -- (S) In the proposed division of the IR limb spectrum there are 29 bands. One way to utilize an individually filtered detector array is through the use of anamorphic optics. The system would contain a square field stop and an anamorphic optical element (such as a toroidal mirror) to produce a rectangular image of the field stop on the 29-element array. Each detector in the array has its own spectral filter. All 29 detectors would be the same size, but the individual detectors would receive only 1/29 of the total energy available. The degradation in signal-to-noise ratio is 29 presuming the detector is signal-photon-noise-limited at that signal level ($D^* \approx 10^{15}$).

(U) This problem of energy splitting can be overcome if the width of the system field stop is increased 29 times. The field of view to the limb becomes 0.5 mrad vertically and 14.5 mrad horizontally. The advantages of this approach are simplicity and high efficiency. The disadvantage is primarily that of inefficient stray light rejection. Light which is scattered by the primary can find its way to the detectors through a 29-fold greater

SECRET
THIS PAGE IS UNCLASSIFIED

field stop area. However, diffracted light from the earth should not be any greater since the field stop was increased in the direction parallel to the earth's horizon. Since the primary is being used approximately $1/2$ deg off-axis, the aberrations (chiefly coma) at the edges of the field of view would be increased. This could be partially accommodated if the spectral bands of least interest are located at the ends of the array. A more severe problem is that of practical detector and filter size limitations. In an $f/3$ system the detector and filter sizes would be approximately 10 mils (0.010 in.). This is beyond the state of the art in filters, but the effective f /number at the filter could be increased to perhaps $f/10$. The filter size would then be 33 mils, and the total focal plane size would be approximately 1.00 in. This makes the optics difficult to package, but such an arrangement is not an impractical solution to the problem of spectral separation. In comparison to the recommended method, this method of using individual cells and separate filters has about the same optical efficiency and greater simplicity, but scattered stray light has been increased by a factor of 39.

Stationary Circular Variable Filter -- Another way of individually filtering the detectors is through the use of a stationary circular variable filter. The wavelength gradients around a circular variable filter can be made steep enough (wide wavelength range in a short distance) so that an effective 0.2-micron wide wavelength passband occurs over a 10-mil distance. This is a practical way of obtaining the small-size filters that are required. The disadvantage is more subtle. The gradient must be chosen as 0.2 micron per 10 mils of arc distance in order to accommodate the narrowest spectral channel with the smallest-size detector. The widest spectral channel however is 0.7 micron, and the corresponding detector would be 40 mils wide. The property of a circular variable filter however is that, as the slit width is increased, more different wavelengths are passed, but no more light is gained at a given wavelength. One end of the long detector sees one wavelength, and the other end of the detector sees only another wavelength. This means, in our example, that the effective transmission of the channel has been degraded by a factor of 3.5. The stationary circular variable filter therefore only overcomes the practical problem of obtaining small-size detectors. This is at the expense of signal-to-noise ratio in the wider spectral passbands. It also requires an even wider slightly curved field stop -- the aspect ratio being 53 to one. The corresponding off-axis angle of the primary parabola is nearly 1 deg.

4.8.3 Monochromator Tradeoffs

When a detector array is placed at the focal point of a monochromator the individual detectors act as the effective exit slit of the system. Since the 29 spectral channels in the scanner do not all have the same spectral bandpass, these detector sizes are all different. The optimum transmission of a monochromator occurs when the entrance slits and the exit slits are the same size optically. There is no advantage to having an exit slit smaller than the entrance slit because no better spectral resolution is achieved, and there is a large net loss in system sensitivity. The detector size is a function of monochromator dispersion and spectral bandpass at the wavelength of

UNCLASSIFIED

interest. The smallest detector is used for the channel in which the product of spectral bandpass and monochromator dispersion is a minimum. All other detectors are then larger. The monochromator should be designed such that, over wide wavelength regions, this product does not change appreciably.

Prism monochromators can be immediately ruled out on several counts:

- Dispersions are not linear with wavelength. This means that the aspect ratio of the detectors changes by a large amount when a prism is used over a wide wavelength range.
- The materials are temperature sensitive, as are both refractive index and dispersion. This temperature dependence disturbs the wavelength limits of the channels.
- Refractive index and dispersion data are not available for prism materials at cryogenic temperatures.
- Most materials useful over the wavelength range of interest are affected by atmospheric water vapor. This hygroscopic behavior compounds the fabrication and handling problems.

Diffraction grating monochromators have the advantage of temperature and environmental stability, linear dispersion with wavelength and ready availability in the desired spectral range. The grating spacing changes in a predictable fashion with the expansion and contraction of the substrate, and this can be accommodated in the design of a cryogenic grating monochromator. The grating blaze can be chosen so that the effective transmission (grating efficiency) complements the desired sensitivity in the various spectral channels. Their sole disadvantage is that a single grating can be used in the first order only over a wavelength range of approximately 2.5:1.

One candidate grating monochromator consists of a single-plane grating used in both the first and second orders simultaneously. If the grating is blazed in the first order at 11 microns, this grating blaze covers the wavelength range of interest with optimum efficiency. However, there is a problem of order overlap with such a monochromator. The second order lies on top of the first order so that order sorting is necessary. This could be accomplished with auxiliary filters, or with Honeywell sandwich detectors or by the method of vertical sorting with a secondary low dispersion operating perpendicular to the main grating. This added complexity of order sorting makes this method unattractive. The primary disadvantage however is that the detectors have an unwieldy aspect ratio. The dispersion in the second order is twice that in the first order. The minimum-size detector accommodates the narrowest spectral channel in the second order. This means that the wider spectral bands in the first order cover a disproportionately long distance in the focal plane. Detectors with BLIP properties having these aspect ratios have yet to be demonstrated.

UNCLASSIFIED

4.9 STRUCTURAL DESIGN

The spectroradiometer for this application is built up from a basic optical housing to which is mounted the primary mirrors, two relay paraboloids and a monochromator system. Baffles and the cryogenic storage tanks are fixed to a deck which, in turn, is attached to the housing and the radiometer split outer skin. Two end covers complete the radiometer subassembly. A radiation shield encircles the radiometer subassembly and is itself encircled by an outer shell to which is attached the in-and-out cryogenic cooling components. The split radiometer outer skin, the radiation shield, and the outer shell are separated by thermal isolators. Finally, the radiation shield and the outer shell are separated by superinsulation.

4.9.1 Optical Housing and Mirrors

The optical housing and the mirrors are made from cast aluminum. The material has a high strength-to-weight ratio and exhibits good stability over the thermal excursion to which it will be subjected. Uniformity of contraction is expected throughout, with a maximum gradient of less than 3°K between any point on the housing and the mirrors. Direct earth radiation is impinging upon the primary and the worst gradients are expected at this location. However, the thermal conductivity expected at the 10 K operating temperature is still sufficient to uniformly distribute the nonuniform heat loading. It is, therefore, a thermal heat sink problem which is solved by copper foil straps connecting the primary directly to the cryogenic tank reservoirs. This copper foil technique is employed for heat sinking all mirrors and the grating. The linear contraction of the single optical housing and the figure of the mirrors have a 1:1 correspondence, thus ensuring alignment and rigidity throughout the expected environmental excursions.

The metal optics are mounted to the optical housing with bolts. The bolt circle is contained within an outer flange, detented such that no stress risers can possibly influence the mirror figure.

4.9.2 Radiation Shield and Outer Skin

Because of the thermal loading and the radiometer system requirement to operate at 10 to 20°K, a radiation shield is required between the outer skin and the radiometer proper. The radiation shield will be at a temperature of 90°K. The outer skin will be at 300°K. The radiation shield and the outer skin are fabricated of aluminum and strengthened by rings to support the 1-atm. gase differential pressure at launch. There is a further requirement of superinsulation between the radiation shield and the outer skin. Cryogenic tubing and supercritical helium performs the cooling function required at the radiation shield. To make the assembly of the complete system possible, the

UNCLASSIFIED

radiation shield and the outer skin provide for separate assembly of the thermal isolators discussed in the next subsection.

4.9.3 Mechanical, Thermally Isolated, Support System

To support the radiometer within the cryogenically cooled system, a mounting technique must be provided which will act as a thermal isolator, and provisions must be made for the change in the inner package dimensions when the package is cooled down. In addition, the isolator must withstand the mechanical loadings during the launch of the rocket. To accomplish this, a compromise must be worked out between the thermal and the mechanical requirements.

The cryogenic heat transfer requirements are 0.50 watt from the radiometer to the radiation shield and 8 watts from the radiation shield to the outer vessel. There is also a heat station at the bottom of the radiometer which will absorb the heat transferred through the cryogenic inlet piping and the axial thrust supports into the radiometer.

Because of the large variation in temperature between the inner and outer vessels the inner vessel containing the radiometer will shrink by 0.045 in. when the unit is cooled down. The radiation shield diameter is also reduced by a similar amount. Therefore, the radial mechanical supports must be designed to accommodate this dimensional variation without causing large stress increases in the structure. If we assume that there will be eight radial mechanical support stations, four at the front and four at the rear, there must be two thermally isolated support (see Figure 93) per station to minimize the heat transfer. Each support must be capable of withstanding vibration and shock loading during launch.

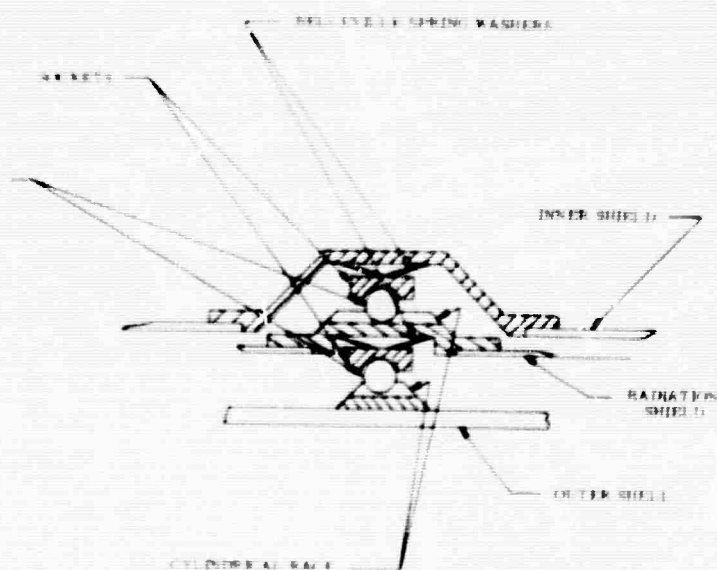


Figure 93. Radiometer Support Points

UNCLASSIFIED

In a paper by R. P. Mikesell and R. B. Scott (Ref. 10), it was shown that 3/8-in. diameter pyrex glass balls are excellent thermal isolators and can support loads of greater than 2000 lbs per ball. (It is of interest to note that HRC has used a pyrex ball support in the collar developed for the Nightscope Program. This device was mounted to a rifle and has successfully withstood the shock of many firings.) It will be necessary to limit the load to less than the maximum for each ball and to provide a means to preload the balls over the dimensional variations caused by temperature effects. This can be done by preloading each ball with a belleville spring washer (see Figure 93).

The belleville spring washer is similar to a flat washer but made of high-strength steel and deformed into a shallow conical form. Because of its nonlinear spring characteristics, heavy loads can be applied to this spring with small deflections, and when moderate to heavy loads are applied small changes in deflection may not create large variations in the load. Therefore, by using well designed supports utilizing the spring shrinkage of the inner vessel will not cause a noticeable reduction of the preload. A load deflection curve for this spring is shown in Figure 94.

It should be noted that there is a variable-spring constant related with the deflection, or

$$\frac{dP}{dX} = K$$

where K, the spring constant, is nonlinear and tends to decrease with increases in deflection. By proper design techniques, the low spring constants associated with the preload deflections can be used to vibrationally isolate the inner package from the higher radial, vibrational, inputs of the outer vessel during the launch period. The vibration model for this system is that of a two mass, two spring system with the vibration input into the first spring.

M_1 is the radiation shield and M_2 is the radiometer. The laws of motion for this system are

$$M_1 \ddot{X}_1 + K_1 X_1 + K_2 (X_1 - X_2) = K_1 X_t$$

$$M_2 \ddot{X}_2 + K_2 (X_2 - X_1) = 0$$

This pair of simultaneous equations can be solved for the amplitudes of the radiometer and the radiation shield in the radial direction. The maximum amplitude will be obtained at a low frequency which may require soft snubbers if it is shown that the clearances are used up in deflecting the springs. High-frequency vibrations will be attenuated rapidly and will have little effect on the radiometer. It should be noted that each outer ball support is grooved in the axial direction. This has been done to provide no resistance to the axial shrinkage of the radiometer. Therefore, all axial loads will have to be resisted

UNCLASSIFIED

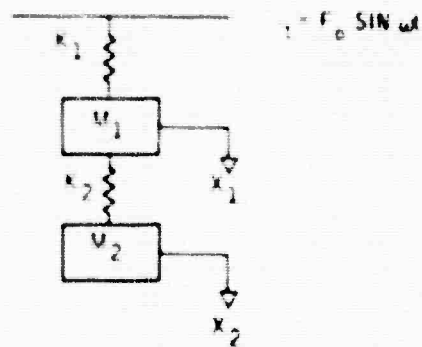
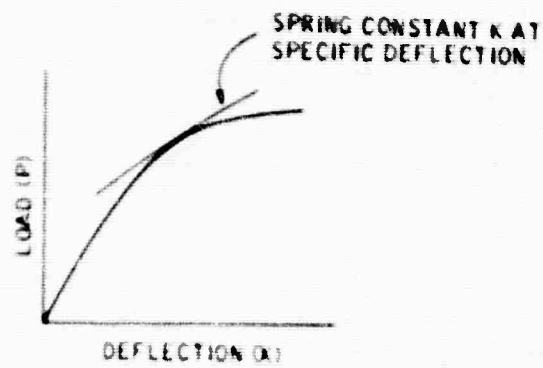


Figure 94. Load versus Deflection Curve for Belleville Spring

UNCLASSIFIED

UNCLASSIFIED

by the axial supports at the bottom of the radiometer. Rotational loads will be resisted primarily by the radial supports with some aid from the axial supports.

A tripod support at the lower end of the radiometer will resist axial thrust. To reduce heat transfer to a minimum while still providing a rigid structure, a three-stage support is required. The first stage is a heat station mounted on 3/8 in. diameter stainless steel tubes. This will support the radiation shield through three stainless steel standoffs which are not directly fastened to the heat station. A long central tension member serves to preload the standoffs on the heat station.

Heat transfer through this rod is reduced by making it as long as possible which, in turn, allows a greater diameter and thus a high resistance to axial tensile loading.

Because of the extremely small heat-transfer requirements between the radiometer and the radiation shield, the pyrex ball mounts must also be used in the third axial stage. These balls (three balls are used) will be preloaded by small-diameter, high-strength tensile members. The balls will resist the thrust loads, leaving the vibrational loads acting primarily on the tension rods. Type 410 stainless steel (or some other high-strength cryogenic material) with a yield strength of more than 100,000 psi will be used for these rods which will have a diameter of approximately 0.090 in. each. This will provide a total cross sectional resistance of 0.018 in. which, with a clamping load of 70% of the yield strength of the rods, will preload the balls with a force of 1800 lbs or 600 lbs each. This should be sufficient to resist vibration loadings from the acceleration forces without attaining sufficient magnitude to exceed the preload. Radial motion will not be sufficient to cause a combined stress exceeding the yield strength of these members.

The low temperature experienced by the inner structural members will increase their strength which, by the use of proper design techniques, will withstand the environmental and temperature stress induced into the radiometer package.

4.10 CRYOGENIC SYSTEM DESIGN

The system proposed uses supercritical helium gas as a single cryogen for detectors and optics. Figure 95 illustrates schematically the proposed system.

The following criteria were used in establishing this design:

- Heat loss of 8 watts from container to radiation shield, preflight

UNCLASSIFIED

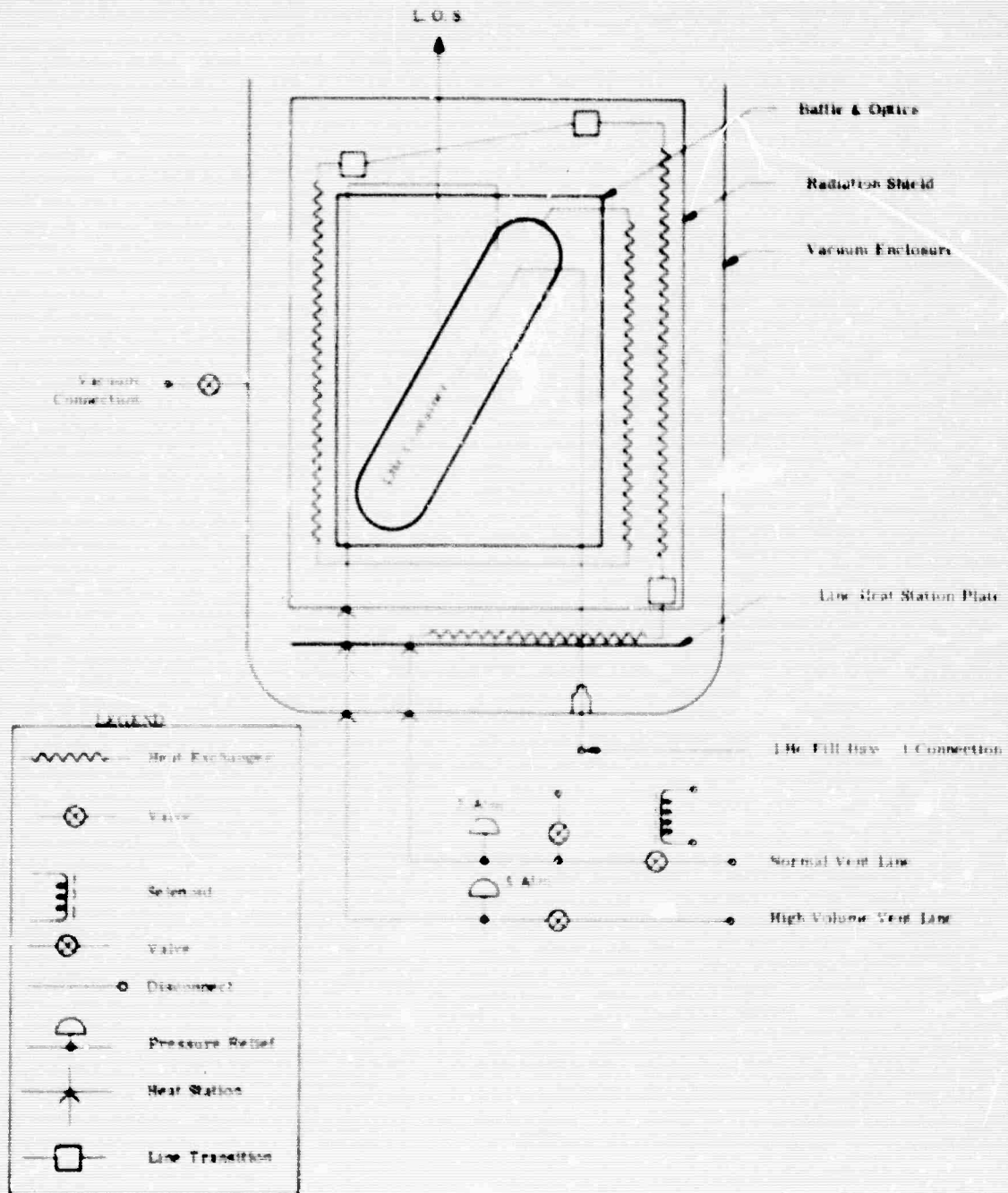


Figure 95. Helium Cryogenic Refrigeration Schematic

UNCLASSIFIED

- 3 watts additional heat loss during flight due to earth radiation into the entrance aperture
- Ground hold time of up to 2 hrs
- Flight time of 20 min
- 50 mw from chopper energy dissipation requirements

The storage container volume required is approximately 5 cubic decimeters (dm^3), giving 623g of LHe.

The LHe is transferred into the storage container in the liquid state at 1 atm in all cases. If the vent line were simply plugged from that point (with no venting relief) the helium would absorb 47J/g at 10°K and reach a pressure of 29 atm, requiring a heavy-walled storage container. Such a supercritical helium system is impractical for this application. Instead, the helium is vented at a predetermined pressure level and provides the advantage over liquid (gas systems) of heat absorption through cold-gas shielding.

To assist in the visualization of the stored helium thermodynamics, Figure 96 presents three temperature-entropy (T - S) diagrams that are simplified to show the desired features. The data are computed from these diagrams and from NBS tabular data on the thermodynamic properties of helium. The boundary conditions are the contents of the storage container with heating incident thereto (0.4 watt), and temperatures up to 7°, whichever is reached first. In the case of the boiling liquid helium, Figure 96, the energy absorbed by the gas venting from the container is not evaluated. It is recognized that this boundary condition is arbitrary because the design will utilize the refrigeration energy of the cold gas. In the upper diagram, A, the enthalpy gained is just that of the heat of vaporization of the liquid helium, from point 1 to 2. If the helium vent is closed off at some time after the filling of the storage container with LHe and allowed to pressurize to 3 atm, then the thermodynamic process follows the path 1-3-4, in the middle diagram. No venting of helium takes place in the path 1-3, but when the container pressure reaches 3 atm, venting will occur along the path 3-4. It can be noted that the storage container temperature is rising during this entire process. In the bottom diagram, C, a similar process takes place but at a pressure of 5 atm.

Supercritical helium thermodynamic properties vary over a wide range in the region immediately above the critical point. The specific heat capacity, C_p , and thermal conductivity, λ , reach very high values in this very narrow zone, and the closer a system can operate to the critical point the higher the values become. From the T - S diagrams, for example, the "flattening" of the isobar lines just above the critical point will readily let one observe the sudden increase of C_p . This type of thermodynamic operation is not done without some problems, though. The immediate supercritical region is not too well explored, and thermodynamic oscillations and instabilities can occur, yielding temperature and pressure fluctuations that compound thermal and

UNCLASSIFIED

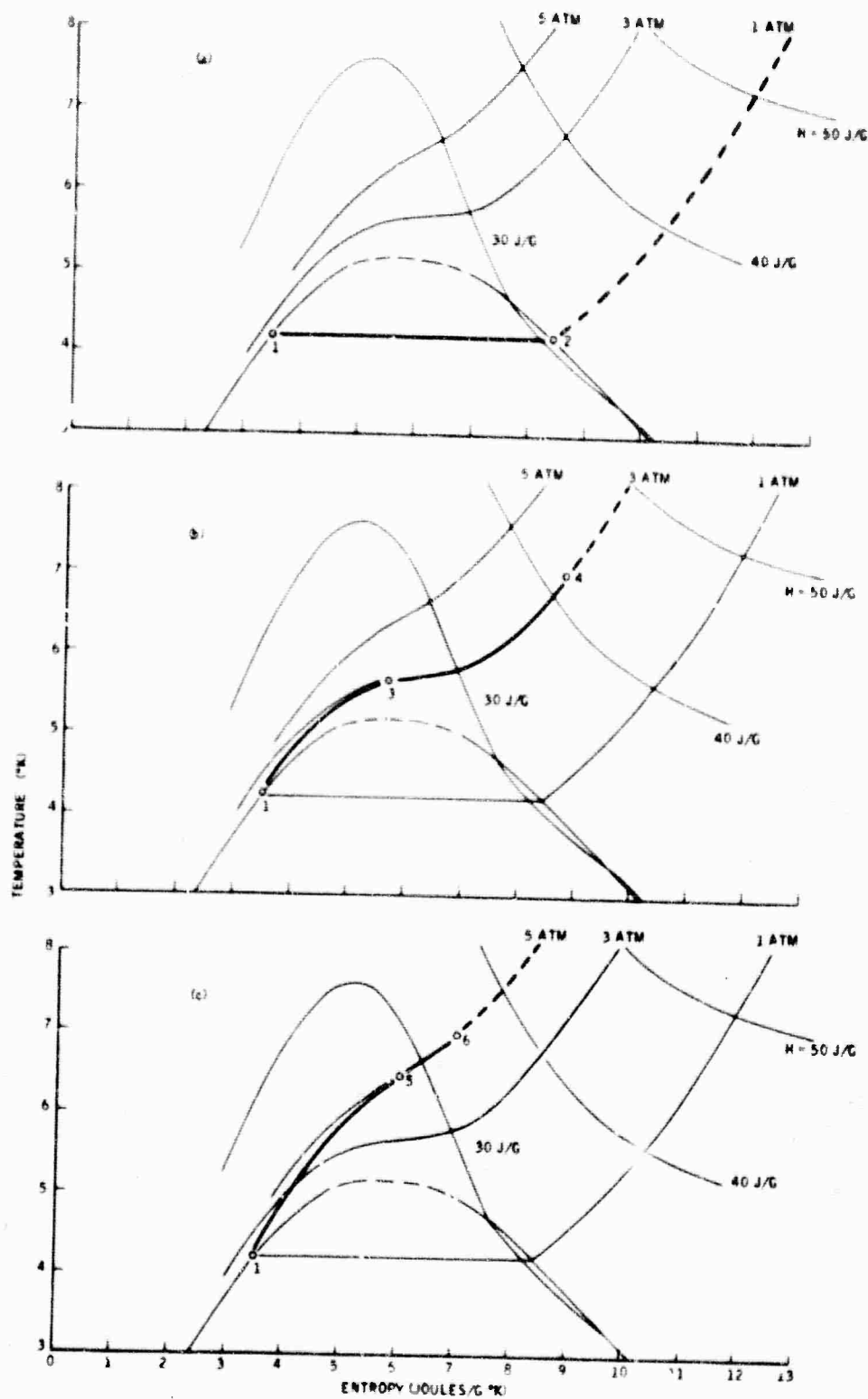


Figure 96. Temperature-Entropy Diagrams

UNCLASSIFIED

UNCLASSIFIED

mechanical design problems. Some of the fluctuations can be damped out by taking advantage of acoustic damping principles.

The next question deals with the length of time that the storage container takes to pressurize, following the initial filling of LHe. Computations have been made to determine the useful time of refrigeration as a function of the percentage of liquid fill in the storage container at the time pressurization starts. The graphical results are shown in Figure 97 for pressurization levels of 3 atm and 5 atm with a 1-atm free boiling reference line. The boundary conditions are a volume of 5 dm³, a heat load of 0.4 watt, and an initial 100% fill. It can be seen that a fully loaded free-boiling helium container will have a useful refrigeration time of about 9 hrs, while the 3-atm case may reach nearly 11 hrs, depending on the time of the pressurization. Five-atm operation shows an increasing operating time as the liquid fill decreases.

The results shown in Figure 98 assume that, during the time required for the container to reach pressure, there is no venting of helium gas through the radiometer and the radiation shield. Presuming that the initial filling operation was conducted slowly so that the resulting gas flow cools the shields, this cutoff of venting gas during pressurization will allow these parts to warm up again and substantially increase the heat load on the storage container. It becomes useful to know how long it would take for a container to reach its venting pressure. Figure 99 illustrates this time factor, showing for the 3 atm case, that the pressurizing time increases from just over 1 hr at 100% fill to over 4 hrs at a 70% fill. Two alternatives can be suggested to achieve the pressurization of the storage container without allowing the remainder of the radiometer to unduly rise in temperature: (1) incorporating an electrical heater in the storage container so as to quickly raise the cryogen energy level to that of the desired pressure or (2) providing a secondary radiation shield heat exchange tubing to permit the passing of an externally fed cryogen (such as liquid nitrogen, LN₂) to the shield. The second method noted can also be used to provide a degree of precooling of the radiometer prior to the feeding of liquid helium to the storage containers.

As previously noted, the concept of using helium as a refrigerant for the radiometer depends heavily upon using the very high enthalpy of the venting gas. Staged thermal protection systems must be considered that progressively add thermal energy, or "extract refrigeration" from the gas. Shown in Figure 95 is a typical system where the gas flows through heat exchanger tubing on the baffle/optical structure so that heating by the planetary radiation during flight can be effectively absorbed at temperatures less than 20°K. Gas flow is then routed to the radiation shield surrounding the radiometer to intercept the major part of the ambient heating of the radiometer. An optimum trade-off temperature for the internal radiation shield is in the area of 60 to 90°K, and the anticipated gas flow will be more than adequate for cooling the shield to these temperatures. To further extract more refrigeration from the helium, a heat stationing of the radiometer plumbing lines and thrust support is also

UNCLASSIFIED

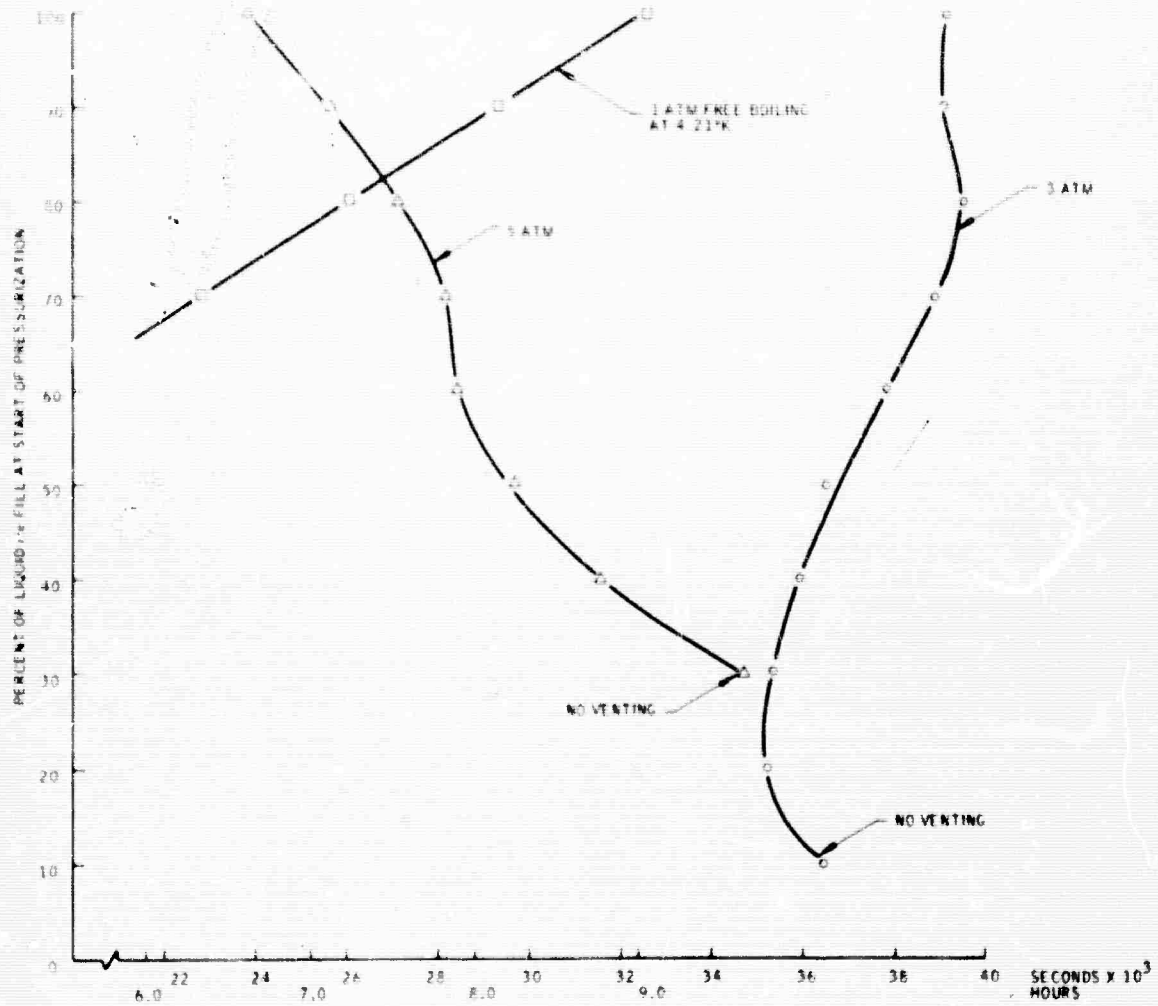


Figure 97. Time of Useful Refrigeration

UNCLASSIFIED

UNCLASSIFIED

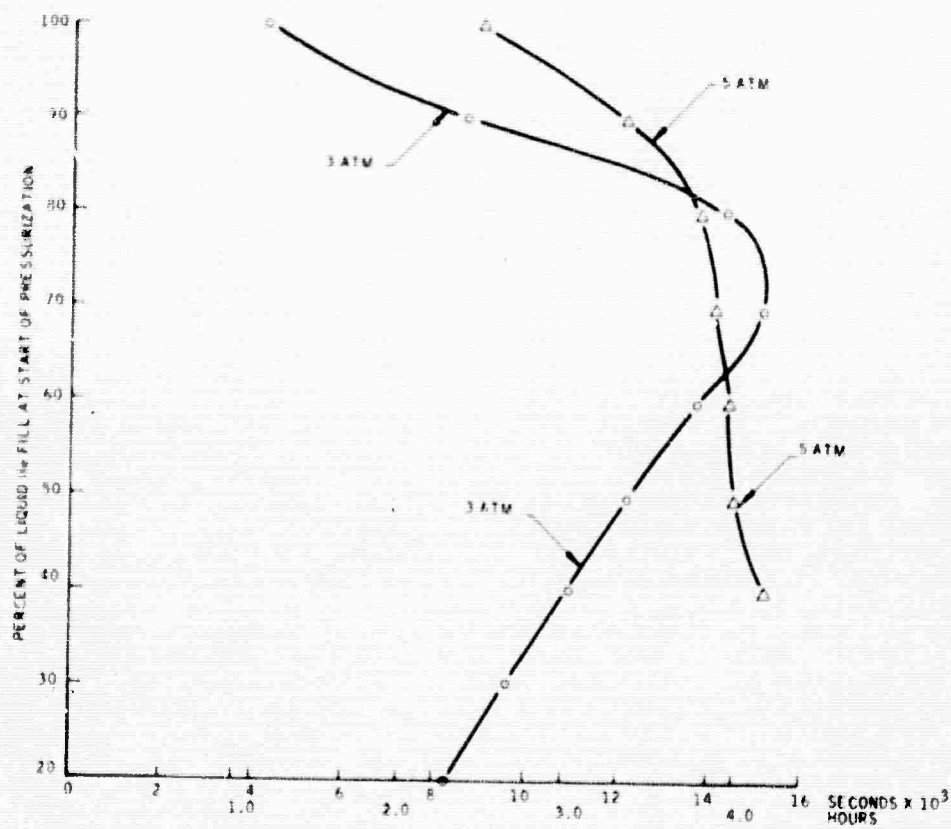


Figure 98. Time of Pressurization

UNCLASSIFIED

UNCLASSIFIED

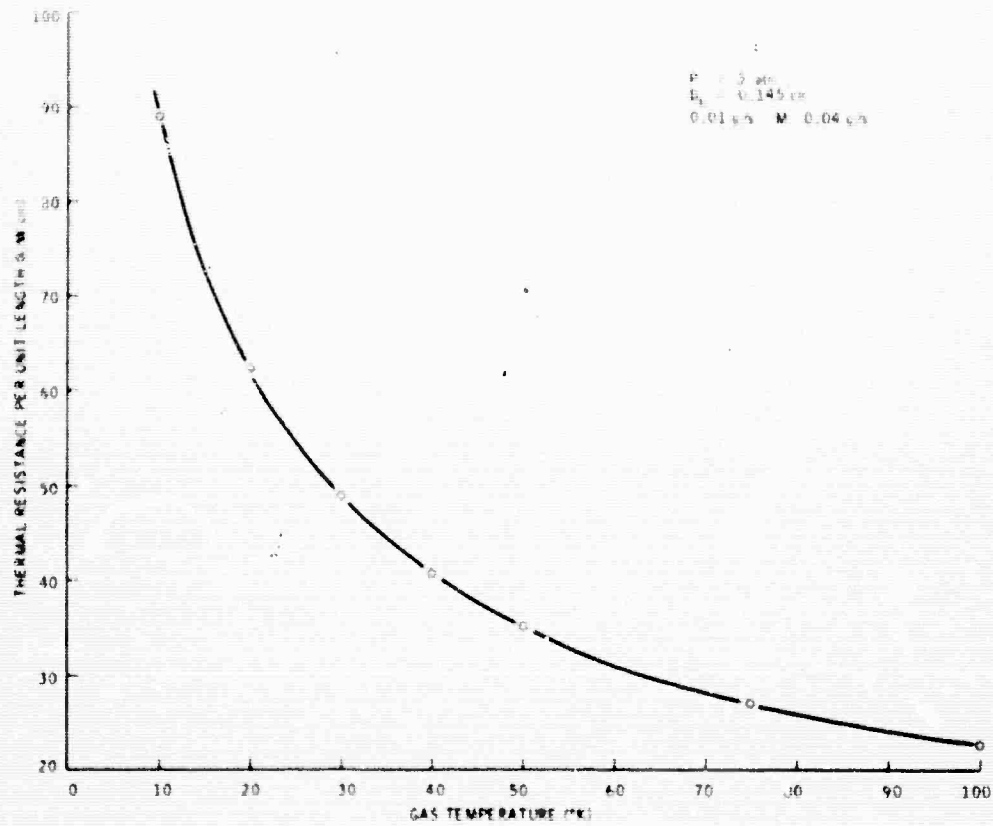


Figure 99. Time Factor in Reaching Venting Pressure

UNCLASSIFIED

UNCLASSIFIED

provided. It is evident that a key requirement of this gas flow system is the efficient transfer of heat from the structural elements to the gas. To this end many systems use small diameter vent tubing for the helium as the heat transfer coefficient becomes greater with smaller hydraulic diameters, D_h . Small diameter tubing can become clogged with frozen gases, however, if the system is not properly handled.

To alleviate the problem of using small-diameter tubing and still obtain small values of D_h , this radiometer will use an internally finned copper tubing. Figure 100 shows (greatly enlarged) the cross section of a duplex finned tubing that is available on the market. The outer tube is drawn down onto the inner tube to provide a very substantial mechanical bond between the fin tips and the outside of the inner tube. The anticipated tube configuration is 0.250-in. OD, and with the inner member being a blanked-off tube or a solid rod. The selected diameter will enable the use of standard copper tubing fitting during the radiometer assembly. The success of this finned tubing depends in part on the heat transfer integrity of the bond between the fin tips and the inner member. Figure 101 shows a 50X and 400X magnification metallurgical view of the bond line. While the bond cannot be described as a cold weld, the mechanical swaging process provides a good thermal interface for heat transfer purposes. The importance of this point is that the surface of the inner member must provide its useful portion of the heat transfer surface area.

The selected heat exchanger tubing has a wetted perimeter, P_w , of 3.52 cm, a flow cross-section area, A_c , of 0.1278 cm², and a D_h of 0.1452 cm, where: $D_h = 4 A_c / P_w$. In computing the convective heat transfer coefficient for heat exchanger tubing being used for helium vent gas, the flow regime is very much in the laminar region with Reynolds numbers, N_{Re} , being less than 10³. Also, the ratio of tubing length to D_h is quite high, typically for this case $L/D_h > 600$. In referring to Kays and London, "Compact Heat Exchangers" for this flow regime and for (essentially) a rectangular tube (each flow channel between the fins being somewhat rectangular), the convective heat-transfer coefficient, h , is inversely proportional to the Reynolds number to the unity power, $h \approx N_{Re}^{-1}$. Therefore, h is independent of the helium mass flow, M , and dependent only on the Prandtl number, $N_{Pr}^{1/3}$, specific heat, C_p , viscosity, microns, and inversely to the D_h . Representing the inverse of h in the form of a thermal resistance, R , per unit length of heat exchanger tubing.

A second thermal resistance must be considered in the gas flow, that is, the resistance associated with the available enthalpy or $R = 1/M C_p$.

For the expected values of mass flow, 0.01 g/s \dot{M} 0.04 g/s, the associated mass flow thermal resistance will be: $20 \text{ k/w} > R > 5 \text{ k/w}$. Thus, the thermal transfer to the helium gas is very good compared to the enthalpy gain and the gas temperature will be quite close to the heat exchanger tube wall temperature.

UNCLASSIFIED

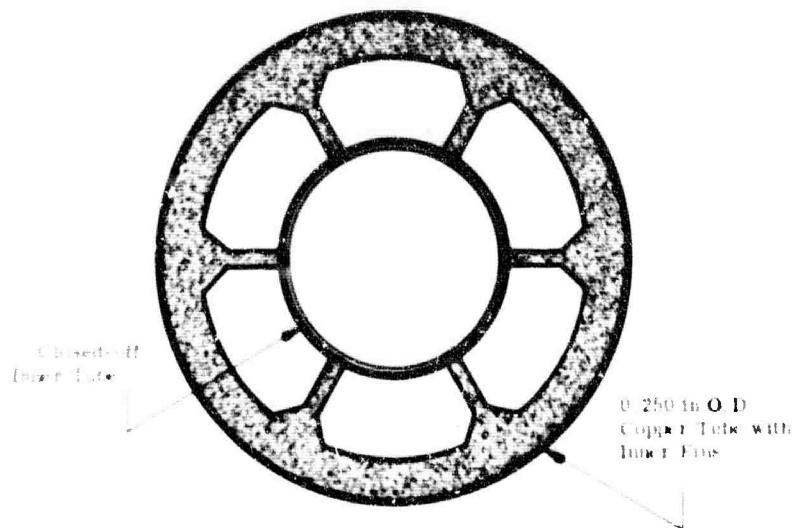


Figure 100. Proposed Heat-Exchange Tube Configuration



(a) 50X



(b) 400X

Figure 101. Bond Line - Heat-Exchange Tubing Fin Tip to Inner Tube Bend

UNCLASSIFIED

UNCLASSIFIED

The practical aspects of filling of the helium storage containers must be considered. Provisions for filling in either a horizontal or a vertical position must be made. Figure 102 shows schematically the canted storage container orientation. The criteria here is to place the container vent outlet in the uppermost position for either a horizontal or a vertical position.

For support mounting two concentric sets of radial ball mounts using pyrex spheres in hardened metal ball seats are proposed, with the intermediate interface of each concentric set being the radiation shield, thus providing a heat stationing of the support thermal transfer. From the outer shell to the radiation shield a total of eight balls will be used with the preload in the area of 200 lbs, and resulting heat transfer of 0.2 watt for each ball or a total conduction of 1.6 watts to the radiation shield.

Between the radiation shield and baffle/optical structure another group of eight balls will be used radially at a preload of about 200 lbs, but the resultant heat transfer is only 0.025 watt each, total 0.2 watt, due to the lower boundary temperatures and resultant decrease in the thermal conductivity of the pyrex glass.

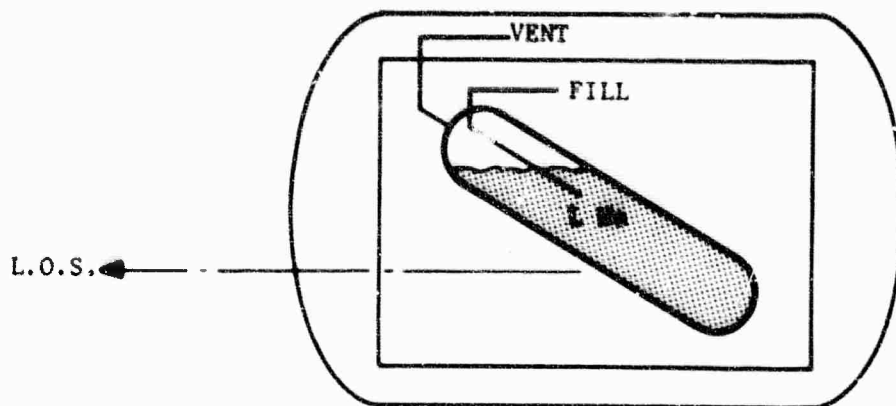
A major portion of the mechanical forces on the radiometer occur during launch and along the thrust axis. The radiometer must be very well supported along this axis, the cylindrical axis of the assembly. Between the baffle/optical structure and the radiation shield a set of three balls and three stainless steel retaining screws are planned with a thermal transfer of 0.075 watt for the balls and 0.075 watt for the retaining screws. From the radiation shield outward to the outer shell the allowed heat transfer can be greater, and the resultant thrust support incorporates a preloaded structure employing stainless steel members that also incorporate the additional heat station. The heat transfer to the radiation shield is expected to be 4.0 watts.

Radiant heat transfer from the outer shell to the radiation shield comprises the major area of this type of transfer. If opposing faces of the respective members were to be merely gold plated with typical emmittances of 0.02, the radiant heat transfer would be about 5.8 watt. To reduce this heating value, a multilayered aluminized Mylar superinsulation will be used.

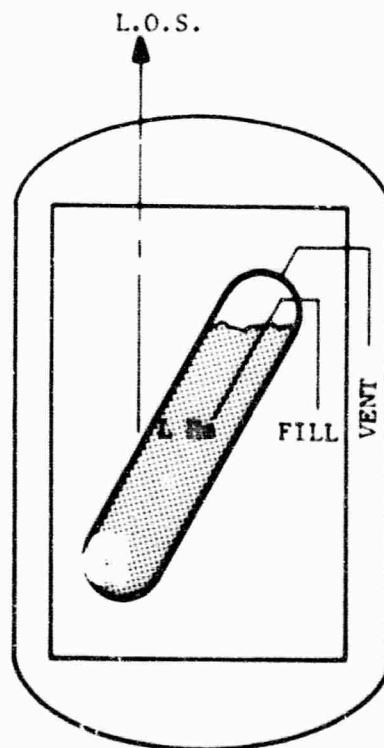
The application of as few as 10 layers of MLI will be effective in reducing the radiant transfer to the radiation shield to about 1 watt, an acceptable value.

Dissipations by the detector system, which occur during flight operations, are predominantly that of the beam chopper which has a value of 0.050 watt. Dissipations by the detectors and their closely associated preamplifiers will be in the milliwatt level and will not have a significant effect on the overall thermal balance of the radiometer. Since the detectors and the chopper must be the coldest elements of the radiometer, they will be very closely coupled

UNCLASSIFIED



HORIZONTAL LOADING POSITION



VERTICAL LAUNCH POSITION

Figure 102. Canted Storage Container Orientation

UNCLASSIFIED

UNCLASSIFIED

with copper thermal straps to the helium storage containers which is less than 7°K by design. It would be expected that the chopper will be no more than 1°K above the container temperature.

Prior to the flight operations, the radiometer will have been evacuated and filled with the helium cryogen. Once a suitable altitude has been reached, the vehicle nose cone will be ejected and the front cover of the radiometer outer shell (vacuum closure) released. With the radiometer pointing near the earth tangent there will be a substantial heat load upon the exposed front of the radiometer. The earth radiation, considered here as diffuse and at 300°K, will impose a heating of about 2.6 watts into the entrance aperture of the radiometer. The remainder of the exposed radiation shield will also have the earth heat load present, but it is expected to be able to retain the MLI on the major portion of the shield and, therefore, not grossly upset the thermal input to the shield.

Radiant thermal energy entering the aperture will be incident on all parts of the baffle, but most of the 2.6 watts will be absorbed within the first 25 cm of the baffle length as shown in Figure 103. An analogy was made of parallel discs with increasing spacing coupled with the geometrical view factors between the entrance aperture disc and discs stationed along the baffle. This analogy will hold provided that the incoming radiation is considered to be from a diffuse source, such as the earth. The two curves describe the ratio of thermal radiant energy incident to any plane relative to the energy entering the aperture, and also shown in step form is the absorbed energy relative to the energy entering the aperture.

For flight times on the order of 20 min, the heat entering the baffle represents a total energy of 3100 J, which is well within the residual energy storage capability of the helium cryogenic system. Of importance is the thermal gradients in the baffle that will result from this sudden impingement of heat energy. By using relatively pure aluminum in the baffle construction, the metallic thermal conductivity will be maintained at a fairly high value. In the temperature range of 5°K to 15°K the conductivity is not far from that of room temperatures, having fallen from a maximum in the region of 20°K to 30°K. In the first 25-cm length of baffle, the heat load will result in temperature gradients of less than 6.2°K ensuring that no part of the baffle will exceed 20°K temperature limits.

4.11 CALIBRATION

The extreme sensitivity of the instrument requires a very high-quality (low-radiation-leakage) cooled-background test chamber for all absolute calibrations (Figure 104). Two chambers which will be suitable are: the Air Force chamber at Tullahoma, Tennessee, and the Honeywell Chamber now under construction.

UNCLASSIFIED

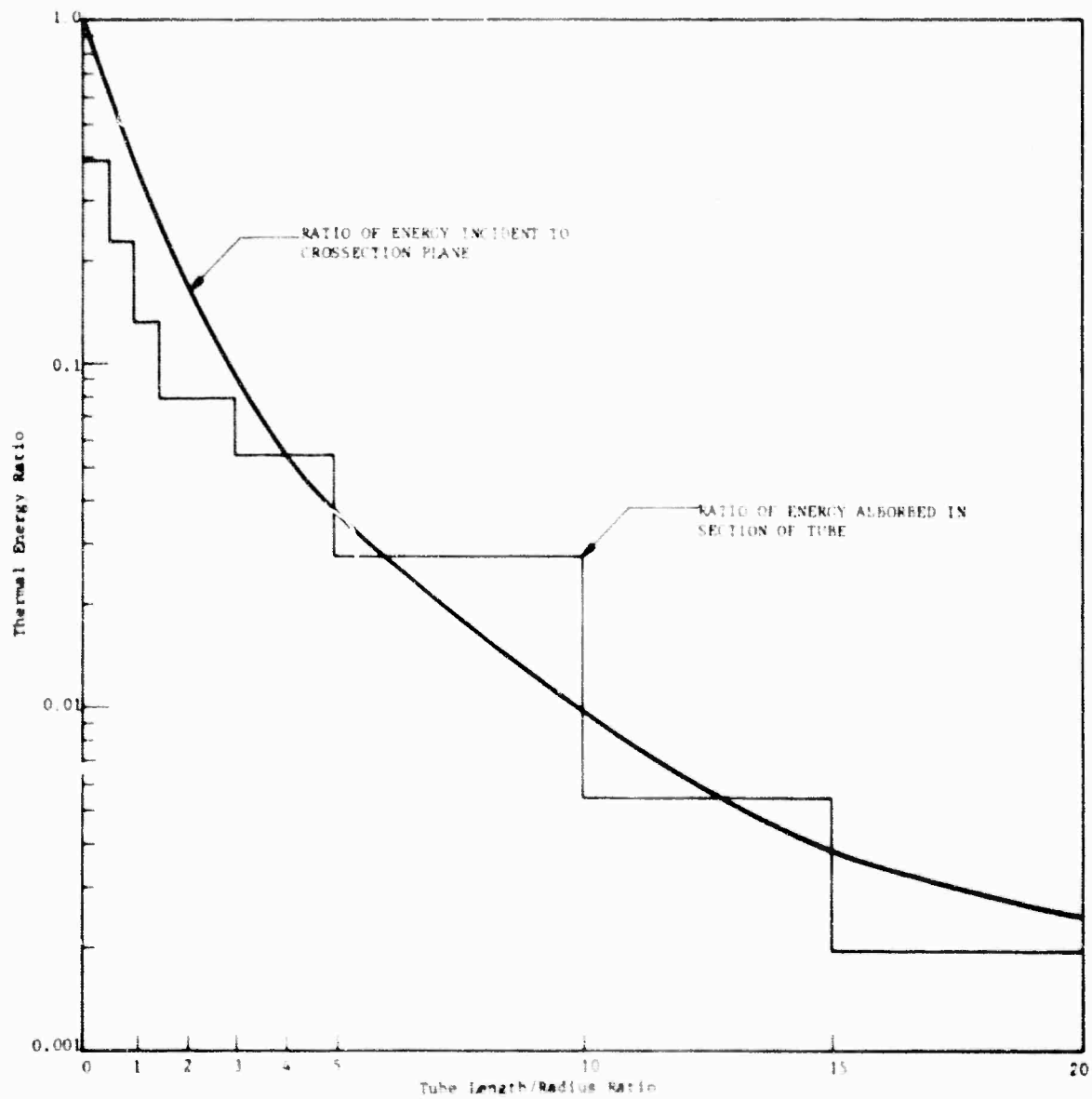


Figure 103. Baffle Length

UNCLASSIFIED

UNCLASSIFIED

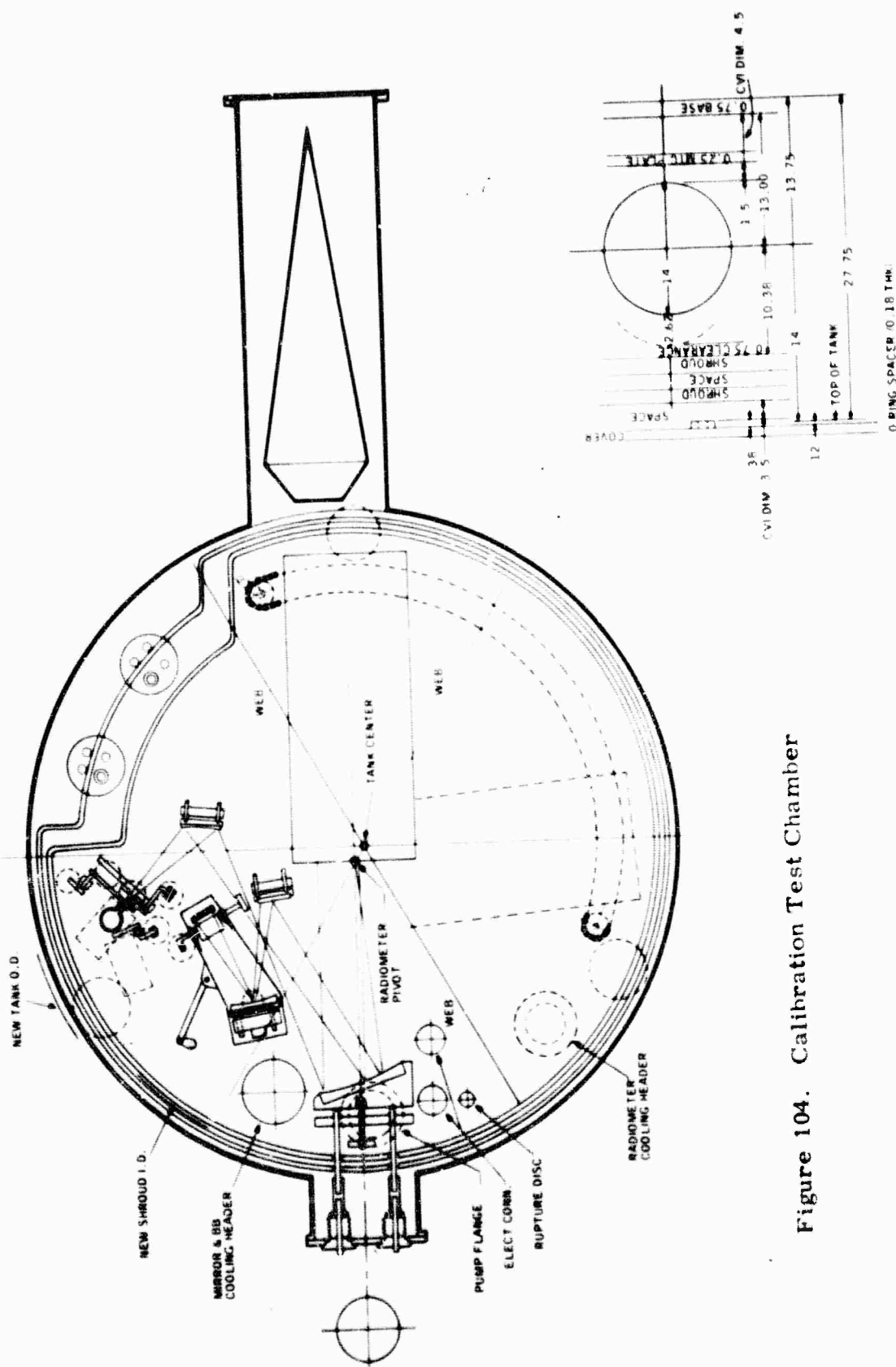


Figure 104. Calibration Test Chamber

UNCLASSIFIED

UNCLASSIFIED

A secondary calibration capability will be provided in the instrument in two places. When the cover is in place a small light (IR)-emitting laser diode (LED) source will act as a source, to traverse the entire optical system. In this way it will be possible to check the operation and calibration of the instrument on the ground, during launch and during ascent, until the cover is removed. Once the cover is off, a second LED can be stimulated on command for inflight calibration. This second diode is located behind the radiation chopper and is only operative while the chopper is closed. The optical system behind the chopper, consisting of the spectrometer and the detectors, are also stimulated. The channels which may be calibrated and checked in this manner depend on the choice of laser diode. Various LED laser diodes are available for IR wavelengths. The choice of calibration diode is still under study, and a diode type will be selected in the design phase of the program.

4.11.1 Description of Honeywell Chamber

Chamber -- The chamber is 78 in. in diameter and 28 in. high. It is fabricated of stainless steel and outfitted with two concentric aluminum shrouds -- an outer shroud cooled to 77°K with liquid nitrogen and an inner shroud cooled to 20°K using liquid helium. A 45-in. chamber extension houses a helium-cooled radiation trap which absorbs collimated radiation passing the radiometer when it is rotated to an off-axis position. The interior of this trap and the inner shroud are painted with 3M Black Velvet to ensure absorptivities greater than 0.9. The chamber is capable of maintaining a vacuum level of 10^{-6} torr.

Blackbody Source and Attenuator -- The blackbody source is configured as an off-axis recessed cone (length/diameter = 3) made from aluminum with internal specular black surfaces. This configuration has demonstrated a directional emissivity of > 0.999 over a cone angle of at least 10 deg. The source is initially directly cooled by liquid nitrogen, and temperature subsequently can be controlled to within 0.1°C using a platinum resistance thermometer within the block and a proportional control amplifier driving a nichrome wire heater.

Directly in front of the source are mounted an aperture wheel, a chopper, and an attenuator. The attenuator is an integrating sphere coated inside with a diffuse, highly reflective paint. This combination is capable of reducing the transmitted source energy by a factor of 10^5 . Output from the attenuator passes through a filter wheel and a variable aperture plate which defines the size of the simulated point source.

Point-Source Optics -- From the point source aperture, the beam is directed in an $f/4$ cone to an elliptical mirror which reimages it. Stray radiation is trapped in the process, and the well-defined beam continues on to an off-axis parabolic mirror which collimates it in the direction of the radiometer. Both the aperture and collimating mirror will be adjustable from outside the chamber through sealed bellows linkages.

UNCLASSIFIED

Extended-Source Optics -- A 2 in. x 4 in. heated flat plate radiates to an elliptical mirror which reimages it just below the point source reimage position. A flat mirror then directs this radiation to the parabola where it is superimposed on the collimated point source beam. The extended source represents a horizontal angular spread of 10 deg and a vertical angular spread of 5 deg, it is adjustable vertically from 1/2 deg to 8 deg below the radiometer optical axis.

All mirrors are made of ULE fused silica, with a gold coating, and are cooled conductively with liquid helium through lines attached to the mounting plate.

Shrouds and Baffles -- Liquid-helium-cooled shrouds and baffles are located within the chamber to minimize stray reflections and self-emission, particularly into the radiometer field of view. All internal exposed surfaces are coated with 3M Black Velvet to achieve absorptivities greater than 0.9.

Temperature Monitoring -- Temperatures of the sources, mirrors, point source aperture, and chamber walls are monitored with platinum resistance surface temperature sensors.

Error Analysis -- A calibration accuracy of approximately 5% is estimated for this chamber.

4.11.2 Calibration Tests

The following tests will be performed to obtain a ground calibration of the radiometer:

- (1) Chamber functional checkout
- (2) Experimental verification of error analysis; the PCC will be calibrated and its accuracy established
- (3) Radiometer functional checkout
- (4) Voltage-irradiance calibration: data will be obtained to produce a curve relating watts/cm² incident on the aperture to output voltage of the radiometer; this measurement will be repeated several times.
- (5) Off-axis rejection measurement; the capability of the radiometer for rejecting off-axis radiation while measuring radiation from a point source will be determined; the radiometer will be subjected to radiation from 1/2 deg to 8 deg off-axis.

UNCLASSIFIED

- (6) Voltage-irradiance calibration verification; upon completion of tests at HI, the radiometer will be shipped to AEDC, Tullahoma, where the voltage-irradiance calibration will be repeated in the 7-volt LWIR sensor test chamber.

The following tests will be conducted to calibrate and verify the stability of the inflight calibrator:

- IFC functional checkout.
- Calibration and stability; the IFC will be operated immediately after each of the voltage-irradiance calibration tests described above (4); these tests will provide a calibration and measure of short- and long-term stability of the IFC.
- Calibration and stability verification; in conjunction with test item (6) above, the IFC will be retested in (2) above at AEDC, Tullahoma, to verify calibration accuracy and stability.

UNCLASSIFIED

SECTION 5 SYSTEM DESIGN

5.1 CANDIDATE ROCKET VEHICLES

5.1.1 Vehicle Comparison

The investigation of rocket vehicles as candidates for the limb radiance measurement mission centered on those having over 200 lb payload and over 300-km altitude capability. Inquiries were made of rocket manufacturers on this basis, soliciting information on configurations and performance for vehicles operational in the 1971 to 1973 time period. Vehicles having one and two stages, within the 13-in. to 31-in. diameter range, and having total impulse in the range of about 3×10^5 to 3×10^6 lb-sec have been noted for consideration. Both solid- and liquid-propelled vehicles were included in the study. In one case, a new and proprietary solid fuel has been suggested as having significantly lower costs and wider temperature tolerance. In general, the rockets of interest are not those prominent in earlier rocket missions, most of which were carried out at lower altitudes, or, where higher altitudes were flown, made use of many stages.

Salient points of comparison of 11 rocket vehicles are given in Figure 105 and Table 22. The former shows graphically the relationship of peak altitude to payload weight as reported by different rocket manufacturers; the latter is a tabulation of key information relating to vehicle application. In Table 23, it is seen that, for payload weights greater than 400 lbs and altitudes greater than about 400 km, 31-in. diameter vehicles are required. Among the smaller-diameter vehicles, Aerobee 350, Astrobee F, and Black Brant VB have the best altitude-weight performance. Of these, Astrobee F is not a flight-proven vehicle, though it may be operational in 1971.

Aerobee 150/170 vehicles have inadequate performance for the limb measurement mission and will not be considered further. Sandhawk-Tomahawk, though capable of altitude performance in the 500- to 700-km range for 100-lb and 200-lb payloads, does not appear adequate either. Its small diameter indicates the need of a bulbous payload with performance degraded to less than that given in Figure 105. Sandhawk has an excellent flight history, having flown 250 to 300 flights in single- and two-stage versions with virtually no failures and with payloads up to 12 in. in diameter weighing 220 lbs. Thiokol has suggested Terrier, a surplus Navy item, as a boost stage for Sandhawk-Tomahawk to raise its apogee perhaps 300 to 400 km. The Terrier-Sandhawk and Sandhawk-Tomahawk combinations have flown but not in the combination of all three vehicles. The altitude-weight possibilities of this three-stage version would bear further study if payload diameter can be of the order of 12 in.

UNCLASSIFIED

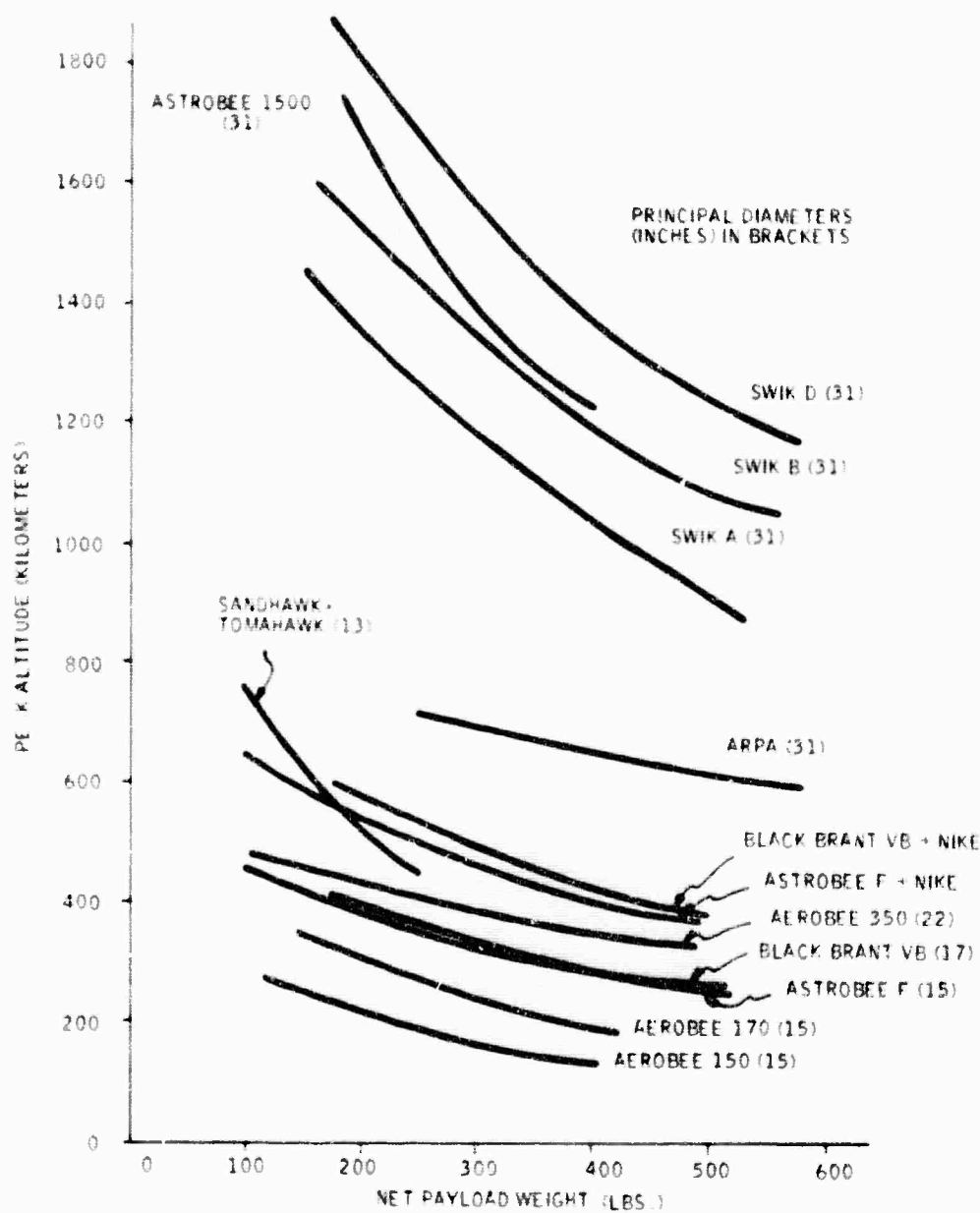


Figure 105. Rocket Vehicle Payload/Weight Comparisons

UNCLASSIFIED

Table 22. Research Rocket Summary

Vehicle	Manufacturer	Principal Diameter (inches)	Price Range (\$1000)	Recovery System Status	History	
					Flights	Success
SWIK A	Atlantic Research	31	210-275	System not available	7	7
SWIK B	Atlantic Research	31	210-275	System not available	0	0
SWIK D	Atlantic Research	31	210-275	System not available	0	0
ARPA	Atlantic Research	31	210-275	System not available	5	5
Astrobee 1500	Aerojet General	31	150-225	System not available	10	6
Aerobee 350	Aerojet General	22	140-	System designed; first flight date late 1969	3	3
Astrobee F	Aerojet General	15	25-30	Will use Aerobee system	In development	
Aerobee 170	Aerojet General	15		Replaces Aerobee 150		
Aerobee 150	Aerojet General	15		System available	Over 600 flights	
Black Brant VB	Bristol Aerospace	17	33-34	Skylark system flown Modified Sandia system over-water flight late 1969. Bristol system available May 1970.	18	0
Sandhawk Tomahawk	Thiokol	13			One flight to date; several flights scheduled late 1969. Over 250 Sandhawk flights (1 and 2-stage versions).	

UNCLASSIFIED

Table 23. Research Rocket Power Plants Summary

Power Plant			Total Impulse (100 lb/sec)			Launch Considerations
First Stage	Booster	Second Stage	First Stage	Second Stage	Total	
Castor (XM-33)	2 Recruits	Antares 1 (X-251)	1,889	534	2,423	Boom or rail, sites include:
Castor (XM-33)	2 Recruits	Antares 2 (X-259)	1,889	640	2,529	Wallops, WTR, Green River,
Castor II (TX 354)	2 Recruits	Antares 2 (X-259)	2,167	640	2,807	Churchill, Johnson Island, Kauai
Castor (XM-33)	2 Recruits	TX-261	1,889	726	2,615	
Aerojet Junior	2 Recruits	Alcore 1B	1,800	258	2,058	Boom
Cluster: 4 Aerobees (Liquid)	Nike (MSE1)		1,142		1,142	Towers at Wallops and WSMR
Dual thrust solid (Developmental)	Can use Nike		557		557	Nike and tower launchers
Aerobee 150 A (Liquid)	Nike					Nike and multi- purpose launchers; also tower launchers
Aerobee (Liquid)	Aerojet Vari- booster (solid)		289		289	Tower launch at WSMR, Eglin, Churchill, Wallops, Natal
26 KS 20,000	Nike boost under study		506		506	Rail
Sandhawk (TE-M-473)	Terrier a possibility	Tomahawk (TE-M-416)	275	94	369	Rail or boom

(Motors have solid propellant except where noted)

UNCLASSIFIED

UNCLASSIFIED

The Black Brant VB is the most likely candidate among the Bristol Aerospace vehicles. The Black Brant IV family has only 10-in. diameter forward hardware, and payload weights heavier than 200 lbs are conjectural. Of this family the Black Brant IVA has flown, its heaviest payload being 198 lbs with apogee altitude of 600 km. Black Brant VB has had 18 flights with no failures. Its 17-in. diameter is compatible with that of Nike, and the possibility of a Nike boost has been under study by NASA. As seen in Figure 105, the predicted performance of Black Brant VB with Nike boost exceeds that of Aerobee 350. The VB has been flown using the Skylark recovery system, and a modified Sandia system has been flown successfully by NRL from Wallops with water recovery. Bristol is developing its own recovery system to be flown in May 1970.

The Astrobe F rocket is a proprietary development which may be operational by 1971. Designed to make use of existing Aerobee subsystems (attitude control, recovery, payload housing and extensions), it features a new solid propellant material. This material has wide range of burning rates which makes it possible, with a single motor, to have a high-thrust delivery for liftoff followed by a low-thrust regime for climb. This dual-mode burning characteristic creates the effect of having an auxiliary booster at launch. In addition, the new material has increased tolerance to temperature extremes and costs an order of magnitude less than conventional solid propellant. The altitude-weight performance of the Astrobe F approaches that of the Aerobee 350, but its cost will be about one-fourth of the 350's. Its altitude-weight performance, as shown in Figure 105, is expected to surpass that of the Aerobee 350 with Nike boost. Although its maximum payload weight has not been specified, Aerojet-General feels it may be 500 lbs or more.

The Aerobee 350, a Nike-boosted, liquid-propellant rocket, was developed by NASA prompted by the need to carry large-diameter optical systems aloft for longer periods. Its altitude-weight performance is the best of the less than 31-in. diameter rockets shown in Figure 105. Its price is also the highest in this diameter class. It has made three successful flights and is considered to be qualified. Eight more flights are scheduled in the next two years from Wallops and White Sands Missile Range -- the only locations at which the 350 is flown. The requirement for a tower restricts launching to these two sites although some consideration has been given at NASA to the possibility of rail launching, using a Nike-Hercules or other heavy-duty rail or boom launcher. Additional tower launchers are estimated to cost about a quarter million dollars. A recovery system for the Aerobee 350, patterned after that of the Aerobee 150, is expected to be flight-tested in late 1969.

The 31-in. diameter vehicles include the Astrobe 1500 and the Castor-based SWIK's and ARPA vehicles. The Castor-based rockets are similar to the Athena vehicle which at mid-1969 had had 116 flights with 91 successful. The standard SWIK (SWIK A) has had seven flights, all of them successful. The SWIK B and D are upgraded versions of the standard SWIK but have not

UNCLASSIFIED

flown. The ARPA vehicle has had five flights, all successful. The commonality of these vehicles can be seen in the Table 23 power plant listing. It is seen that they can use Castor I or Castor II first stages with two strapped-on Recruit motors for boost; second stages are Hercules Antares 1, Antares 2, or the Thiokol TX-251 motor. These are similar motor combinations to those used for the first and second stages of Athena, the vehicle used in penetration-aids research. The Castor NM-33 with two Recruit boost motors has been successfully flown over 200 times, and the Castor TX-354 motor is used as the second stage of the Scout launch vehicle.

The similarity of the Atlantic Research SWIK vehicles and the Aerojet-General Astrobee 1500 can be noted. The Astrobee 1500 uses the Aerojet Junior as a first stage augmented by two Recruit boosters in the manner of the SWIK vehicles. The Alcor 1B is the second stage. The Aerojet Junior motor was originally developed for the Jupiter program and has been used as the backup second stage of the Scout vehicle. The Alcor motor was developed for use as an upper stage in the Scout program, and the Alcor 1B, an improved version of the original Alcor, was developed for the Athena program. The Astrobee 1500 has a first-stage total impulse of about 1.8×10^6 pound-seconds, nearly that of the SWIK A, B, and ARPA vehicles, but its second-stage total impulse is about one-third to one-half of these vehicles.

Of the 31-in. diameter vehicles shown in Figure 105 the ARPA has the lowest altitude performance. The weight of this vehicle, both before and after propellant burning, is appreciably heavier than that of the SWIK A, making it a less likely candidate.

5.1.2 Summary and Conclusions

An investigation of rocket vehicles operational in the 1971-1973 time period was made using information contributed by four vehicle manufacturers. The vehicles considered have one or two stages, and most use auxiliary boost for high initial thrust. Both solid- and liquid-propelled vehicles were included in the survey.

Vehicles having less than 22-in. principal diameter have peak altitudes below 400 to 500 km with payloads of 300 to 500 lbs. For higher missions, it is necessary to resort to 31-in. diameter vehicles having peak altitudes on the order of 900 to 1500 km. These larger vehicles have significantly higher costs, and none have recovery experience. However, if flown from a range having a central latitude, it is estimated that their more extensive view coverage would make necessary about half the number of flights as would be the case using less than 22-in. rockets flown from a southerly and northerly latitude.

For missions in the peak altitude range of 300 to 400 km, the Nike-boosted Astrobee 350, Astrobee F, and Black Brant VB are candidates. Of these,

UNCLASSIFIED

Astrobee 350 is limited to tower-launch locations and is considerably more expensive than the other two candidates. Astrobee F has attractive features but its availability in 1971 is not ensured. Black Brant VB requires qualification flights with the Nike boost but offers a competitive price, a good flight record, and a slightly larger payload diameter than the Astrobee F.

For missions in the peak altitude range above 1000 km, SWIK A and Astrobee 1500 have flight experience. SWIK B and D offer best altitude-payload weight performance and proven motors although not flight-proven in these specific combinations.

For this program, the Black Brant VB has been selected as the candidate vehicle, offering 250- to 300-km altitudes with net payloads in the range of 300 lbs and an excellent success record. In addition, this vehicle offers the possibility at a simple extension to 500-km altitudes through addition of a Nike boost stage.

5.2 SELECTED VEHICLE DESCRIPTION

The Black Brant V is a single-stage, solid-propellant, rocket available in three standard configurations - VA, VB, and VC. These three configurations are similar in external appearance and launch weight but differ in that the VB and VC have a higher-performance motor than the VA. The VA and VB have three external fins and are designed to be launched from a 35-ft long boom-type launcher fitted with underslung forward and rear rails which provide 15 ft of travel and zero tipoff. The VC has four fins and is designed for launch from existing towers at Wallops Island and White Sands. The Black Brant V motor characteristics are shown in Table 24, and typical performance data for the three configurations are shown in Table 25.

Figure 106 shows the nominal apogee height versus gross payload weight for the three standard Black Brant V configurations. These data show that the Black Brant VB has the highest performance; therefore this configuration is covered in greater detail in the following paragraphs.

The Black Brant gross payload is the total weight forward of station 0.0 (Figure 107) including the nose cone, any cylinder extensions required and the igniter housing. The standard nose cone weighs 53 lbs, the Black Brant VB igniter housing weighs 19 lbs, and the standard cylinder extensions weigh approximately 7 lbs plus 1 lb per inch of length. Figure 108 shows the apogee versus payload weight for launch angles between 75 and 87 deg. In this illustration, the net payload is gross payload less the weight of the standard nose cone, igniter housing and a 21-in. cylinder extension. As an example, the Black Brant VB will carry a net payload of 300 lbs to an apogee between 250 and 300 km, depending on quadrant elevation.

UNCLASSIFIED

5-10

Table 24. Black Brant V Motor Characteristics

Item	Configuration	
	VA	VB and VC
BAL Motor Designation	15KS25000	26KS20000
Length (inch)	210	210
Diameter (inch)	17.2	17.2
Grain Configuration	6 Pt. Star Center	Shell-Slot
Auto-ignition temp ($^{\circ}\text{F.}$)	527	527
Total impulse (lb-sec)	383,000	506,000
Average thrust (lb.)	25,200	17,025
Average chamber pressure (psi)	810	663
Burning time (sec)	13.2	26.9
Action time (sec)	18.1	32.4
Operating temperature range ($^{\circ}\text{F.}$)	0 to 120	-10 to +125

Table 25. Typical Black Brant V Performance
Data (308-pound gross payload)

Item	Configuration		
	VA	VB	VC
Q.E. (deg)	85	85	85
Apogee (km)	181	375	352
Time to apogee (sec)	220	330	310
Range at impact (km)	93	269	258
Time to impact (sec)	410	605	580
Maximum velocity (ft/sec)	6200	8500	8500
Maximum longitudinal acceleration (g)	16	15	15
Maximum dynamic pressure (lb/ft ²)	11,600	5,900	5,900
Terminal roll rate (rps)	0 or 4	0 or 4	0 or 4
Burnout (sec)	T + 18	T + 33	T + 33
Burnout altitude (km)	18.9	38.7	38.7

UNCLASSIFIED

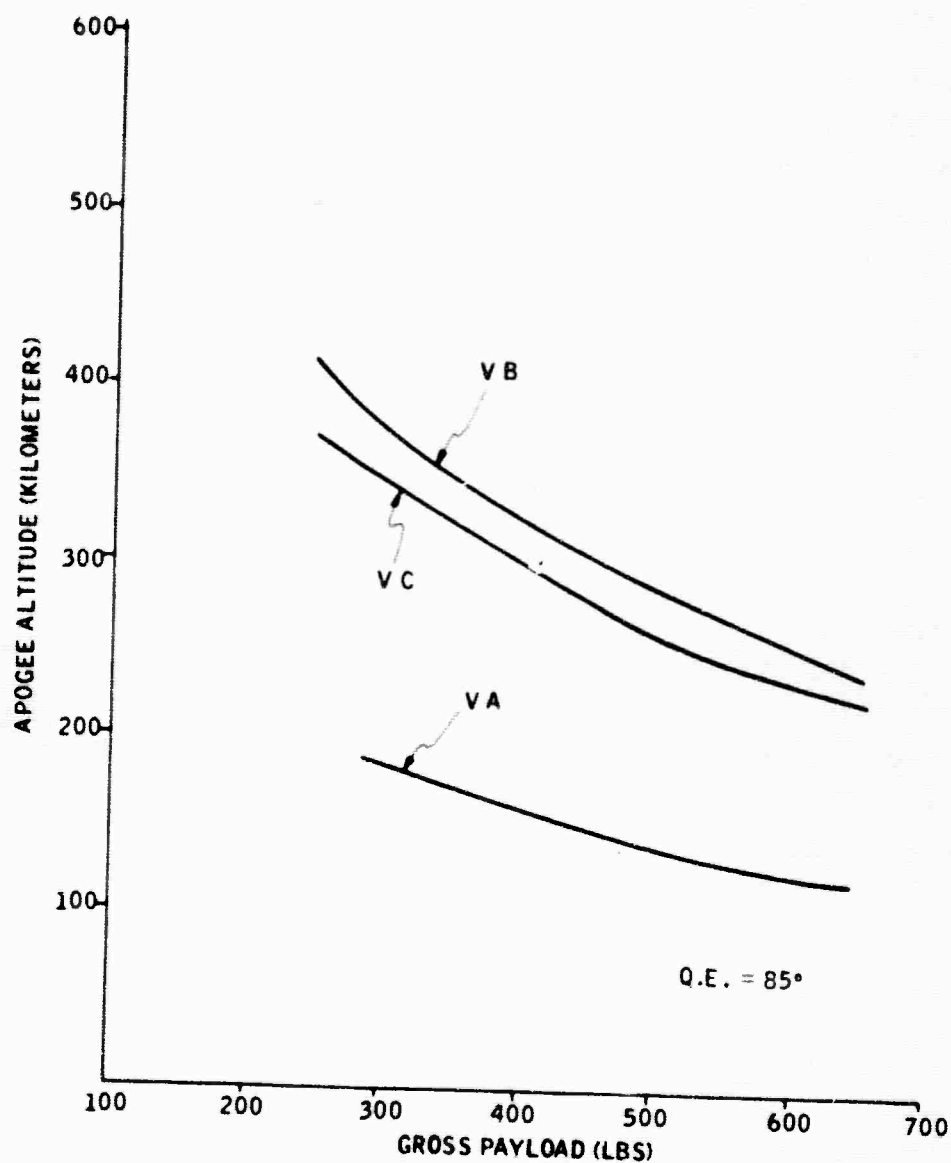


Figure 106. Black Brant V Apogee versus Gross Payload Weight

UNCLASSIFIED

UNCLASSIFIED

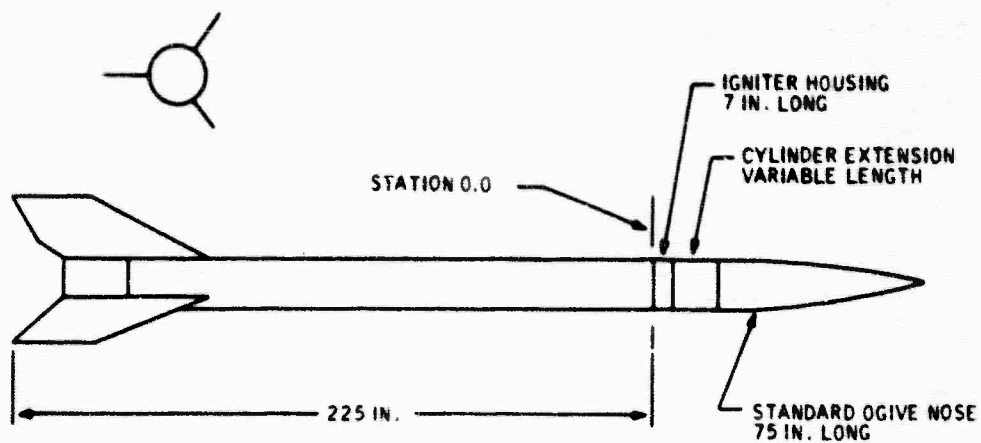


Figure 107. Black Brant VB Configuration

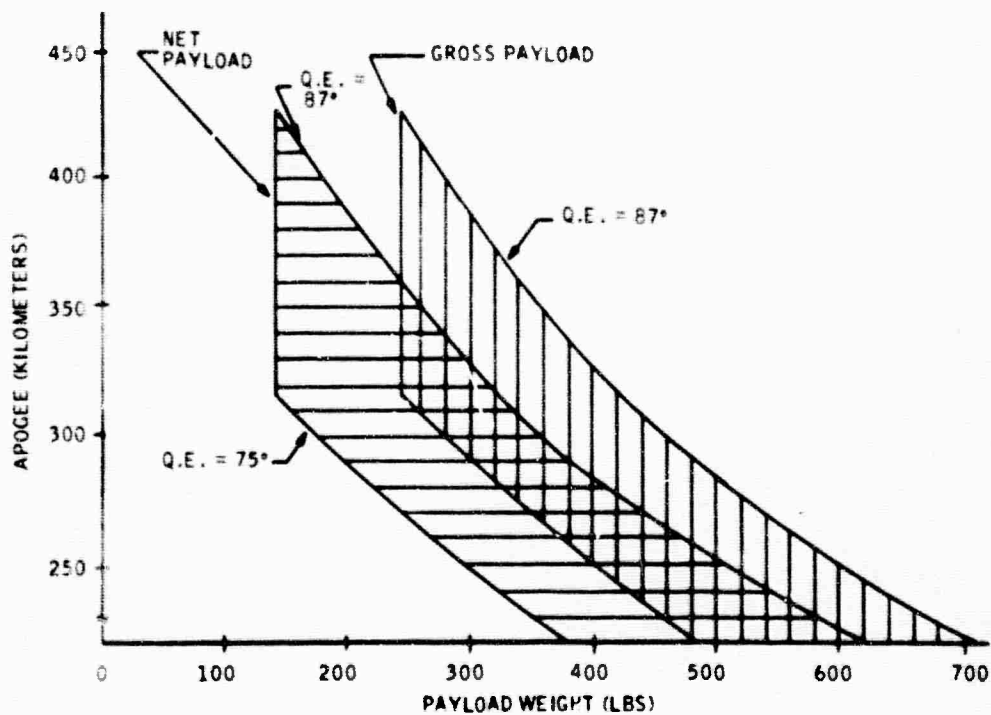


Figure 108. Black Brant VB Apogee versus Payload Weight

UNCLASSIFIED

UNCLASSIFIED

The Black Brant VB launch acceleration will vary from a maximum of over 16 g's to a maximum of less than 10 g's depending on payload weight, launch angle and other factors. Figure 109 shows the launch acceleration time history for several typical launch configurations.

The Black Brant VB standard nose is an ogive fairing with a 4.25:1 fineness ratio available either in stainless steel or fiberglass. The nose fairing is 75 in. long with a maximum diameter of 17.2 in. The payload compartment length can be increased to a maximum of 145 in. by adding standard cylindrical extensions. Figure 110 shows the center of gravity restrictions for Black Brant VB payloads.

The Black Brant VB can be flown with fins set to produce either a nominal zero (± 0.5 rps) rate or be set to give the roll history shown by Figure 111.

There have been 18 flights of the Black Brant VB, through August 1969, with no failures. The predicted success ratio for achieving expected altitudes and flight performance of 99%.

The payload recovery system history for the Black Brant V is as follows: The Skylark recovery system has been used on the Black Brant VA. Five recovery systems have been flown; the last three resulted in successful recoverys. The five systems were all launched from Churchill with land recovery. The Skylark recovery system is 17.05 in. long, weighs 70 lbs, has an impact velocity of 30 ft/sec with a 500-lb payload and will recover a payload with a maximum gross weight of 500 lb.

Bristol Aerospace is designing a parachute recovery system specifically for the Black Brant VB and VC. Both the logic system and the parachute have been independently flown. This system is 12 in. long, weighs 70 lbs, uses a 28-ft main chute, has an impact velocity of 28.3 ft/sec with a 400-lb payload and will recover a maximum payload of 500 lbs. This system is scheduled to be launched aboard a Black Brant VC in May 1970 followed by a second launch from White Sands in November 1970.

The Naval Research Laboratories are flying a modified "Sandia" recovery system on Black Brant VBs. The standard parachute has been replaced by a larger unit to permit recovery of heavier payloads. The first launch is scheduled for November 1969. The Air Force Cambridge Research Center is reported to have scheduled two Black Brant VB launches from Eglin with recovery. An "air snatch" is planned using a C130 aircraft. The recovery system used would be similar to the Bristol system but with heavier shrouds. Figures 112 and 113 show typical impact range and impact dispersion data for the Black Brant VB. Impact dispersion can be reduced to approximately one-third of that shown by Figure 112 by using the Black Brant VC and a tower launch from Wallops or White Sands.

The current price of Black Brant V rockets is shown by Table 26. The prices are in US dollars and are FOB Winnipeg, Canada.

UNCLASSIFIED

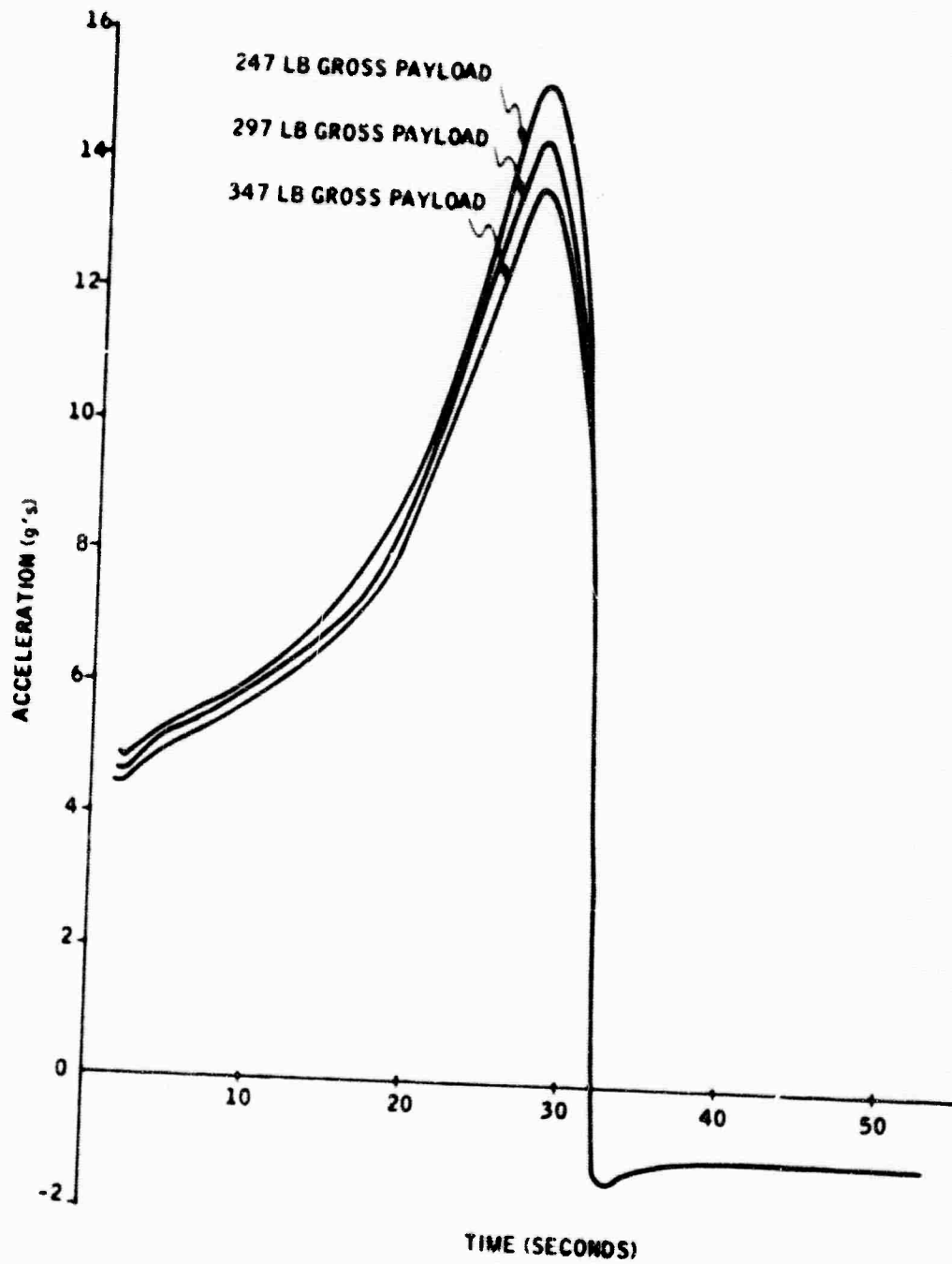


Figure 109. Black Brant VB Acceleration versus Time

UNCLASSIFIED

UNCLASSIFIED

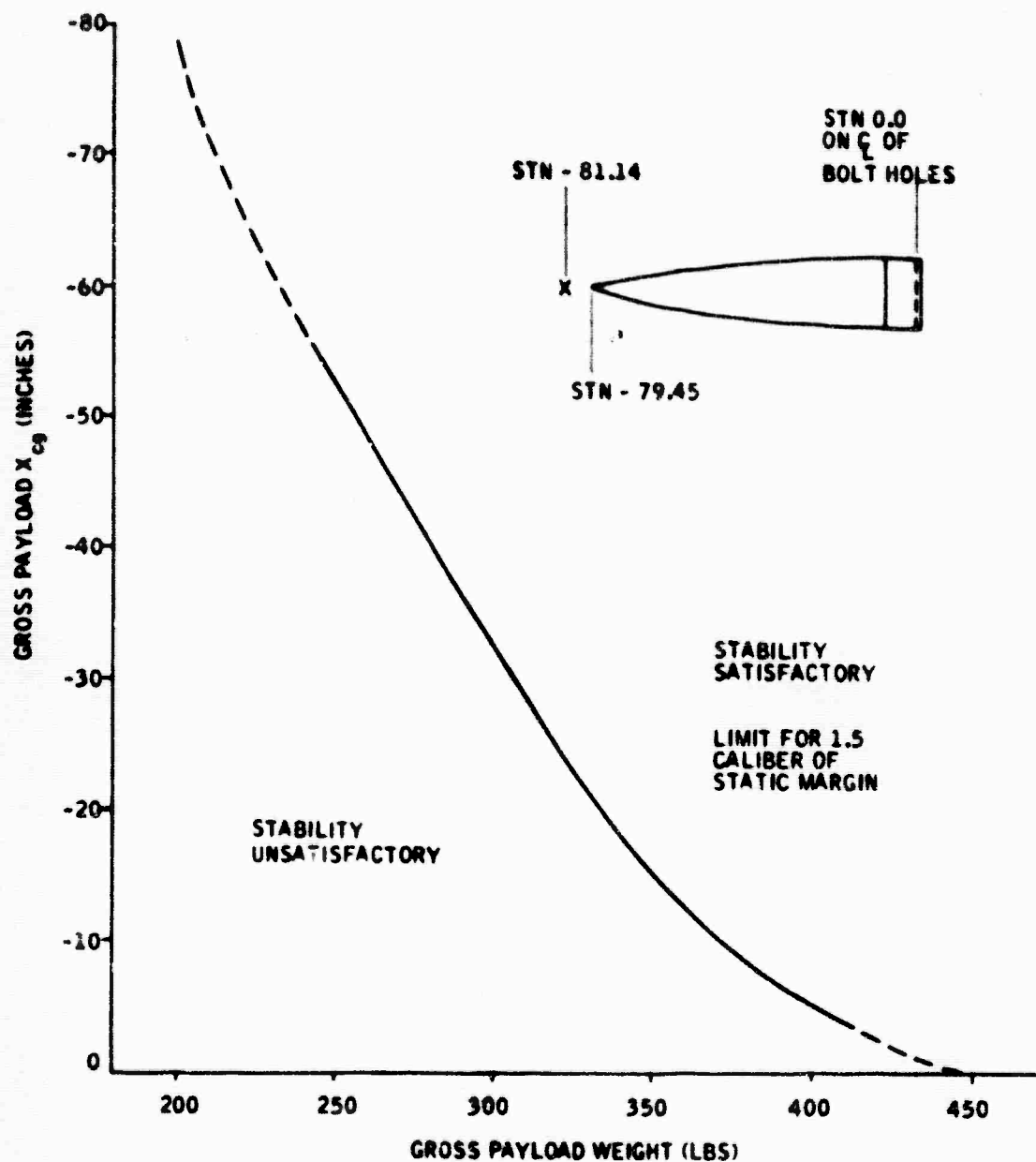


Figure 110. Black Brant VB Standard Nose Assembly Gross Payload X_{cg} versus Gross Payload Weight

UNCLASSIFIED

UNCLASSIFIED

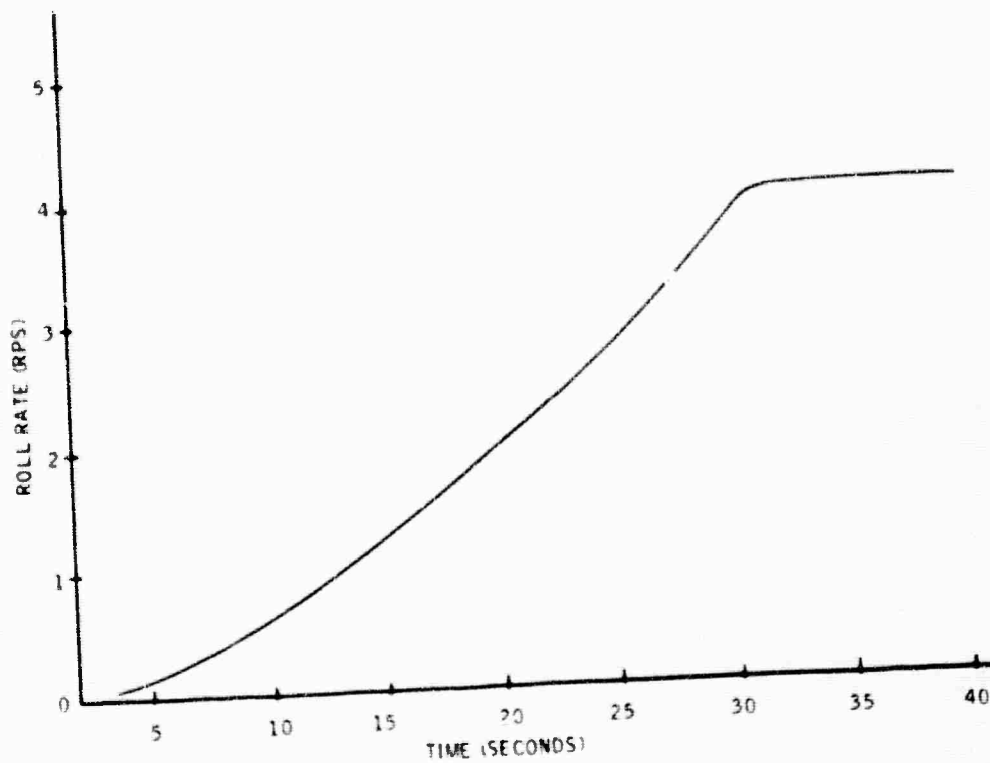


Figure 111. Black Brant VB Roll Rate versus Time

UNCLASSIFIED

UNCLASSIFIED

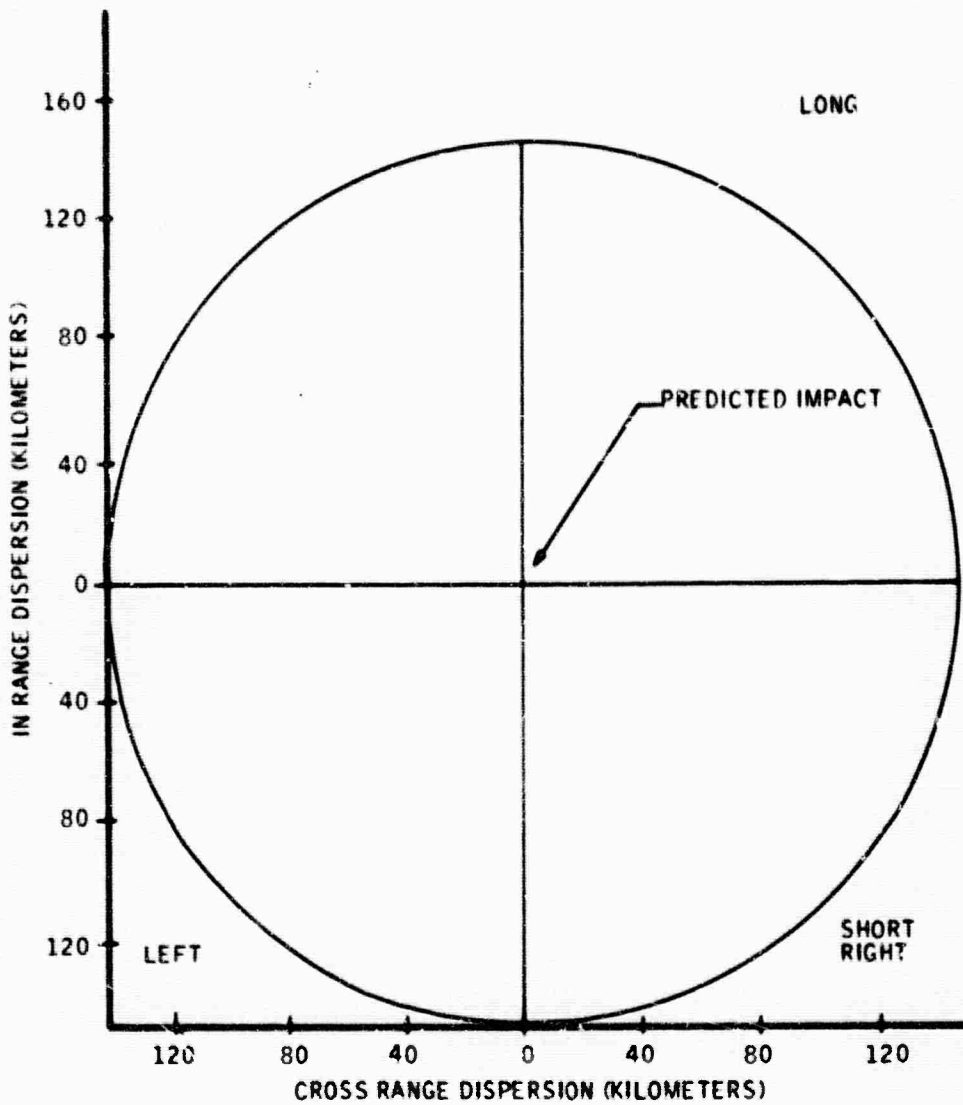


Figure 112. Black Brant VB Three-Sigma Impact Dispersion

UNCLASSIFIED

UNCLASSIFIED

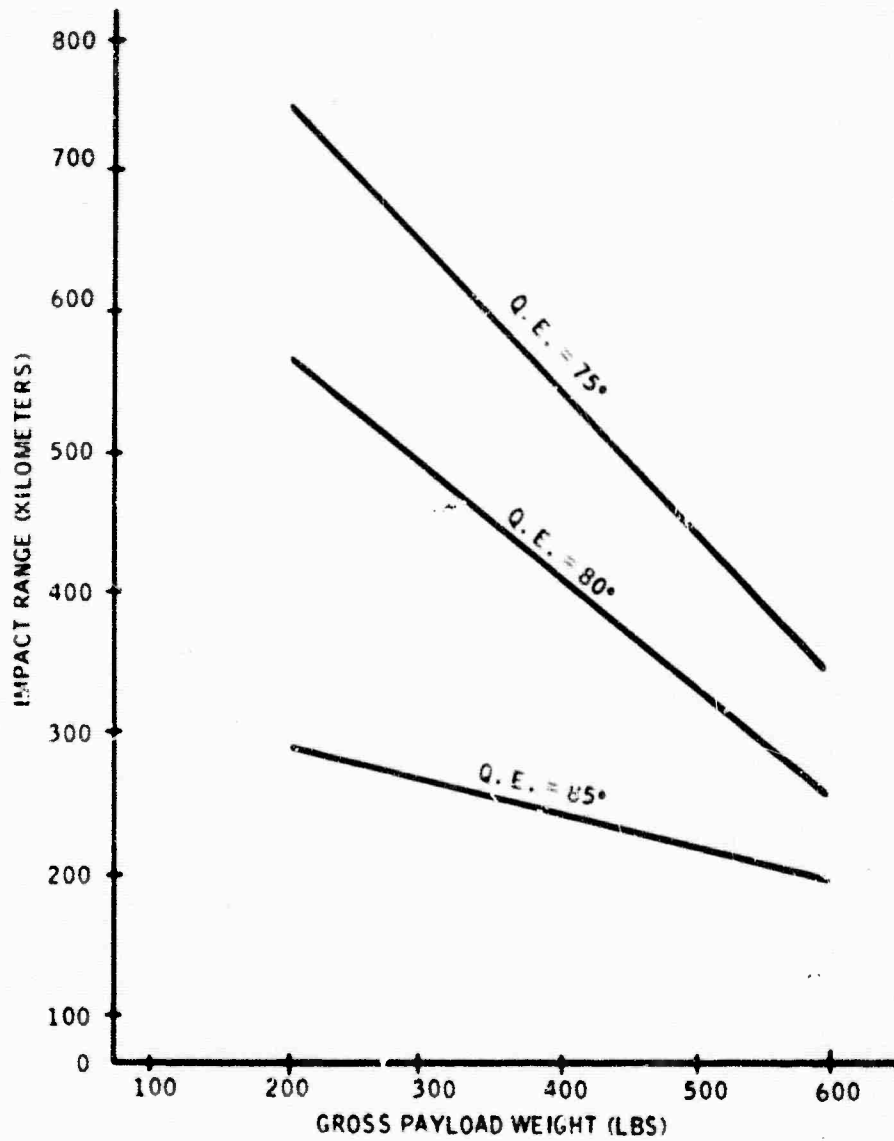


Figure 113. Black Brant VB Impact Range versus Gross Payload

UNCLASSIFIED

UNCLASSIFIED

Table 26. Cost of Black Brant V Rockets

Part No.	Description	Cost		
		BP VA	BB VB	BB VC
600-00045	Nose assembly including:	\$ 2,230	\$ 2,230	
-00017	Fiberglass ogive nose fairing			
-00013	Igniter housing with forward launch lug			
600-00045	Nose assembly including			\$ 2,236
-00017	FRP fiberglass ogive nose fairing			
-00115	Igniter housing filtered with ribbing shoes			
600-00046-1	15 KS25,000 rocket motor including igniter assembly	\$16,940		
600-00046-3	15 KS20,000 rocket motor igniter assembly		\$23,580	\$23,580
600-00048	Nozzle assembly	\$ 1,060		
600-00048-3	Exit cone assembly		\$ 1,350	\$ 1,350
600-00047	Tail assembly including: aft body assembly with rear launch lugs and fin assembly	\$ 6,320	\$ 6,320	
600-00047-11	Tail assembly including: 4-fin assembly and rubbing shoes			\$ 8,130
Total Cost		\$26,500	\$33,480	\$35,290

UNCLASSIFIED

The Black Brant altitude-payload performance can be increased by using a boosted system similar to that used on the Aerobee 170 and Aerobee 350. With this system, a Nike booster is attached to the bottom of the Black Brant through a spigot system.

The Nike adds an average of 50,000 lbs of thrust for the first 3.2 sec of flight and then falls away from the Black Brant. Figure 114 shows a preliminary comparison of the altitude-payload weight performance of a Black Brant VB and a Nike-boosted Black Brant VB. It is estimated that the use of the Nike booster system would add from \$6,000 to \$7,000 to the cost of the Black Brant VB in addition to the cost of development engineering and rocket qualification flights.

The addition of a Nike-boosted stage to the Black Brant results in an increase in apogee altitude and an increase in the total time available for measurement. Trajectories have been computed for the Black Brant VC, and these are shown in Figure 115. About 80 sec are consumed in pre-measurement maneuvers in both cases. The apogee altitude in the Nike-boosted case is about 45% higher, and the total measurement time is 480 sec or about 23% longer than if the VC were not Nike boosted.

The Black Brant VB has slightly better performance than the VC as shown in Table 27. These are nominal values with a gross payload weight of 547 lbs and Q. E. of 85 deg.

Table 27. Performance Comparison of Black Brant Vehicles

Vehicle	Nike-Boosted	Apogee Altitude (km)	Measurement Time (sec)
VB	No	270	420
	Yes	390	510
VC	No	250	390
	Yes	360	480

5.3 AUXILIARY SUBSYSTEMS

The proposed auxiliary subsystems consist of the payload supporting structure, attitude control, attitude determination, telemetry, tracking, electrical power, separation, and recovery.

UNCLASSIFIED

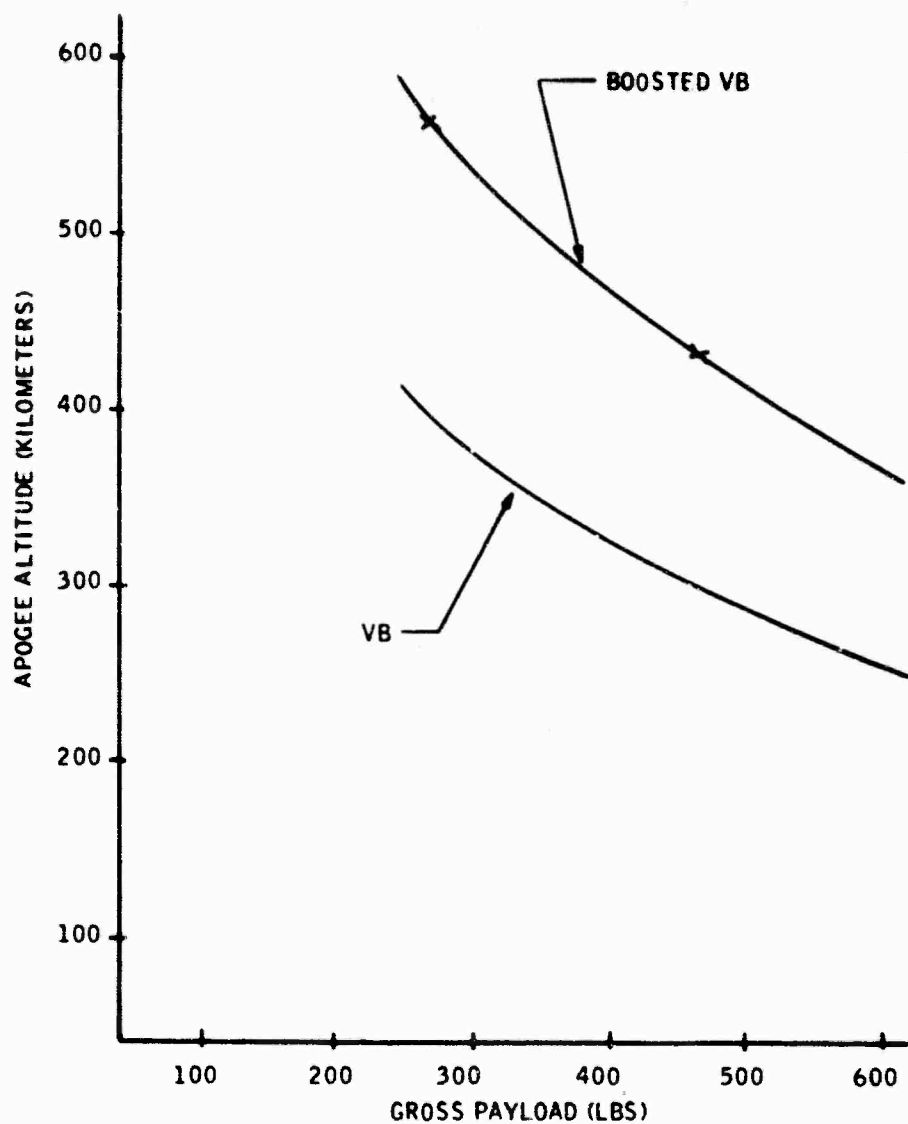


Figure 114. Apogee versus Gross Payload Weight for Boosted and Unboosted Black Brant VB

UNCLASSIFIED

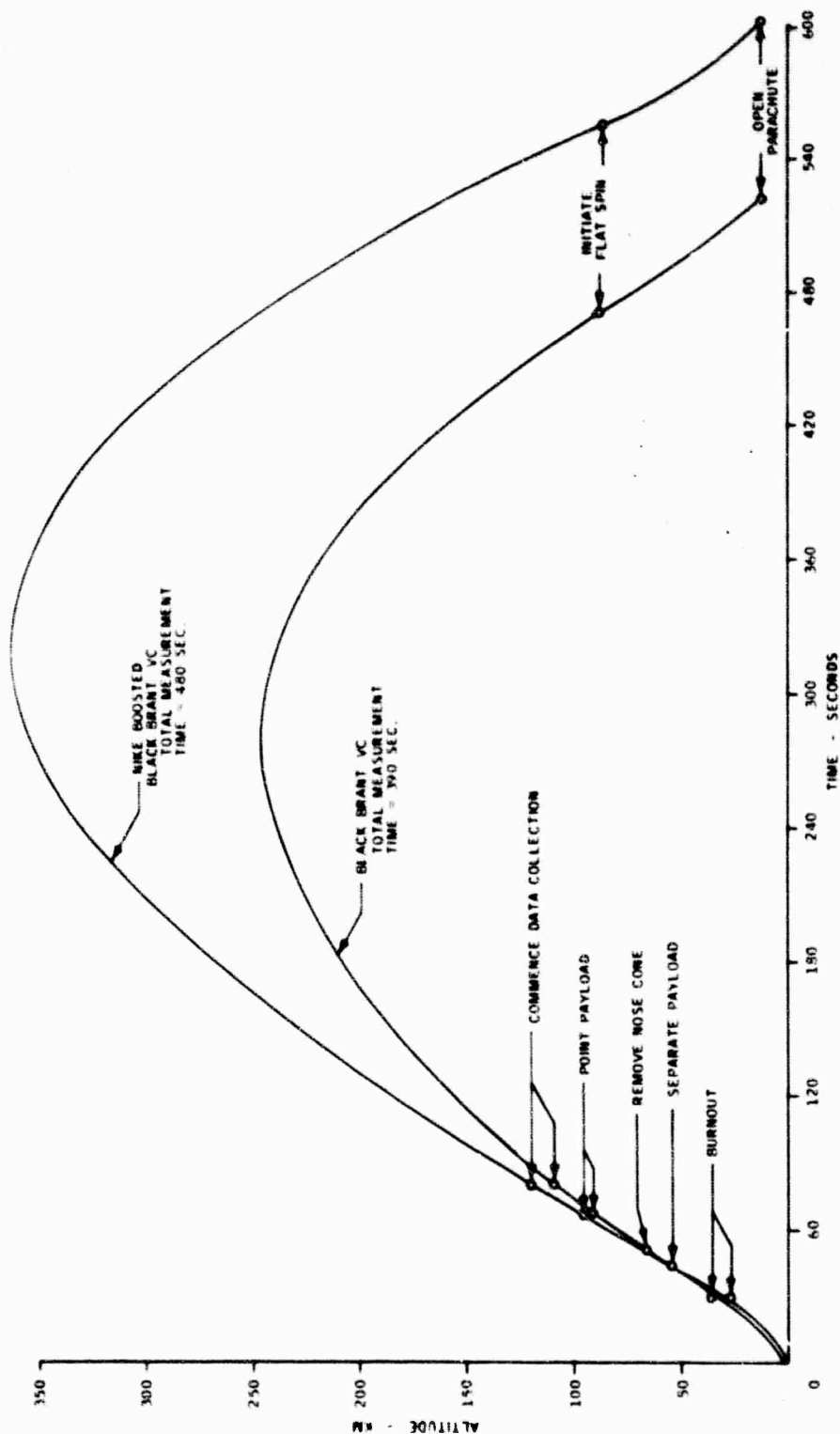


Figure 115. Black Brant Probe Trajectories

UNCLASSIFIED

The integrated payload is designed to be contained in a standard Black Brant VB nose fairing as shown by Figure 116. Table 28 shows the individual auxiliary subsystem weight, volume and power allocations. This subsection describes the recommended characteristics of these subsystems.

5.3.1 Attitude Control Subsystem

This subsection presents the probe vehicle attitude control subsystem requirements and constraints, a functional description of the recommended attitude controller, a description of its physical configuration, a discussion of the system mechanization, and a brief description of the inertial sensors proposed in addition to the basic attitude reference system. The attitude reference system is discussed as a separate item.

Requirements and Constraints -- The launch environment through which the attitude control system must survive is described later in this subsection, since the attitude determination system is more sensitive to the launch accelerations and vibrations than the attitude control subsystem. The following describes the major functions of the attitude control system.

- Control system is activated at termination of boost and payload separation.
- All three vehicle rates are nulled, and payload is aligned to local vertical.
- Horizon scan mode is initiated. Vehicle is maneuvered to alternately scan between 11 and 17 deg of the horizon in a vertical plane at rates of 0.6 deg/sec and to maneuver between scan planes at a higher rate.
- Prior to entry, all vehicle rates are nulled, and payload is aligned with roll axis normal to flight path to minimize aerodynamic heating and damage.

The following payload parameters have been assumed for purposes of sizing the attitude control system:

- Moments of inertia

$$I_x = 5.05 \text{ slug-ft}^2$$

$$I_y = I_z = 32.8 \text{ slug-ft}^2$$

- Payload weight

$$w_0 = 469 \text{ lbs}$$

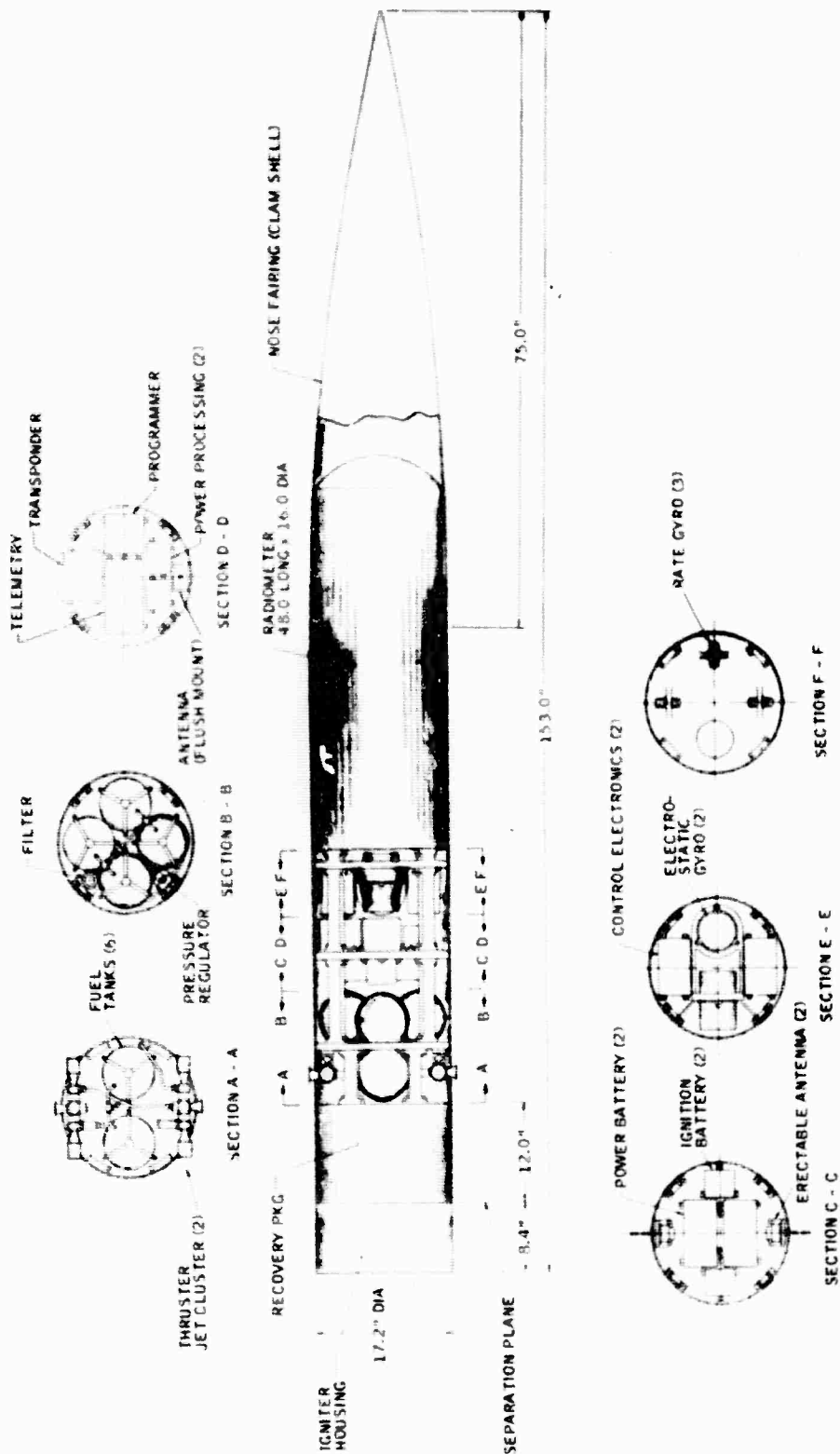


Figure 116. Proposed Payload Configuration

UNCLASSIFIED

Table 28. Rocket Payload Size Allocations

Item	Weight (pounds)	Volume (in. ³)	Power (watts)
Research Package Radiometer (including electronics and cooler)	100	14 inch diam x 48 inch long	20
Payload Pointing Two ESGs, 3 rate gyros	27	450	24
Computer and Controller	22	670	32
Helium Storage, control and jets	35	250	1
Electrical Ignition Batteries and Circuitry	4	60	--
Power batteries (2)	14	200	--
Power Processing and control	8	150	20
Wiring Harness and connectors	8	150	--
Programmer	7	120	3
Communications Transmitters	6	90	26
Transponder	6	100	37
Antennas and cabling	6	--	--
Structure Structure, supports, adapters fairings, heat sink, bellows	130	3600	--
Recovery Package	70	17 inch diam x 12 inch long	--
Total	440		166

UNCLASSIFIED

- Horizon scan rate

$$\omega_s = 0.6 \text{ deg/sec}$$

- Between-scan maneuver rate

$$\omega_m = 3 \text{ deg/sec (max)}$$

- Terminal spin rate

$$\omega_t = 0.5 \text{ rps (max)}$$

This is the maximum expected residual roll rate when the zero-spin angle is selected for the Black Brant VB fins.

- Attitude control lever arms

$$l_x = 8 \text{ in.}$$

$$l_y = l_z = 30 \text{ in.}$$

- Premaneuver limit cycle characteristics

$$\text{Attitude deadband} = \pm 1.0 \text{ deg}$$

$$\text{Rate deadband} = \pm 0.1 \text{ deg/sec}$$

The propellant used by the attitude control system has been dictated to be helium gas, since there is concern that any other gas might interfere with the optical experiment. Even nitrogen gas has been ruled out, since the possibility exists that it could combine photochemically with free ozone, forming oxides of nitrogen, which absorb in regions of experimental interest.

The attitude control system for the radiometer probe flight series will be designed to meet the above requirements. Detailed performance specifications will be prepared at the start of the program to ensure compatibility between the attitude control system and the system requirements, based on detailed performance analysis and error analysis. The following subsections give some of the details of the attitude control configurations tentatively selected.

Functional Description -- The function of the recommended attitude control system for the radiometer probe flight series is to maneuver the vehicle in a controlled sequence of azimuth and elevation excursions at specified angular rates. To provide the capability of maneuvering and aiming the payload to within 1 deg of a preselected pointing attitude, the recommended attitude controller uses:

UNCLASSIFIED

- An attitude reference system which uses two two-degree-of-freedom electrically suspended gyros to define the actual pointing direction, in addition to providing the data for accurate (1 arc min) postflight attitude history reconstruction
- A cold-gas (helium) reaction system which maneuvers the payload with respect to the attitude reference
- Rate gyros for damping; control electronics; and telemetry signal conditioning
- A programmer to provide the desired in-flight attitude sequence

Prior to launch, the attitude reference system will be aligned by means of a prelaunch alignment control system. This system optically determines the attitude between the attitude reference system coordinate frame and an earth-fixed frame, and subsequently loads the appropriate constants into the attitude programmer to provide the desired attitude sequence.

During the boost phase of the flight, the attitude controller is maintained in a "passive" or "noncontrolling" state; however, the attitude reference system maintains the inertial reference established prior to launch.

After the boost phase, the payload section is separated from the booster. The attitude controller is activated by a timer signal and begins to rate-arrest the payload in each of the three axes -- pitch, yaw, and roll. The vehicle is then maneuvered to an appropriate prescan attitude. The vehicle is then commanded by the programmer to scan from 11 to 17 deg of the horizon in a vertical plane at rates of 0.6 deg/sec. Between scans, the vehicle is maneuvered between scan planes and oriented in elevation at a higher rate. The details of the horizon scan motion will vary from flight to flight, depending on the particular objectives of the flight and possibly modified due to previous flight experience and experimental results. The programmer and attitude control capacity will be sized on a basis to accommodate any foreseeable attitude command profile.

Before atmospheric entry, all vehicle rates are nulled, and the payload is aligned with the roll axis normal to the velocity vector to minimize aerodynamic heating and payload damage.

Table 29 summarizes the expected impulse requirements for the attitude control system. Worst-case situations have been assumed to limit the maximum gas requirements.

Assuming an average specific impulse for the helium gas thrusters of 140 sec, this means that 1 lb of helium must be stored by the attitude control system.

UNCLASSIFIED

Table 29. Attitude Control Total Impulse Requirements

Maneuver	Impulse ΔJ (lb-sec)
Rate arrest and initial alignment	65
Between-scan maneuvering	21
Horizon scan rate initiation and arrest	21
Miscellaneous limit cycling	10
Reentry rate arrest and alignment	6
Gas reserve and contingency allotment	17
Total Impulse	140

Physical Configuration -- The attitude control system recommended for the radiometer experiment probe vehicle draws heavily on the extensive attitude control hardware experience Honeywell has accumulated on the suborbital Scanner program and the Athena and Athena II programs. These programs are all suborbital probe-type flights with attitude control requirements similar to the current set of requirements.

The attitude control system consists of the following major components:

- Six 7-in. diameter spherical, high-pressure helium gas reservoirs
- One in-line filter (10-micron nominal rating)
- One pressure control regulator
- Six reaction jets and tube extenders (nominal 1-lb thrust jets)
- Two jet-array manifolds
- Tubing assemblies and fittings for connecting system components
- Two pressure transducers (0 to 500 psia; 0 to 5000 psia)
- Two gas-fill valves
- One pressure-relief valve
- Three rate gyros (sensing pitch, yaw, and roll rates) and mounting block
- Control electronics assembly

UNCLASSIFIED

- Event programmer
- System wiring harness

The placement of the major attitude control components was shown in Figure 116.

Inertial Sensors -- In addition to the basic attitude information from the attitude reference system, the attitude control system uses rate information from three miniature rate gyros. These gyros are mounted in a triad block and sense rates around each of three mutually perpendicular axes of the attitude controller. The outputs of the roll, pitch, and yaw rate gyros are used to control the probe vehicle during the rate-arrest modes and are combined with attitude signals to provide rate damping during attitude maneuvers.

The recommended rate gyro is a GN90D Gnat miniature rate gyro and is a single-degree-of-freedom spring-restrained instrument. This gyro contains a synchronous hysteresis-type spinmotor rotating at 24,000 rpm. The rotor runs outside the stator to provide maximum wheel momentum with minimum size and weight. The dynamically-balanced rotor runs on preloaded ball bearings to maximize motor life. The spinmotor is hermetically sealed in an inert atmosphere. The gyro gimbal is supported between an isoelastic, low-hysteresis torsional spring and a miniature, low-friction jeweled pivot. An infinite-resolution, variable-reluctance pickoff provides an output signal proportional to the input turning rate. A mechanical damping compensator, immersed in silicone fluid, provides a reasonable constant damping ratio for extra protection against shock and vibration. The external steel housing is gold-plated for corrosion resistance and effective hermetic sealing. Figure 117 is a cutaway view of the Gnat rate gyro.

The GN90D rate gyro's linear range is 40 deg/sec, and it can withstand a 1260-deg/sec input for 2 min. The scale factor for this gyro is 110 millivolts/deg/sec.

5.3.2 Attitude Determination Subsystem

This subsection presents the probe vehicle attitude determination system requirements and constraints, a description of the candidate systems considered and the rationale for the selected system, a detailed technical description of the recommended attitude determination system, and a discussion of the requirements for data processing and telemetry. The proposed attitude determination system is based on two Honeywell strapdown electrically suspended gyros (ESG). The accuracy requirements for the probe flight, the nature of the candidate launch vehicle ride, and the desirability of complete freedom in launch time and attitude maneuvering combine to make an ESG system a most attractive candidate for this type of probe series.

UNCLASSIFIED

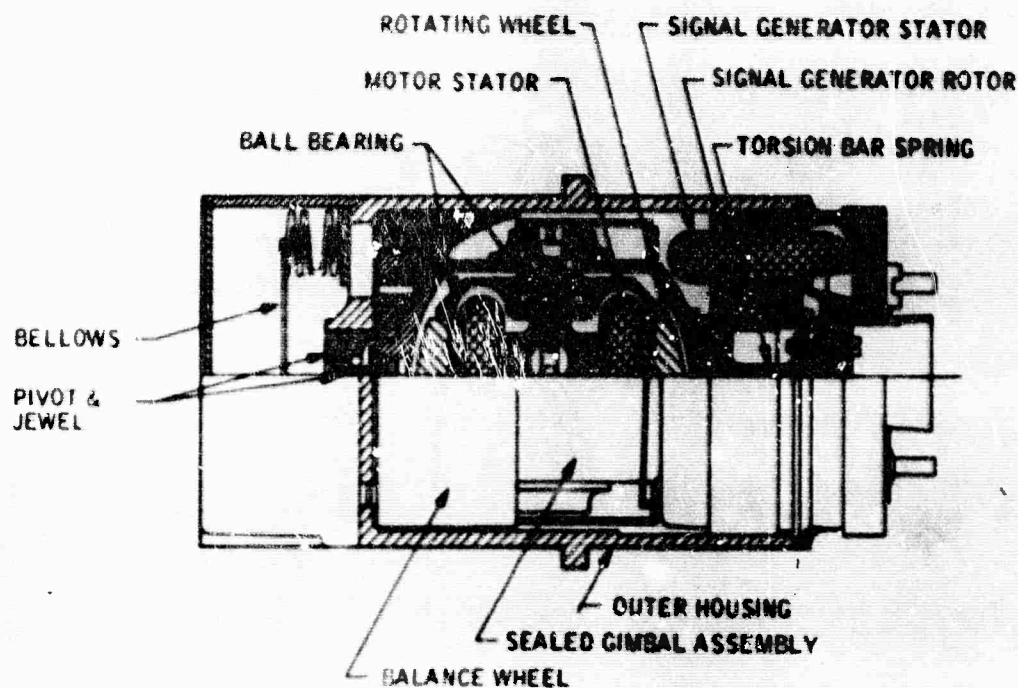


Figure 117. Cutaway View of Gnat Gyro

Requirements and Constraints -- The launch environment through which the attitude reference system must survive (and in the case of the ESG system operate accurately) is that of the Black Brant VB, manufactured by Bristol Aerospace Limited, Winnipeg, Canada. The Black Brant VB provides one of the softest rides of any sounding rocket currently produced, and is a single-stage rocket with attendant lack of explosive stage separation. These features are among the factors which make an ESG attitude reference system attractive.

The maximum longitudinal acceleration characteristics of the booster are shown in Figure 118. The maximum amplitude is 15 g's. The maximum cross-axis accelerations expected are ± 2 g's. The maximum shock environment experienced is during ignition, when a 70-g/sec acceleration rate of change is experienced. Flight diagnostic records indicate that no appreciable shock inputs occur during flight. The maximum vibration experienced by the Black Brant VB is 3-g peak (sine wave) 2 KHz to 40 Hz, and 0.036 in. peak to peak (sine wave) 40 Hz to 15 Hz. The vibration experience in flights to date has been of quite short duration, occurring in several bursts each of a few milliseconds.

UNCLASSIFIED

UNCLASSIFIED

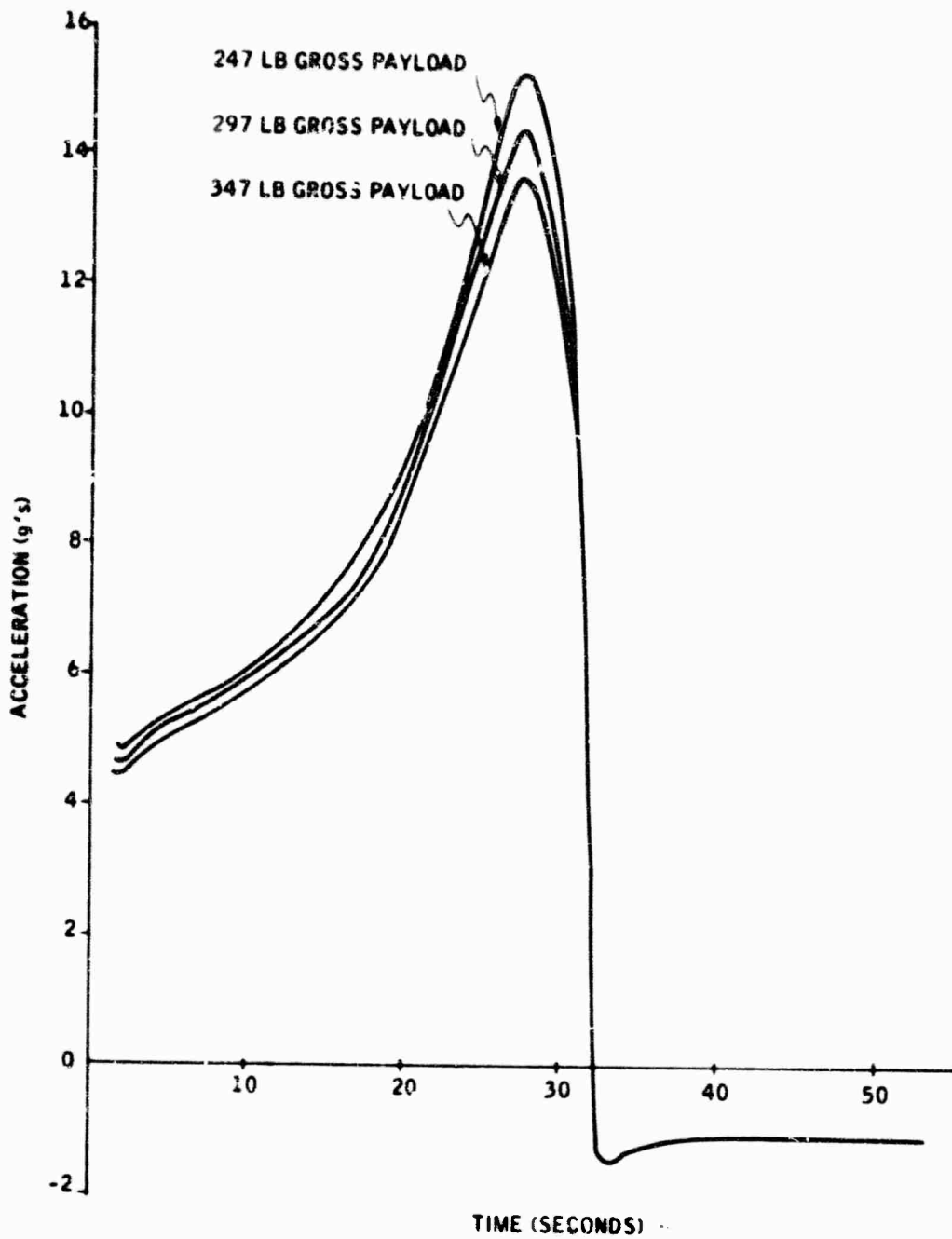


Figure 118. Booster Longitudinal Acceleration Characteristics

UNCLASSIFIED

UNCLASSIFIED

The maximum payload radiation air temperature is of the order of 70°C. Lower values are easily obtained with proven standard insulation techniques. The payload compartments can be sealed, if necessary, to maintain sea level ambient pressure.

The angular accuracies required from the attitude reference system are as follows:

- Postflight attitude reference accuracy
 - Roll -- 1.0 arc min (1σ)
 - Pitch -- 1.0 arc min (1σ)
 - Yaw -- 1.0 arc min (1σ)
- Real-time onboard attitude reference accuracy
 - Roll -- 1.0 deg (1σ)
 - Pitch -- 1.0 deg (1σ)
 - Yaw -- 1.0 deg (1σ)

These accuracies are required only when the radiometer is performing an active horizon scan at angular rates of 3.0 deg/sec or lower. The accuracy requirements can be relaxed somewhat during the maneuvers between scans. The 1-arc-min accuracies are required only during postflight data analysis. Thus, the raw attitude reference data can be telemetered to the ground and complex onboard calculations are not necessary.

Wide-bandwidth real-time attitude data is not necessary, since angular rate information for stability is available from the attitude control system rate gyros. Time constants or lags of up to 0.2 sec can be tolerated in the real-time attitude data.

With the ESG system, the errors in the prelaunch alignment combined with the errors incurred during the boost phase and the zero-g experiment phase must be small enough to meet the 1-arc-min requirement. Errors in boresighting the ESG system to the radiometer optics are a part of this 1-arc-min allocation. If an attitude reference system which is based on celestial sensors is used, then the capability exists for reducing errors and attaining the required performance after thrust termination.

The attitude reference system for the radiometer probe flight series will be designed to meet the above requirements. Detailed performance specifications will be prepared to ensure compatibility between the attitude reference system and the system requirements, based on detailed performance analysis and error analysis.

UNCLASSIFIED

Candidates and Selected System -- Several alternate approaches to attitude determination were considered for the radiometer probe experiment series. The nature and timing of the probe series places a somewhat different weighting on the decision factors than would normally be the case for an operational satellite tracking system. The benign environment of an operational orbital vehicle and the extended periods for stellar acquisition and zero-g drift-trimming make a stellar-inertial system like the Honeywell/LMSC SPARS (Space Precision Attitude Reference System) an ideal candidate for this job. However, for the probe experiment attitude reference the requirement is medium accuracy attitude reference for short flight times with the emphasis on operational flexibility, night, day, or twilight operation, and elimination of vehicle pointing or scan constraints for attitude reference purposes.

A number of alternate existing attitude reference systems have been examined for possible application to the radiometer probe experiment series. These candidates include the Honeywell/LMSC SPARS system and derivatives, the Aerobee Mark II attitude control system, the LMSC SPARCS system, various photomultiplier tube star mapper systems, various star tracker systems, and a system based on the electrically suspended gyro (ESG).

The electrically suspended gyro has been examined in the past for other rocket probe programs and has been ruled out because of severe launch vehicle environments, including high acceleration and explosive stage separation shocks in multistage boosters. The Black Brant VB, which is the candidate launch vehicle for this flight series, has the soft ride characteristics which make the ESG system attractive for the first time in a probe program. An attitude reference and control system based on the ESG appears to have such a decisive advantage over other candidates that it is the recommended approach for this program. The following subsections describe in detail the details and features of the ESG attitude reference system.

ESG Attitude Determination System Description -- The data processing system accepts pulse signals generated by the ESG optical pickoffs, and telemetry signals from a ground-based computer. These are converted to usable form and used to produce attitude control signals and output data. The control signals position the vehicle such that the radiometer is in proper relationship to the local vertical. Telemetered output includes pickoff identified direction cosine and radiometer signals. A typical installation of the ESG system is shown in Figure 119. Figure 120 delineates signals which are produced by the intervening hardware. The processor block diagram, Figure 121, shows a more hardware-oriented picture of the system. Assemblies which must be used to produce the proper signals are shown.

The system accepts signals from the ESG optical pickoffs and from the telemetry receiver. The gyro rotor is free spinning and carries a pattern which contrasts in reflectance with the rest of the rotor surface. The pattern is a series of lines, each of which is sensed by a microscope-type optical pickoff when it crosses the pickoff field of view. The pattern on the

UNCLASSIFIED

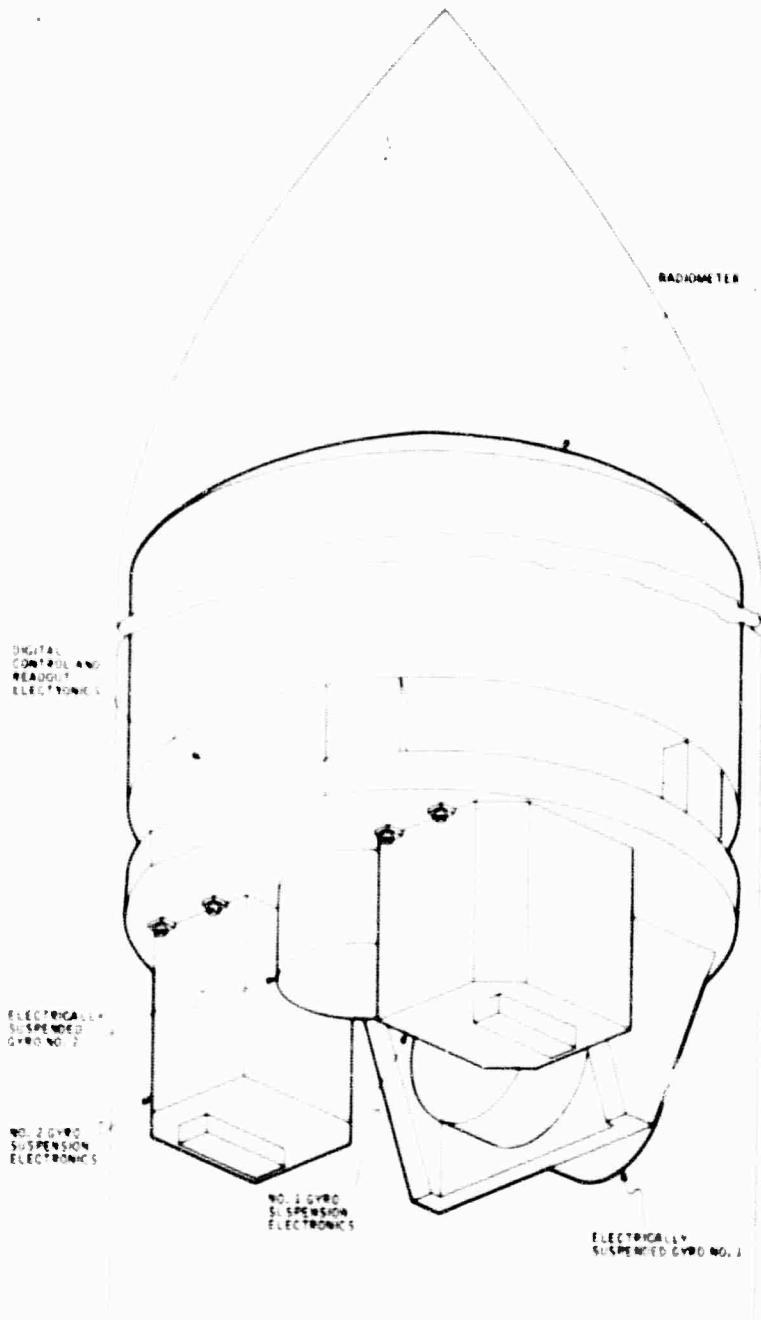


Figure 119. Typical Installation of ESG System

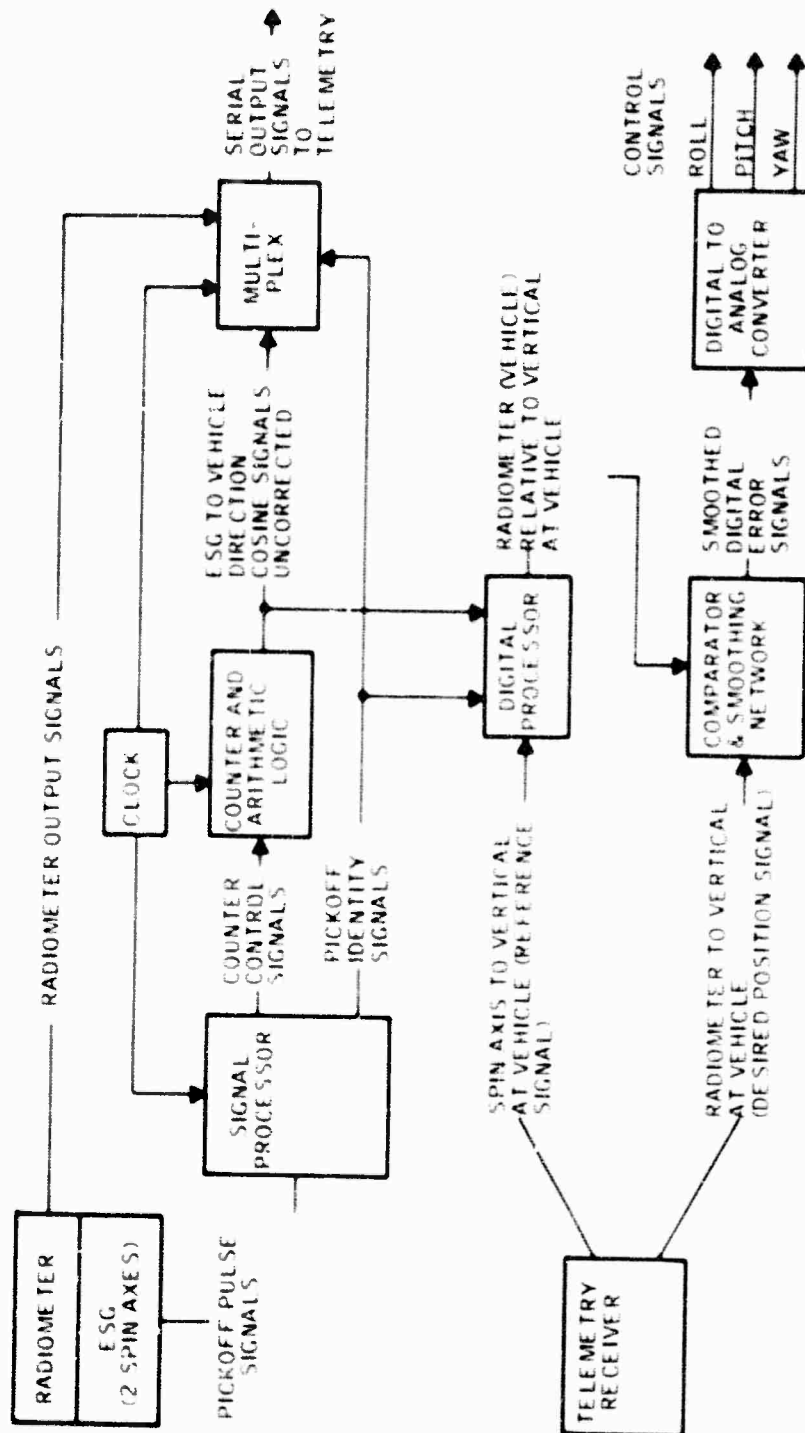


Figure 120. Data Processor Signal Flow Chart

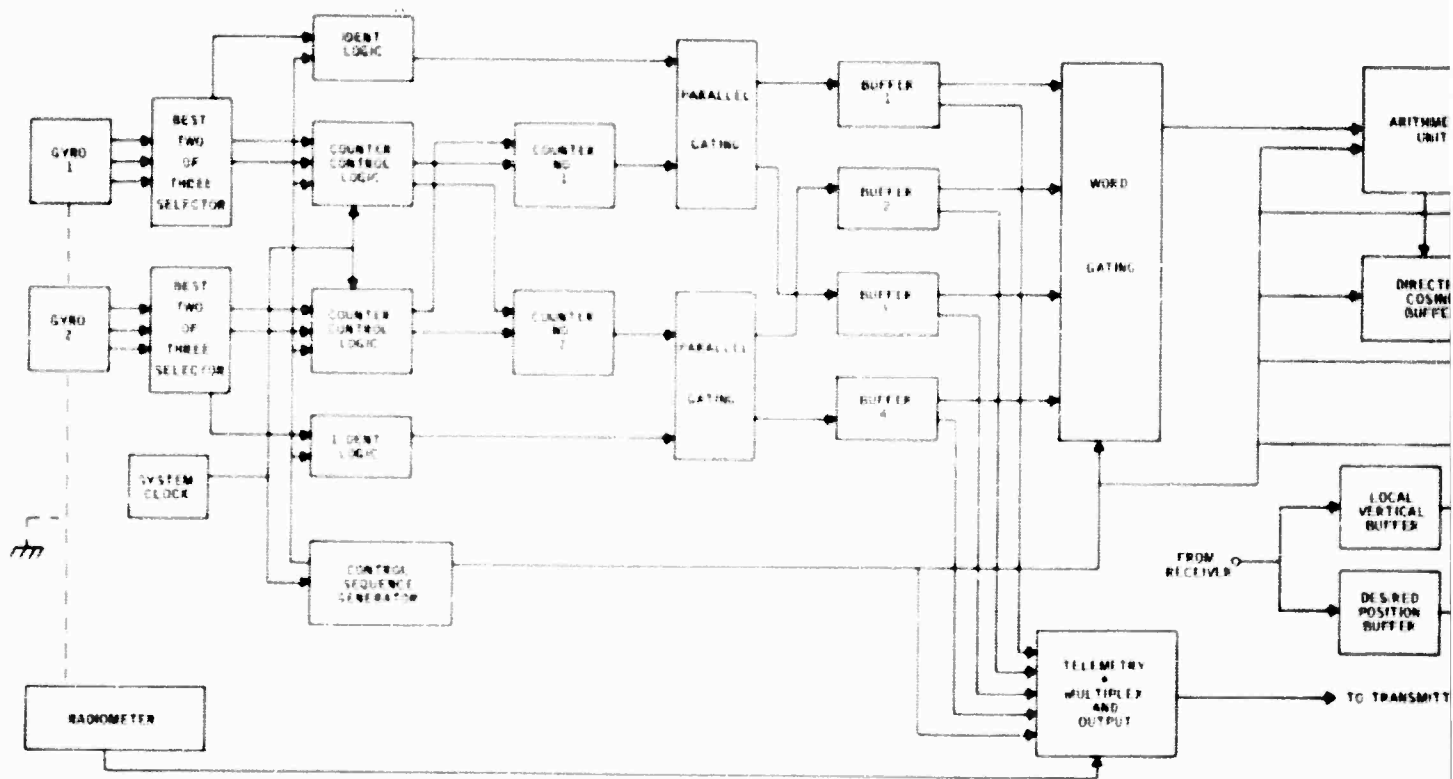
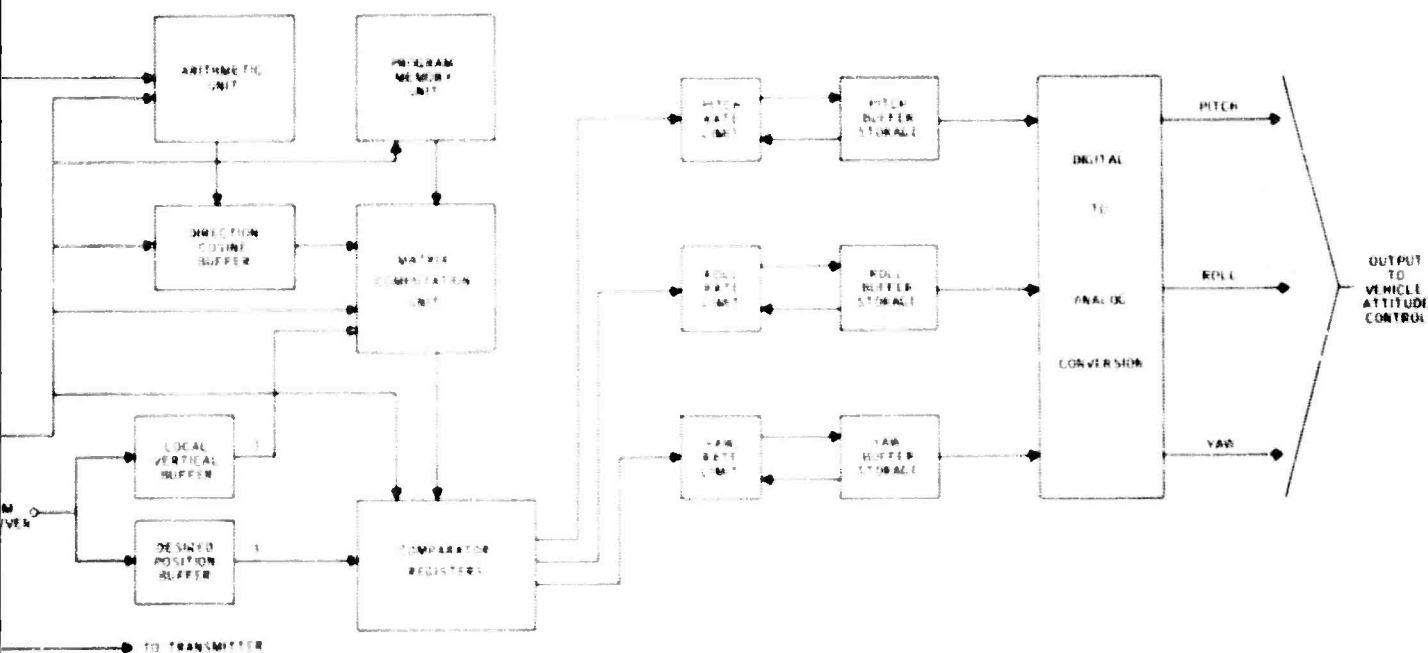


Figure 121. Processor Block



Processor Block Diagram

UNCLASSIFIED

rotor is formed by a mask which is carefully made to contour the lines such that the time differences between output pulses is a measure of the cosine of the angle between the spin axis and pickoff axis.

The pickoff contains optics, a light source, a sensor photo diode and amplifier. The amplifier output is a pulse with level of several volts, sufficient to drive the circuits which follow.

A signal processor accepts this pickoff pulse train and produces from it two types of output. The first is a set of sequencer-controlled start and stop gating voltages. These are level-compatible with a high-speed counter and contain information from the desired number of rotor revolutions which will be averaged to reduce error in the start-stop sequence. The second output is an identity tag which identifies the pickoff which was used to obtain the data. This information is needed so that the reference axis may be properly identified in the subsequent computations.

The counters and arithmetic logic produce numbers which describe the present position of the gyro spin axis relative to the pickoff axes. Since the pickoffs have been aligned to the vehicle axes and the alignment angles are known, this information also may be used to give alignment of the radiometer relative to the gyro spin axes.

These signals (uncorrected for alignment) are telemetered back to the tracking station along with the radiometer output data. These signals are corrected, and alignment data is added by a ground-based computer as described in a previous subsection.

The programmer produces two signals. The signals are the desired angle of the radiometer relative to vehicle vertical and the proper relationship between gyro spin axes and vehicle vertical at that time. The latter signal is used to correct the direction cosines and produce the proper reference frame manipulations which will result in the present vehicle axis angles relative to a local vertical coordinate frame. These present angles are compared to the (former) desired radiometer angles relative to the same frame of reference. Error is produced when the vehicle is displaced from the desired position.

These error signals must be smoothed to remove the effects of bad data produced by noise pulses or from other sources. This smoothed error indication is input to a digital to analog converter which produces levels proportional to the number appearing from the comparator. These levels define the thruster effort which must be applied about the three vehicle axes to effect control of the radiometer attitude.

Processor Hardware -- The processor block diagram (Figure 121) defines, at an assembly level, the key items of the system.

UNCLASSIFIED

Three gyro pickoffs each produce a pulse train when they are viewing a part of the pattern. Analog detectors are used to produce voltage levels from each pickoff output line. The relative magnitude of these levels is used to choose the best two of three pickoffs. Gating and shaping networks controlled by this comparator are used to transmit the chosen pickoff signals to counter gating logic. Comparator outputs are also used to produce a code signal which identifies the pickoff being used for a particular data point.

A 10-MHz clock is used as the basic system operating timer. Countdown circuits produce the various sequences of control signal needed by the entire processor. Pulses from the clock are gated to counter-accumulator by the pickoff signal to produce numbers proportional to the pattern time differences.

The system sequences produces a six-word pattern for readout and arithmetic control. Three of the words are long, determined by maximum time needed for the desired number of rotor revolutions to occur. Three other words are short, determined by the time needed to transfer and manipulate the data in the arithmetic section. Two sets of data are needed for each point, a long count (entire rotor revolution) and a short count (from reference to timing mark). The signals may be designated A and B (pickoff) and 1 and 2 (gyro) and L and S (long and short). Two counters are used, and the word control gating follows Table 30.

Other sequences are also generated as needed to serialize output data and control the arithmetic and memory operations. These sequences are generated under word-level command.

At the end of each counting cycle, the numbers generated are gated into a set of four buffers (words 2, 4, 6). Buffer 1 and 2 are used to hold the short-count data, 3 and 4 hold long-count data. At word 5, the information from number one gyro is used to compute the direction cosines for that gyro axis relative to the pickoff frame. These cosine signals are uncorrected for pickoff-to-radiometer alignment angles but are sufficiently accurate for guidance control. At the beginning of words 1, 3, and 5, the counter output from the previous cycle is gated to the multiplex unit where it is processed for transmission back to the tracking station.

Word gating brings the desired counter signals to the arithmetic unit for computation of direction cosines. The arithmetic output is gated into a buffer-storage unit where it is held prior to computation of the vehicle control signals.

At this time, the proper vertical information dependent on gyro 1 output is placed in the telemeter buffers. One word later the gyro 2 dependent vertical reference signals are transmitted and stored. The programmer computes the desired location signals. At this point all the information necessary for computation of attitude control signals is available.

Table 30. Word Control Gating

Word	1	2	3	4	5	6
Counter Control	AIS BIS	Reset and Transfer Gating	A1L A2L	Reset and Transfer Gating	A2S B2L	Reset and Transfer Gating
Arithmetic Control	Compute Gyro 2 Cosines		Compute Control Error Signals		Compute Gyro 1 Cosines	
Multiple N. Out	Transmit A2S, B2S	Transmit Radiometer	Transmit AIS, BIS	Transmit Radiometer	Transmit A1L, A2L	Transmit Radiometer
Multiple N. In	Control Signals	Gyro 1 Dependent Vertical Reference	Control Signals	Gyro 2 Dependent Vertical Reference	Control Signals	Desired Location Signals

UNCLASSIFIED

For this computation, the pickoff identity code is used to define the proper transform matrix and computation algorithm to be used. This is taken from the program memory unit and is used in the matrix computation unit with the previously computed cosines and the local vertical reference signals to do the reference frame manipulations needed to define vehicle axis angles relative to vertical at the vehicle. These angles are compared to the desired angles from the telemeter buffers. The difference signals from the comparator are proportional to roll, pitch and yaw error angles.

These numbers must be conditioned to eliminate the effects of missing or bad data points. The conditioner compares present data to previous data and deletes points which differ by more than a set amount. The limits are precalculated to allow margin from normal vehicle rates.

The digital-to-analog conversion converts the pitch-roll-yaw error numbers and produces a filtered level output which is used to control the vehicle thrusters.

Attitude Determination Error Analysis -- The two ESGs will be "hard mounted" to the radiometer package, and the radiometer package will have reference surfaces for alignment purposes. Prior to flight, with the ESG's operating, the alignment of the radiometer package with respect to some known coordinate system will be determined.

At any time after the initial alignment, the outputs of the ESGs may be used to indicate the orientation of the radiometer package with respect to the known coordinate system. Errors in this indicated attitude may be conceptually divided into the following components:

- Initial alignment errors
- Shifts in the alignments between the ESGs and the radiometer package after the initial alignment
- ESG drift errors after the initial alignment
- ESG readout errors

Any correlations among these error components are so very small that they may be neglected. The variance of the total error is thus related to the component variances by the usual rss formula

$$\sigma_T^2 = \sigma_{IA}^2 + \sigma_{AS}^2 + \sigma_{GD}^2 + \sigma_{RO}^2$$

where

T = total

IA = initial alignment

UNCLASSIFIED

AS = alignment shifts

GD = gyro drift

RO = gyro readout

For the high-accuracy, postflight analysis requirement of 1 arc min, 1σ , each of three axes, a preliminary error budget has been established

$\sigma_{LA} = 0.4$ arc min

$\sigma_{AS} = 0.4$ arc min

$\sigma_{GD} = 0.5$ arc min

$\sigma_{RO} = 0.7$ arc min

$\sigma_T = 1$ arc min

These numbers represent 1σ errors present in each data point, and data points will come at a rate of about 23 per sec. At the maximum expected vehicle rate of 7 deg/sec, the vehicle will move less than 8 min per data point, in a nearly torque-free environment. Data smoothing should be able to reduce that portion of the error above due to readout errors, which are largely uncorrelated, point to point. A smoothed attitude estimate should then be in error by only 0.75 arc min, 1σ , each of three axes.

Another point to consider is that the gyro drift figure above corresponds to the amount of drift accumulated by the end of the mission. Early in the mission, this figure will be reduced by about 25 %. Amounts budgeted for initial alignment error and especially for alignment shift error are generous.

Initial Alignment -- A detailed initial alignment procedure has not been worked out. From an accuracy standpoint, however, there are several optical methods available with accuracies well within the 0.4-arc-min-per-axis (1σ) amount budgeted for initial alignment error. The critical feature of initial alignment is in obtaining the alignment within a short time prior to launch. Gyro drift accumulates from the time of initial alignment to the end of the mission, so it is important to keep this time as small as is reasonable. Currently, estimates of gyro drift have been made assuming initial alignment within ten minutes of launch time. It is likely that this time could be increased, if that is required by launch constraints, with a somewhat more careful initial gyro startup procedure, and perhaps a more complex gyro drift prediction procedure.

Alignment Shifts -- The detailed design of the connection between the ESG package and the radiometer package is not complete at this time, therefore, exact alignment shifts between the two packages are hard to estimate. The amount (0.4 arc min, each axis, 1σ) budgeted for alignment shifts, however, is very large for any reasonable mechanical connection.

UNCLASSIFIED

ESG Drift Errors -- Unpredictable changes in the orientation of the ESG spin axes in inertial space between the time of initial alignment and the time of readout will cause errors in the indicated radiometer orientation. Motion of the ESG spin axes in inertial space is termed raw gyro drift, and the unpredictable part of this motion is termed compensated gyro drift. There are three levels of possible compensation:

- No Compensation - The simplest way to use the ESGs is to assume that they are stable in inertial space. This is also the least accurate way to use the gyros, but it is adequate for some aspects of the present mission.
- Mass Unbalance Compensation - Part of the raw gyro drift may be attributed to gyro mass unbalance. Compensating for this portion of the raw drift requires only knowledge of the orientations of the gyro spin axes with respect to the non-gravitational acceleration of the gyros. For compensation purposes it would be adequate to consider that the gyro spin axes were fixed in inertial space and that the nongravitational accelerations of the gyros were those corresponding to a nominal flight profile. In fact, the entire drift compensation procedure would require only the initial alignment information as input data.
- Electric Torque Compensation - After mass unbalance compensation, a large part of the remaining gyro drift may be ascribed to torques on the gyro rotors due to the electric suspension forces which support them. Compensating for electric torque drift requires knowledge of the orientations of the gyro spin axes to the gyro cases on a near continuous basis. This information will, of course, be available - it is just the gyro readout information - but it may not be available on a continuous basis. Even if continuous information were available, electric torque drift compensation is fairly complex, requiring much gyro laboratory test data and a large computer program.

The simplest (lowest numbered) of the above schemes which results in an adequately low value for compensated gyro drift should be chosen. The ESGs proposed for this mission will have raw drift rates less than about 0.1 deg/hr (except during the short-duration launch which will produce about as much raw drift in 30 sec as would be produced in 5 min on the ground. Thus, for the low-accuracy (1-deg), real-time interface with the onboard attitude control system, no drift compensation need be done, provided that the time duration between initial alignment and launch is less than a few hours.

High-accuracy (1 arc min) postflight data analysis will require some drift compensation. If initial alignment were obtained only 10 min prior to launch, raw gyro drift would be about 3 arc min at the end of the 15-min flight.

UNCLASSIFIED

After mass unbalance compensation, the ESGs proposed for this mission will have compensated drift rates less than 0.03 deg/hr. Assuming initial alignment 10 min before launch, the gyros would be expected to drift an unpredictable 0.9 min by the end of the 15-min flight. This is too large a number to be acceptable. There are two ways to reduce the unpredictable drift. The obvious way is to compensate for electric torque drifts. This would lower the compensated drift rate to less than 0.01 deg/hr, or 0.3 arc min by flight's end, an acceptable result, but at a high cost in terms of complexity. The other way to reduce the compensated drift rate is to pick the initial orientations of the ESG spin axes within their cases so that electric torques are small. As was mentioned earlier, electric torques are dependent on the orientation of the spin vector in the case. Not mentioned earlier, however, was the fact that some orientations of the spin vector in the case produce extremely low values of electric torque. Since the time between initial alignment and launch is assumed to be short, the orientation of the spin axes in the case will be reasonably constant during that period. Picking an orientation where electric torque is low will reduce compensated gyro drift prior to launch. After launch, although it has not yet been included in the computations, the low specific force on the gyro cases will lead to smaller drift rates than previously indicated. A combination of mass unbalance compensation, proper initial orientation of the gyro spin vectors, and a short time between initial alignment and launch should keep compensated gyro drift to less than 0.5 min (each axis, 1σ) at the end of the flight.

ESG Readout Errors -- Each ESG has three optical pickoffs mounted on its case which view the rotor surface. Lines inscribed on the rotor surface are sensed by the pickoffs as the lines on the spinning rotor pass through the pickoff field of view. The pickoff outputs are used to turn on and off counters which, when on, count some high (10 to 100 MHz) stable clock signal. The counters, then, time the transit between lines on the rotor surface.

In current practice, the ratio of the time of transit between two lines on the rotor surface to the time of a complete rotor revolution (the transit time of one line) is nominally equal to the cosine of the angle between the pickoff axis and the rotor spin axis. Two such angles are needed to determine the rotor spin axis, so two pickoffs are needed for a single readout. Two pickoffs are inadequate, however, for all-attitude operation, as the sensitivity to error in a measurement of the cosine of an angle becomes unacceptably high as the angle goes to zero. Three pickoffs, properly placed, ensure that two accurate outputs are always available.

A counter rate of 10 MHz will be adequate for this mission. A 700-rps rotor spin rate, coupled with a 10-MHz counter, yields the fact that a one-count counter error corresponds to

$$(1 \text{ count}) \left(700 \frac{\text{rev}}{\text{sec}} \right) \left(360 \frac{\text{deg}}{\text{rev}} \right) \left(60 \frac{\text{min}}{\text{deg}} / 10^7 \right) \approx 1.5 \text{ arc min}$$

UNCLASSIFIED

which is higher than the allowable error. Averaging over 10 revolutions for each readout will reduce this error by a factor of $\sqrt{10}$ to about 0.5 arc min.

While each of the two ESGs must have three optical pickoffs, making a total of six pickoffs; and, while each pickoff must be able to provide two outputs - the time of transit between the two lines on the rotor, and the time for an entire rotor revolution - only two counters are necessary. The two counters are used sequentially to provide all the necessary output information. First the two counters are used to measure the average transit time, over 10 rotor revolutions, between the two lines on gyro 1 rotor for the two appropriate pickoffs as selected by onboard logic. Then the same measurement is made on gyro 2. In a third measurement cycle, one counter is used for each gyro to measure the average times (over 10 revolutions) of complete rotor revolutions for the two units. The total time for a readout is then (3/70) sec, so about 23 data points/sec will be produced.

A maximum vehicle angular rate of 3 deg/sec is equivalent to 2.57 arc min per 10 rotor revolutions. However, the averaging procedure will produce an output corresponding to the attitude of the vehicle at the midpoint of the averaging cycle if the vehicle angular rates are constant. Degradation of readout (at low angular rates) is not a function of the angular rate itself, but of the angular acceleration. As the vehicle is in a nearly torque-free environment when accurate readout is required, vehicle dynamics should not significantly degrade the readout process. In fact, it is then constancy of angular rates which allows the three counters to be shared between the two gyros. Even though both gyros cannot be read out simultaneously with this scheme, post flight data filtering will allow nonsimultaneous measurements to be combined.

Besides one-count errors, there are several other sources of error in the readout, independent of the one-count errors, of about 0.3 arc min. These come from line placement errors, triggering errors, and the like. Combined with the one-count errors, rms fashion, this makes a total of 0.58 arc min. Leaving a generous allowance of 0.4 arc min for dynamic effects and for effects of nonsimultaneous measurements still yields an rms total readout error of 0.7 arc min, each axis, 1 σ .

Data Rates -- Ten rotor revolutions make 1/70 sec. After each 10 revolutions, two numbers must be transmitted, each possibly as large as the number of cycles in 1/70 sec of 10 MHz. Equivalently, two numbers must be transmitted, each of 14 bits, 70 times per sec, for a total data rate of 1960 bits/sec. Additionally, some quality bits, tag bits, and some redundant information will be sent, with the total data rate remaining below 2.8 K bits/sec.

Postflight Data Processing -- The recommended postflight signal processing is shown in Figure 122. The first step in ground data processing is to obtain the relationship of the ESG spin vectors with respect to the radiometer package

UNCLASSIFIED

UNCLASSIFIED

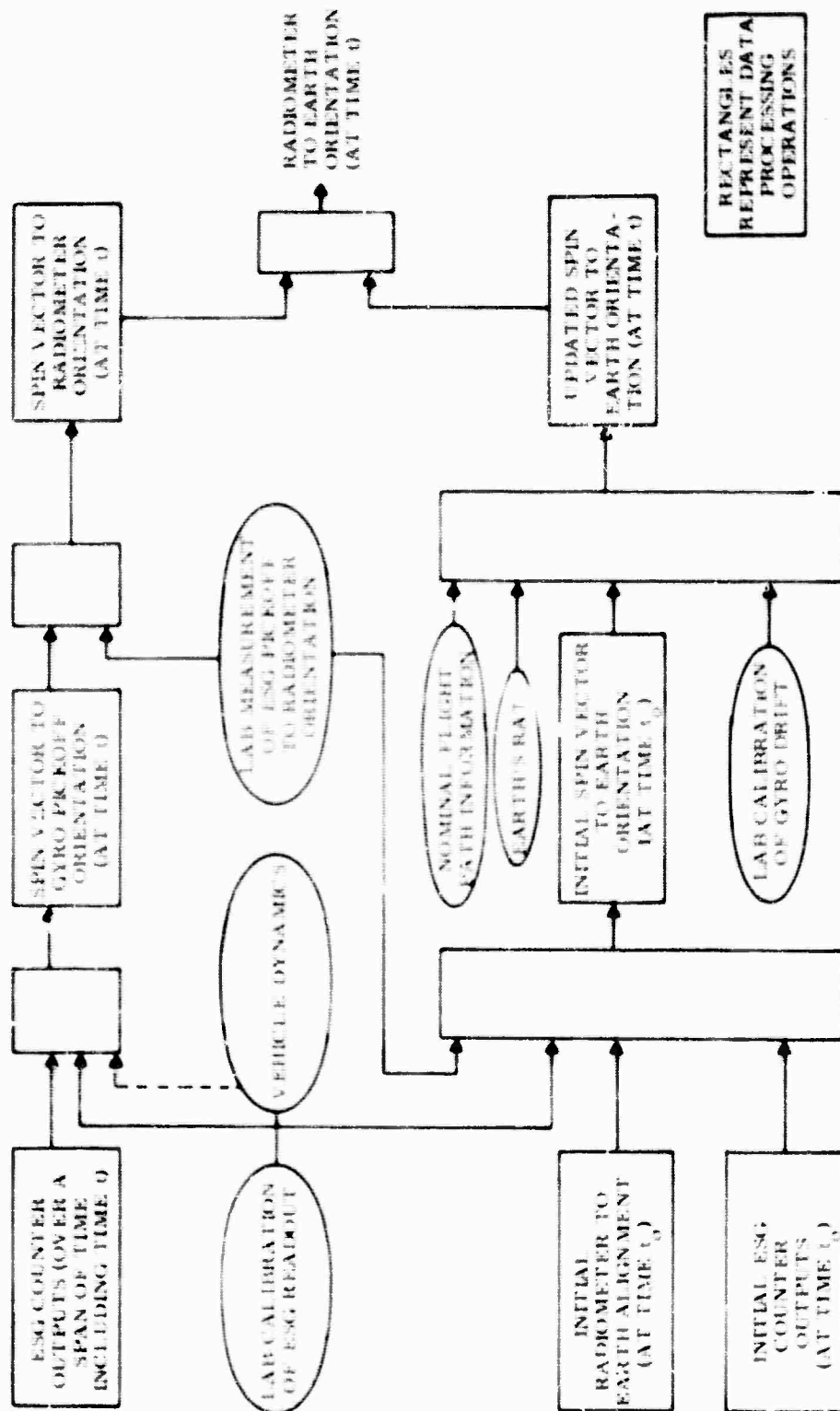


Figure 122. Information Flow Diagram

UNCLASSIFIED

UNCLASSIFIED

as functions of time. This involves manipulating the telemetered counter data, using a laboratory readout calibration of the ESGs, and the laboratory measured orientation of the ESG cases with respect to the radiometer. Since only two counters are used on a shared basis to provide the six outputs necessary to read out two ESGs, the six outputs are not obtained simultaneously. They must be adjusted, or smoothed, or interpolated, to come up with six outputs corresponding to the same time. This process may involve some knowledge of the instrument package dynamics, which are expected to be simple.

A parallel set of ground computations, using data taken only during the initial alignment period, predicts the orientations of the ESG spin vectors in earth coordinates. The initial value of these orientations is determined by the initial alignment procedure. Prediction of changes after the initial alignment involves a simple earth's rotation computation, plus a gyro drift computation which is based on a laboratory calibration of gyro drift. Some knowledge of the nominal vehicle flight path may also be necessary.

Combining the ESG-to-radiometer orientation with the ESG-to-earth orientation yields the desired radiometer-to-earth orientation.

Gyro Package Operating Procedures -- Five modes of operation are described for the ESG attitude reference package:

- Storage
- Startup
- Operation prior to launch
- Launch and experiment
- Post-experiment and landing

Storage -- The gyro package shall be connected to a gyro vacuum maintenance unit and its source of power during the general period of storage. The vacuum maintenance unit contains a vacuum readout gauge and the power supplies which operate the combined pump/gauge unit which is an integral part of each gyro. During transportation and assembly transition, the gyro vacuum pump may be left unenergized for a few days without harm.

The gyro vacuum maintenance unit is a part of the ground equipment.

Start-Up -- A typical start-up procedure is described as follows: One hour or more before the intended flight, begin the procedure by connecting the gyro package to the main power bus of 28 vdc. This will energize the gyro electronics (except suspension), gyro electro-optical pickoffs and gyro vacuum systems. Next, both gyro rotors will be suspended. Each gyro rotor will then be spun up to approximately 700 rps, and any rotor wobble will be damped out. Each gyro rotor will be torqued to its planned starting attitude. The steps from power-on to attitude torquing would normally be carried out with

UNCLASSIFIED

the rocket in its horizontal, initial prelaunch attitude. Start-up controls and power to spin up and damp the gyro are part of the ground equipment. After spinup is completed, spin controls and power are disconnected from the rocket; the gyro rotors continue to spin (coast) through the remaining pre-launch, launch, and experiment periods. The length of time required to start the ESG attitude reference system is estimated to be 15 min.

Gyro Operation Prior to Launch -- Following gyro startup, the gyro attitude reference package is in its basic operational mode. At some convenient time prior to launch, the vacuum pump power supply can be turned off, or disconnected as the case may be. The vacuum pump(s) need not be operated during flight.

Attitude reference data would be collected during this time period for later correlation with the ground optical alignment data recording. The ground optical equipment should be usable with the rocket either in its horizontal attitude or in the vertical, ready-to-launch attitude. If the rocket is raised into its vertical attitude less than 10 min prior to launch, the optical alignment equipment set need not perform with the rocket vertical.

Launch and Experiment -- The gyro package is in its attitude reference performance phase measured from the last point (timewise) of optical alignment data correlated in the ground recording mode. Thereafter, through launch and the radiometer experiment the ESG attitude reference package provides attitude reference signals via telemetry for experiment correlation and other attitude reference signals in real time for onboard attitude control. No torquing signals are applied to the gyros whose spin axes remain fixed in inertial space except for the minor angular error which occurs during the performance period. No command or input signals are required for the gyro system.

Post-Experiment and Recovery -- A programmed or commanded signal will indicate completion of the radiometer data scan. An onboard gyro function controller will now prepare the ESG attitude reference system for landing and recovery. The safest approach is one of shutting down the ESG attitude reference system prior to landing. The function controller will apply an electromagnetic field to each gyro to run down the rotors to zero speed. The gyro rundown operation will be programmed controlled; allocated time will be approximately 2 min. At the end of the rundown period, each gyro rotor will be "set down" within its ceramic envelope in readiness for landing. Main system power, other than that for suspension electronics, may or may not be turned off prior to landing.

5.3.3 Telemetry Subsystem

A detailed block diagram of the proposed telemetry subsystem is shown in Figure 123. A PCM-FM system was chosen because of the data accuracy requirements and because the number and rates of data channels would have required two telemetry transmitters for the FM system.

UNCLASSIFIED

The use of PCM telemetry reduces system error by eliminating undetectable error in the RF link. Typical FM-FM systems add 1 to 5 % of fullscale error to the data from this source. A PCM-FM system will have a small percentage of bit errors (nominally 1 in 10^5 , in this case); however, with error detection coding these can be identified and not seriously degrade the data.

An FM-FM system would require two transmitters using the complete set of IRIG Standard constant-bandwidth subcarrier channels available for transmission in the VHF band. It appears from preliminary analysis that a single transmitter will be sufficient for the PCM-FM system resulting in one-half the transmitter power requirements. It should be pointed out that the ground stations are better equipped for handling FM-FM than PCM-FM telemetry, and this ground equipment constraint may require use of the FM-FM link.

The telemetry system has three main sources of data to process. These are the radiometer subsystem, the attitude determination subsystem, and the status and environmental measurements in the payload.

The radiometer will have 18 channels of data output. Fifteen of the channels will have a 0- to 50-Hz frequency response bandwidth modulating a 240-Hz chopping signal. The chopping signal is introduced in the optical input path to the radiometer with a mechanical chopper. These 15 channels will be simultaneously sampled in synchronism with the chopper at a rate of 240 samples per sec per channel. The remaining three channels will have a fine-resolution spectral scan as well as the radiometer spatial scan and will require a factor of eight higher frequency response and chopping rate. A separate chopper will be used for channels operating at 1920 Hz. These three channels will be simultaneously sampled at a rate of 1920 samples per sec per channel.

The 18 radiometer channels, using sample and hold circuits, will be multiplexed to a common A/D converter. The A/D converter, operating on 0- to 5-volt inputs, will provide 8-bit binary outputs at a conversion rate of nominally 9360 samples/sec. Logarithmic amplifiers are used in the radiometer subsystem on each channel to reduce the dynamic range of the output from 10^6 to approximately 140. Measurement accuracy will be approximately ± 3.5 % rms of reading.

The attitude determination subsystem consists of two strapdown, electrically suspended gyros. The outputs will consist of a readout of four 16-bit binary registers at a rate of 100 samples per sec per register. As shown in Figure 123, these outputs will be serially shifted out and sequenced in the PCM data stream.

UNCLASSIFIED

The status and environmental measurement points have not been defined in detail. Preliminary estimates indicate there will be approximately 40 points. It is desirable on a multiflight program such as this to have the early flights well instrumented to identify failures and their causes so they can be corrected on succeeding flights.

As shown in Figure 123 the status and environmental points will be multiplexed in to the A/D converter. These test points will be sampled only during periods when the radiometer is not scanning the horizon of interest. This will be during the scan reversing intervals and vehicle attitude shifting intervals and will replace the radiometer outputs during that time.

All data and sync words will be multiplexed into a serial bit stream with parity added for modulating the transmitter. A standard word and frame structure as defined in the PCM Standards of IRIG document 106-66 will be used. The bit rate, including data, parity, and frame synchronization, will be nominally 102,000 bits per sec.

The transmitter size depends very strongly on the capabilities of the ground receiving equipment. The following calculation is based on equipment available at the Wallops Island launch site and a maximum transmission distance of 400 km.

Assume:	Vehicle transmission line loss	=	2.0 db
	Fading loss	=	6.0 db
	Polarization loss	=	3.0 db
	1-watt transmitter	=	+30.0 dbm

Then:	Trans. P	=	+30.0 dbm
	Trans. ant. loss	=	- 2.0 db
	Trans. ant. gain	=	0.0 db
	Propagation loss	=	-132.0 db
	Fading loss	=	- 6.0 db
	Polarization loss	=	- 3.0 db
	Receiver ant. gain	=	+28.0 db
	Receiver sensitivity	=	+105.5 dbm
	Margin	=	20.4 db

If 12.5 db is required at the receiver for signal-to-noise ratio, the net margin is 7.9 db, which should be adequate to cover cases in the telemetry system where the coverage in the power pattern of the vehicle antennas could dip as much as 4-5 db below isotropic.

UNCLASSIFIED

The receiving antennas at the Fort Churchill range have a 19-db gain compared to the 28-db gain of the larger antennas at Wallops Island. To compensate for the 9-db difference, a 10-watt transmitter will have to be used on the payload for launches from Fort Churchill.

The total size, weight, and power estimates for the telemetry subsystems are 170 in³, 12 lbs, and 56 watts. These estimates do not include heat sink weight for the unit. A detailed thermal analysis must be conducted to determine the mounting configuration for the transmitter.

Principal areas of work to be done on the telemetry subsystem are:

- Detail design of the subsystem
- Antenna design and pattern measurement
- Thermal analysis and packaging
- Integration and coordination with ground stations

5.3.4 Tracking Subsystem

The experiment scanning accuracy requirements dictate position and altitude accuracy requirements of ± 200 m, 1 σ , through the measurements portion of the flight. At an expected maximum range of 400 km, a tracking transponder will be required on the vehicle.

For launches at Fort Churchill, the AN/FPQ-11 will be used as the ground tracking radar. The Range supplies and installs the AN/DPN-41 transponder to be compatible with their ground radar. This radar operates in the 2700- to 2950-MHz frequency range. Estimated accuracy of this system is ± 25 yards in range and ± 0.5 mils in azimuth and elevation. At a 400-km range the az-el errors will be up to ± 200 m.

The AN/DPN-41 transponder contains its own power supply operating off five HR3 Yardney Silvercells. The total weight and volume of the transponder system, including antennas, will be approximately 8 lbs and 120 in.³, respectively.

Tracking radars in use at Wallops Island include the AN/FPS-16, SPANDAR, and the AN/FPQ-6. The SPANDAR unit operates in the same frequency range as the AN/FPQ-11 and may be compatible with the AN/DPN-41 transponder. It would be highly desirable to have the same type of transponder for each launch range to avoid having to make mounting modifications in the payload.

Skin tracking radar should also be used as a backup system for each launch. Although unable to maintain track over the full trajectory, they can provide a highly accurate track through the first 50 to 100 km of flight. The

UNCLASSIFIED

flight profile could be generated by extrapolation from this initial track to provide useful data in the event of failure in the primary transponder tracking system.

Principal areas of work to be done on the tracking subsystem are: integration and coordination with ground stations; selection of compatible transponder; antenna design and pattern measurement; thermal analysis and packaging.

5.3.5 Electrical Power Subsystem

The electrical power subsystem furnishes the rocket system with a continuous source of electricity. The subsystem basically consists of three electrically isolated battery supplies for vehicle, payload and recovery package power. Qualified, off-the-shelf, batteries are available for each application.

The vehicle supply provides power to circuits associated with nose cone removal, payload separation and other pulse-type loads. This supply consists of two small, electrically isolated, batteries connected to the redundant vehicle control circuits. The battery is a high-discharge, remotely activated, silver-zinc battery. Activation time is less than one minute with a stand lifetime of six hours. An internal heater is provided. The battery has provisions for external heater power, external activation and external monitoring of the battery voltage.

The payload power supply uses two silver-zinc secondary batteries. These batteries are capable of supplying the required electrical loads for 2 hrs with output voltage limits of 23.5 to 26 volts. The two batteries are normally operated electrically isolated to minimize interference between payload subsystems. Provisions are provided to allow either battery to supply the entire payload in the event of a battery failure. Circuits are provided to allow the payload to operate from external power and to allow the batteries to be charged when mounted in the rocket payload.

The recovery package power is provided by a separate battery. This battery has sufficient capacity to activate recovery circuits and to operate the recovery beacon for 24 hrs.

The electrical power subsystem must remain compatible with the power utilizing subsystems, the rocket-payload configuration and rocket launch procedures throughout the design period. The electrical power subsystem must monitor the above areas continuously as the payload system progresses to the final design. Specific tasks which will be accomplished during the design period are as follows:

- Electrical Power Allocation -- The electrical power allocations for the individual utilizing subsystems will be continuously monitored throughout the design period. The amount of power

UNCLASSIFIED

and the type of power for each subsystem and the influence of individual utilizing loads on the electrical bus will be evaluated and controlled so as to result in the best overall system design.

- Rocket Payload Configuration -- The size, volume and weight, allocation for the electrical power subsystem must remain compatible with electrical power performance and reliability requirements. Continued comparison of the size allocation and the preflight and inflight environment with electrical performance, control and reliability requirements will be required throughout the design and build phases. Size, performance, and cost of silver-zinc, silver-cadmium and nickel-cadmium batteries will be traded off if required.
- Rocket Launch -- The electrical power subsystem must be compatible with rocket-payload launch requirements. Items of concern are ground operating time on the battery supply and launch site external power and battery charging facilities. The electrical power subsystem will be designed to meet the requirements as utilizing subsystem preflight checkout procedures and launch site selection or finalized during the design period.

5.3.6 Structure

The outer structure of the payload consists in large part of standard BBVB components. The nose fairing is a tangent ogive clamshell structure which is jettisoned to expose the experiment radiometer. Aerodynamic loads on the nose fairing are transferred around the radiometer, through the first and into the second of four Black Brant standard extension cylinders, at which location the first attachment to the inner structure is made. From that point on, parallel load paths through both the inner and outer structure will be available to carry the loads into the igniter housing, which is the rearmost section of the payload.

The internal construction of the payload is intended to follow the general method of structural support and load distribution as has been successfully used with the BBVB vehicle on other programs. Figure 116 is a preliminary conceptual drawing of the payload configuration. As shown, the major portion of the payload length is comprised of the spectral radiometer, shown as a right cylinder (16-in. diameter x 48 in. long) with a pressure dome on the forward end. The balance of the payload is positioned aft of the radiometer in separate functional equipment decks. These decks are interconnected longitudinally by four structural members between each deck and are also attached to the outer structure to provide the required strength and rigidity to withstand the launch, flight, and recovery loads.

UNCLASSIFIED

Attachment of the experiment radiometer to the first equipment deck is accomplished at four points around the circumference at the rear of the radiometer. The instrument is stressed so that its structure will be adequate to carry the loads necessitated by this cantilevered-type mounting. The section immediately aft of the radiometer provides mounting and alignment provisions for the attitude and rate gyros and associated electronics. This location enables the closest possible alignment between these sensors and the radiometer to be achieved and maintained throughout the flight.

Located behind the attitude and rate sensing section is the power and communications deck, followed by the reaction control gas system, recovery section and igniter housing.

A weight breakdown of the system is shown in Table 31.

UNCLASSIFIED

Table 31. Weight Breakdown

Item	Weight (lbs)
Nose fairing	53.0
STD cylindrical extension (2) 21.7" @ 28 lbs	56.0
STD cylindrical extension (1) 16.3" @ 23 lbs	23.0
STD cylindrical extension (1) 11.3" @ 18 lbs	18.0
Igniter housing	19.0
Radiometer	80.0
Attitude and rate-sensing section	54.9
(2) ESG	27.0
(3) Rate gyros	1.5
(2) Electronics assemblies	8.4
(1) Wiring harness	
Mounting and connecting structure	15.4
Electric power and communications section	68.5
(2) Batteries, ignition	4.0
(2) Batteries, power	14.0
(2) Power-processing assemblies	4.0
(1) Programmer	5.0
(1) Transponder	8.0
(1) Telemetry assembly	12.0
Rocket and payload instrumentation	2.5
Antennas	2.0
Wiring harness	3.0
Mounting and connecting structure	14.0
Reaction control gas system	53.7
(6) Titanium storage tanks	21.6
(1) Press regulator	3.8
(1) Press relief valve	0.5
(1) Gas filter	2.2
(1) Fill valve	0.1
(6) Thrusters and nozzle extensions	6.5
(2) Gas manifolds	1.6
Tubing and fittings	1.3
Mounting and connecting structure	16.0
Recovery section	65.0
Total	491.0

SECTION 6

PROGRAM PLAN AND COSTING

6.1 GROUND RULES

The recommended probe program calls for 10 launches covering the seasonal, diurnal and geographic variation. These launches will be held at a northern launch site (assumed here to be Fort Churchill) and a temperate site (assumed here to be Eglin Field). In addition a minimum-cost program has been described which calls for three probes launched from a northern site.

A baseline program plan was issued to obtain costing information. This schedule is shown in Figure 124. A general statement of work and test plan was issued. Approximately one year is allocated to procurement, fabrication and testing of the sensor, attitude system, auxiliary systems and integrating structure. It has been assumed that a single contractor will be responsible for the instrument system. The system would, after qualification and test, be delivered to AFCRL as an integrated assembly, for installation on a Black Brant VB. Costs of the rocket have been obtained and are included in the estimates. Cost of data reduction to calibrated radiance-position data have been estimated. AFCRL integration and test range costs have not been included in these estimates. It should be understood that all cost information are rough order-of-magnitude estimates based on the design baseline presented in this report. All cost quotes, with the exception of the cost for the Black Brant VB, were obtained from divisions of Honeywell. Model Statements of Work were issued and a response generated through the normal quoting channels. No negotiations were held against these estimates; hence the rough order of magnitude.

For quoting purposes, the integrated instrument package was broken into 5 subsystems, and costs are collected against these subsystems. The subsystem areas are:

- System design and system analysis during fabrication/test
- Attitude determination and control subsystem
- Radiometer
- Auxiliary subsystems (power, telemetry, recovery)
- Integrating structure

As part of the baseline instructions, it was assumed that four flightworthy integrated instrument systems would be required to meet a launch schedule calling for 10 launches in one year. It was further assumed that a minimum

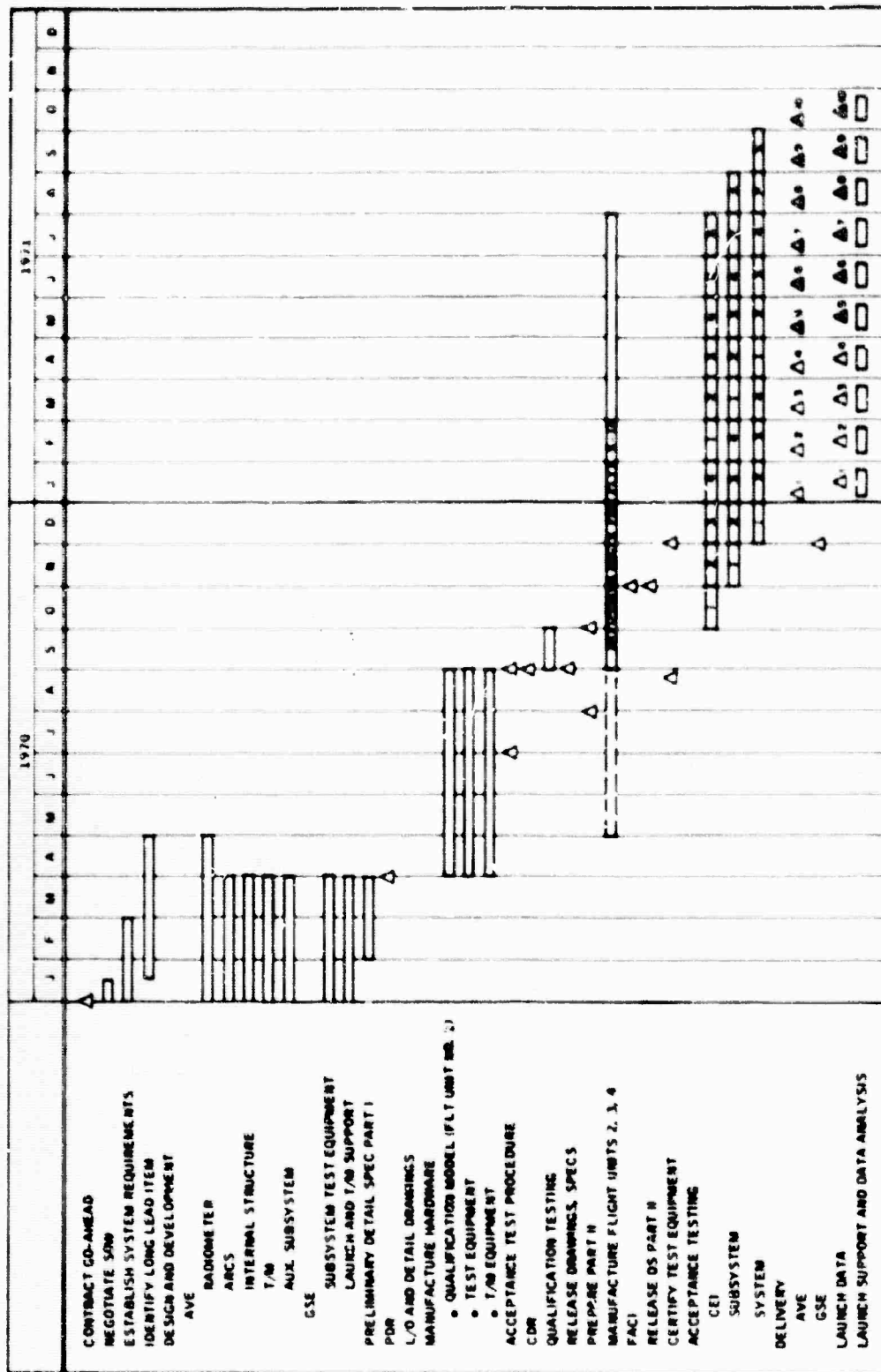


Figure 124. Integrated Instrument System Program Plan

qualification program would be required on each subsystem, that the integrating structure would be qualified with dummy instruments and a system test of the integrated system would be required.

6.2 STATEMENT OF WORK

(1.0) General

This statement of work covers the design, development, fabrication, test and data reduction of an integrated instrument system. This system is designed to measure the spectral radiance of the earth limb in the LWIR. The system consists of the following subsystems:

- (a) Spectral Radiometer
- (b) Attitude Reference and Control System (ARCS)
- (c) Integrating Structure
- (d) Telemetry
- (e) Power
- (f) Auxiliary Measurement Systems
- (g) Ground Support Equipment

The integrated instrument system will be delivered to AFCRL (CRE), Hanscom Field, Bedford, Massachusetts, for final integration and flight. Recorded telemetered data will be delivered to Honeywell Inc., Minneapolis, for reduction to calibrated radiance and position data. These data will be delivered to AFCRL (CROR) for final data analysis.

The program is a ten (10)-flight program, with first flight scheduled during the month of January 1971. A minimum qualification and test program will be required. Four (4) flight systems and two (2) GSG systems will be delivered in accordance with the appended milestone chart. Upon recovery, the flight systems will be returned to Honeywell Inc., Minneapolis, for refurbishment. One set of GSE equipment will be delivered to AFCRL, and one retained at Honeywell. The equipment to be fabricated and delivered under this statement of work are as defined in section 6.4.

(2.0) System Design

(2.1) Requirements

The basic requirements for this program are established in the foregoing sections of this report. During the design phase, a continuing effort in the study of requirements shall be undertaken to allow for iteration of requirements and design.

(2.2) Spectral Radiometer

A spectral radiometer shall be designed. The design given in Section 4 shall be used as a baseline design. A design-to specification shall be issued. A critical design review shall precede the issuance of this specification.

(2.3) Attitude Reference and Control System

An attitude reference and control system shall be designed. The design given in Section 5 shall be used as a baseline design. A design-to specification shall be issued. A critical design review shall precede the issuance of this specification.

(2.4) Integrating Structure

An integrating structure, whose function is to provide an alignment mount for the radiometer and attitude determination package and provide for inclusion of a telemetry power subsystem and the interconnection wiring, shall be designed. Provision shall be made for mounting with a GFE recovery package and with the Black Brant VB vooster. The design given in Section 5 shall be used as a baseline design for a tradeoff study to establish a final design. A design-to specification shall be issued. A critical design review shall precede the issuance of this specification.

(2.5) Telemetry

A telemetry subsystem shall be specified using off-the-shelf components. A requirements specification shall be issued.

The telemetry system will be a PCM-FM system, maximum bit rate 102 kilobits. Analog-to-digital conversion will be provided for 29 radiometer channels, two channels of attitude reference system output, and up to 40 housekeeping data channels.

(2.6) Power

A power supply subsystem shall be specified using off-the-shelf components. A procurement specification shall be issued. Three electrically isolated power supplies shall be utilized for each system, providing vehicle, payload and recovery power.

(2.7) Auxiliary Measurements

A study shall be made of the requirements for temperature, voltage and pressure measurements. A system shall be designed to interface with the telemetry system to provide these measurements. A design-to specification shall be issued.

(2.8) System Integration and Test

Integration specifications shall be derived. An overall test schedule will be established for developmental, acceptance, proof testing and system integration testing. Test specifications shall be written.

(2.9) Data Processing System

A data processing system shall be designed and design specifications for computer programs issued.

(2.10) Ground Support Equipment

(2.10.1) Cryogenic Cart

A cryogenic cart will be designed to provide on-site cryogenic support for the radiometer. A build-to specification will be issued.

(2.10.2) Alignment System

A system will be designed to provide final alignment of the Attitude Reference and Control System before launch. A build-to specification will be issued.

(3.0) Fabrication

(3.1) Spectral Radiometer

A spectral radiometer shall be produced in accordance with the build-to specification and section 6.4.

(3.2) Attitude Reference and Control System

An attitude reference and control subsystem shall be produced in accordance with the build-to specification and section 6.4.

(3.3) Integrating Structure

An integrating structure shall be fabricated in accordance with the build-to specification.

(3.4) Telemetry System

The telemetry subsystem components shall be purchased in accordance with the procurement specifications.

(3.5) Power

The power supply subsystem shall be purchased in accordance with the procurement specifications.

(3.6) Auxiliary Measurement System

The auxiliary measurement subsystem shall be produced in accordance with the build-to specification.

(3.7) Subsystem Integration

The subsystem components shall be assembled into an integrated system in accordance with the integration specification.

(3.8) Data Processing

Computer programs shall be written, de-bugged, and validated with sample runs in accordance with the design specifications.

UNCLASSIFIED

(3.9) GSE

(3.9.1) Cryogenic Cart

A cryogenic cart will be produced in accordance with the design-to specification.

(3.9.2) Alignment System

An alignment system will be produced in accordance with the design-to specification.

(4.0) Test

(4.1) Qualification

(4.1.1) Radiometer

The radiometer shall be tested as a unit to the flight environment acceleration and shock envelope. The radiometer shall be tested in a thermal environment representing the extremes of the ground and flight environment.

(4.1.2) Attitude Reference and Control Subsystem

The attitude reference and control subsystem shall be tested as a unit to the flight environment shock and acceleration envelope.

(4.1.3) Structure

The integrating structure shall be tested with simulated packages (mass and size) representing radiometer, attitude reference and control subsystem, telemetry and power subsystem to the flight environment shock and acceleration envelope. Instrumentation shall be incorporated in this test to measure acceleration and shock transmissibility and amplification.

(4.2) Functional Testing

(4.2.1) Radiometer

The radiometer shall be tested for functional operation at the manufacturing facility. The radiometer shall then be delivered to Honeywell Inc., Minneapolis, for performance testing and integration.

UNCLASSIFIED

(4.3) Performance

(4.3.1) Radiometer

After proof of functioning, the instrument shall be delivered to Honeywell, Minneapolis, for performance testing. Additional performance cross-checks will be made at the AEDC (ARO) cold-chamber, Tullahoma, Tennessee. Upon completion of performance testing, the instrument shall be delivered to Honeywell, Minneapolis, for integration.

(4.3.2) Attitude Reference and Control

The attitude reference and control system shall be tested for performance in accordance with the test plan.

(4.3.3) Telemetry System

The telemetry system shall be installed in the integrating structure and tested for interconnection integrity. Antenna pattern tests shall be made during this test sequence.

(4.4) Systems Test

The integrated system will undergo a system test in accordance with the test plan.

(5.0) Flight Program

(5.1) Flight Support

Honeywell shall provide technician and engineering support during the flight program.

(5.1.1) Launch Support

Honeywell will supply technician support.

(5.1.2) Refurbishment of Recovered Equipment

Honeywell shall refurbish and test recovered equipment. The test program for refurbished equipment will be identical to the test program for original equipment.

UNCLASSIFIED

(5.1.3) Data Reduction

Honeywell will provide data reduction services to reduce recorded flight data to calibrated radiance and position data.

(6.0) Program Control Requirements and Documentation

Submit plans for approval:

- Configuration Control Plan
- Reliability Plan
- Quality Plan
- Operation and Maintenance Plan
- Personnel Support Plan
- Subcontract Procurement Plan

(6.1) Configuration Control Plan

Control all contract end-item devices, subsystems and systems to approved "Design to" baseline specifications. Departures from the baseline will be controlled by engineering change control procedures, directing configuration changes to released documentation.

"As-built" hardware will be verified to the "as-engineered" data specified to an end-item serial number device.

Documentation records will be maintained that will associate specific design data to the specific set of hardware, including part number, drawing revision letters, ECO log for serialized units, traceability recording where necessary at device, subsystem or system level to support performance data.

(6.2) Reliability Maintainability

A limited reliability/maintainability analysis is required.

Analyses shall be performed to predict the system MTBF and the system maximum time to repair.

All test information shall be computed and compared to model predictions of reliability/maintainability.

UNCLASSIFIED

(6.3) Quality Assurance

A quality program in accordance with the requirements of MIL-I-45208A and the approved quality assurance plan shall be provided.

(6.4) Operation and Maintenance Procedures

A set of operation and maintenance procedures shall be developed for the integrated instrument system.

(6.5) Personnel Subsystems

A limited analysis shall be performed to ensure that no degradation of performance or maintenance occurs due to the personnel subsystem.

(6.6) Data

The established Honeywell Data Control function will be used for integrating the data management effort with the Program Control Office. Honeywell's standard data management system conforms to MIL-D-1000, with drawings, specifications prepared to MIL-STD-100. Data transmittals will be prepared on CDRL DD1423 forms in accordance with categories and frequency negotiated in statement of work.

Data management will be primarily concerned with data to be delivered to ARPA as directed by contract SDRL's.

6.3 TESTING

6.3.1 Development Testing

Because of the short time scale proposed for the spectral radiometer, it will be necessary to rely for development testing upon the radiometer and chamber presently being fabricated at Honeywell as an investment program. This radiometer is similar to the proposed radiometer, with the exception of the multiple-channel spectral array; that is, the forebaffle, blackbody absorbing baffles, pin-hole Lyot lens and general optical configuration are essentially identical. Testing of the completed radiometer is scheduled to begin in March 1970. Tests have been conducted on the blackbody baffle concept with excellent results. Preliminary testing of the Lyot lens principle has been conducted and a direct test of a visible light analog will be conducted. Other tests are tentatively scheduled to examine the cascaded effect of these baffles in a scattering environment. Scattering measurements on optical surfaces of the mirrors have been made at 10.6 microns with excellent

UNCLASSIFIED

results. Testing of the completed assembly for sensitivity and near on-axis stray light rejection will be accomplished by the end of April. This radiometer will be cross-tested at AEDC, Tullahoma, in March 1970. The Honeywell chamber is capable of accepting the proposed instrument with no modification. A design for testing high-rejection cold filters is presently under way.

6.3.2 Qualification Testing

Again, because of the short time scale, qualification testing will be held to a minimum. Because the spectral radiometer is a sealed vacuum assembly testing for humidity, temperature, fungus, etc. will be held to a minimum. It is proposed that the environmental testing be accomplished in one of the Honeywell 5-ft diameter vacuum chambers. Tests will be for helium leak rate on exposure to expected environmental temperatures, for coolant hold-time and for warmup under simulated flight environment. A solar simulator is available for this series of tests.

The radiometer will be checked for alignment hold after cooldown and will be tested for alignment after exposure to simulated flight acceleration, shock and vibration.

The program plan is predicated upon a successful qualification schedule. Fabrication of the four radiometers is phased in one-month intervals. Failure of qualification will result in the failed unit being placed at the end of the delivery schedule, rework of instruments in the pipeline after redesign and designation of the second unit as qualification unit.

The major problems in design of this instrument are not environmental. The flight environment is relatively benign and similar instruments have been successfully flown in more severe environments. We do not anticipate difficulty in qualification of the instrument.

6.3.3 Performance Testing

The instrument will be tested for function at the point of fabrication, and performance testing will be conducted at Minneapolis in the Honeywell chamber, with a cross-test at the USAF Tullahoma facility.

Functional testing will consist of the following:

- Cooldown and alignment check in vacuum
- High-amplitude continuity check and verification of array operation

UNCLASSIFIED

- Chopper operation
- Leak-check of cryogenic system
- Spectral check at high amplitude.

Performance testing in Minneapolis will consist of sensitivity, spectral resolution and near on-axis (less than 5-deg) stray light rejection of an extended source.

Performance testing at Tullahoma will consist of a cross test of sensitivity and measurement of stray light rejection for off-axis (greater than 10-deg) radiation using goniometric techniques.

6.3.4 Long-Wavelength Infrared (LWIR) Test And Calibration Chamber

A LWIR test and calibration chamber, presently in the design phase, has been fabricated at Honeywell. The primary purpose of the chamber is to verify performance of cooled, LWIR radiometric instruments. The chamber is specifically designed to accommodate radiometric instruments which operate in the 5- to 25-micron spectral region and which include the following two primary performance features:

- Extremely high sensitivity typical of BLIP operation
- Extremely high rejection of stray radiation outside the normal field

To test these performance features, the chamber will be evaluated, cooled to cryogenic temperatures to eliminate internal thermal emission, and carefully baffled to prevent multiple reflections of stray radiation within the chamber.

Inasmuch as this chamber is an experimental facility, its secondary purpose is to provide the means to investigate and assess the problems encountered with BLIP operation and stray-radiation rejection in terms of LWIR sensors.

Special provisions included within the chamber which accommodate the various tests include:

- Separate cooled choppers for both radiation sources (point and extended) to distinguish on-axis from off-axis radiation

UNCLASSIFIED

- Filter wheels and variable temperature sources to stimulate spectral response of targets and backgrounds
- Adjustable radiation attenuator for wide dynamic range measurements
- Internal baffling and blackbody-type cavity traps to attenuate stray radiation
- Angular adjustment of point source with respect to extended source

In addition, the chamber design allows for growth in terms of testing wide field radiometer configurations.

The chamber contains two radiant sources of variable temperature (20°K to 300°K) and aperture, cold, variable frequency choppers, filter wheel, radiation attenuator, a primary collimating mirror, a relay mirror and an extended source projector mirror. One radiant source is a standard blackbody which provides the low-level signals for primary on-axis calibration of point and extended sources. In addition, the intensity of this source can be increased to accommodate baffle attenuation measurements at large angles off-axis. The second source is a heated button whose radiation is projected to an angular position near the point source and which simulates a portion of the earth's radiation. This source provides a way of testing near field attenuation factors against extended sources.

The chamber contains two shrouds, an intermediate shroud at liquid nitrogen temperature (77°K) and an internal shroud at or near liquid helium temperature (4°K - 20°K). The helium shroud is painted and baffled completely on the inside. In addition, each radiant source, as well as the collimated beam, is shielded by specially designed conical traps. These internal baffles and traps reduce stray radiation from scattering within the chamber.

6.4 TASK PLANS

The program activities to be accomplished during this program are shown in Figure 125.

Three phases of activity provide a comprehensive approach to systems baseline management. Each phase will provide adequate definition to define a baseline requirement.

Program management will define the major tasks and subtasks from the statement of work. These tasks and subtasks will be defined as an entity in the performance of completion of a task: i.e., a subcontract procurement task will be a completed task and a service performed by a project supervisor will be work accomplished for the specific service. (See Figures 126 and 127.)

UNCLASSIFIED

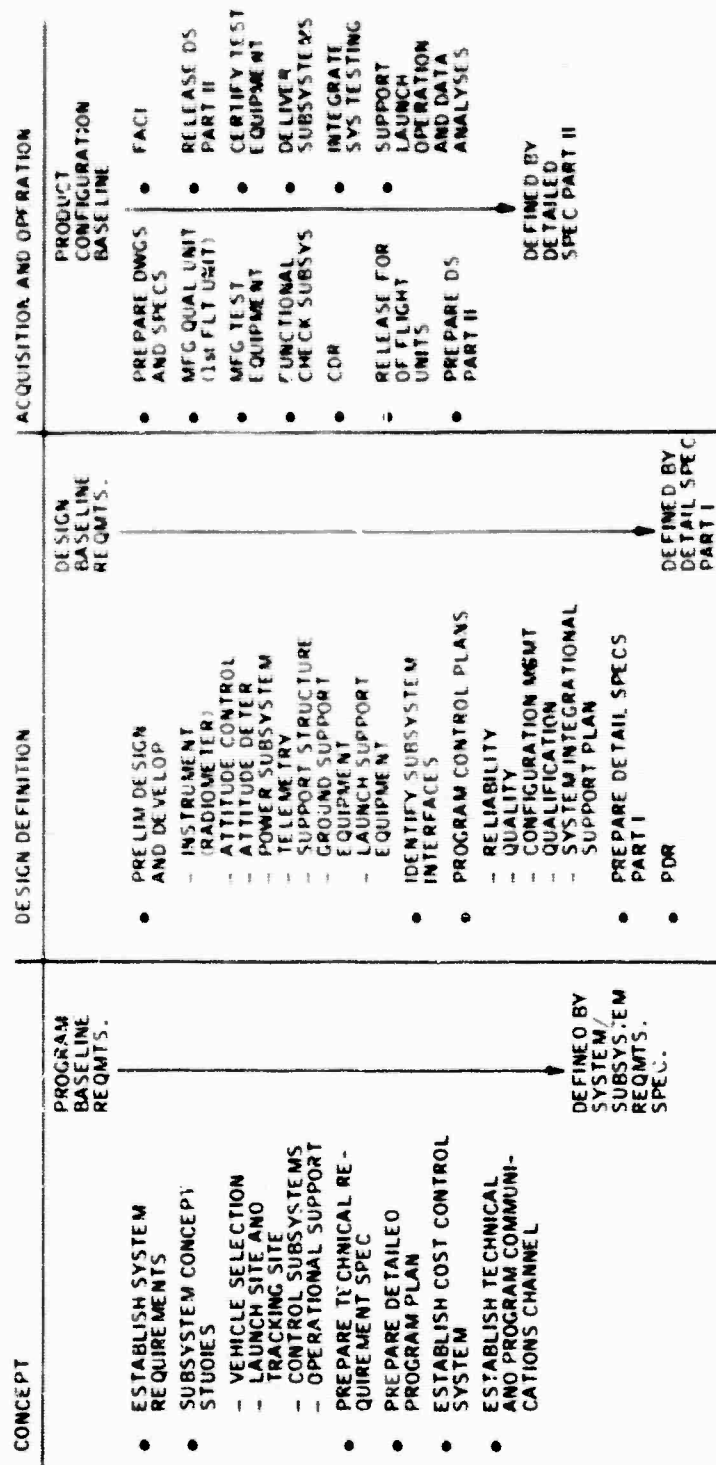
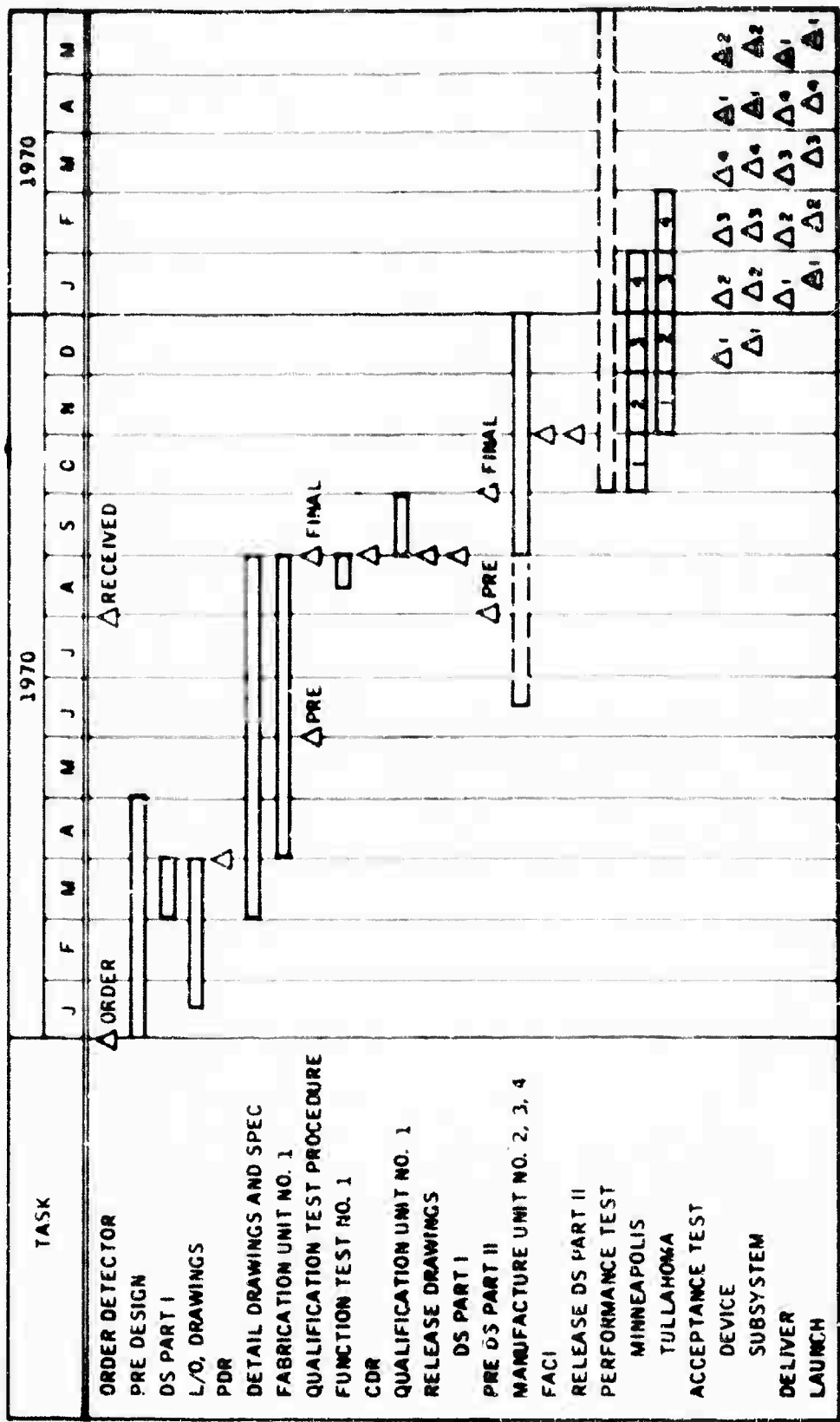


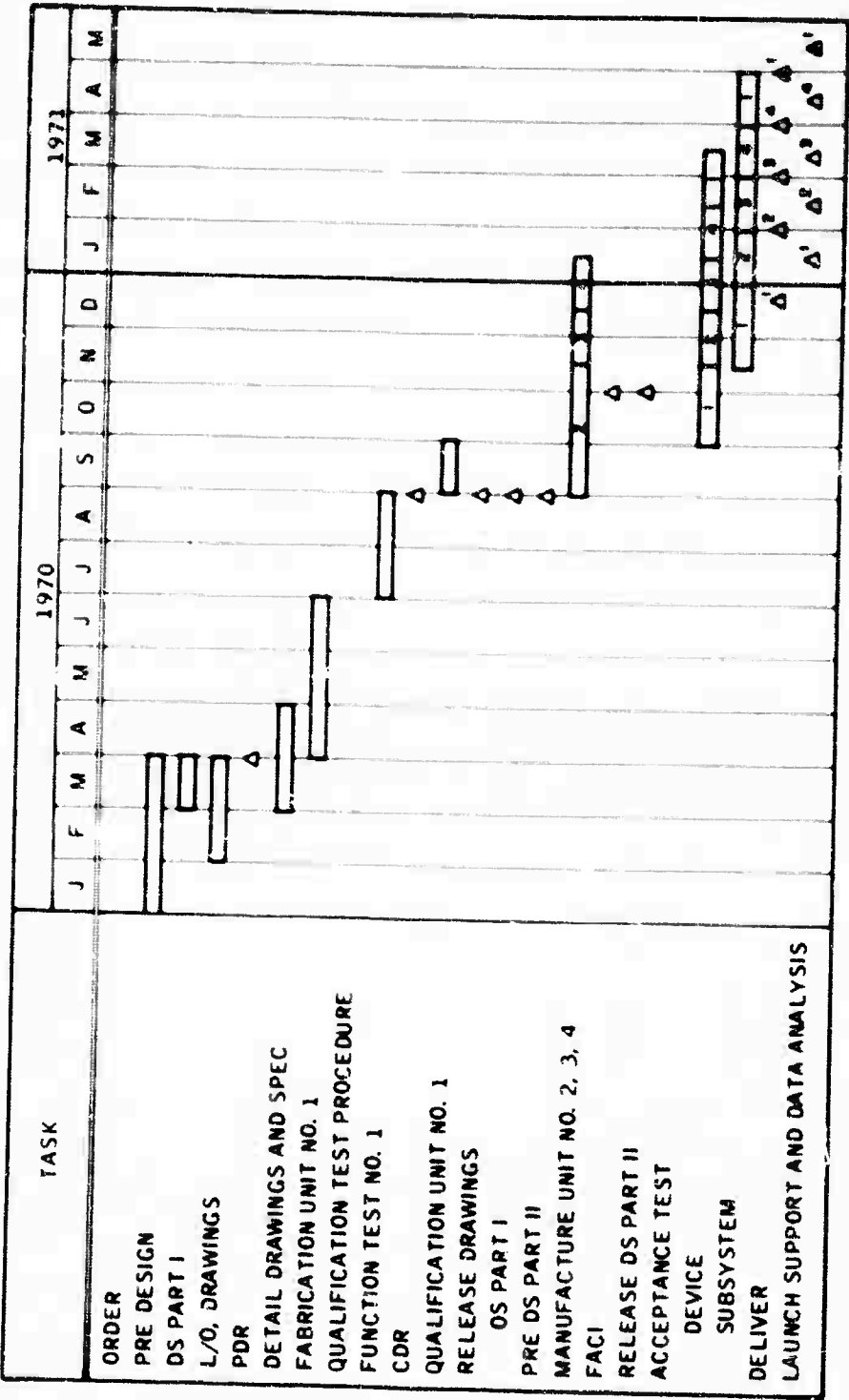
Figure 125. Activities Flow Diagram

UNCLASSIFIED



△ KEY MILESTONE
△ REFURBISH RADIOMETER

Figure 126. Radiometer Flow Plan



Δ KEY MILESTONE
◊ REFURBISH ARCS

Figure 127. ARCS Flow Plan

UNCLASSIFIED

6.4.1 System Task

Upon receipt of contract, a final statement of work will be negotiated with the total Integrated Instrument System objectives and tasks defined to include analyses, design, development, fabrication, test and operational support.

Basic approaches to be employed during the program or serve as a constraint are as follows:

- The total system and its elements will be analyzed to define all requirements and interfaces, i.e., mission, systems, subsystems, components and parts.
- Design and development will result in a set of preliminary detail specifications to define a subsystem, or CEI function, configuration envelope, I/O characteristics and interface definition.
- Testing will be conducted to verify the performance capabilities for given operating conditions. Qualification testing will be accomplished to the extent necessary to design proof the system for mission application.
- Designs will be controlled by documentation that specify mechanical, electrical, thermal, etc. definitions, with rigorous control to ascertain that all manufactured and/or procured items can be verified by quality.
- Test equipment shall be adequate to simulate and check out the performance of a system.

6.4.2 Design and Definition

The total integrated system consists of radiometer, ARCS, auxiliary measurement devices, power supply, internal support structure, telemetry and vehicle (including recovery system). Detail specification (part II) will be generated on each of these subsystems at completion of approximately three months of design and development analyses. At this time a Preliminary Design Review (PDR) will be conducted to present the recommended design approach to the program. Customer approval of design and development techniques and guidelines is the direction to proceed with manufacture of the first unit.

6.4.3 Manufacturing

Subsequent to PDR, subcontractors are notified to begin manufacture of the first unit. Detail drawings and specifications are issued internally at Honeywell to begin fabrication of ARCS, support structure, and AGE.

UNCLASSIFIED

equipment. Manufacturing of the first unit will be accomplished to pre-released drawings that are subject to informal change control procedures. This permits design changes to be made on working master drawings with all changes recorded and reviewed by cognizant project engineer.

The first unit fabricated will be subjected to limited qualification testing. To ascertain the integrity of the qualification unit, a critical design review (CDR) will be held prior to environmental qualification testing. This will be the second design review in which ARPA/AFCRL personnel participate to determine the subsystem compatibilities and the integrity of the design.

At completion of CDR, all drawings and Part I specifications will be released as they become finalized.

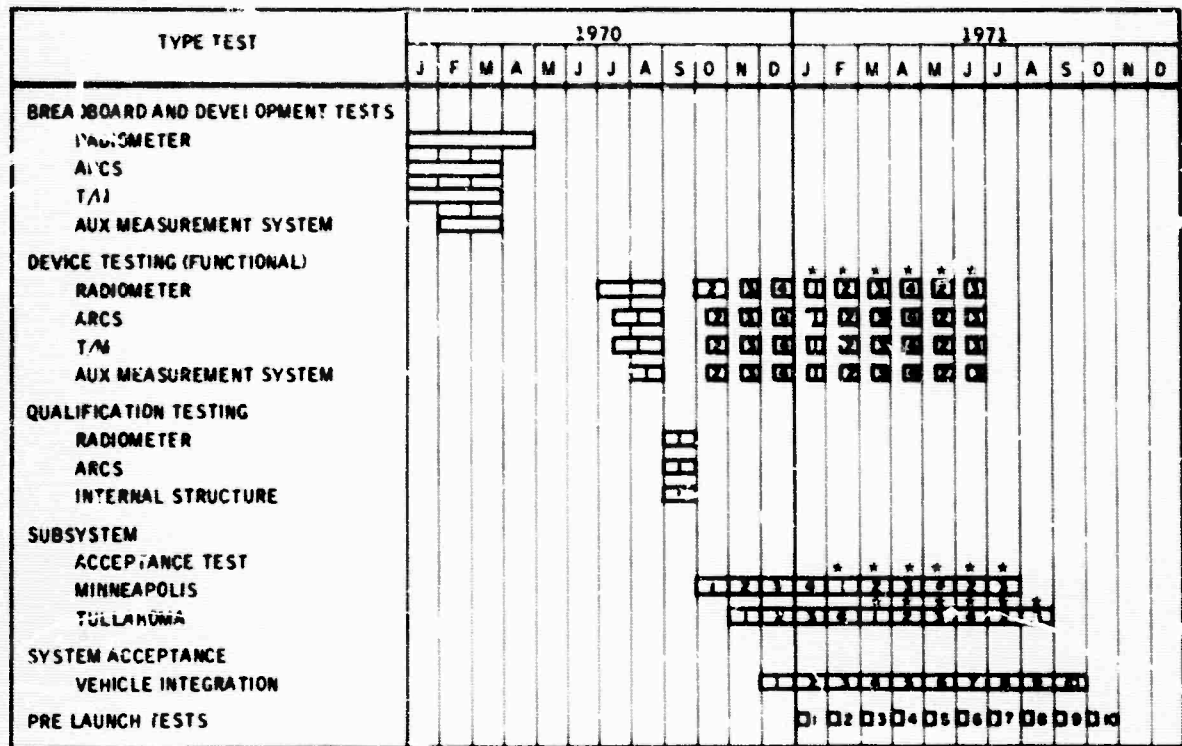
Environmental testing on the first unit will be conducted at the CEI device level to the extent necessary to design proof test the configuration. Upon completion of qualification testing both at Honeywell and its subcontractors, the "build-to" detail specification Part II will be updated to reflect the qualification model (flight unit number one) and issued for acceptance test procedure verification.

Manufacture of flight units two, three and four shall begin at release of documentation. At the completion of manufacture of the second unit (including subcontracted devices) a "FACI" Review will be held. The second flight unit configuration will be reviewed for compatibility of the hardware with released and formally control documentation. This review will also serve to establish the validity of the acceptance testing of hardware by direct comparison of the acceptance test methods and test performance parameters of the specified hardware.

6.4.4 Testing

Testing will be accomplished in accordance with a master test plan schedule. A preliminary test plan and schedule are shown in Figures 128 and 129, with procedures to be delineated by test engineers and quality assurance. The overall test program will consist of breadboard testing as necessary for the specific function; development testing to define interfaces and environmental effects on performance limits; functional testing of a completed device prior to qualification testing or flight environment checks, minimal qualification testing as determined by the necessity of a proven design or a state-of-the-art application; subsystem acceptance testing to specified performance limits; system integration testing at the launch facility.

UNCLASSIFIED



- 1 QUALITY UNIT (1ST FLIGHT UNIT)
- 2 2ND FLIGHT UNIT
- 2 REFURBISHED FLIGHT UNIT NO. 2

Figure 128. Test Schedule

UNCLASSIFIED

UNCLASSIFIED

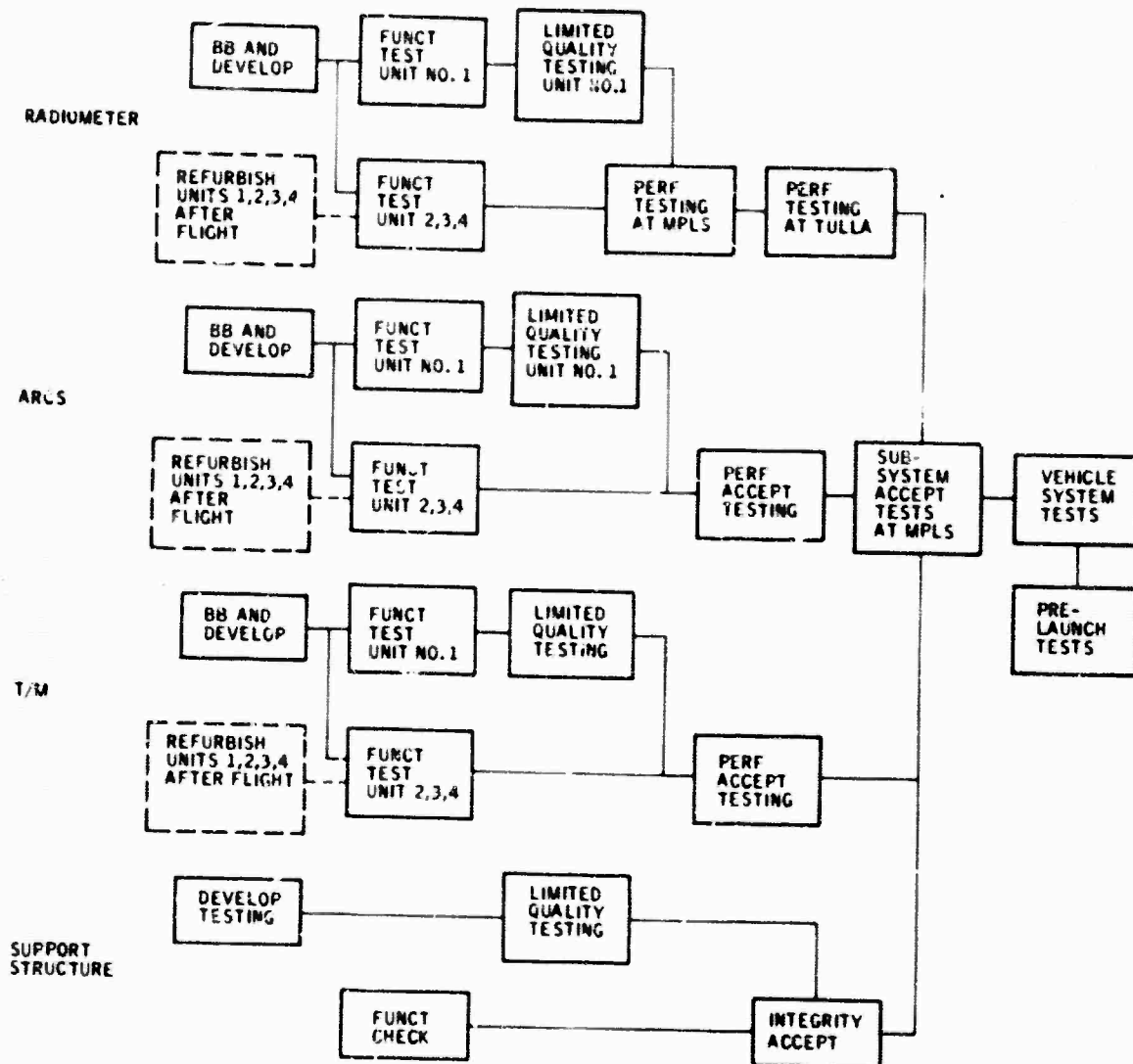


Figure 129. Master Test Plan

UNCLASSIFIED

UNCLASSIFIED

6.4.5 Flight Program

Launch Support -- Field service engineers, with systems engineering support, will be provided at the launch facility for each flight. This support begins with prelaunch testing and follows through launch execution. The software and operating procedures for data handling and processing will be developed and available for all launch activity.

After launch, data handling and analysis will be processed at Honeywell, Minneapolis, computer facility and reports prepared documenting each flight's measurement.

Refurbishment -- Predicated on the fact that each integrated instrument system will be recovered from flight, the radiometer, ARCS, telemetry, auxiliary measurement units, and power supplies will be returned to Honeywell, Minneapolis, for re-acceptance testing. Upon satisfactory retesting of the individual devices, the units will be remounted to the support structure and subjected to subsystem and systems test in preparation for another launch.

6.5 OPERATION AND MAINTENANCE PROCEDURES

Honeywell will develop a set of operation and maintenance procedures for this program. These procedures will be based on the results of a maintainability analysis along with the applicable extensive background of experience gained from similar programs. The procedures will contain but not necessarily be limited to:

- Assembly and calibration to special test equipment
- Detailed maintenance techniques
- Maintenance intervals
- Special operating procedures

6.6 CONFIGURATION CONTROL

Honeywell believes that applying the principles of configuration management -- as described by DOD, NASA, and the military services -- constitutes a logical approach to sound management of technical requirements and products. As a result, a major Honeywell effort has produced an operating system which effectively provides precise identification and control of the configuration of a product. Honeywell has demonstrated its capability to manage configuration on such NASA, Air Force, and Navy programs as Mercury, Gemini, Apollo, Agena D, Athena, F-111, Polaris, MOL, and Mariner Mars '69. During the performance of these contracts, Honeywell's configuration system has undergone strict audit and review by Government agencies and prime contractors and has received outstanding recommendations from both.

UNCLASSIFIED

Honeywell's system will meet all configuration management requirements of this program. The Honeywell system fully provides for configuration identification, control, status accounting, and reporting. The system further provides for verification that the "as-built" configuration meets the "as-designed" configuration from initial definition of equipment throughout the life of the program.

To take advantage of the concepts set forth by DOD and NASA Honeywell has established a Configuration Management System which achieves these requirements and provides additional tools for sound management. The result of this work is a system which gives precise control of the configuration of the product, and makes the data extremely visible, accessible, retrievable, and timely.

The Honeywell system is based upon capturing the engineering definition only once, at its source. Through the use of an H-1800 computer, this data is made available in the form needed for baseline definition, change control, precise product control, scheduling, accounting, and produce verification. All identifying data is entered into a data bank and is updated for all changes. Thus, the exact configuration of each serialized end item is established and maintained. This single source of data is used to prepare the engineering information in the format needed for each application.

All of Honeywell's major subcontractors will be required to meet the configuration identification, control, accounting and verification requirements stated. Those subcontractors whose existing configuration management systems meet those requirements will be permitted to utilize their own systems. Those subcontractors who cannot meet these requirements will be required to adopt those features of Honeywell's system needed to bring them into compliance. Although Honeywell utilizes a computer for its system, a computer is not required to operate the system.

The configuration control Engineering Change Flow Diagram which Honeywell will use for this program is shown in Figure 130. This control process was used with success in the Mariner Mars '69 program and is typical of others used at Honeywell. This process can be adjusted to meet special customer requirements.

6.7 COST ESTIMATE

Two cost estimates have been prepared, one for the baseline ten-probe experiment and one for the minimum three-probe experiment. As noted above government costs for test, mating with vehicle, and flight support are not included in these estimates.



Figure 130. Engineering Change Flow Diagram

UNCLASSIFIED

6.7.1 Ten-Flight Program

The proposed budgetary costs assume a ten-flight probe program using the Black Brant VB rocket. The costs of this rocket are also estimated below for information purposes; rocket is assumed to be GFE. The costs below include four (4) integrated instrument systems (assuming payload recovery and re-use) contractor launch support and preliminary postflight data reduction.

Integrated Instrument System (four)	\$ 4,154,000
Launch Support	<u>158,000</u>
Total LBM	4,312,000
G&A @20.7%	<u>893,000</u>
Total Cost	5,205,000
Fee @7%	<u>364,000</u>
CPFF	\$ 5,569,000

The ten launch vehicles supplied by the Government (ten boosted Black Brant VB rockets plus development of a Nike booster) have an estimated value of \$ 800,000.

The LBM breakdown of the contractor effort to subsystem level is as follows:

Spectral Radiometer	\$ 1,575,000
Attitude Reference and Control System	1,127,000
Electrical and Power System	83,000
Structure	225,000
Telemetry and Tracking System	348,000
Recovery System	60,000
System Design	100,000
Testing	500,000
Launch Support	158,000
Data Processing	<u>136,000</u>
	\$ 4,312,000

UNCLASSIFIED

6.7.2 Three-Flight Program

The proposed costs assume a three-flight program using the Black Brant VB rocket. The costs below include two integrated instrument systems, and one refurbishment, launch support and preliminary postflight data reduction:

Integrated Instrument (2)	\$ 1,584,500
Launch Support	<u>47,400</u>
Total LBM	1,631,900
G&A @20.7%	<u>326,380</u>
Total Cost	1,958,280
Fee at 7%	<u>137,060</u>
CPFF	\$ 2,095,340

The three launch vehicles are to be supplied by the government at a unit cost of \$42,000, resulting in a total cost for launch vehicles of \$126,000.

The LBM breakdown of the contractor effort to subsystem level is as follows:

Spectral Radiometer	600,000
Attitude Control System	250,000
Electrical and Power System	4,600
Structure	112,500
Telemetry and Tracking System	174,000
Recovery System	18,000
System Design	50,000
Testing	150,000
Launch Support	47,400
Data Processing	58,400

UNCLASSIFIED

REFERENCES

1. J. Dodgen, Symposium on IR Sensors, N68-27793, March 1967.
2. AFCRL 69-0552, Atmospheric Radiance Model for Limb Viewing Geometry in the Five to Twenty-five Micron Spectral Region, Contract F19628-69-C-0258, October 1969.
3. A. J. Kentor, Speculative Mean Monthly Temperatures in the Arctic (75°N) Stratosphere (25-55 km), J. of Geophysical Research, Volume 71, No. 10, May 1966, 2445.
4. NASA CR-66190, The 15 Micron Infrared Horizon Radiance Profile, Horizon Definition Study, October 1966.
5. W. J. McArthur, Horizon Sensor Navigation Errors Resulting from Statistical Variations in the 14-16 Micron Band, August 1964, Contract AF-04(695)-526.
6. S. Rangarajan, A. Worldwide Anomaly in the Concentration of Ozone above 40 km, J. of Atmospheric Sciences, Volume 26, May 1969, 613.
7. B. G. Hunt, Journal of Geophysics Research, Vol. 71, 1966, pp 1385-1398.
8. D. E. Bode, Low-Noise Cadmium and Copper-Doped Germanium Arrays (U), AD392031, Santa Barbara Research Center, 31 August 1968 (SECRET).
9. H. Nagaoka, Diffraction Phenomena in the Focal Plane of a Telescope with Circular Aperture, due to a Finite Source of Light, Philosophical Magazine and Journal of Sciences, Series 5, Vol. 45, No. 272, January 1898, pp 1-23.
10. R. P. Mikesell and R. B. Scott, Heat Conduction Through Insulating Supports in Very Low Temperature Equipment, J. of Res. of the National Bureau of Standards, Vol. 57, No. 6, December 1956.

PRECEDING PAGE BLANK-NOT FILMED

UNCLASSIFIED

APPENDIX A
SPECTRAL RADIANCE AND SIGNAL-TO-NOISE RATIO
AS A FUNCTION OF TANGENT HEIGHT

UNCLASSIFIED

UNCLASSIFIED

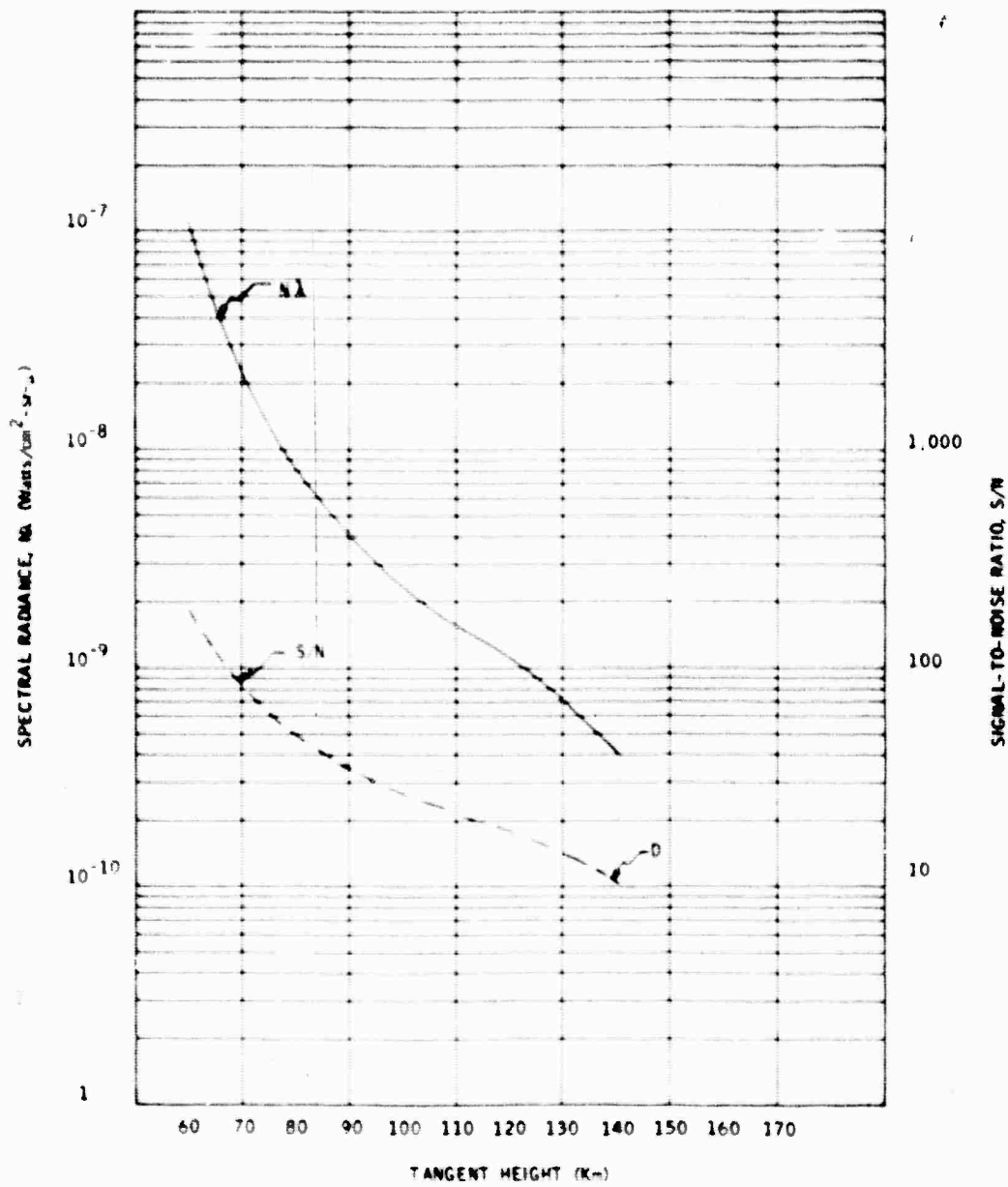


Figure A1. 5.0- to 5.7-micron Spectral Band

UNCLASSIFIED

UNCLASSIFIED

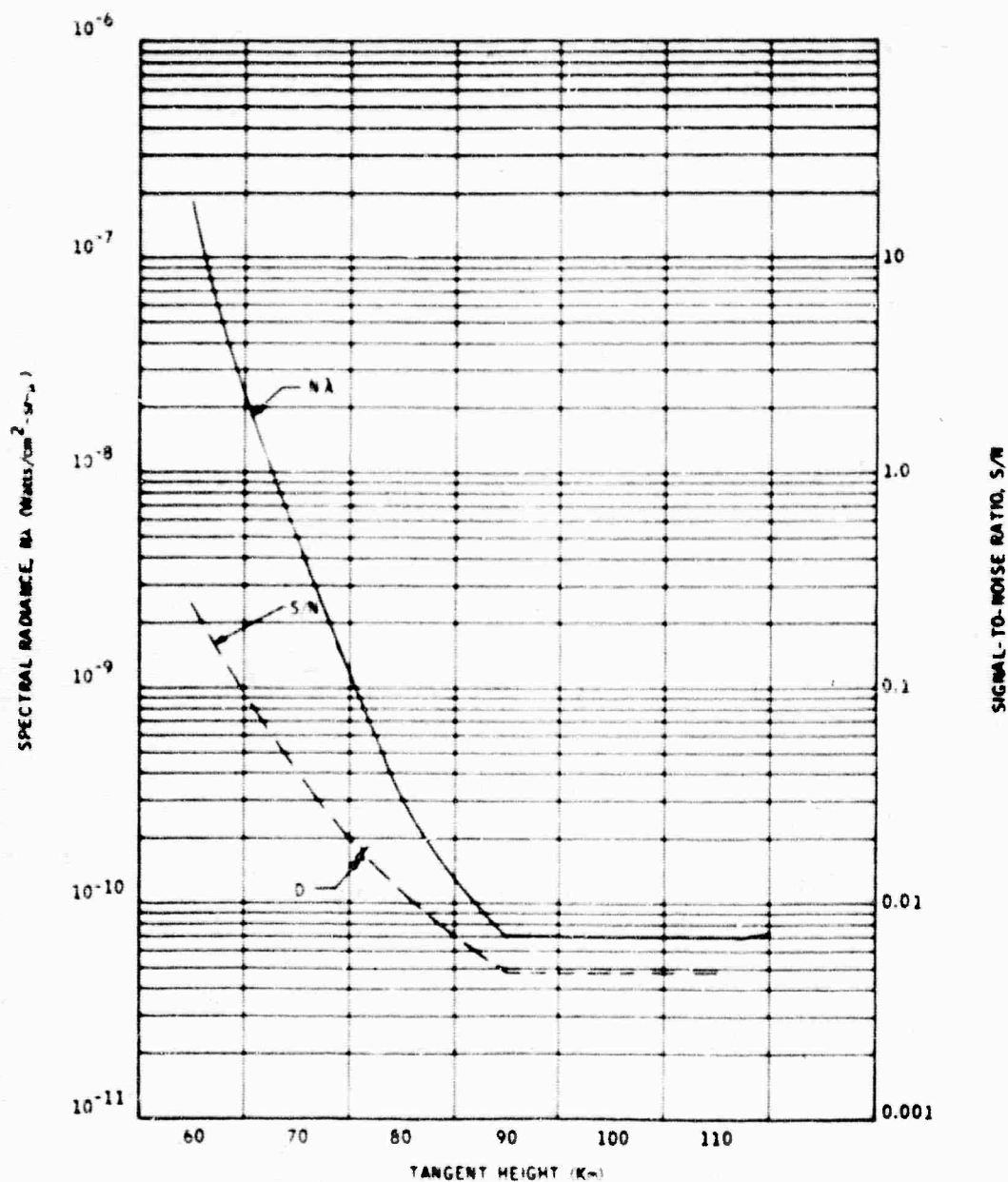


Figure A2. 5.7- to 6.4-micron Spectral Band

UNCLASSIFIED

UNCLASSIFIED

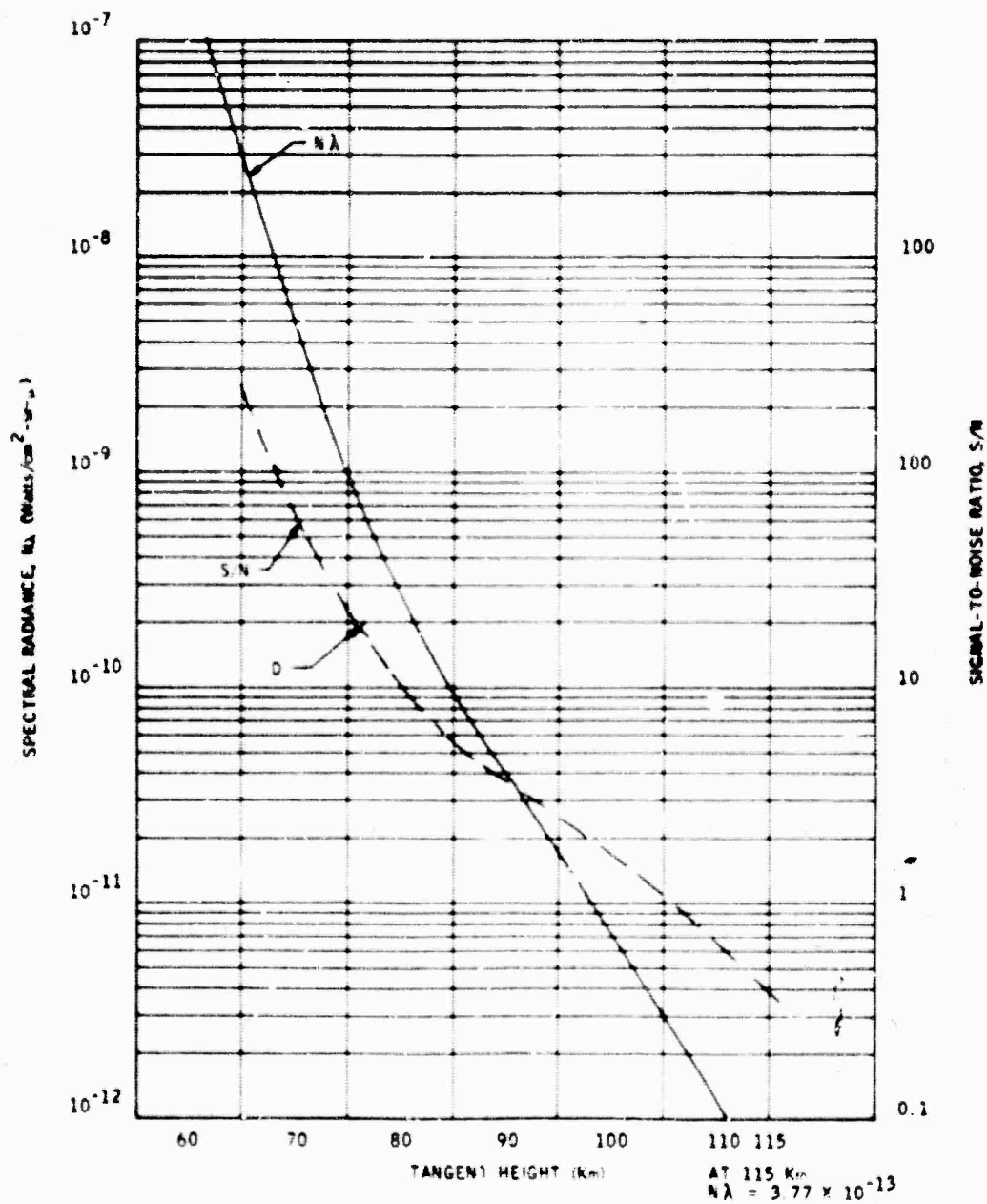


Figure A3. 6.7- to 7.0-micron Spectral Band

UNCLASSIFIED

UNCLASSIFIED

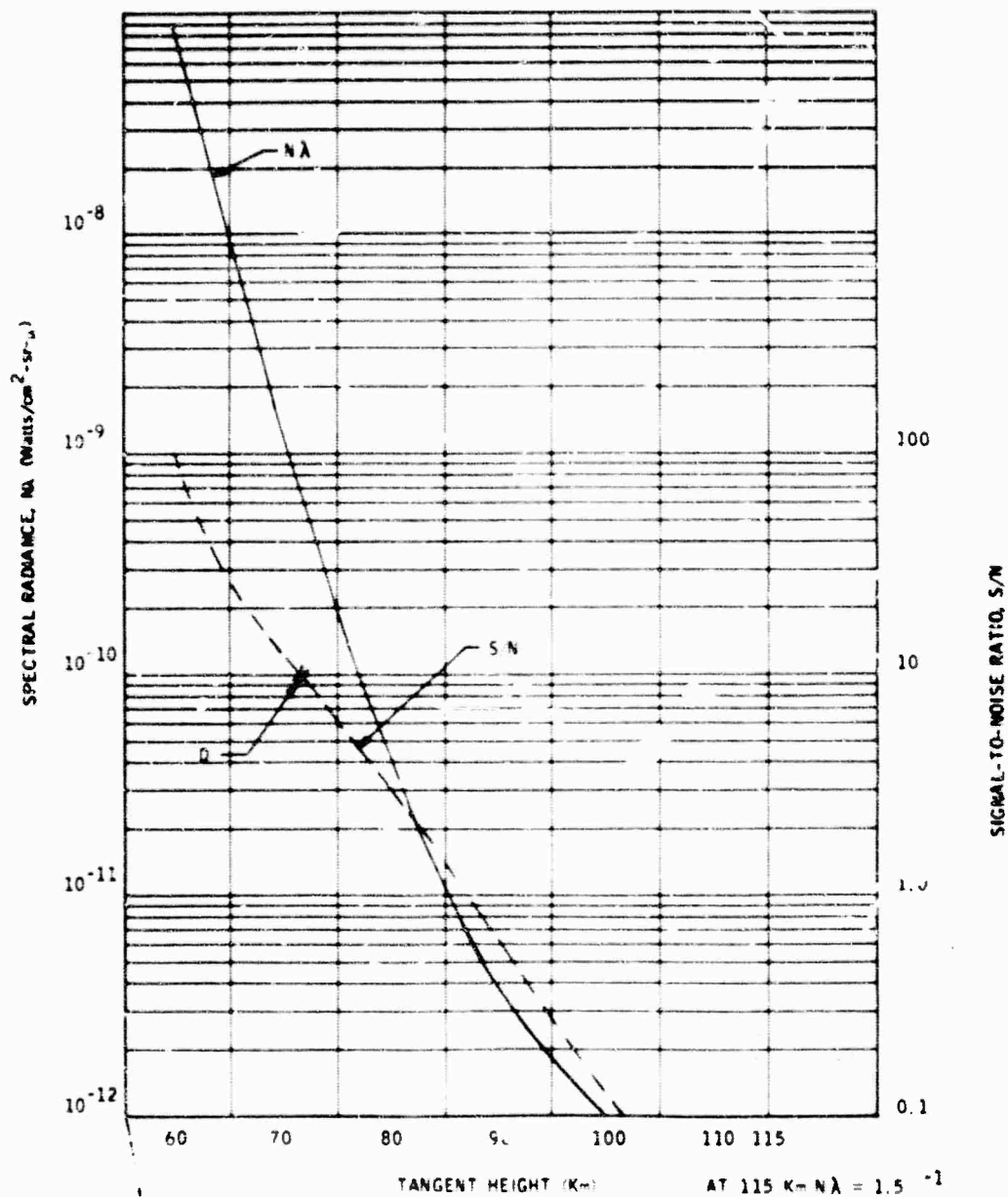


Figure A4. 7.0- to 7.2-micron Spectral Band

UNCLASSIFIED

UNCLASSIFIED

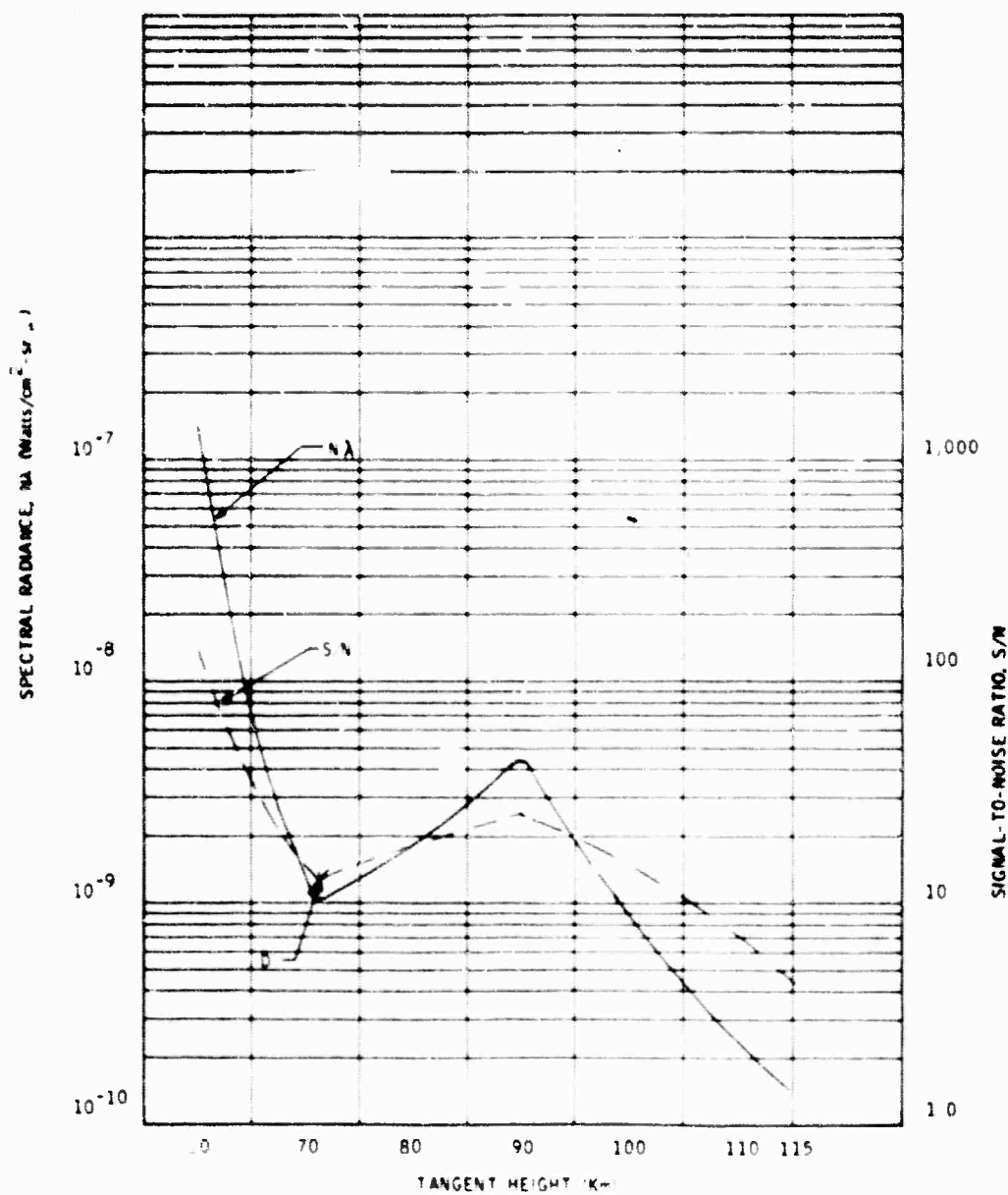


Figure A5. 7.4- to 7.6-micron Spectral Band

UNCLASSIFIED

UNCLASSIFIED

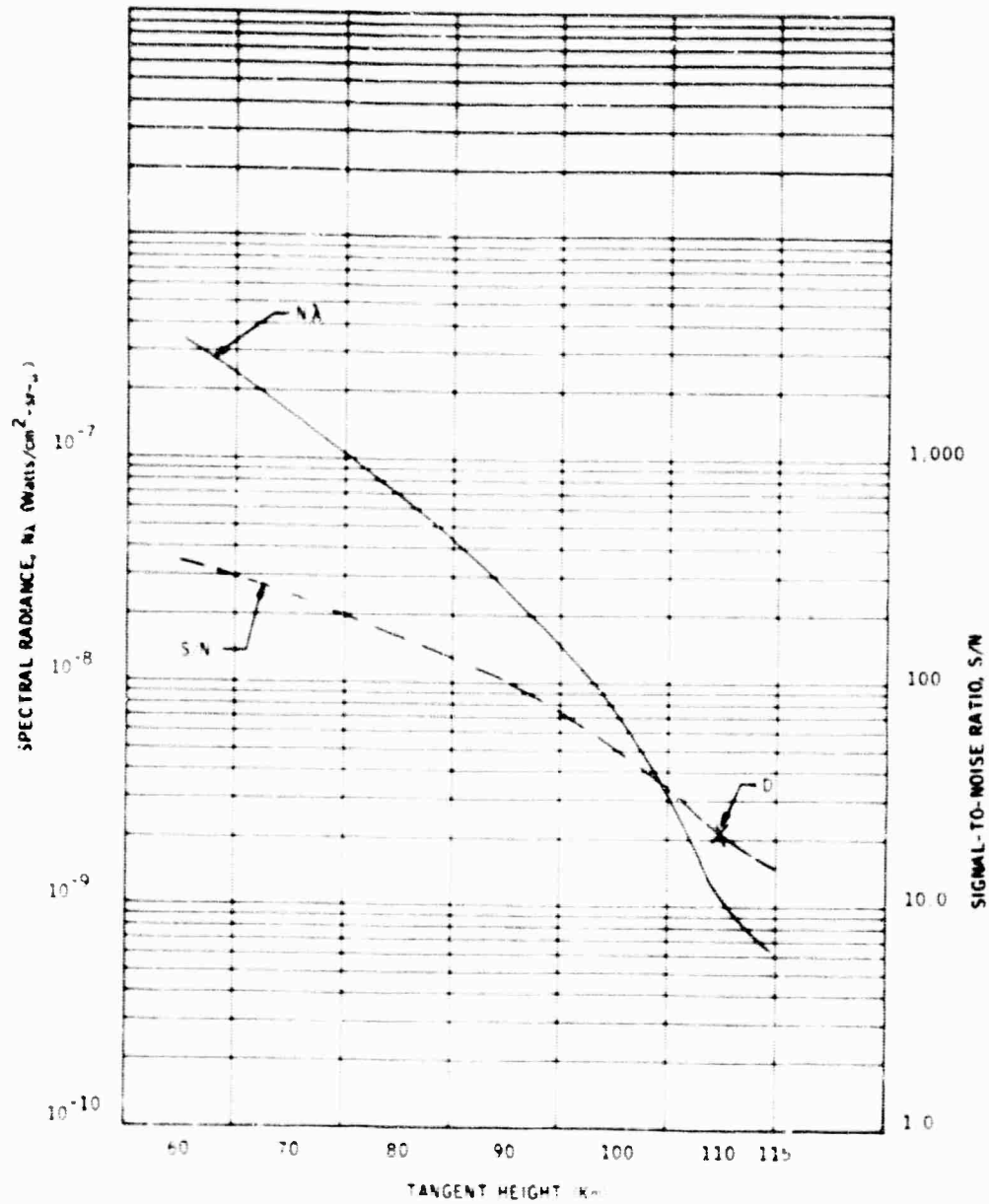


Figure A6. 7.6- to 8.0-micron Spectral Band

UNCLASSIFIED

UNCLASSIFIED

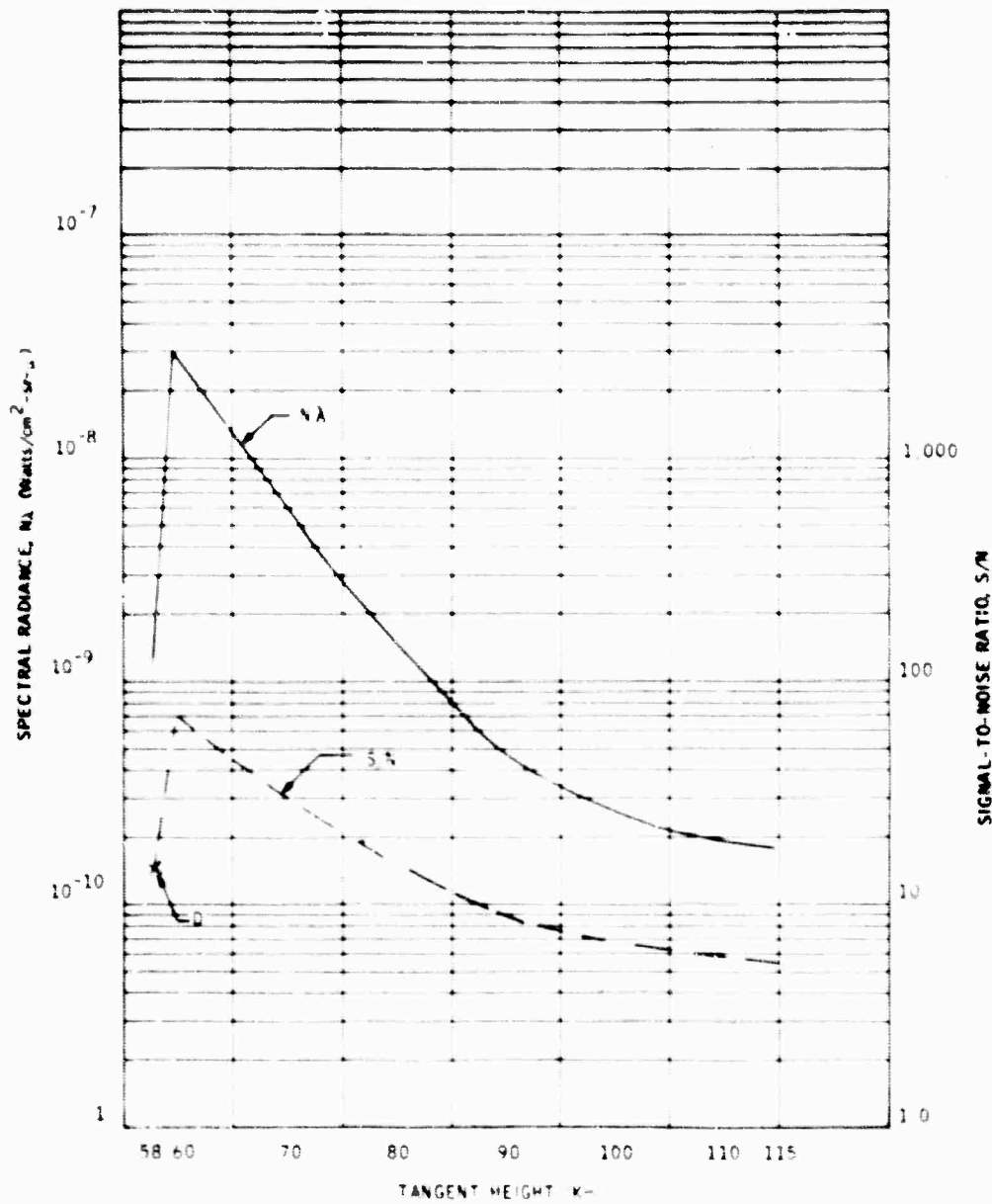


Figure A7. 8.1- to 8.3-micron Spectral Band

UNCLASSIFIED

UNCLASSIFIED

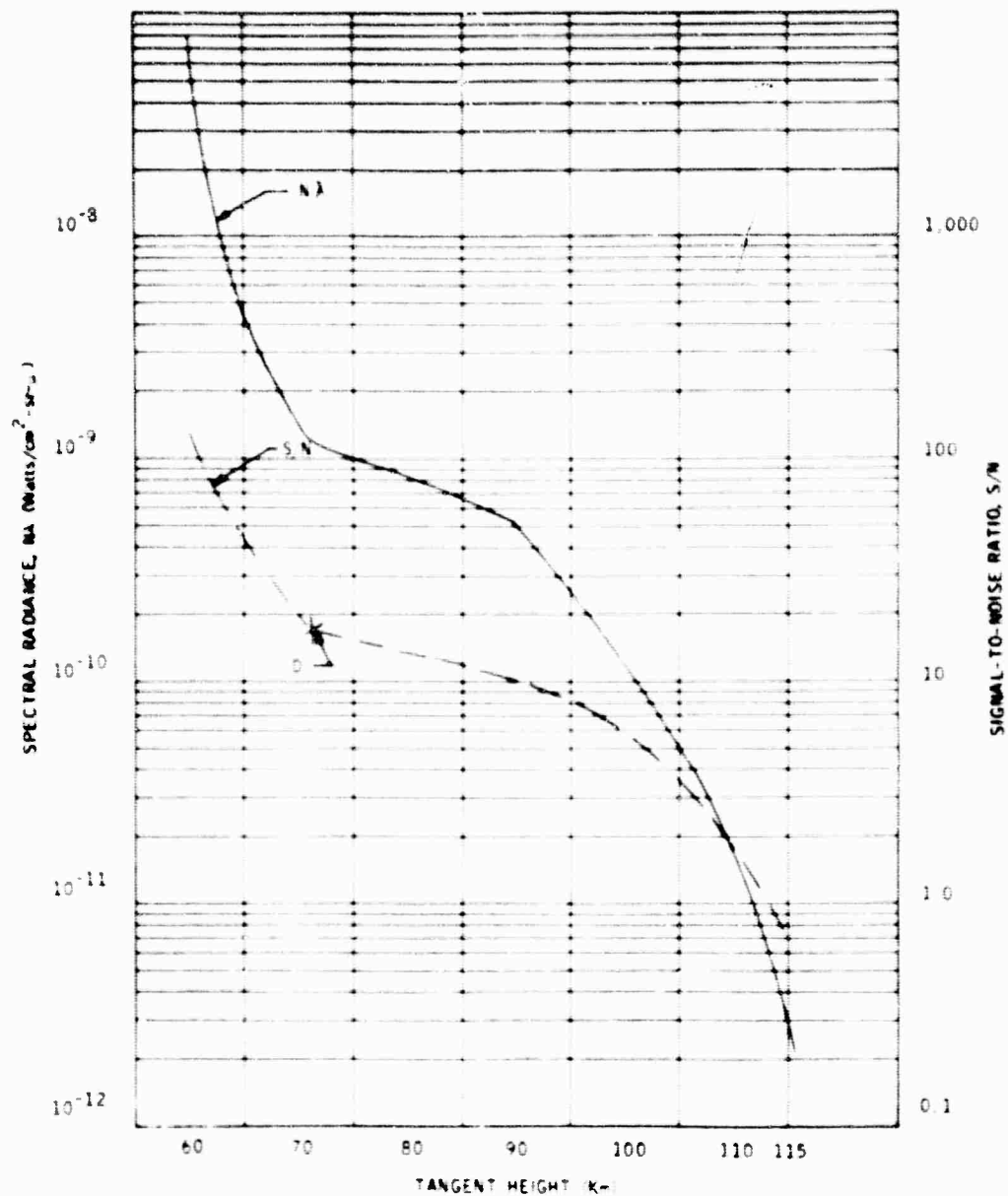


Figure A8. 9.1- to 9.3-micron Spectra. Band

UNCLASSIFIED

UNCLASSIFIED

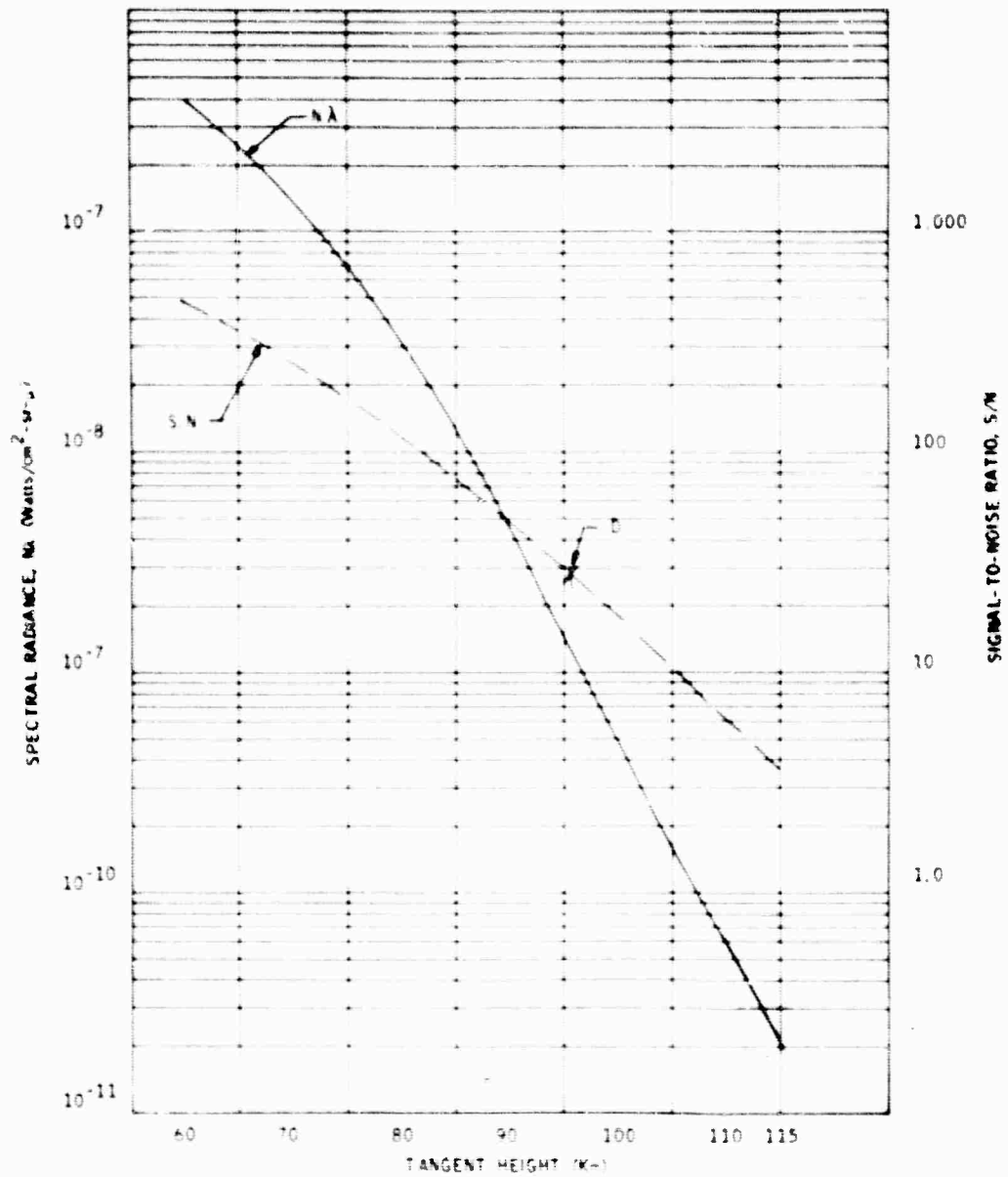


Figure A9. 9.3- to 10.0-micron Spectral Band

UNCLASSIFIED

UNCLASSIFIED

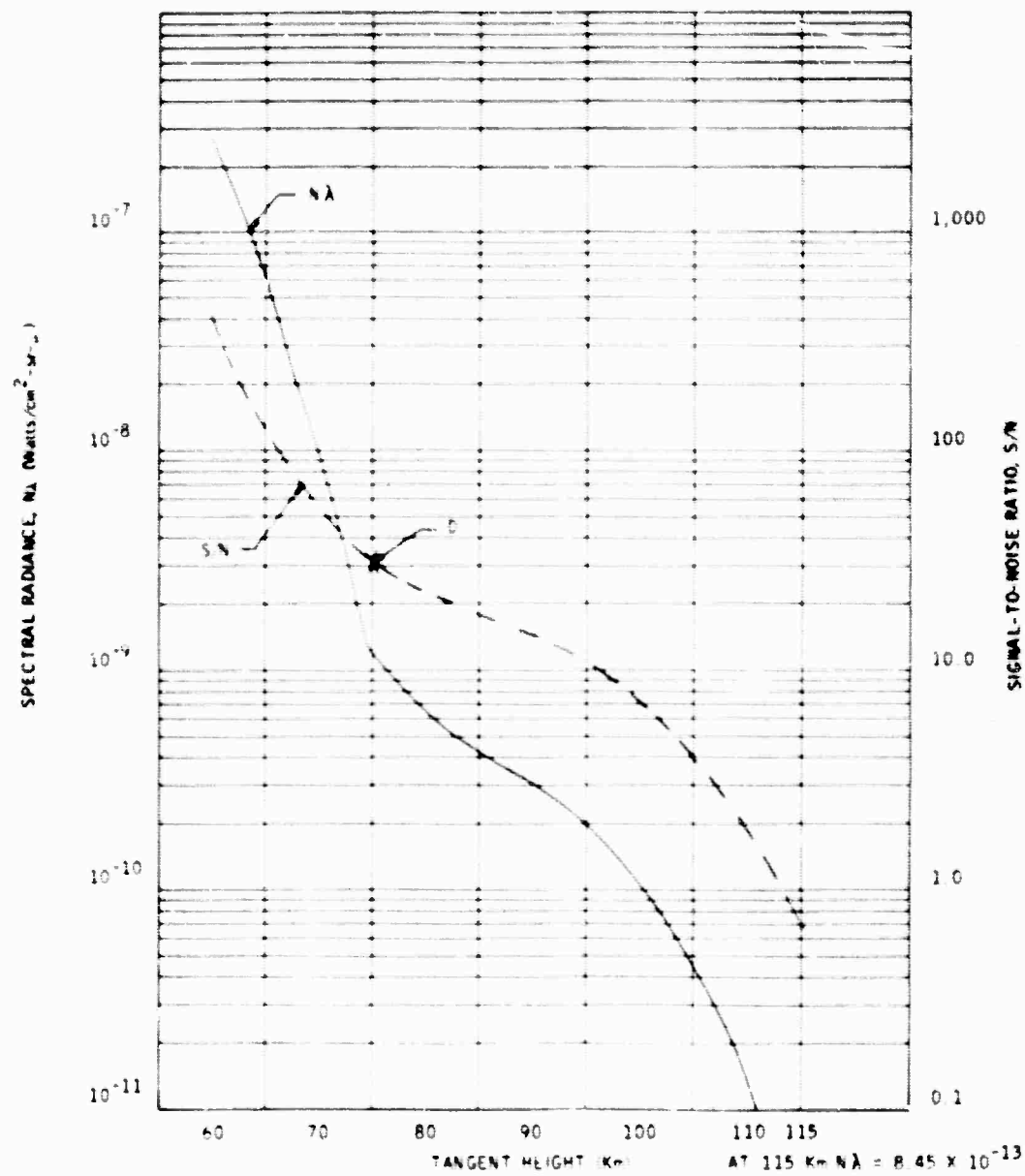


Figure A10. 10.0- to 10.8-micron Spectral Band

UNCLASSIFIED

UNCLASSIFIED

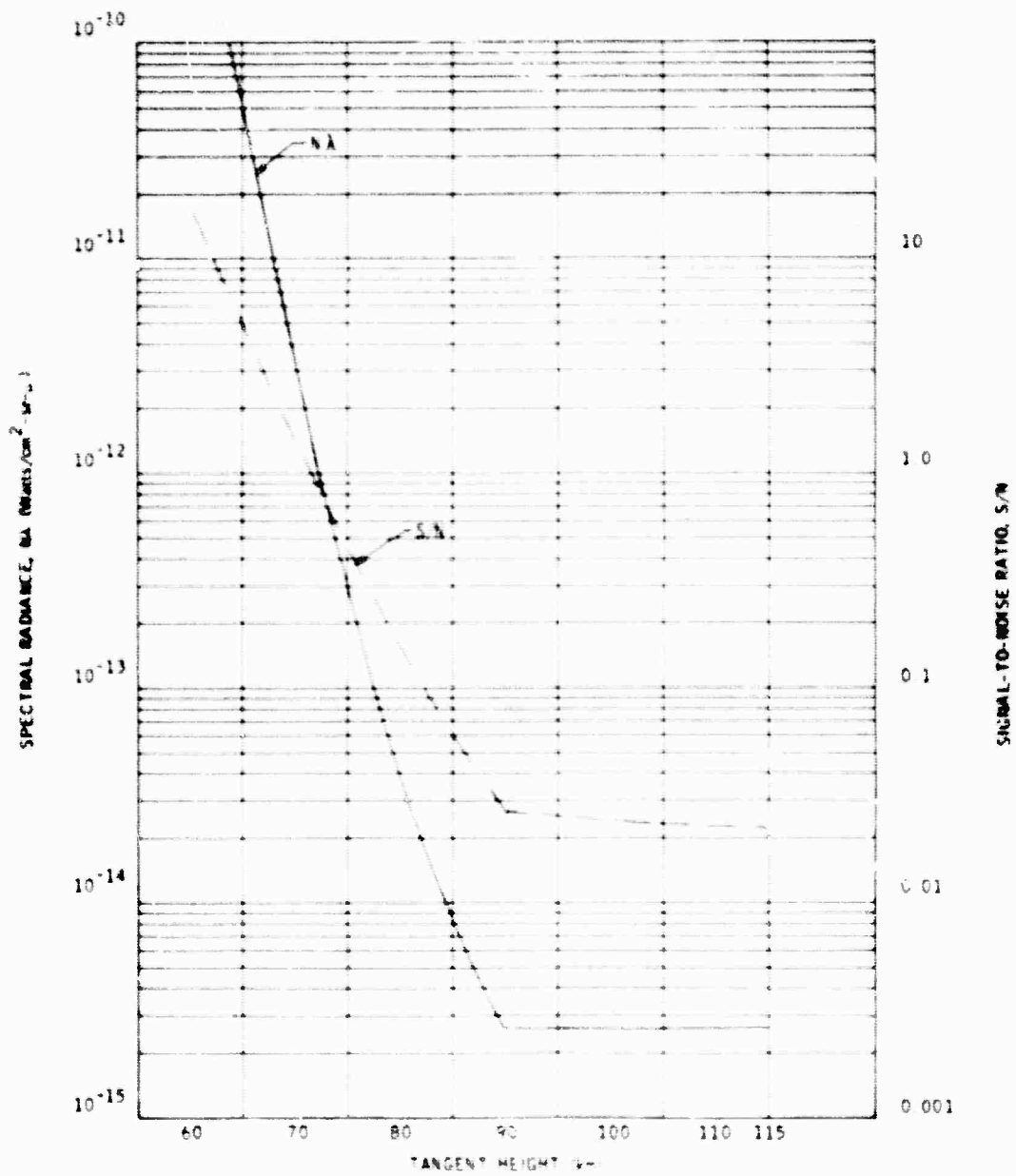


Figure A11. 11.0- to 11.3-micron Spectral Band

UNCLASSIFIED

UNCLASSIFIED

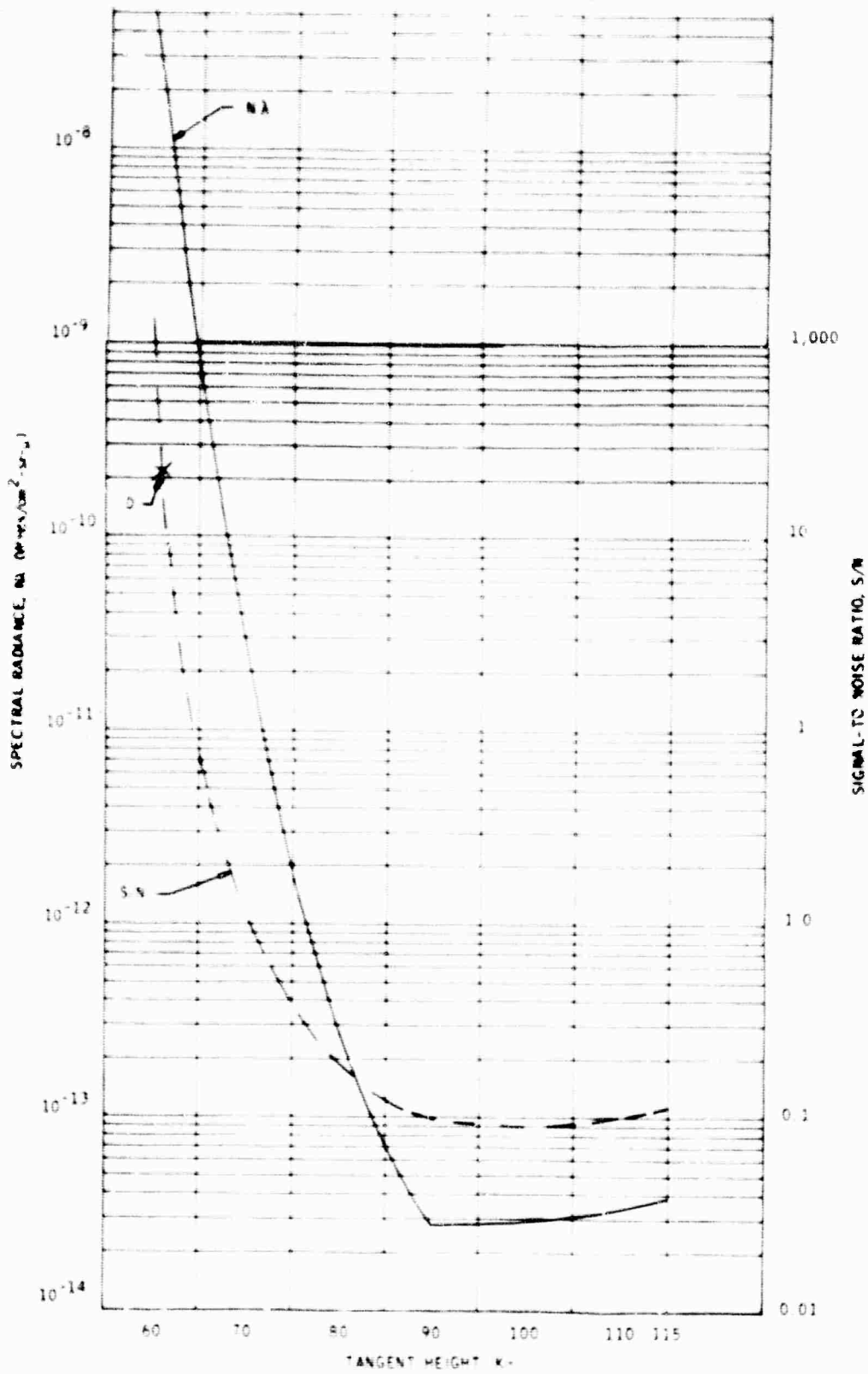


Figure A12. 12.0- to 13.0-micron Spectral Band

UNCLASSIFIED

UNCLASSIFIED

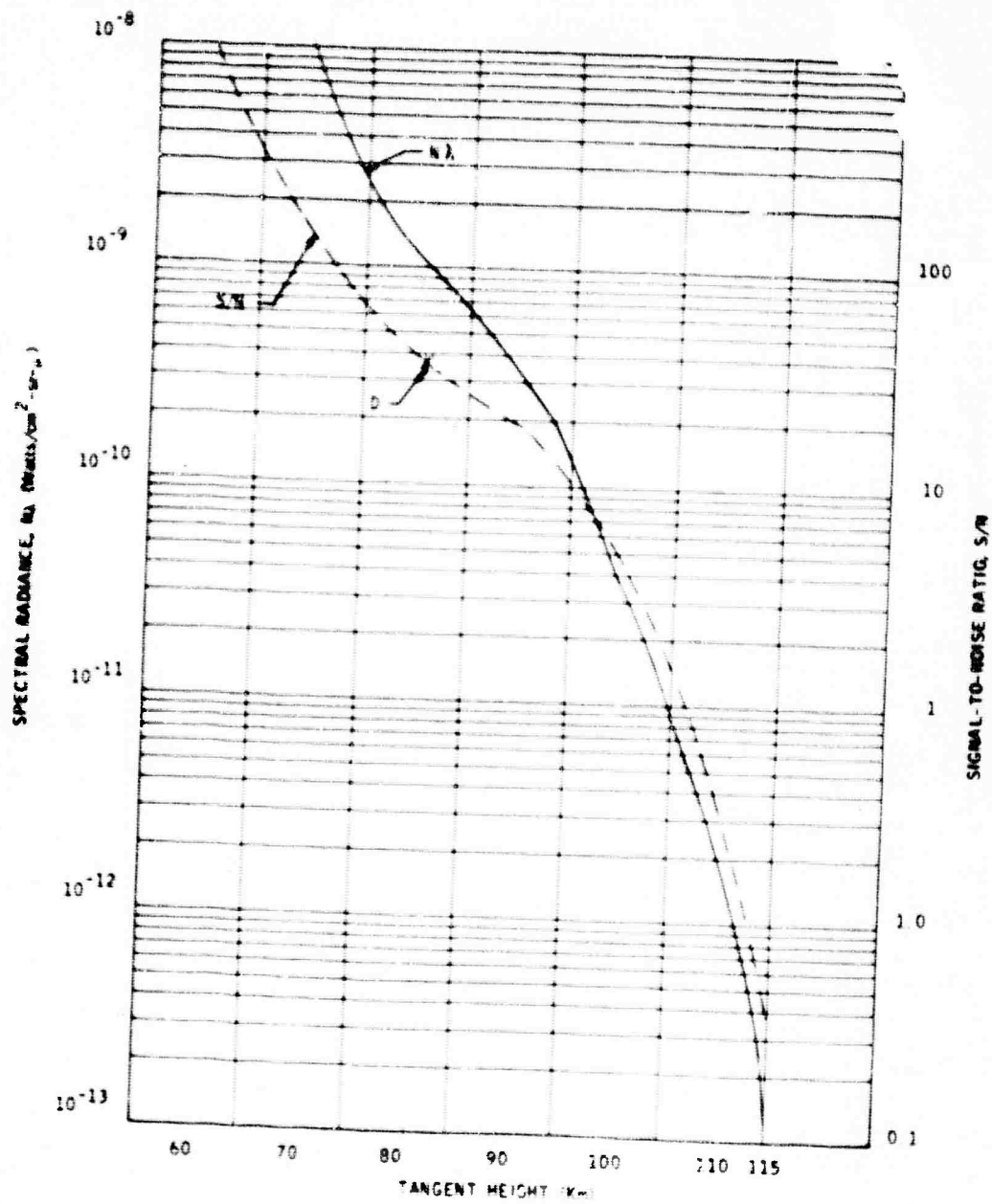


Figure A13. 13.1- to 14.0-micron Spectral Band

UNCLASSIFIED

UNCLASSIFIED

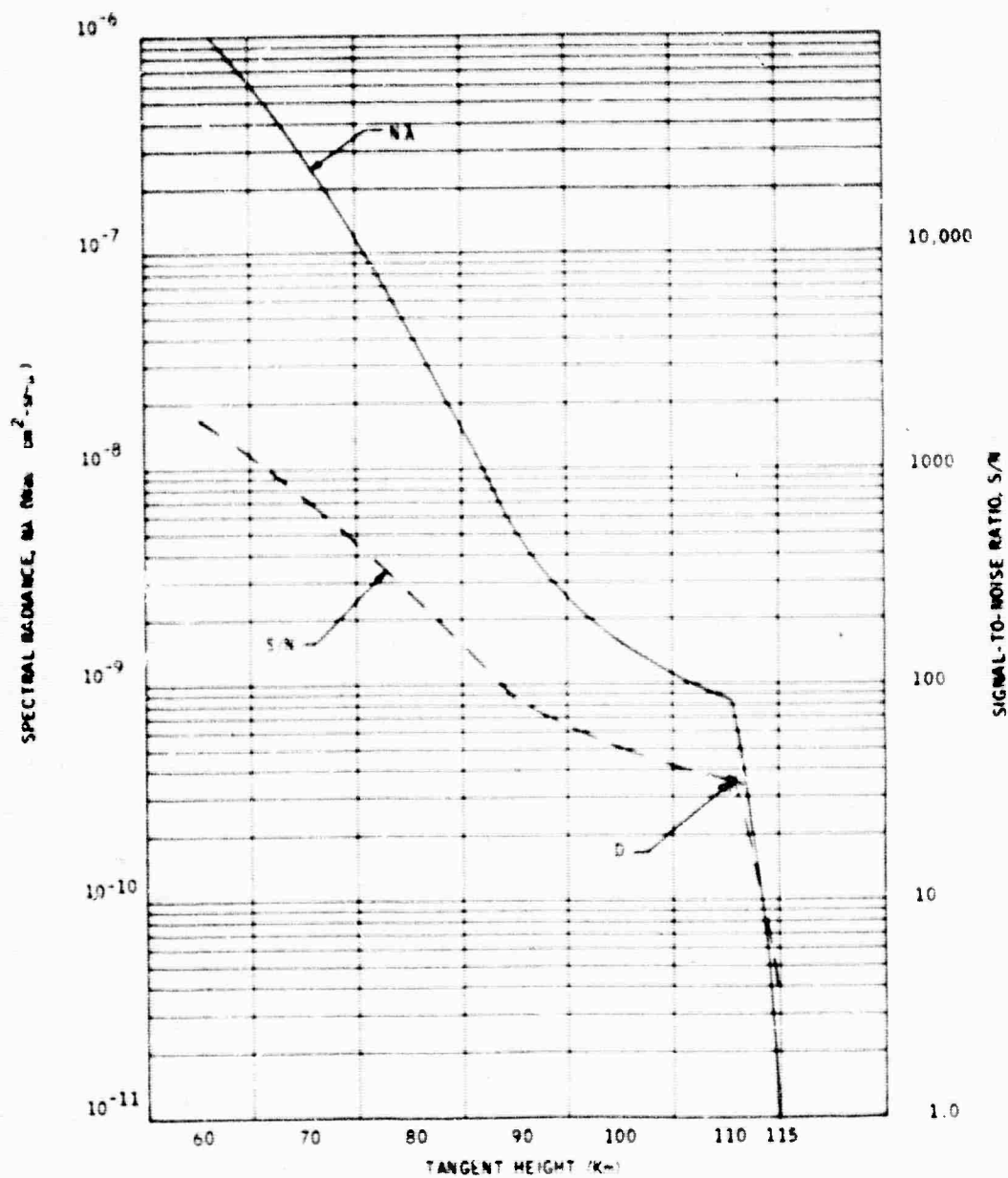


Figure A14. 14.0- to 15.0-micron Spectral Band

UNCLASSIFIED

UNCLASSIFIED

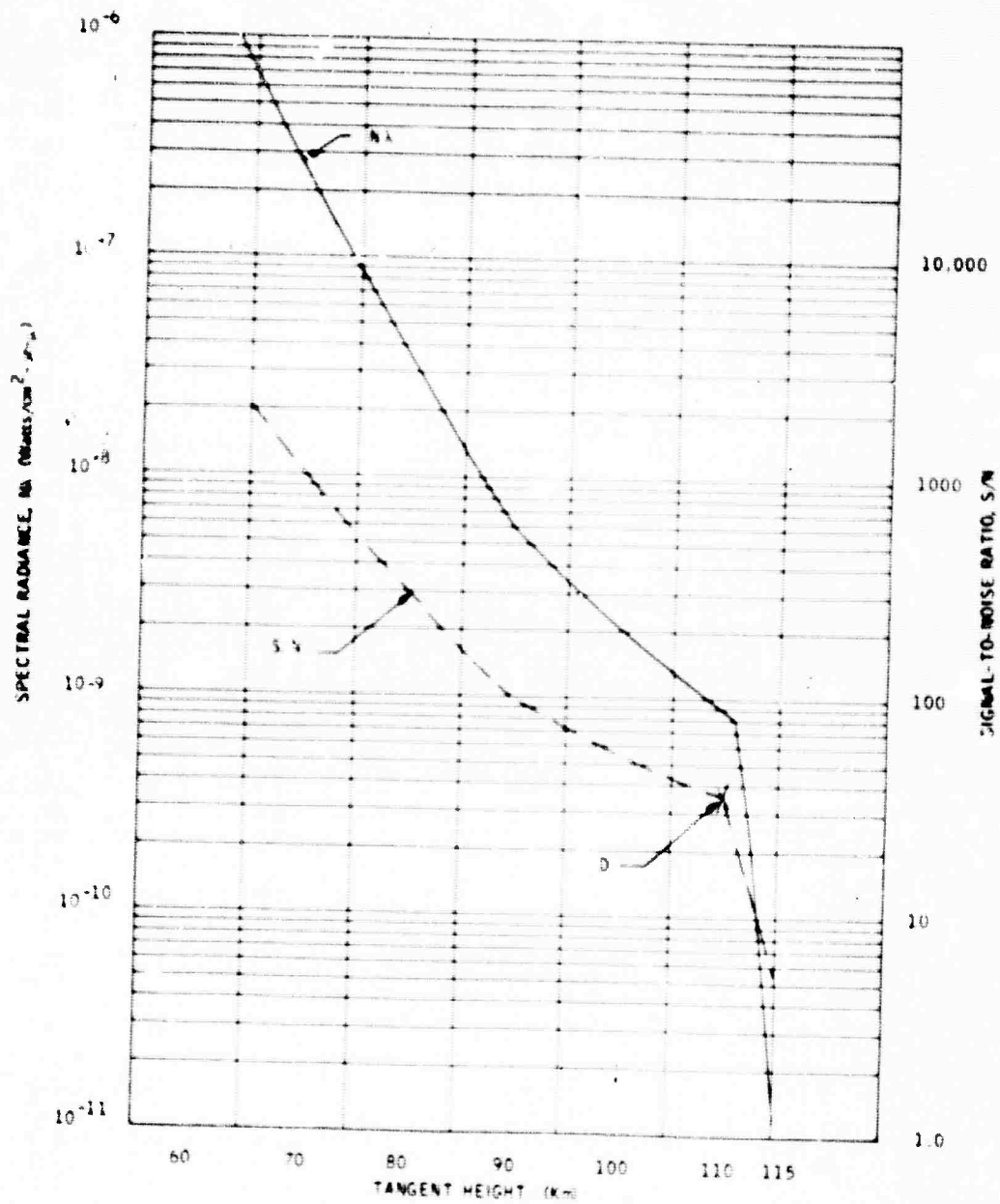


Figure A15. 15.0- to 16.0-micron Spectral Band

UNCLASSIFIED

UNCLASSIFIED

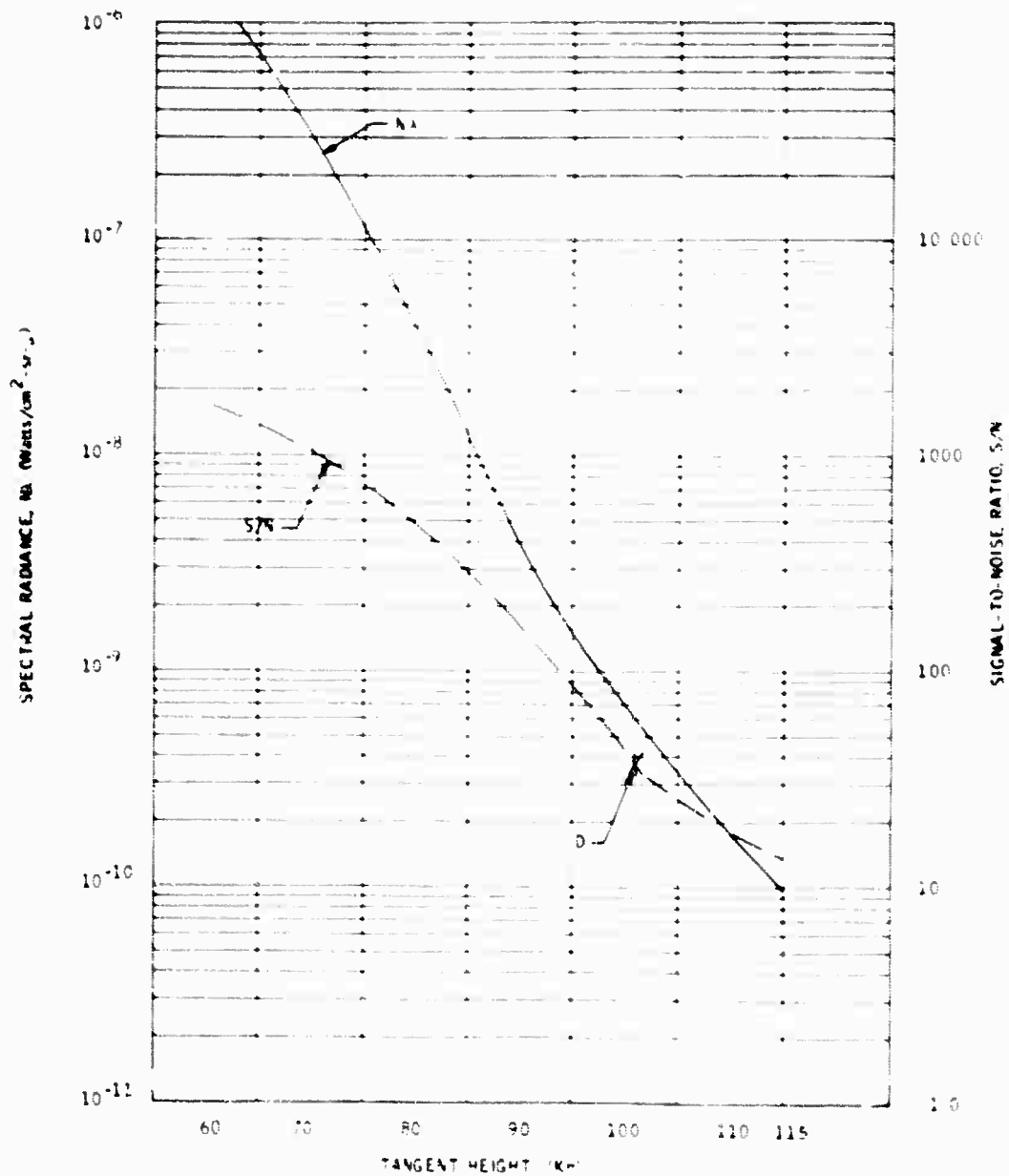


Figure A16. 16.0- to 17.0-micron Spectral Band

UNCLASSIFIED

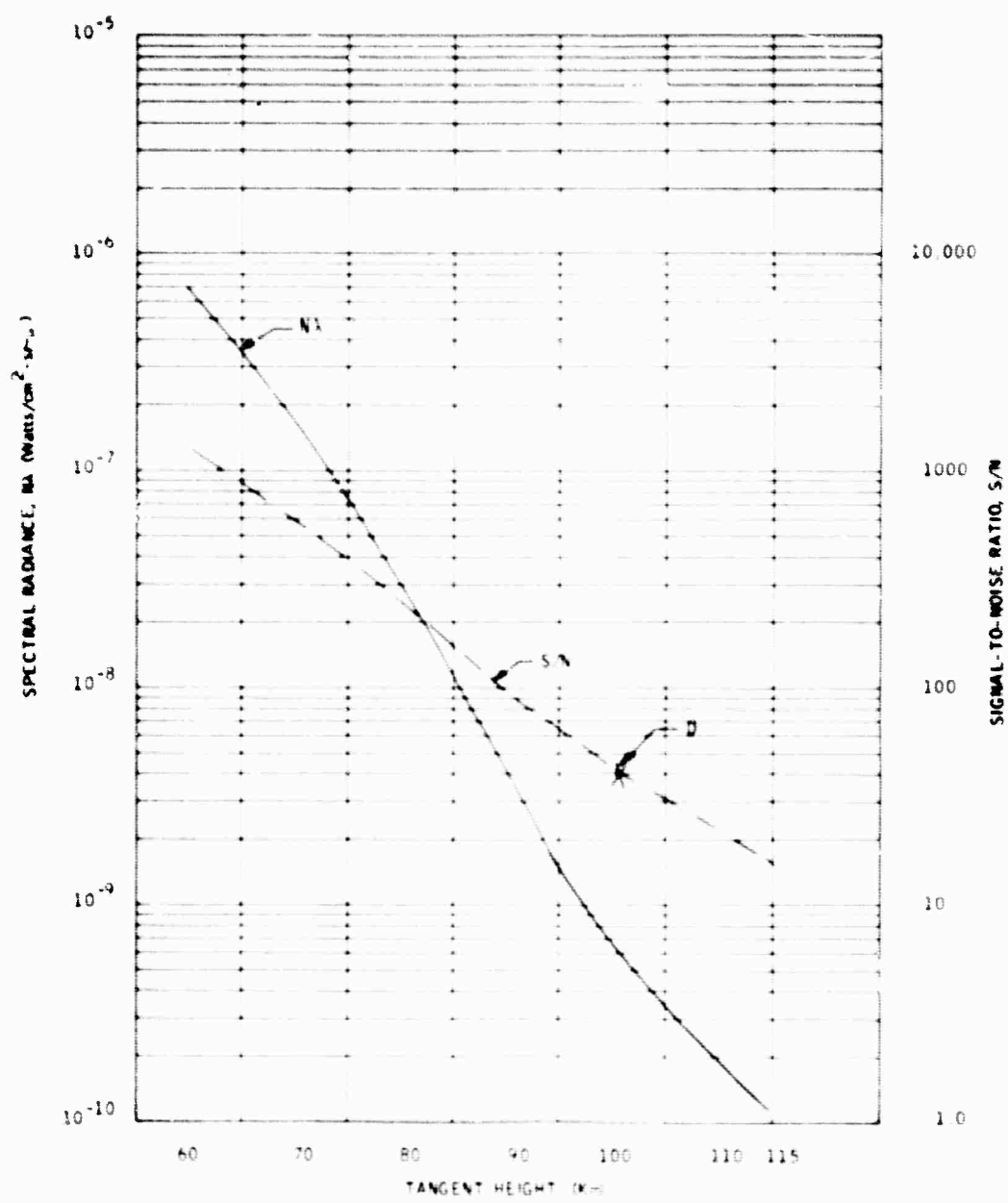


Figure A17. 17.0- to 18.0-micron Spectral Band

UNCLASSIFIED

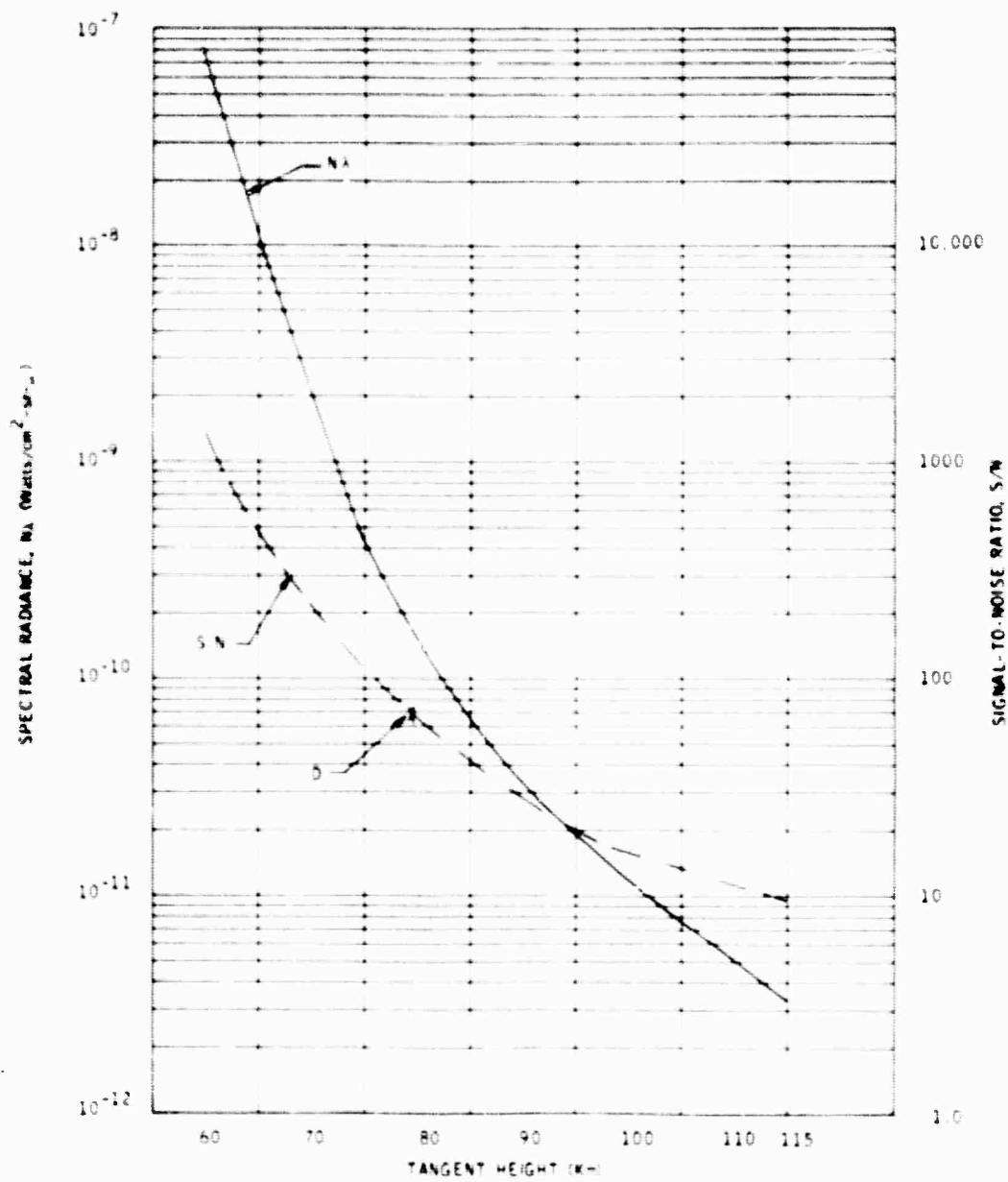


Figure A18. 18.0- to 25.0-micron Spectral Band

UNCLASSIFIED

UNCLASSIFIED

Security Classification

DOCUMENT CONTROL DATA - R & D

(Security classification of title, body of abstract and indexing annotation must be entered when the overall report is classified)

1. ORIGINATING ACTIVITY (Corporate author)
Honeywell Inc., Aerospace Division
2600 Ridgway Parkway
Minneapolis, Minnesota 55413

2a. REPORT SECURITY CLASSIFICATION
SECRET

2b. GROUP
4

3. REPORT TITLE

SYSTEM AND INSTRUMENT DESIGN FOR AN EARTH LIMB MEASUREMENTS PROGRAM (U)

4. DESCRIPTIVE NOTES (Type of report and inclusive dates)

Scientific Final 1 April 1969 - 1 January 1970 Approved 8 Dec 70

5. AUTHOR(S) (Last name, middle initial, first name)

Robert M. Carlson
Joseph S. Titus
Glenn H. Wise

6. REPORT DATE

15 April 1971

7a. TOTAL NO OF PAGES

311

7b. NO OF REFS

10

8a. CONTRACT OR GRANT NO. ARPA Order No. 1366

F19628-69-C-0258

8b. ORIGINATOR'S REPORT NUMBER(S)

AFM-442 (SP-5030)

Final Report (Phase II)

9. PROJECT NO.

8692

• DOD Element 62301D

10. OTHER REPORT NUMBER(S) (Any other numbers that may be assigned this report)

AF CRL-70-0496

11. DISTRIBUTION STATEMENT

In addition to security requirements which apply to this document and must be met, each transmittal outside the Department of Defense must have prior approval of AF CRL (OPR), L. G. Hanscom Field, Bedford, Massachusetts 01730.

12. SUPPLEMENTARY NOTES

This research was supported by the Advanced Research Projects Agency.

13. SPONSORING/MILITARY ACTIVITY

Air Force Cambridge Research Laboratories (OPR)
L. G. Hanscom Field
Bedford, Massachusetts 01730

14. ABSTRACT

Requirements for a spectral radiometer to measure the earth limb in the long-wavelength infrared have been established. Temporal and spatial sampling requirements for an experimental program to define the variation in the limb radiance have been investigated. An experimental program using probes has been designed to meet these requirements. The conceptual design of a long-wavelength infrared spectral radiometer is included in the experiment design.

DD FORM 1473

REPLACES DD FORM 1473, 1 JAN 66, WHICH IS OBSOLETE FOR 2-DAY USE

UNCLASSIFIED

Security Classification

~~SECRET~~

REF 00000

Long-wavelength infrared earth limb measurement spectral radiometer

SEVENTH

~~UNCLASSIFIED~~
~~Security Classification~~

THIS REPORT HAS BEEN DELIMITED
AND CLEARED FOR PUBLIC RELEASE
UNDER DOD DIRECTIVE 5200.20 AND
NO RESTRICTIONS ARE IMPOSED UPON
ITS USE AND DISCLOSURE.

DISTRIBUTION STATEMENT A

APPROVED FOR PUBLIC RELEASE,
DISTRIBUTION UNLIMITED.